DEVELOPMENT AND PHOTOCATALYTIC PROPERTIES OF POTASSIUM TITANATE NANOSTRUCTURE EMBEDDED RESIN COMPOSITES

A THESIS SUBMITTED TO
THE GRADUATE SCHOOL OF NATURAL AND APPLIED SCIENCES
OF
MIDDLE EAST TECHNICAL UNIVERSITY

BY

DERYA KAPUSUZ

IN PARTIAL FULFILLMENT OF THE REQUIREMENTS
FOR
THE DEGREE OF DOCTOR OF PHILOSOPHY
IN
METALLURGICAL AND MATERIALS ENGINEERING

FEBRUARY 2016

Approval of the thesis:

DEVELOPMENT AND PHOTOCATALYTIC PROPERTIES OF POTASSIUM TITANATE NANOSTRUCTURE EMBEDDED RESIN COMPOSITES

submitted by **DERYA KAPUSUZ** in partial fulfillment of the requirements for the degree of **Doctor of Philosophy in Metallurgical and Materials Engineering Department, Middle East Technical University** by,

Prof. Dr. Gülbin Dural Ünver
Dean, Graduate School of **Natural and Applied Sciences** _____

Prof. Dr. C. Hakan Gür
Head of Department, **Metallurgical and Materials Engineering** _____

Prof. Dr. Abdullah Öztürk
Supervisor, **Metallurgical and Materials Eng. Dept., METU** _____

Assoc. Prof. Dr. Jongee Park
Co-Supervisor, **Metallurgical and Materials Eng. Dept., Atılım Uni.** _____

Examining Committee Members:

Prof. Dr. İshak Karakaya
Metallurgical and Materials Eng. Dept., METU _____

Prof. Dr. Abdullah Öztürk
Metallurgical and Materials Eng. Dept., METU _____

Prof. Dr. Hasan Göçmez
Materials Science and Eng. Dept., Dumlupınar University _____

Prof. Dr. Caner Durucan
Metallurgical and Materials Eng. Dept., METU _____

Assoc. Prof. Dr. Hilal T. Şaşmazel
Metallurgical and Materials Eng. Dept., Atılım University _____

Date: 05.02.2016

I hereby declare that all information in this document has been obtained and presented in accordance with academic rules and ethical conduct. I also declare that, as required by these rules and conduct, I have fully cited and referenced all material and results that are not original to this work.

Name, Last name : Derya Kapusuz

Signature :

ABSTRACT

DEVELOPMENT AND PHOTOCATALYTIC PROPERTIES OF POTASSIUM TITANATE NANOSTRUCTURE EMBEDDED RESIN COMPOSITES

Kapusuz, Derya

Ph.D., Department of Metallurgical and Materials Engineering
Supervisor: Prof. Dr. Abdullah Öztürk
Co-Supervisor: Assoc. Prof. Dr. Jongee Park

February 2016, 178 pages

Structural and functional properties of potassium titanate (PT; $K_2O.nTiO_2$, n=2, 4) nanostructures synthesized by sol-gel and hydrothermal methods were investigated with respect to titanium/potassium (Ti/K) ratio and their nano-growth mechanisms were elucidated. Produced powders were characterized by XRD, electron microscopy (SEM, TEM) and gas adsorption (BET) techniques for phase, morphology and surface analyses, respectively. PT nanostructures were mixed with three UDMA-TEGDMA (UT) resin monomer mixtures in the order of increasing TEGDMA molar ratio of UT-2 (30%), UT-1 (50%), UT-3 (70%). Polymerization of the composites was accomplished by halogen light curing. Tensile, hardness, wear, water sorption/solubility and bioactivity tests were performed to determine the performance of the composites. The energy band gap (E_g) of PT powders, the photocatalytic activity of PT powders and PT-UT composites were measured by UV-Vis Spectroscopy equipped with diffuse reflectance (DR) module. Methylene Blue (MB) dye degradation tests were performed to evaluate photocatalytic performance. It was demonstrated that both sol-gel and hydrothermal growth of PTs originate from an amorphous-like network. Potassium hexa-titanate (PHT, n=6) nanowires could be obtained by calcination of sol-gel derived amorphous network at temperatures as low as 600 °C. As the calcination temperature increased to 800 °C, potassium tetra-titanate (PTT, n=4) formation became significant.

In addition, the size and aspect ratio of PTs increased as the calcination temperature and time increased (1-3 h). In sol-gel process, potassium hollandite (PH, KTi_8O_{16}) was an intermediate phase upon PHT crystallization. However, PHT and PTT nanowires grew directly from the hydrothermal solution under autogeneous pressure. Analysis indicated that amorphous network combined into sheets, crystallized into PTs and then split due to increased strain. The highest average size of sol-gel derived PT whiskers depending on Ti/K ratio were measured as 214 ± 113 nm in diameter and 4.9 ± 2.5 μm in length. The size of split PT nanowires were measured as 39 ± 14 nm in diameter and 1.14 ± 0.4 μm in length, after 24 h of hydrothermal treatment at 180 °C. The size of the nanostructures decreased as the hydrothermal duration increased to 48 h due to further splitting. Hydrothermal treatment provided PTs having E_g lower than widely used commercial TiO_2 (P25, Degussa®) powder. Analysis of PT-UT composites revealed that mechanical and functional performances of the composites were mainly related to the PT embedment amount and dispersion efficiency. The lowest specific wear rate was achieved for the composite containing 5 wt % hydrothermally synthesized PT embedded UT-1 (50% UDMA – 50% TEGDMA, molar) mixture as 6.5 ± 0.6 $*10^{-6}$ mm^3/Nm by 5 wt % hydrothermally produced PT embedded UT-1 (50% U-50% T, molar) mixture. Similarly, tensile strength and elastic modulus of UT-1 mixture increased from 40.4 ± 1.7 MPa to 42.5 ± 0.2 MPa, and from 0.7 ± 0.04 GPa to 0.9 ± 0.1 GPa, respectively by embedding 5 wt % hydrothermally synthesized PT. The water sorption and solubility values were higher than 40 $\mu g/mm^3$. The MB degradation test and analyses after simulated body fluid immersion showed that PTs preserved their photocatalytic performance and bioactivity in the composite form. MB degradation of composites in 24 h increased with increased PT embedment in the composite.

Keywords: potassium titanate, sol-gel, hydrothermal, photocatalytic, resin composite.

ÖZ

POTASYUM TITANAT NANOYAPI KATKILI REÇİNE KOMPOZİTLERİN GELİŞTİRİLMESİ VE FOTOKATALİTİK ÖZELLİKLERİ

Kapusuz, Derya

Doktora, Metalurji ve Malzeme Mühendisliği Bölümü
Tez Yöneticisi : Prof. Dr. Abdullah Öztürk
Ortak Tez Yöneticisi : Doç. Dr. Jongee Park

Şubat 2016, 178 sayfa

Bu tez çalışması, sol-jel ve hidrotermal yöntemler kullanılarak üretilen potasyum titanat (PT; $K_2O.nTiO_2$, n=2, 4) nanoyapılarının yapısal ve fonksiyonel özelliklerinin titanium/potasyum oranına (Ti/K) bağlı olarak incelenmesini nano-büyüme mekanizmalarının belirlenmesini içermektedir. Elde edilen tozların, XRD, elektron mikroskobisi (SEM, TEM) ve gaz adsorpsiyon (BET) teknikleri kullanılarak sırasıyla faz, morfoloji ve yüzey analizleri yapılmıştır. PT tozları üç farklı UDMA-TEGDMA (UT) reçine monomer karışımına eklenmiştir. Kullanılan monomer karışımlarında TEGDMA oranı UT-2 (%30), UT-1 (%50) ve UT-3 (%70) sırası ile artmaktadır. Polimerleştirme işlemi halojen ışık kullanılarak gerçekleştirilmiştir. Kompozitlerin performanslarını belirlemek için çekme, sertlik, aşınma, su emme/çözünürlük ve biyoaktivite testleri uygulanmıştır. PT tozlarının enerji bant aralıkları (E_g), PT tozlarının ve PT-UT kompozitlerinin fotokatalitik aktiviteleri difüz reflektör (DR) modülü donatımlı UV-Vis spektrofotometre kullanılarak ölçülmüştür. Fotokatalitik performansın belirlenmesi için metil mavi (MV) boyası bozunum testi uygulanmıştır. Elde edilen sonuçlar, hem sol-jel hem de hidrotermal yöntem kullanıldığında, PT kristallenmesinin amorf bir yapı içerisinde başladığını göstermiştir. Sol-jel yöntemi ile üretilen amorf yapıda 600 °C de kalsinasyon işlemi sonucunda potasyum hegza-titanat (PHT, n=6) nanotellerinin oluşumu belirlenmiştir.

Kalsinasyon sıcaklığı 800 °C'ye arttırıldığında ise potasyum tetra-titanat (PTT, n=4) oluşumu belirginleşmiştir. Ayrıca, kalsinasyon sıcaklığı ve süresindeki artış (1-3 saat) PT nanoyapılarının boyut ve boy/en oranlarında artışa sebep olmuştur. Sol-jel sürecinde potasyum hollandit (PH, KTi_8O_{16}) fazının PHT kristallenmesi öncesinde ara faz olarak oluştuğu belirlenmiştir. Fakat, hidrotermal çözelti içerisinde PHT ve PTT nanotelleri doğrudan kristallenmektedir. Yapılan analizler, amorf yapının tabakalar halinde birleştiğine, PT yapıların kristallendiğine ve de oluşan gerinim sebebiyle PT nanotellerine bölündüğüne işaret etmektedir. Sol-jel yöntemi üretilen örneklerden Ti/K oranına bağlı olarak ölçülen en yüksek PT ince fiber çapı 214 ± 113 nm, boyu 4.9 ± 2.5 μm'dir. 180 °C'de 24 saat reaksiyon sonucu bölünen PT nanotellerinin ortalama çapı 39 ± 14 nm, boyu 1.14 ± 0.4 μm'dir. Reaksiyon süresi 48 saate çıkarıldığında ortalama boyutlar daha fazla bölünme sonucu küçülmüştür. Hidrotermal reaksiyon ticari olarak satılan TiO_2 tozundan (P25, Degussa®) daha düşük E_g 'e sahip PT nanoyapılarının üretilmesini sağlamıştır. PT-UT kompozitleri üzerinde yapılan analizler, kompozitlerin mekanik ve fonksiyonel özelliklerinin temelde PT katkı miktarı ve dağılım verimine bağlı olduğunu göstermiştir. En düşük aşınma hızı ağ. % 5 hidrotermal yöntemle üretilmiş PT katkılı UT-1 kompozitinden, $6.5 \pm 0.6 * 10^{-6}$ mm^3/Nm olarak ölçülmüştür. Ağ. % 5 hidrotermal yöntemle üretilmiş PT katkısı çekme mukavemetinin katkısız UT-1 polimerine kıyasla 40.4 ± 1.7 MPa'dan to 42.5 ± 0.2 MPa'a artışını sağlamıştır. Benzer olarak, elastik modül 0.7 ± 0.04 GPa 'dan 0.9 ± 0.1 GPa'a yükselmiştir. Kompozitlerin su emme değerleri 40 $\mu g/mm^3$'nin üzerindedir. MV bozunum ve simule vücut sıvısına tabi tutularak yapılan biyoaktivite testleri PT nanoyapılarının fotokatalitik ve bioaktiflik özelliklerini kompozit matris içerisinde koruyabildiğini göstermiştir. Kompozitin 24 saat içerisindeki MV bozunum hızı PT katkı miktarı ile artış göstermiştir.

Anahtar Kelimeler: potasyum titanat, hidrotermal, fotokatalitik, reçine kompoziti

To the memory of my grandmother; the woman, whom I still miss everyday...

ACKNOWLEDGEMENTS

First of all, I would sincerely record my deepest gratitude to my supervisor; Prof. Dr. Abdullah Öztürk for his guidance and encouragement throughout the dissertation research. He always supported and guided me on this long journey. I would also like to thank to my co-supervisor, Assoc. Prof. Dr. Jongee Park for his creative ideas. I would also like to express my thanks to my committee members Assoc. Prof. Dr. Hilal T. Şaşmazel and Assoc. Prof. Dr. Y. Eren Kalay. I would like to extend my sincerest thanks to Assoc. Prof. Dr. Y. Eren Kalay for his help and guidance on TEM analysis and Serkan Yılmaz for his technical support on TEM imaging. I would like to express my special thanks to my lab-mates Lütfi Ağartan, Sıtkı Can Akkuş, Başak Aysin, Nursev Bilgin and Melis Kaplan for their never-ending support and patience even at my craziest moments. I will always remember our exhausting but enjoyable working times in the lab. In addition, I would also like to thank to my friends Şerif Kaya, Kıvanç Korkmaz and Mehmet Ali Recai Önal for their endless friendship.

I acknowledge TUBITAK for funding me by 2214-A Scholarship between March 2014 and March 2015 for a scientific visit to Prof. Dr. Michel Barsoum's Research Group at Drexel University, USA. Also, I would like to mention that this work has been financially supported by TUBITAK 110M206 Project and METU Scientific Human Resources Development Program (ÖYP-DPT). Their supports are greatly acknowledged.

I would like to extend my sincerest gratitude to Prof. Dr. Michel Barsoum, Prof. Dr. Yury Gogotsi and Assoc. Prof Dr. Caroline Schauer for helping me gain experience on polymer composites and biomedical applications of nanomaterials. Also, I would like to thank to my lab-mates at Drexel University, especially Joseph Halim, Chunfeng Hu, Sankalp Kota and Darin Tallman for their help and nice friendship.

Finally, I would like to thank to my mother for always encouraging me and being beside me, no matter what. Words cannot express how much she means to me.

TABLE OF CONTENTS

ABSTRACT v
ÖZ vii
ACKNOWLEDGEMENTS x
TABLE OF CONTENTS xi
LIST OF TABLES xv
LIST OF FIGURES xvii
LIST OF ABBREVIATIONS xxiii

CHAPTERS
1. INTRODUCTION 1
1.1 Objective and significance of the dissertation 3
1.2 Overview of the chapters 4
2. BACKGROUND INFORMATION AND LITERATURE REVIEW 7
2.1 Potassium titanate nanostructures 7
2.1.1 Synthesis 7
2.1.2 Structure and morphology 9
2.1.3 Utilization 10
2.1.3.1 Photocatalytic degradation of pollutants 10
2.1.3.2 Ion-exchange processes 15
2.1.3.3 Composite reinforcement and biological applications 16
2.2. Methacrylate resins and resin composites as model systems for PT embedded biomedical composites 18
2.2.1 Polymerization reactions of methacrylate resins and resin composites 19
2.2.2 Types of inorganic reinforcements for dental resins 21
2.2.3 Silanization (Silane coupling) 26
2.2.4 Main problems associated with composite resins 28

3. EXPERIMENTAL PROCEDURES 31
3. 1. Synthesis of PTs by sol-gel technique 31
3.1. 1. Materials 31
3.1. 2. Procedure 32
3. 2. Synthesis of PTs by hydrothermal treatment 34
3.2. 1. Materials 34
3.2. 2. Procedure 34
3.3 Dispersion of agglomerates by sonication 36
3.4 Production of dental resins and composites 37
3.4. 1. Materials 37
3.4.2 Procedure 38
3.4.2. 1. Silanization 38
3.4.2. 2. Polymerization (Curing) 38
3. 5. Characterization and testing 43
3.5. 1. X-Ray diffraction (XRD) analysis 43
3.5. 2. Electron Microscopy analyses 43
3.5.3 Differential thermal analysis 45
3.5.4 Gas (N_2) adsorption (BET) analysis 45
3.5. 5. UV-Vis spectroscopy measurements 47
3.5.5.1 Energy band gap measurement by diffuse reflectance 47
3.5.5.2 Methylene blue degradation test 48
3.5. 6. Wear test 50
3.5.7 Hardness test 52
3.5.8 Tensile test 54
3.5.9 Water absorption and solubility test 55
3.5.10 Bioactivity test 56
4. RESULTS AND DISCUSSION: POTASSIUM TITANATE NANOSTRUCTURES SYNTHESIZED BY SOL-GEL AND HYDROTHERMAL METHODS 57
4. 1 Sol-Gel synthesis of PT nanostructures 57
4.1.1 Phase analysis by XRD 57
4.1.1.1 Powders obtained after calcination at 600 ºC 57

4.1.1.2 Powders obtained after calcination at 800 ºC.....61
4.1.2 SEM analysis.....63
4.1.2.1 Powders obtained after calcination at 600 ºC.....63
4.1.2.2 Powders obtained after calcination at 800 ºC.....65
4.1.3 Surface area (BET) analysis.....67
4.1.4 Growth mechanism of PT whiskers by sol-gel process.....69
4.1.5 Determination of band gap energy of PTs synthesized by sol-gel process.....77
4.1.6 Photocatalytic degradation performance of sol-gel derived PTs.....82
4.2. Hydrothermal synthesis of PT nanowires.....85
4.2.1 Phase analysis by XRD.....85
4.2.2 SEM analysis.....89
4.2.3 Surface area (BET) analysis.....91
4.2.4 Growth of potassium titanate nanowires by hydrothermal treatment.....94
4.2.5 Determination of E_g of hydrothermally synthesized PT by UV-Vis/DRS.....104
4.2.5.1 Effect of reaction time on energy band structure.....104
4.2.5.2 Effect of potassium concentration ($KOH^{aq.}$) on energy band structure.....108
4.2.6 Photocatalytic degradation performance of hydrothermally synthesized PTs 110
5. RESULTS AND DISCUSSION: POTASSIUM TITANATE NANOSTRUCTURE EMBEDDED UDMA-TEGDMA RESIN COMPOSITES..113
5.1 Neat UT resin mixtures.....113
5.1.1 Wear analysis.....114
5.1.2 Hardness test.....116
5.1.3 Tensile test.....117
5.1.4 Water sorption and solubility.....119
5.2 Sol-gel derived PT embedded UT resin composites.....121
5.2.1 XRD analysis.....121
5.2.2 Wear analysis.....123
5.2.3 Hardness.....123
5.2.4 Conclusive remarks of preliminary experiments on sol-gel derived PT embedded UT resin composites.....126
5.3 Hydrothermally synthesized PT embedded UT resin composites.....127
5.3.1 XRD analysis.....127

5.3.2 Wear analysis 128
5.3.2.1 As- prepared PTs 128
5.3.2.2 Post-treated PTs (sonication, silanization) 129
5.3.3 Hardness test 132
5.3.4 Tensile test 134
5.3.5 SEM analysis of fracture surfaces 136
5.3.6 Water sorption and solubility 140
5.3.7 Methylene blue degradation 141
5.3.8 Bioactivity of PT embedded UT resin composites 142
5.4 Evaluation of PT embedded UT composites and comparison to commercial composites 145
6. CONCLUSIONS 149
6.1 Sol-gel synthesis of PT nanostructures 149
6.2 Hydrothermal synthesis of PT nanostructures 150
6.3 PT embedded UT composites 151
REFERENCES 155
APPENDICES 165
A. METHYLENE BLUE DEGRADATION CALCULATIONS 165
A1. MB degradation of sol-gel derived powders 165
A2. MB degradation of hydrothermally synthesized powders 169
CIRRICULUM VITAE 173

LIST OF TABLES

TABLES

Table 3. 1 Precursor composition and synthesis conditions of sol-gel derived nanostructures. 33

Table 3.2 Precursor composition and synthesis conditions of sol-gel derived nanostructures. 35

Table 3. 3 Composition of neat resin mixtures.....40

Table 3. 4 Composition of sol-gel derived PT embedded UT resin composites. 41

Table 3. 5 Composition of hydrothermally synthesized PT embedded UT resin composites. 42

Table 3. 6 Composition of 5-wt % hydrothermally synthesized PT embedded UT resin composites. 42

Table 3. 7 Chemicals used and composition of 10 x SBF solution prepared. 56

Table 4. 1 Comparison of peak positions and intensities in the patterns of xero-gels with ICDD cards of KCl and α-K_2O. 60

Table 4. 2 Diameter and length of PT whiskers obtained after calcination at 800 °C. 67

Table 4. 3 Thermodynamic data for the formation of PT.....101

Table 5. 1 Specific wear rate (WR), average friction coefficient (μ), and surface roughness of neat UT resin mixtures. 114

Table 5. 2 Hardness (HV 0.3 - NI) and NI-E of neat UT resin mixtures. 116

Table 5. 3 Ultimate tensile stress (σ_{UTS}), elastic modulus (E) and yield stress (σ_y) of UT neat resin mixtures. 118

Table 5. 4 Water sorption and solubility of UT resin mixtures. 120

Table 5. 5 Vickers hardness (HV 0.3) of 10-50-wt % hydrothermally synthesized PT embedded UT composites. 133
Table 5. 6 Vickers hardness of 5-wt % hydrothermally synthesized PT embedded UT composites after sonication and silanization. 133
Table 5. 7 Tensile test results of 5-wt % hydrothermally synthesized PT embedded UT resin composites after sonication and silanization. 135
Table 5. 8 Water sorption and solubility of PT reinforced UT resin composites. .. 140

Table A. 1 Apparent degradation rate (k; min^{-1}) of sol-gel derived powders calcined at 600ºC. 166
Table A.2 Apparent degradation rate (k; min^{-1}) of sol-gel derived powders calcined at 800 ºC. 168
Table A.3 Apparent degradation rate (k; min^{-1}) of hydrothermally synthesized powders at 180 ºC for 24 h at 5-20 M $KOH^{aq.}$ 171

LIST OF FIGURES

FIGURES

Figure 2. 1 Crystal structures of potassium hexa-titanate ($K_2Ti_6O_{13}$, PHT) 9
Figure 2. 2 Schematic representation of photocatalytic degradation reactions.....11
Figure 2. 3 Schematics of energy band structure types of a semi-conductor showing charge transition from valence band (VB) to conduction band (CB). 13
Figure 2. 4 Schematics of PTT-$Ni(OH)_2$ formation through ion-exchange processes for the development of high performance supercapacitors.[55] 16
Figure 2. 5 Schematics showing molecular structures of BisGMA, UDMA, and TEGDMA monomers and CQ/DMAEMA initiator/co-initiator (amine). 20
Figure 2. 6 Schematic illustration of LDH reinforcement into dental resin matrices. 25
Figure 2. 7 Schematics of urchin-like HAp reinforcement 26
Figure 2. 8 Schematic representation of cross-section of a dental resin matrix reinforced with filler particles and silica.....27

Figure 3. 1 Route followed for the synthesis of PT nanostructures by the sol-gel method.....33
Figure 3.2 Route followed for the synthesis of PT nanostructures by the hydrothermal treatment. 35
Figure 3. 3 Appearance of PTs after sonication in water and ethanol. 36
Figure 3. 4 Photographs of the molds and samples produced showing the size and shape of the final composite products.....39
Figure 3. 5 a) BET isotherm types and b) Hysteresis loops according to IUPAC classification.....46
Figure 3. 6 Schematic illustration of the MB degradation testing. 49
Figure 3. 7 Molecular structure of MB dye.....50

Figure 3. 8 Representative surface profile of the resin specimen tested for wear. The inset is the photo of the specimen with worn surface track. 51
Figure 3. 9 Typical load-displacement curve obtained via NI testing. 53
Figure 3. 10 Vickers diamond indenter shape and a typical indent trace on sample surface. 54

Figure 4. 1 XRD patterns of the xero-gels synthesized at Ti/K ratio of 1, 1.5, 2.5 and 3.5..... 58
Figure 4. 2 XRD patterns of the powders obtained after calcination for 1-3 h at 600 ºC for Ti/K ratio of a) 1, b) 1.5, c) 2.5, and d) 3.5 (PH: potassium hollandite, PHT: potassium hexa-titanate) 59
Figure 4. 3 XRD patterns of the powders obtained after calcination for 1-3 h at 800 ºC with Ti/K ratio of a) 1, b) 1.5, c) 2.5, and d) 3.5..... 62
Figure 4. 4 SEM images of the sol-gel derived whiskers obtained after calcination at 600 °C with increasing Ti/K ratio of 1, 1.5, 2.5 and 3.5 (top to bottom), at calcination times of 1, 2 and 3 h (left to right). 64
Figure 4. 5 SEM images of the sol-gel derived whiskers obtained after calcination at 800 °C with increasing Ti/K ratio of 1, 1.5, 2.5 and 3.5 (top to bottom), at calcination times of 1, 2 and 3 h (left to right). 66
Figure 4. 6 a) BET isotherms and b) BJH mesopores size distribution (Pore diameter versus volume) of sol-gel derived PTs obtained by calcination at 800 °C for 3 h. ... 68
Figure 4. 7 Schematic illustration of the growth stages of sol-gel derived powders. 70
Figure 4. 8 TG-DTA analysis thermograms of xero-gels a) DTA b) TGA 72
Figure 4. 9 Crystal structures of PH and PHT along [001] projection..... 74
Figure 4. 10 TEM images of the sol-gel derived PTs obtained after calcination at 800 °C for 3 h for Ti/K of a) 1, b) 1.5, and c) 2.5..... 76
Figure 4. 11 a) R% versus energy b) K-M transform (F(R) and Tauc plots c) indirect and d) direct transitions of the xero-gels..... 77
Figure 4. 12 The variation in E_g of sol-gel derived powders before calcination with respect to their Ti/K ratio. Note that the data points for E_g of P25 powder are shown at Ti/K=0..... 78

Figure 4. 13 The variation in E_g of sol-gel derived powders obtained after calcination at 600 °C (a, b, c) for 1-3 h and 800 °C (d, e, f) for 1-3 h, respectively. Note that the data points for E_g of P25 powder are shown at Ti/K=0.....80
Figure 4. 14 MB degradation rates of sol-gel derived powders obtained after calcination at a) 600 ºC and b) 800 ºC for 1-3 h. Note that the data points shown at Ti/K=0 of each graph represent the MB degradation rate of P25 powders tested under identical conditions. 83
Figure 4. 15 XRD patterns of unreacted P25 powder and KOH pellets. 85
Figure 4. 16 XRD patterns of hydrothermally treated powders using 5-20 M $KOH^{aq.}$ at 180 °C for a)3 h b) 12 h c) 24 h and d) 48 h. 86
Figure 4. 17 XRD patterns of the powders synthesized by hydrothermal treatment using 20 M $KOH^{aq.}$ at 180 °C for 3 h. 88
Figure 4. 18 SEM images of PT nanostructures obtained by hydrothermal treatment at 180 °C with increasing hydrothermal treatment time of 3, 12, 24 and 48 h (top to bottom) and $KOH^{aq.}$ molarity of 5, 10, 15 and 20 M (left to right).....90
Figure 4. 19 SEM images of PT nanostructures obtained by hydrothermal treatment at a) 120 and b) 150 °C with hydrothermal treatment time of 3 h at 20 M of $KOH^{aq.}$ 91
Figure 4. 20 BET isotherms of powders after hydrothermal treatment using a) 5 M b) 10 M $KOH^{aq.}$ and BJH mesopores size distribution (Pore diameter versus adsorbed volume) at c) 5 M and d) 10 M $KOH^{aq.}$ at 180 °C for 3-48 h. 92
Figure 4. 21 TEM images of PT nanowires a) aggregates, b) whisker, c) splitting nanowires (lamellar), d) single nanowires. 95
Figure 4. 22 TEM image of P25 powder surface. Insets are P25 aggregates, FFT and iFFT of the P25 surfaces. 96
Figure 4. 23 TEM images of the nanostructures hydrothermally synthesized by using 10 M KOH at 180 °C for 3 h, showing the growth of nanowires from an amorphous Ti-O-K network.....97
Figure 4. 24 TEM images of the nanostructures hydrothermally synthesized by using 10 M $KOH^{aq.}$ at 180 °C for 3 h.....98
Figure 4. 25 TEM image of splitting surface of the nanostructures hydrothermally synthesized by using 10 M $KOH^{aq.}$ at 180 °C for 3 h. 99

Figure 4. 26 TEM image of splitting surface of the nanostructures hydrothermally synthesized by using 10 M KOH at 180 °C for 24 h. 100
Figure 4. 27 a) R% versus energy b) K-M transform (F(R)) and Tauc plots c) indirect and d) direct band transitions of the nanostructures hydrothermally synthesized at 180 °C using 5 M $KOH^{aq.}$ 104
Figure 4. 28 a) R% versus energy b) K-M transform (F(R)) and Tauc plots c) indirect and d) direct band transitions of the nanostructures hydrothermally synthesized at 180 °C using 10 M $KOH^{aq.}$ 105
Figure 4. 29 The variation in E_g of hydrothermally treated powders at 180 °C for 3-48 h using a) 5 M b) 10 M $KOH^{aq.}$ Note that the data points for E_g of P25 powder are shown at time=0. 106
Figure 4. 30 a) R% versus energy b) K-M transform (F(R)) and Tauc plots c) indirect and d) direct band transitions of the nanostructure hydrothermally synthesized at 180 °C using 20 M $KOH^{aq.}$ for 3 h. 107
Figure 4. 31 a) R% versus energy b) K-M transform (F(R)) and Tauc plots c) indirect and d) direct band transitions of the nanostructures hydrothermally synthesized at 180 °C for 24 h using 5-20 M $KOH^{aq.}$ 108
Figure 4. 32 The variation in E_g of hydrothermally treated powders at 180 °C for 24 h using a) 5 - 20 M $KOH^{aq.}$ Note that the data points for E_g of P25 powder are shown at $KOH^{aq.}$ molarity=0. 109
Figure 4. 33 The variation in E_g of hydrothermally synthesized powders at 180 °C for 24 h, with respect to variation of $KOH^{aq.}$ molarity. Note that the data points for E_g of P25 powder are shown at $KOH^{aq.}$ molarity=0. 110

Figure 5. 1 Typical stress-strain curves of neat UT resin mixtures. 118
Figure 5. 2 XRD patterns of the 5-wt % of sol-gel derived PT embedded UT resin mixtures..... 122
Figure 5. 3 a) WR, b) friction coefficient (μ) and c) surface roughness (R_a) of 5-wt% sol-gel derived PT embedded UT composites compared to neat UT resin mixtures. (UT- (1-3)-SG-5) 124
Figure 5. 4 a) Nano-indentation (NI) hardness (H) and b) elastic modulus (E) of 5-wt % sol-gel derived PT embedded UT resins..... 125

Figure 5. 5 XRD patterns of 5-wt % hydrothermally synthesized PT embedded UT composites before and after sonication and/or silanization. 128
Figure 5. 6 Specific WR, friction coefficient (μ) and surface roughness (R_a) of 10-50-wt% hydrothermally synthesized PT embedded UT composites compared to neat UT resin mixtures. (UT- (1-2)-HD-(10-50)).....130
Figure 5. 7 Specific WR, friction coefficient (μ) and surface roughness (R_a) of 5-wt% hydrothermally synthesized PT embedded UT composites after sonication and silanization (UT-(1-3)-HDS/HDSS-5).....131
Figure 5. 8 Typical stress-strain curves of neat and 5 wt % hydrothermally synthesized PT embedded UT resin composites: a) UT-1, b) UT-2 and c) UT-3 after sonication and silanization. 134
Figure 5. 9 Typical fracture surfaces of a) neat, b) 5-wt % hydrothermally synthesized PT embedded UT resin. 136
Figure 5. 10 Fracture surfaces of samples failed under tensile test. a) UT-1 b) UT-1-HDS-5 c) UT-1-HDSS-5 d) UT-2 e) UT-2-HDS-5 f) UT-2-HDSS-5 g) UT-3 h) UT-3-HDS-5 and i) UT-3-HDSS-5. Bar is 20 μm.....138
Figure 5. 11 Fracture surfaces of samples failed under tensile testing showing a) whisker pull out b) whisker bundle pull out c) crack bridging normal to crack propagation direction d) heterogeneous dispersion of PT and silica within the resin matrix caused by silanization treatment. 139
Figure 5. 12 MB degradation performance of UT-2 resin mixture and UT-2-HD composites in which 10-50-wt % hydrothermally synthesized PT embedded without sonication and silanization. 142
Figure 5. 13 XRD patterns of SBF treated neat and 5 wt % hydrothermally synthesized PT embedded (sonicated and/or silanized) UT resin mixtures for 10 days. 143
Figure 5. 14 EDS spectra of a) neat UT1 resin and 5 wt % sonicated PT embedded UT composites b) UT-1- HDS-5 c) UT-2-HDS-5 d) UT-3-HDS-5 after 10 days of SBF immersion (Insets: SEM images of SBF treated composite surfaces; left; bars100μm, right: bars 5 μm).....144
Figure 5. 15 Photographs of produced resin and composites.....147

Figure A.1 UV-Vis absorbance curves of MB solutions interacted with sol-gel derived powders calcined at 600 ºC: a) Ti/K=1 b) Ti/K=1.5 c) Ti/K=2.5 d) Ti/K=3.5 for 1 h e) Ti/K=1 f) Ti/K=1.5 g) Ti/K=2.5 h) Ti/K=3.5 for 2 h and i) Ti/K=1 j) Ti/K=1.5 k) Ti/K=2.5 l) Ti/K=3.5 for 3 h. 165
Figure A.2 Linear fit curves of MB degradation of sol-gel derived powders obtained by calcination at 600 °C with respect to time according to 1st order kinetics approach. (ln (C/C_o) versus t). 166
Figure A.3 UV-Vis absorbance curves of MB solutions interacted with sol-gel derived powders calcined at 800 ºC: a) Ti/K=1 b) Ti/K=1.5 c) Ti/K=2.5 d) Ti/K=3.5 for 1 h e) Ti/K=1 f) Ti/K=1.5 g) Ti/K=2.5 h) Ti/K=3.5 for 2 h and i) Ti/K=1 j) Ti/K=1.5 k) Ti/K=2.5 l) Ti/K=3.5 for 3 h. 167
Figure A. 4 Linear fit curves of MB degradation of sol-gel derived powders obtained by calcination at 800 °C with respect to time according to 1st order kinetics approach. (ln (C/C_o) versus t). 168
Figure A.5 UV-Vis absorbance curves of MB solutions interacted with hydrothermally synthesized powders at 180 ºC for 24 h at a) 5 M b) 10 M c) 15 M d) 20 M $KOH^{aq.}$ 169
Figure A.6 Linear fit curves of MB degradation of hydrothermally synthesized powders at 180 °C for 24 h at 5-20 M $KOH^{aq.}$ with respect to time, according to 1st order kinetics approach. (ln (C/C_o) versus t). 170

LIST OF ABBREVIATIONS

MB: Methylene blue

PT: Potassium Titanate

PM: Potassium Methylate

UT: UDMA-TEGDMA

CQ: Camphorquinone

DMAEMA: Dimethyl amino ethyl methane

PHT: Potassium Hexa-Titanate, $K_2Ti_6O_{13}$ ($K_2O.6TiO_2$)

PTT: Potassium Tetra-Titanate, $K_2Ti_4O_9$ ($K_2O.4TiO_2$)

PH: Potassium Hollandite $KTiO_{16}$

FFT: Fast Fourier Transform

iFFT: Inverse Fast Fourier Transform

E_g: Energy band gap

CHAPTER 1

INTRODUCTION

Potassium titanates (PTs) with a general formula of $K_2O.nTiO_2$ where n=2, 4, 6, 8 received special attention due to their superior properties along with their ease of processing and economical production. The leading types of potassium titanate family are potassium tetra- (n=4) and hexa-titanate (n=6) phases that will hereafter be abbreviated as PTT and PHT, respectively. Depending on their potassium (K) content, PTs have unique crystal structures enabling them to be produced in various morphologies such as nanorods, nanowires and whiskers. Both titanates have monoclinic crystal structure with space group of C2/m, but PTT is richer in K than PHT.[1] PHT has a tunnel (cage) type structure whereas PTT has layered type structure that allows the K ions to be displaced by ion-exchange mechanism through chemical reactions.[2,3]

Among high aspect ratio nanomaterials, PT nanowires and whiskers are of interest due to their high surface area and enhanced photocatalytic activity. PT nanostructures have been shown to be advantageous for special applications like photocatalytic removal of pollutants[4-10] water splitting[11], solar cells[12], nuclear waste treatment[13], electrochemical[14], ion exchange[3] applications and gas sensors.[5,15] PT nanowires and whiskers are on one hand biocompatible and photoresponsive; on the other hand they have good mechanical properties.

Owing to their superior surface area and high aspect ratio, they could be used to support polymeric matrices to enhance their mechanical and functional properties. PT whisker reinforced resin composites could be used as an alternative material to asbestos that is detrimental to human health, in automotive brake pads.[16,17] Especially PHT whiskers and fibers have been employed as reinforcing phases in polymeric matrices to increase the abrasion resistance of resins. The remedial effect of increasing interaction surface area of fillers with the polymer in composite matrices is well known. However, in spite of their biocompatibility, there has not been a publication concerning the use of nanosize PTs in biomedical polymers yet. Moreover, the effects of processing conditions on the growth mechanisms and final morphology of PT nanowires have not been disclosed very well.

Desirable properties of PTs make them potential candidate materials for not only environmental purification but also as fillers for dental composite restorations that necessitate bioactivity, strength and aesthetics at one hand. More importantly, PTs have good potential to serve self-cleaning function due to their photocatalytic activity when the composite surfaces are irradiated by ultraviolet light. In this respect, dental filling resins are good candidates as model systems to introduce PTs to biomedical composite research.

In the last decades, composite dental fillings are the most commonly used materials for treatment of dental caries since they provide adequate properties and can mimic the natural tooth color.[18] The main problems associated with composite fillings are the formation of secondary caries and operator-skill dependence during handling and application into the tooth cavity.

The present problems associated with nanoparticle reinforced dental composites are in the processing that requires severe homogenization during mixing within a viscous polymeric network in order to get good mechanical attachment at the polymer-whisker interface.

In order to overcome mechanical interlock problem, silanization and silica particle addition have been tried. According to the available recent literature, there is not even a single study concerning the embedment of PTs in polymeric matrices to be used in dental restorations. Moreover, the properties and behavior of PT embedment in any biomedical composites have not been disclosed yet.

1.1 Objective and significance of the dissertation

The objective of this dissertation is twofold. The first objective is to produce and characterize PTs with a chemical formula of $K_2O.nTiO_2$ (where n=4, 6) at different size and morphology by using sol-gel/calcination and hydrothermal methods. In spite of good peculiarities, synthesis of PTs is a challenging issue since it is difficult to obtain them as single titanate phase and separate from each other during synthesis or by post-treatment processes. The effects of synthesis conditions on the final properties of PTs produced by both methods have been investigated. Moreover, the growth mechanisms of PTs were elucidated with respect to synthesis method performed. The second objective is to reinforce dental resins (UDMA/TEGDMA; UT) with PTs to produce PT reinforced UT resin composites. Because PTs can degrade organic pollutants in solution, they have potential to preserve their activity in polymer matrices. Hence, they can provide self-cleaning ability to a dental filling just by daylight irradiation during service in mouth.

The composites produced were characterized by X-ray diffraction (XRD), electron microscopy (SEM, TEM), diffuse reflectance (DR) UV-Vis spectroscopy and gas adsorption (BET) characterization techniques. The characteristics and mechanical properties of the composites produced were also investigated. This dissertation is devoted to investigate the use of PTs as dental resin reinforcement for the first time in the open literature. Therefore the experiments were based on understanding this novel type composite behavior, rather than focusing on development of dental composite alternatives directly.

They are amongst the ideal candidate reinforcement materials for dental applications because they are bioactive and have moderately better mechanical strength than the dental resins. The findings of this dissertation study have a potential to open a new application areas. This dissertation study not only reports the use of PTs as reinforcement phase in dental filling composites but also investigates whether their photocatalytic performance in polymeric matrices is preserved for the first time in the open literature.

1.2 Overview of the chapters

The dissertation can be considered in two main parts, which are

a. Synthesis, characterization and testing of PTs by sol-gel and hydrothermal methods.
b. Production, characterization and testing of PT embedded UT resin composites.

In Chapter 2, the background information and literature review on synthesis and properties of PTs and methacrylate resins are summarized. In Chapter 3, the experimental procedures followed, the characterization and testing principles in the dissertation are given. Chapters 4 and 5 summarize the findings on PT synthesis and neat and PT embedded UT resins, respectively.

The framework of Chapter 4 is formed in the following perspective:

a.1 Sol-gel/hydrothermal synthesis results
a.1.1 Characterization (XRD, SEM, BET, UV-Vis spectroscopy)
a.1.2 Photocatalytic activity testing (by methylene blue degradation)
a.1.3 Crystallization and growth mechanism behind sol-gel/hydrothermal reactions.

The framework of Chapter 5 is formed in the following perspective. The characterization and testing methods include XRD and SEM characterizations, wear, tensile, hardness, photocatalytic activity and bioactivity tests.

b.1 The characterization and testing results of neat UT resins

b.2 The characterization and testing results of sol-gel derived PT embedded UT resin composites

b.3 The characterization and testing results of hydrothermally synthesized PT embedded UT resin composites

In Chapter 6, the conclusions on findings of the dissertation experiments are summarized.

CHAPTER 2

BACKGROUND INFORMATION AND LITERATURE REVIEW

2.1 Potassium titanate nanostructures

Among alkali-metal titanates, PTs which contain potassium cations (K^+) interleaved between TiO_6 octahedra are a family of well-recognized materials with their artificial layered or cage type molecular structure. The information on synthesis and properties of this cage/tunnel type titanate family with monoclinic crystal structure is huge. Their structures are of great importance owing to their outstanding photocatalytic and ion-exchange properties at nano-scale.

2.1.1 Synthesis

In the last decades, there have been various studies reporting the synthesis of PT nanostructures in the form of nanowires, rods, or whiskers because they provide increased surface area compared to fibers or particles. The most widely used methods are reported as sol-gel and/or calcination[10,19-21], molten salt[22-24], hydrothermal synthesis[4,14,25-33], and flux growth.[11,34] In flux growth systems, there is a need for a flux composition, which in most cases is expensive and/or corrodes the container upon processing.[35-37] In direct calcination or flux methods, using TiO_2 and K_2CO_3 as precursors, it is difficult to control the particle size and morphology of the products.[34,38] Recently, Ponce-Peńa et al.[34] reported the use of boric acid as flux for the production of PHT fibers as a cheaper alternative, however, the final size of the products were determined not only by the melting conditions around 1200 °C but also by the cooling conditions after calcination at 900 °C and higher.

Molten salt method has been shown to be more advantageous than solid-state reactions in terms of large-scale production owing to the lower synthesis temperature. Recently, by forming molten KCl from stoichiometric K_2CO_3, Wang et al.[22] managed to produce $K_2Ti_8O_{17}$ whiskers from rutile at 760-800 °C in 4 h. The method allows for high crystalline and well dispersive whisker production however, it is limited to the production of $K_2Ti_8O_{17}$ for the time being.

One of the good examples of sol-gel/calcination method for whisker production was reported by Kang et al.[20], in which they started sol-gel reaction at room temperature by using alkoxide titanium (Ti) and K precursors; tetraethyl ortho-titanate and potassium methylate, respectively. The aging reaction was followed by calcination treatment of xero-gels at 850-1050 °C at 3 h. They showed that depending on the initial Ti/K ratio, PTT and PHT whiskers at different sizes could be produced. The hydrothermal systems were reported to provide formation of nanostructures in solution, even after reactions in adiabatic reactors at 200 °C and lower temperatures under autogeneous pressure. For instance, Wang et al.[29] reported the formation of high aspect ratio PHT nanowires after hydrothermal reaction of TiO_2-KOH solutions at 180 °C.

Among these methods, sol-gel and hydrothermal methods are advantageous in terms of achieving high surface area and controllable chemistry at relatively lower cost. Using sol-gel reactions followed by hydrothermal is also an efficient method for getting high surface area nanowires/whiskers. Janes et al.[21] developed a sol-gel like colloidal system using titanium isopropoxide dissolved in 2-propanol and added KOH into this solution. The reactions were similar to hydrolysis and condensation of sol-gel derived systems. After filtration, the precipitates were heated at 220 °C under autogeneous pressure in an autoclave. They stated formation of PHT from an amorphous matrix first. PTT started to precipitate after 48 h at hydrothermal conditions. Even though there are a variety of methods concerning the production of PTs starting with solution derived hydrothermal synthesis has higher potential in terms of both phase and morphology/size control to produce nanowires or rods.

2.1.2 Structure and morphology

PTs could be processed as nanorods/wires[14,30,39-42], whiskers[10,19,22,26] or even as films.[43] The crystalline structure and properties of PTT and PHT phases are schematically shown in Figure 2.1. PTT is richer in potassium (K) than PHT. But, both have monoclinic crystal structure with space group C2/m. PHT has a tunnel type crystal structure in which the structural unit composes of three TiO_6 octahedra forming the tunnels by sharing corners. The K^+ ions are enclosed by this tunnel structure and cannot escape when in solution.[1] Whereas in PTT, K^+ cations are placed between the layers which are not attached to each other from the corners. PTT has a layered type structure and it allows the K^+ ions to be displaced freely. This type of structure allows ionic exchange through chemical reactions.

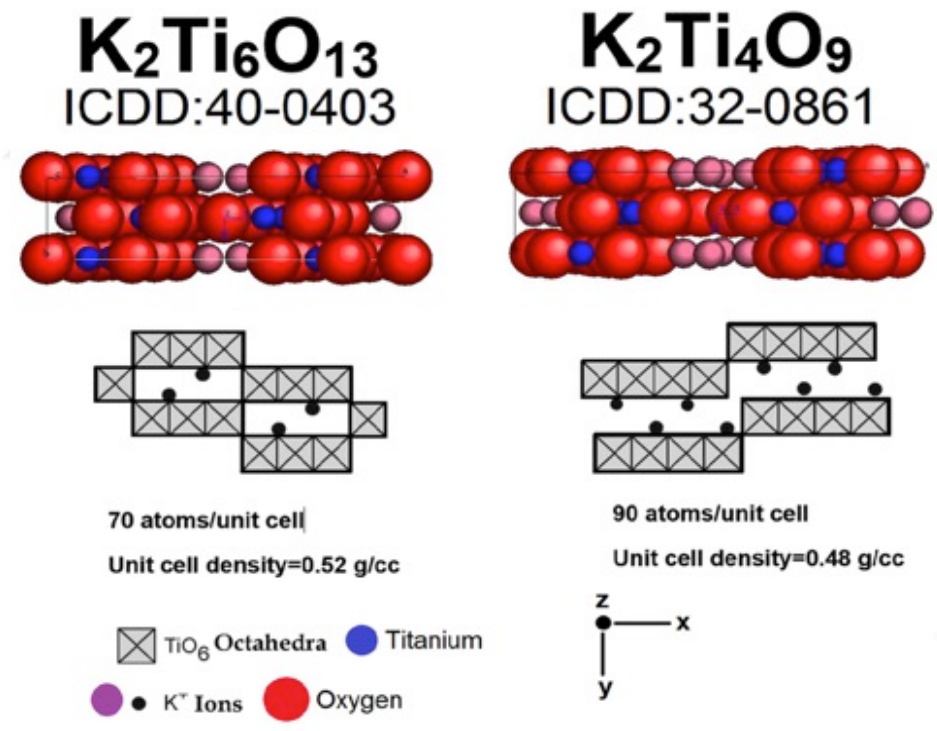


Figure 2. 1 Crystal structures of potassium hexa-titanate ($K_2Ti_6O_{13}$, PHT) and potassium tetra-titanate ($K_2Ti_4O_9$, PTT).

2.1.3 Utilization

Alkali titanates have been utilized especially in electrochemical[14]and photocatalysis applications.[4,9,10] owing to their photocatalytic and ion-exchange capabilities. Among alkali titanates, PTs received special attraction due to their specific photochemical properties. Because of their unique, one-dimensional morphology and cage/layered type crystal structures, PTT and PHT have been widely used as ion-exchange materials[2], heat insulators[34], solar cells[12], reinforcing phases for polymers[21], as photocatalysts to remove organic pollutants [22,26], in nuclear waste treatment[13] and gas sensors. [5,15] Therefore main applications and/or research on PTs are based on photocatalytic reactions, ion-exchange processes and composite reinforcement.

2.1.3.1 Photocatalytic degradation of pollutants

The treatment of industrial wastes has been a critical topic for environmental issues. Chemical, textile, and medical industry generates a wide range of highly toxic wastes. Cationic dyes such as Methylene Blue (MB) are widely used in textile industry as antimicrobial agents. When they present in aqueous ecosystems like in wastewater, they are highly toxic, carcinogenic and mutagenic.[44]

Semiconductor photocatalysis offers a very promising way for the removal of organic or inorganic contaminants from water. The common semiconductors for photocatalysis have a band gap energy (E_g) less than 3.5 eV, which is comparable to the specific energy of the photons of UV/visible light[45]. Hence, almost all semiconductors are photoactivated by using UV-light and that necessitates substantial electrical power input. TiO_2 has been one of the most commonly used photocatalyst due to its photostability, non-toxicity, strong oxidation power and low cost of production.[44,46] The details of degradation mechanism of TiO_2 derived materials have been given elsewhere.[47] Basically, after irradiation with light, the energy (hv) that is equal or higher than the E_g of the photocatalyst is absorbed.

Electrons (e^-) receive this energy from the photons and migrate from valance band (VB) to conduction band (CB), leaving holes (h^+) behind. The difference between the lowest (CB) and highest (VB) of a semi-conductor material is called as the (forbidden) E_g. It is one of the most relevant properties in semi-conductor physics since it reflects the optical properties of a material such as photocatalytic performance. The degradation of the contaminants proceeds by the formation of hydroxyl radicals (•OH) through the reactions of h^+ with the OH^- groups or the adsorbed H_2O on their surfaces.[48] The schematic representation of the reactions is summarized in Figure 2.2.

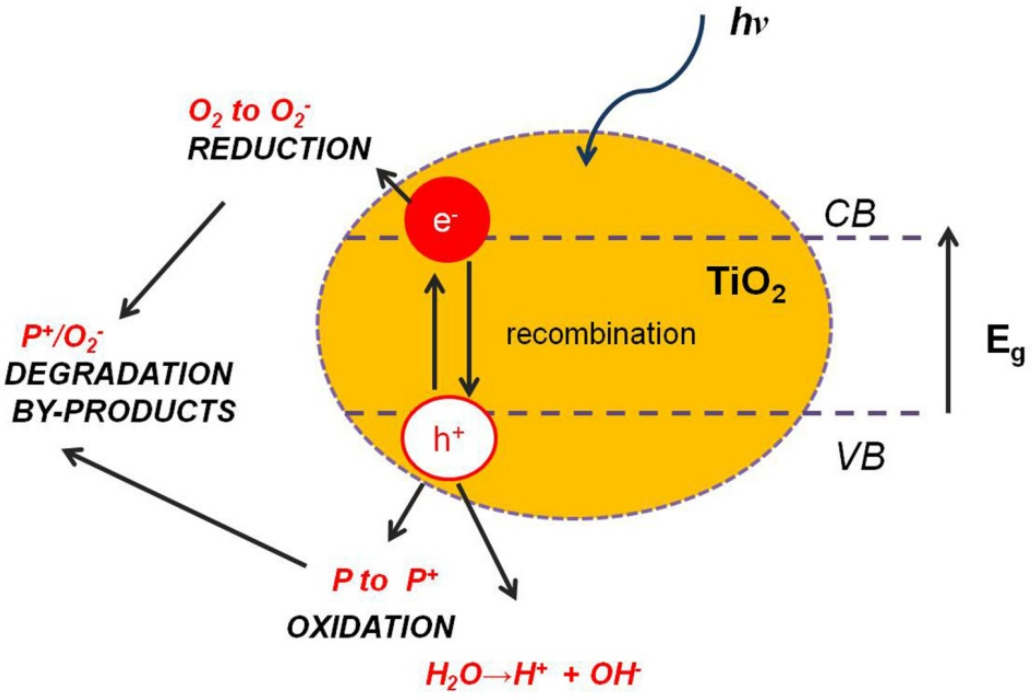


Figure 2. 2 Schematic representation of photocatalytic degradation reactions based on TiO_2 photocatalysis

The free radicals are unstable and extremely reactive.[48] This capability of forming radicals provide complete mineralization of both less reactive or strong pollutants.[44] Moreover, the charge carriers are extremely reactive and may recombine on the surface of the photocatalyst in very short time. The recombination is a common problem and evident in rutile phase of TiO_2. Amano et. al.[7] reported that E_g for anatase is 3.21 eV and it is 3.04 eV for rutile. But, rutile is less photoactive than anatase, because, the average recombination rate of e^-/h^+ pairs is higher despite its lower E_g. The unique combination of anatase and rutile phases in P25 powder (Degussa™, ~20% Rutile and 80% Anatase) makes it one of the best TiO_2 photocatalysts. Thus P25 can be photoactivated at an intermediate E_g between 3.05 - 3.10 eV.[5,46]

As mentioned earlier, in order for charge carriers (e^-/h^+) to form in a photocatalytic reaction, sufficient energy that is specific to E_g must be provided. Types of the energy band transitions (VB to CB) of a semi-conductor which occur by absorption of a photon with energy higher than E_g are schematically shown in Figure 2.3. Electrons in a rigid material occupy certain energy levels, which are separated by forbidden gaps, called as '*band*'s. There are two types of band-to-band transitions in a material; direct or indirect. They are also classified as allowed or forbidden. In an allowed direct transition, aid of a phonon is not needed to sustain the momentum. But in a forbidden direct transition, which is less likely to occur, finite momentum of photons is required. In indirect transitions, at least one phonon aids the transition by absorption or emission of one phonon to maintain the momentum.[49]

Uv-Vis/DRS is the most common method for determination of E_g. The optical excitation of electrons from VB to CB is reflected by an increase in absorbance at a certain wavelength that is specific to its E_g. [49] Several attempts have been made for decreasing E_g thereby red shifting the absorption edge to solar spectrum and preventing recombination of carriers to obtain photocatalysis reactions driven by solar light.

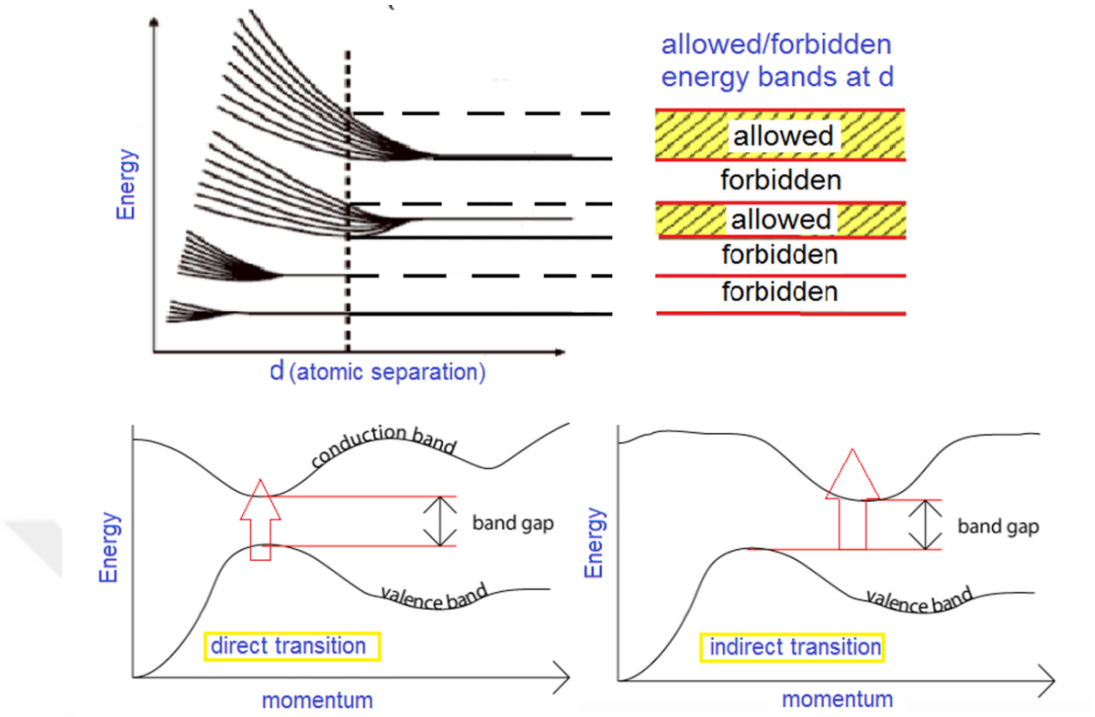


Figure 2. 3 Schematics of energy band structure types of a semi-conductor showing charge transition from valence band (VB) to conduction band (CB).

The significant approaches for decreasing E_g are doping with metal/non-metal ions to create mid-states in the transition gap and/or increasing the surface area and crystallinity to control the recombination rate. Through TiO_2 photocatalysis studies, the different precursors and/or fabrication techniques, the particle shape and size have been shown to affect the energy band structure as well as the photocatalytic reaction order and the conditions.[7] Development of solar light active photocatalytic materials with high surface area, stability and low recombination rate is a subject of extensive current research in this field. The contribution of amorphous titania on photocatalytic ability is negligible. Methods to form or use anatase powder with high degree of crystallinity and surface area are on demand.[46]

High surface area with good crystallinity is the major achievement for a good photocatalyst because they provide more probability to form interaction surfaces with the contaminants. Among high aspect ratio nanomaterials, titanate nanowires/whiskers are of remarkable interest due their high surface area and enhanced photocatalytic activity making them the best candidates for environmental purification.[33]

For all semiconductors including PTs, direct and indirect transitions can occur simultaneously. However, the latter cannot be detected from the absorbance spectrum due to its high energy and low probability.[49] The major transition conducts the behavior of the semiconductor however, it is very difficult to differentiate between them experimentally. This difficulty of differentiation makes precise measurement more complex.

Many researchers have reported rutile to have a direct E_g of 3.06 eV and indirect E_g of 3.10 eV. Anatase has been reported mostly to have only an indirect one as 3.23 eV.[50] However, values from 2.86 to 3.34 eV were also reported for direct E_g of anatase[51], which is determined by the variations in the crystallite size, impurities content and the type of the transition. So, it is commonly concluded that direct transition of anatase phase is more favorable.

In order to clarify the conflicts on TiO_2, Lopez and Gomez[49] investigated the variations of the calculated E_g of P25, with anatase and sol-gel derived TiO_2. They showed that the conflicting results in related literature depend mainly on the type of band-to-band transition and the equation used. They used the major equations and expressed the differences in calculated E_g values of the same material. The E_g of P25 is theoretically 3.2 eV. By using n=2 they calculated E_g as 3.26 eV, for n=1/2 as 3.68 eV. Only by extrapolating F(R) it was calculated as 3.51 eV. Results were fluctuating similarly for anatase TiO_2 and sol-gel derived TiO_2. Finally, they concluded that it is better to use n=2 for indirect allowed transition for TiO_2 because of highly accurate result that is close to 3.2 eV.

2.1.3.2 Ion-exchange processes

Ion exchange reactions provide practical approaches for the synthesis of compounds, which cannot be prepared by heat treatment processes. Layered titanates are good examples that allow for ionic exchange owing to their layered structures. It has been reported by several researchers that PTT contains variable amounts of potassium and water in the interlayer.[52,53]

The adjacent layers in PTT shift relative to each other hence there are two kinds of interlayer spacing. Some potassium are placed in y=1/4 and the rest in y=3/4.[53] Izawa et. al.[53] reported that PTT transforms to $H_2Ti_4O_9.H_2O$ by exchanging K^+ in aqueous HCl solution. They also mentioned that H_3O^+ can partially be substituted for K^+ in $H_2Ti_4O_9.H_2O$ even in KCl solution. Lee et. al.[52] showed that fibrous PTT transformed to layered $H_2Ti_4O_9.H_2O$ through exchanging K^+ with H^+ in HCl solution, but in order for complete transformation, all K^+ had to be exchanged and $(Ti_4O_9^{2-})_n$ layers must have been kept sheet like.

One other good example of ion-exchange of PTs is reported by Li et. al.[54] They have shown that Sn^{2+} incorporated PTT nanoribbons can be prepared by an acid-free ion exchange reaction in methanol at room temperature. They stated that the Sn^{2+} incorporated PTT had narrower E_g than PTT and the photocatalytic activity tested by H_2 evolution and rhodamine B degradation was enhanced.

Different studies show that ion exchange mechanism does not only allow for the room temperature synthesis of materials but also enhance functional properties such as photocatalytic or electrical performance. A recent study performed by Zhou et. al.[55] showed that PTT nanowires can be used effectively in supercapacitor electrodes by their Ni^{2+} ion exchange capability. In Figure 2.4, the schematics summarizes the PTT-$Ni(OH)_2$ layer formation through ion exchange reactions on PTT. Moreover, the SEM images show the fibrillar morphology of PTT in nanoscale.

Briefly, during the hydrothermal process PTT nanowires were formed on Ti surfaces where K^+ ions were dispersed on TiO_6 octahedra. By the alkaline treatment, ion exchange between Ni^{2+} and K^+ occurred and $Ni(OH)_2$ nanosheets were formed on PTT leading to PTT-$Ni(OH)_2$/Ti core-shell structures. The above mentioned study claimed that in addition to their advantageous nanowire structure that provides efficient interaction between the electrolyte ions and the active materials, PTT derived nanostructures can also provide excellent capacitance properties.

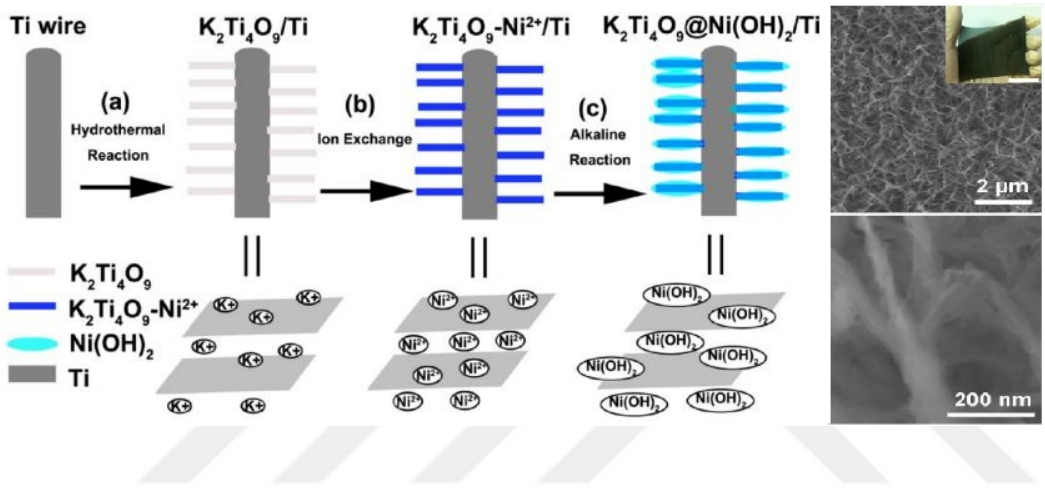


Figure 2. 4 Schematics of PTT-$Ni(OH)_2$ formation through ion-exchange processes for the development of high performance supercapacitors.[55]

2.1.3.3 Composite reinforcement and biological applications

PT fibers with $n \geq 4$ have been successively used as micro-reinforcements for the formation of composites utilized in several areas. Research is mostly focused on using thermoplastic polymers such as polyamides, polyolefins, polyether ketones, etc. The most significant studies on polymer composites were on the asbestos replacement of PHT fibers in automotive brake pedals due to their remarkable antifriction enhancement.[16,17,56]

Polypropylene (PP), as one of the largest polyolefins consumed in industry is a common plastic significant for load bearing applications. To boost its mechanical performance, many micro-reinforcers have been used such as mica, calcium carbonate, clay, etc. But, using PHT fibers has been more successful since they can be processed easily at low cost. Tjong et. al. [57] showed that the elastic modulus and the tensile strength increased with increased PT content. The impact strength decreased gradually with increasing PT then leveled off above 23 wt %.

The bioactivity/biocompatibility of potassium titanates were investigated by immersing them into simulated body fluid (SBF) and by cell studies by several researchers.[8,58,59] Li et al.[59] showed that PT whiskers were bioactive in SBF solution after treatment of the whisker surfaces by HCl and NaOH solutions at 60 °C for 48 h. Moreover, Park[8] showed that HAp grows from SBF solution on PHT whiskers under certain conditions. He also showed that the photocatalytic activity of PHT whiskers upon degradation of methylene blue was accelerated by the HAp coating. As the previous researchers suggested, PT nanostructures – in most cases, nanowires and whiskers – are bioactive and photo-responsive materials that can be used to support polymeric matrices to enhance their mechanical and functional properties. In spite of their bioactivity along with their toughening effect when filled in polymers, there has not been a report concerning the use of PT whiskers as fillers in biomedical composites yet.

As mentioned before, one good example of biomedical applications of whisker reinforced composites is dental filling composites. Si_3N_4 and SiC whiskers have shown promising performances in reinforcing dental resins. However, due to their intensively black color and highly abrasive nature, the use of Si_3N_4 and SiC whiskers and their biocompatibility are limited.[60,61] For increased levels of whisker loading in these systems, entanglement of high aspect ratio whiskers is an important problem since there is a risk to entangle and ball up during processing within the monomer resins. Mixing and fusing silica on the whiskers help them avoid entanglement and decrease agglomeration tendency.[62]

2.2. Methacrylate resins and resin composites as model systems for PT embedded biomedical composites

The resin technology has emerged much since the development of reinforced Bisphenol A-glycidyl methacrylate (Bis-GMA, 2,2-Bis (2'-hydroxy-3'-methacryoxypropoxy) phenylene) propane) by Bowen.[63] In dentistry, most resins are derived from methacrylate, particularly methyl methacrylate. Acrylic resins can be classified in two groups according to their thermal behavior; the cross-linked polymers (thermosets) and the linear polymers (thermoplastics). Among acrylic resins, dimethacrylates form a cross-linked, multifunctional polymer structure whereas mono-functional methacrylate resins (linear) form thermoplastic resins.

During the last few decades, the increasing demands in aesthetic dentistry and adverse health effects of amalgam due to mercury vapor release have led to mandatory development of resin composites for direct restorations with improved physical and mechanical properties, and clinical longevity. The commercial structure of acrylic resins is composed of a powder package and a liquid to be mixed together. The powder contains the beads of poly-methyl methacrylate (<50 μm) and a chemical initiator (e.g. peroxide) including the pigment to provide natural tooth color. The liquid consists of the methyl methacrylate monomer and activator, which is usually a tertiary amine.[64] Due to low values of elastic modulus of acrylic resins, they are far more flexible than natural tooth that may lead to marginal break down or poor durability. In addition, material loss caused by abrasion is a common problem for this type of restorations.[64]

Direct filling materials, such as tooth colored dental resins and composites, can be applied in paste form and cured in the tooth cavity and allow for replacement of the damaged tooth tissue without disturbing the integrity of the tooth and its function.[65] An investigation on dental care business reported in 2005 showed that methacrylate based resin composites were used in more than 95% of anterior and 50% of posterior direct teeth fillings.[66]

Despite the remarkable increase in their commercial utilization, composite fillings still suffer from relatively lower mechanical strength than amalgam and formation of secondary caries. As a result, they have lower median lifespan than amalgams. That is, 13 years for amalgam and 5-7 years for resin based composites.

2.2.1 Polymerization reactions of methacrylate resins and resin composites

BisGMA is commonly used as base monomers in composite formulations. BisGMA is a high molecular weight resin which can form strong and stiff polymeric matrices.[65] But, the high viscosity and multiple functional groups require the use of a low viscosity diluent monomer. As the polymerization progresses, the mobility of monomers decreases resulting in pendant methacrylate groups and unreacted monomer trapped in the material.

When cured, these systems often have incomplete double bond conversion after polymerization. Low levels of conversion affect the physical properties and decrease the overall strength.[67] Triethylene-glycol dimethacrylate (TEGDMA) provides the monomer mixture to be more fluidic due to its low viscosity and this increased mobility of monomers helps to increase the cross-linking density.[65,67,68]

The Camphorquinone (CQ)/amine systems for generating radicals are widely used for the light induced polymerization of dental resin composites. The photo initiator is CQ that requires a co-initiator (amine) to propagate the reaction. The tertiary amines do not absorb light but interact with the activated CQ to produce reactive species.[69] Dimethyl amino ethyl methacrylate (DMAEMA) is a common tertiary amine, which is used usually with CQ. The molecular structures of BisGMA, TEGDMA, and UDMA monomers and CQ (initiator)/DMAEMA (co-initiator) system are shown in Figure 2.5.

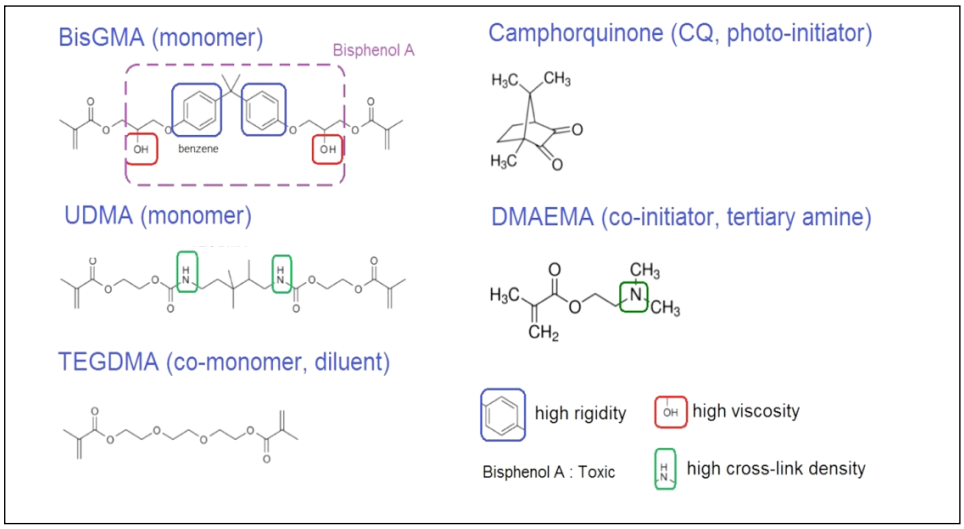


Figure 2. 5 Schematics showing molecular structures of BisGMA, UDMA, and TEGDMA monomers and CQ/DMAEMA initiator/co-initiator (amine).

The polymerization (physically curing) reaction proceeds basically in three stages, which are initiation, propagation and termination.[70-72]

i) Initiation. First, light is absorbed by CQ in the blue region (468 nm) and leads to the n to π* transition of the dicarbonyl group. After the dicarbonyl group is stimulated in the monomer mixture, CQ enters the exciplex state, the non-bonding electrons can be promoted to a π* antibonding orbital. The excited n to π* transition interacts with an amine molecule and forms an exciplex. Within this exciplex, CQ accepts an electron from amine and form the radical ion pair, and abstracts a hydrogen atom from the tertiary amine that results into primary radical. From this reaction free radicals, which show reactivity to break the unsaturated carbon bonds of the monomer, through hydrogen abstraction, called the propagation phase.

ii) Propagation. This latter radical then attacks the carbon double bonds of the monomers.

ii) Termination. Termination occurs when the active two chain ends react together and form an inactive macromolecule, ending the chain growth.

Improved matrix properties and filler-matrix coupling methods have mostly overcome the problems associated with the earlier restorative material microstructures and production routes.[70] Formation of a polymeric network is highly dependent on the structure of the monomer/co-monomers used as well as the polymerization conditions employed. In direct restorative applications, the monomers are better be selected to yield densely cross-linked glassy polymer networks that provide high modulus and strength, resistance to swelling and staining.

2.2.2 Types of inorganic reinforcements for dental resins

Bis-GMA and UDMA based resins have been reinforced by a variety of inorganic fillers to improve their performance. In common commercial composites, the amount of fillers comprises at least 30% in volume of the dental resins. Fillers have been used to form micro-filled and/or nano-filled hybrid composites to increase the wear resistance, decrease the polymerization shrinkage and modify the color of the restoration. A classification through the filler morphology, though it is not a commonly used classification, provides a good approximation in terms of an understanding the background on how filler particles work to support resin matrices.

- ***Spherical Fillers***

The use of apatite particles as fillers in dental resins offered an increase in wear resistance and polishability at first but had high reflective index and lower strength than the other type of light cured dental resins.[73,74] Thus, unmodified apatite crystals cannot be used in the applications where heavy load is applied. Mica-apatite glass ceramic particles with different amount of porosity and composition were also incorporated into dental resins. It was stated that[73] when doped with high amount of porous apatite particles, strength was lower than the one doped with denser. It may be a good way of mimicking underlying dentine structure and mechanical properties.

However, the porosity may influence lower silanization efficiency that is needed for providing a good wetting between the organic matrix and the particles. Xia and his group[75] showed that dental resins could be reinforced by TiO_2 nanoparticles with diameters smaller than 50 nm. TiO_2 has been used as an additive in dental materials to match the opaque properties of teeth. But using TiO_2 nanoparticles as additives to enhance the mechanical properties of dental resins has not been successful due to inconsistent agglomeration of TiO_2 nanoparticles.

Many methods have been attempted to prevent the aggregation by modifying its surface with surfactants, ligands and proteins. Nanoparticles were coated with organosilanes (ATES) in order to increase bonding strength between the matrix and the nanoparticles. It has been shown that microhardness and flexural strength increased by reinforcement. Sun et al.[76] showed that even addition of small amounts (0.06 wt%) of acid modified TiO_2 nanoparticles doubled the hardness of the resins and there was an optimum amount of nanoparticles that can be effectively loaded into resin without intense aggregation. It is clear that addition of TiO_2 nanoparticles to substantially improve mechanical properties of the resins is still a concept rather than a fact.

- ***High Aspect ratio Fibers and Whiskers***

Various high strength - high modulus fibers have been investigated to enhance flexural strength and fracture toughness of resins. It has been proved that fiber network in resin matrix changes the stress dynamics positively when applied onto natural tooth interface.[77] From the point of composite mechanics view, fibers are preferred to particles for reinforcing materials since they can provide larger load transfer. They can also facilitate some well-known toughening mechanisms such as fiber bridging, fiber deflection, and fiber pull-out. It is expected that mixing fibers in various sizes with higher levels of loading can enhance composite strength, modulus, and wear resistance.[75] Such fibrous materials include organic polymer fibers, silica and glass fibers, ceramic whiskers, and carbon nanotubes.

Incorporation of fibrous materials significantly increases stiffness, flexural strength, fracture toughness and fatigue resistance of the resin composites but, the chemical stability, aesthetics and handling properties of the composites are still unsatisfactory.

Moreover, glass fibers reinforced composites exhibit decreased mechanical properties after prolonged storage in water. For example, flexural strength and fracture toughness of a commercially available dental composite DC-Tell (DCS Dental, Switzerland) containing 38 wt% short glass fibers decreased by 66% and 60%, respectively after storage in water for 3 months.[78] The flexural strength did not recover the same level of the dry group after dehydration.

Chen et al.[66] investigated the reinforcement of Bis-GMA/TEGDMA dental resins (without any silica particles) and its composites (with conventional glass fillers) with various fractions of HAp nanofibers. They concluded that 5-10 wt% addition of HAp to dental resins increased the biaxial flexural strength while larger mass fractions could not further improve or even reduce the mechanical properties. The relative good dispersion of HAp nanofibers at low mass fraction was the primary reason for improved mechanical performance.

Xu et al.[62] showed that impregnation of extremely strong Si_3N_4 or SiC whiskers with silica beads could result two-fold increase in composite strength and toughness. Silica particles were fused onto individual whiskers to facilitate whisker silanization to minimize whisker entanglement by facilitating their dispersion and to enhance whisker retention in the matrix by providing roughness on the whisker surfaces. These whiskers are single crystals possessing a high degree of structural perfection and hence superior strength and toughness values. Tensile strength of Si_3N_4 whiskers is very high -approximately 50 GPa - when compared to glass fibers with that of 3 GPa and 0.1 GPa for bulk glass particles.[62]

In addition, the morphology of the whiskers is highly elongated (diameter 0.5 μm, length 5 μm) with the potential benefit of bridging matrix microcracks and preventing them from propagating as well as providing resistance to dislodgement from the matrix during wear process. Beyond the benefits of strengthening effects, it has been reported that these fibers can reduce the polymerization shrinkage as well.

- ***Layered Materials and Other Fillers with Irregular Shape***

In recent years, there has been a great interest on use of composites in which nano-sized layered fillers are dispersed in a polymeric matrix. The effective use of urchin-like HAp nanoparticles[79] and Layered Double Hydroxide (LDHs)[80] as reinforcements in dental resins have been tried to increase the bonding of resin molecules in between and at the resin-reinforcement interface. These types of layered/urchin-like structures have high potential to provide mobility of resin during composite formation. LDHs are composed of hydroxy layers of bivalent and trivalent ions. They have the general formula $[M(II)_{(1-x)-})M(III)_x(OH)_2](A_{x/n})\ mH_2O]$.

By the exchange of bivalent (Mg, Ni, Zn, Cu or Co as M(II)) with trivalent ions (Al, Cr, Fe or Ga, as M(III)) positive residual charges are generated in the structure and charge balance is protected with the presence of anions ($(CO_3)_2$, F, Cl, NO_3 as A_n) and water molecules placed between the layers[80]. In a recent study by Tammaro et al.[80] F releasing LDHs were shown to be good reinforcements for BisGMA-TEGDMA system, up to 20 wt% loading level. They have shown by dynamic mechanical analysis (DMA) that the storage moduli of the reinforced resins increased but the deformation at break was slightly lower and toughness remained unchanged. One important advantage of LDH reinforced system is the F release by time. They have stated that when F anions are detached from the inside surface of the layers upon polymer processing, the lamellae are delaminated and well dispersed in the resin.[80] The dispersion of these nano-sized layers creates more interaction surfaces for filler-matrix interaction and provides better chemical interlocking at the interface.

On the other hand, the un-delaminated layers can intercalate polymers into the spaces where the ions are released. The F diffusion through the resin can be controllable so that the biocompatibility and tissue regeneration is positively affected. The mechanism of LDH reinforcement in the resin matrix is schematically illustrated in Figure 2.6.

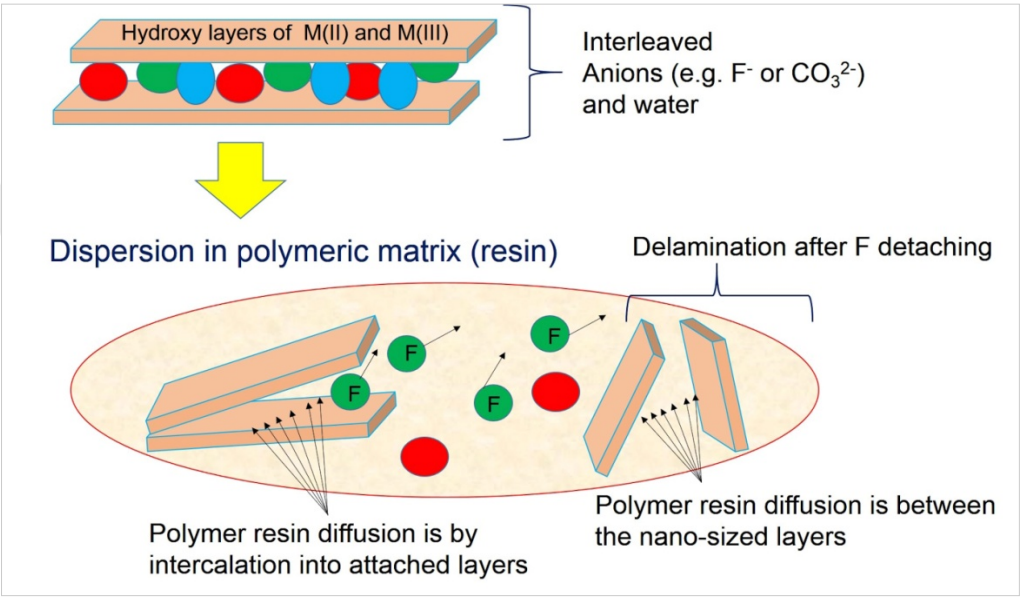


Figure 2. 6 Schematic illustration of LDH reinforcement into dental resin matrices.

A recent study on urchin-like HAp reinforcement carried out by Liu et al.[79] is a promising work. The SEM image of urchin-like HAp reinforcement is shown in Figure 2.7 along with an inset image of a real urchin. The arrows in the figure point out the spaces between the spines that provide higher interaction area for polymer diffusion, hence the mobility of monomers – the flow – is not restricted. Liu et al.[79] reinforced BisGMA-TEGDMA system with silanized urchin-like HAp up to 30 wt% and irradiated by microwave source. They stated that the fillers dispersed homogeneously up to 20 wt%.

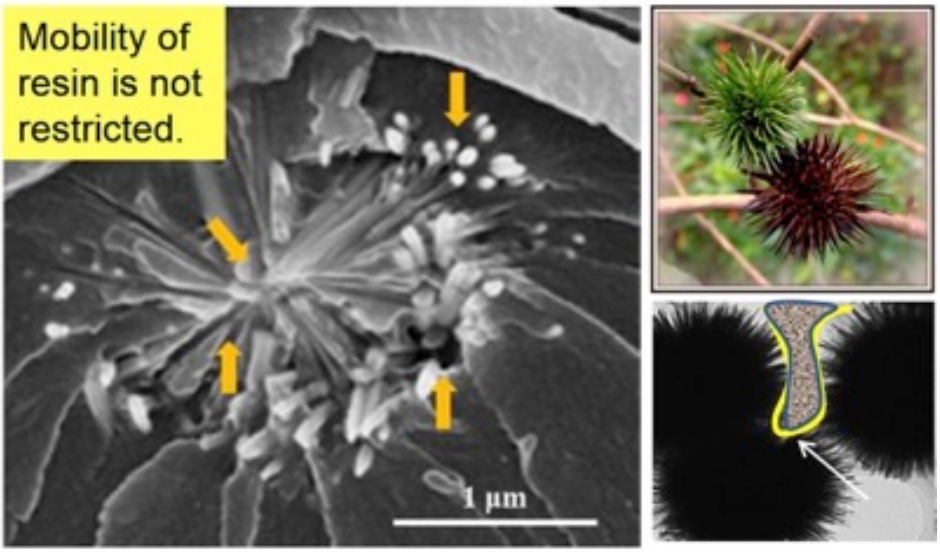


Figure 2. 7 Schematics of urchin-like HAp reinforcement

The well-dispersed fillers increased the interface contact and therefore, the mechanical strength. They concluded that urchin-like HAp surfaces provided better properties than HAp whisker reinforcement. It is clear that irregular shaped, nano-sized particles provide better interaction at the filler-resin interface and better mechanical properties. They also offer higher loading amounts without restriction of mobility of the resin. Unfortunately, the aggregation of the nano-sized particles is the one and the biggest problem.

2.2.3 Silanization (Silane coupling)

Silane coupling is an important process performed to support the adhesion between filler and the resin matrix of a dental composite. Silane coupling increases hydrolytic stability of the composite owing to hydrophobic nature of the silanes.[81,82] It has been also reported that silane coupling slows down the degradation processes[83], protects the filler surface against fracture[84], and improves distribution and stress transmission from the flexible resin matrix to the stronger filler surfaces.[85]

The typical cross-section of dental composite reinforced by filler particles and silica (SiO_2) to enhance wettability and interaction is shown schematically in Figure 2.8. Silanization forms a link between the resin matrix and the filler surfaces. The resin matrix and the fillers have different chemical compositions. However, by silane coupling, they are bound to each other by Si-O linkages called siloxane bonding (≡Si-O-Si≡). In addition, by the organo-functional group of silane and the reactive groups of the resin can bind through covalent bonding. The reactivity depends on the distribution of silane on the filler surfaces.[86] The most common coupling agent is methacryloxy propyl trimethoxy silane (δ-MPS) that binds to the filler surface and copolymerizes with the methacrylate polymer.[87]

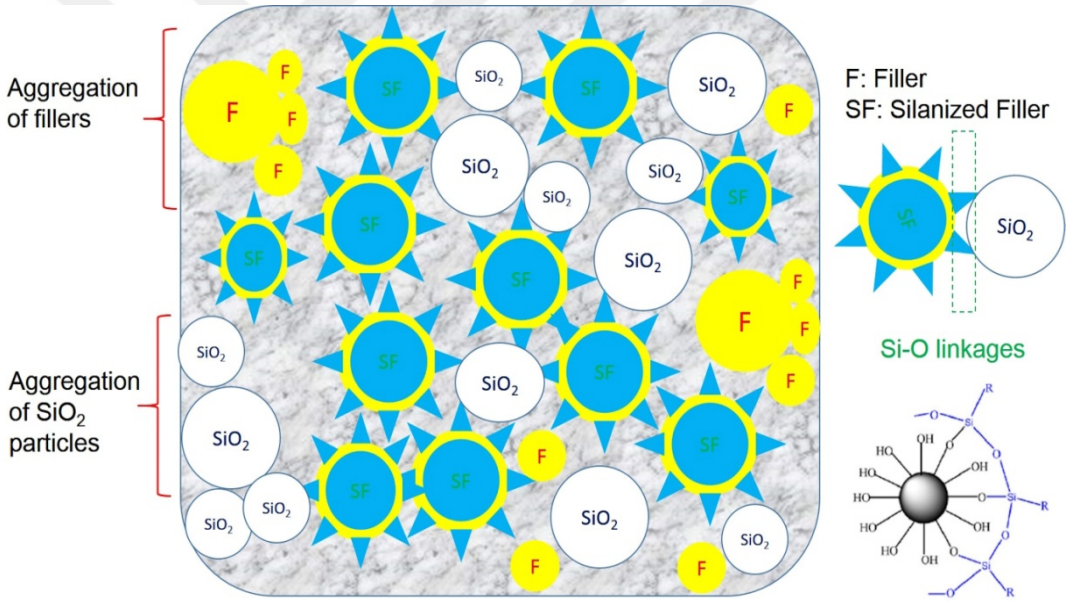


Figure 2. 8 Schematic representation of cross-section of a dental resin matrix reinforced with filler particles and silica.

The amount of coupling is an important factor since incomplete coverage of filler surfaces causes inefficient bonding with the resin matrix as also shown in Figure 2.8. The inefficiency of coverage result in non-uniform dispersion, aggregation of untreated fillers, increased viscosity, and accordingly decrease in mechanical performance.[84] Excess amount of silane can also cause deterioration in the structure by decreasing the hydrolytic resistance in the aqueous environment of mouth.[86]

This section presents a brief literature review on the mechanism of silane coupling and the problems that may arise during processes. However, the decrease in dental restorative lifespan is composed of many concerns that affects and have been affected by each other. The next section presents a brief literature review on the critical problems that lead to the deterioration of final performance of the restorative.

2.2.4 Main problems associated with composite resins

Main problems associated with the production and usage of the resin composites are outlined in the subsections below.

- ***Alignment and Dispersion of the Inorganic Fillers***

The dispersion of the filler particles in a resin matrix is of critical importance since dental restoratives are light-cured. The mechanical and optical properties, and the final biocompatibility are significantly affected by the light penetration upon curing. Basically, light first propagates through the monomer mixture and stimulates the photo-initiator molecules to react with amines and form radicals.[88] As the thickness of the initial mixture increases, light penetration through the material gets slower. In addition, the scattering of light by the fillers further decreases the penetration. Mechanical strength is directly reflected by the polymerization efficiency and filler-matrix interface homogeneity, as well as the refractive index of the final microstructure.

If light cannot propagate to the deepest level of the bulk, then there would always be some unreacted monomers trapped inside the whole polymerized network. Thus, even upon operation inside the tooth cavity, there is a product-type dependent limit for the maximum thickness that can be applied and cured at once. A recent study indicated the maximum thickness that can be cured at once as 6 mm achieved by bulk-fill composites with around 80 wt% filler content.[89]

In terms of toughening mechanisms that are operational for filler particles inside a polymer network, homogeneous dispersion is the key parameter. For high-aspect ratio fillers, crack deflection and/or bridging mechanisms work to increase the durability of the structure against masticatory attacks especially in occlusal surfaces. Considering that the maximum thickness of occlusal surfaces as 2.5 mm[90], the composite must fulfill the homogeneity of the natural tooth surface. The agglomeration of fillers must be prevented, filler-matrix interface must be homogeneous and the applied filling must be clean in terms of any unreacted constituent.

- ***Polymerization Shrinkage***

The other critical problem regarding the resins composite is the polymerization shrinkage. It occurs because by polymerization, the van der waals spaces between monomer molecules change into covalent spaces.[91] This shrinkage creates contraction stresses in the composite restoration and severe contraction stresses cause deformation in the surrounding tooth structure. But most probably, the significant amounts of polymerization shrinkage lead to the formation of a gap between the filling and the tooth, causing leakage and development of secondary caries.[65] It also creates spaces at the filling-tooth interface and cause the filling to drop. The amount of shrinkage is highly related to the amount of diluent co-monomer (i.e. TEGDMA in most cases). Since TEGDMA is a low molecular weight monomer, the mobility of reactive monomer species is increased and the polymerization efficiency increases with increasing TEGDMA content.[65]

Along with polymerization efficiency, the polymerization shrinkage is promoted. Increasing the high molecular weight monomer ratio (e.g. BisGMA, UDMA) can decrease polymerization shrinkage, however, it leads to unacceptable viscosity, causes handling issues and limits the maximum applicable filler-loading percentage. There should be a balanced ratio of monomer/co-monomer that is specific to the system properties such as filler type, morphology, polymer resin properties, etc.

- ***Toxicity of Unreacted Monomers***

As mentioned earlier, toxicity has been the major reason for the restorative resin composites to replace amalgam in the first place. However, especially BisGMA, which includes a Bisphenol A group (see Figure 2.5), is known to be toxic. There are a few known cases of allergic reactions triggered by composite resins. In overall, they are safe to use but further improvements would be favorable.[65] Unless additional chemicals are involved, the toxicity of a standard dental resin/filler/initiator system is closely related to the low polymerization efficiency, since unreacted monomers become trapped inside the network. Thus the toxicity problem should be considered together with the other problems mentioned.

CHAPTER 3

EXPERIMENTAL PROCEDURES

In this chapter, the experimental procedure followed for the production, characterization, and testing of PT nanostructures are given in detail. PT nanostructures were synthesized by two different techniques; i) sol-gel processing, and ii) hydrothermal treatment. Each method yields the synthesis of PTs having different structural and functional properties depending on the process parameters. The effects of the following process parameters on the structure and properties of the final products synthesized by both techniques were investigated.

- Ti/K ratio (molar)
- Temperature of the reaction /post-treatment
- Reaction time

3. 1. Synthesis of PTs by sol-gel technique

3.1. 1. Materials

Tetraethyl orthotitanate (TEOT, $Ti(OC_2H_5)_4$, Merck 821083) and potassium methylate (PM, CH_3OK, Merck 820746) were taken as the precursors for titanium and potassium, respectively. Ethanol (>99.8%, C_2H_5OH, Sigma-Aldrich 32221) was used as the dispersion media. Hydrochloric acid (12 M, HCl, Merck 100314) was used as the acid catalyst to accelerate hydrolysis reactions during sol-gel transformation. All chemicals were used in as received form.

3.1. 2. Procedure

The synthesis procedure of the potassium titanate nanostructures by sol-gel technique was based on the previous study performed by Kang et al.[20] The synthesis route is shown schematically in Figure 3.1. For a typical synthesis, TEOT was added to 20 mL of absolute ethanol at predetermined amounts. After 5 min of stirring, PM was added into this mixture. For all synthesis procedures, all additions were made under continuous stirring on a magnetic stirrer.

PM amount was kept at 0.1 mole (2.039 g) and TEOT amount was varied to establish the desired Ti/K (molar) ratio. Then, when the homogeneous dispersion of precursors in ethanol was attained, 1.5 mL of HCl (37 %) was added drop wise. After that, the *sol* was left at 40 °C for 30 min while continuous stirring. The pH of the solutions just before gelation was around 6- 7. The pH was measured using pH test strips. Depending on their Ti/K (molar) ratio, the sols were gelled in various time periods though all of which were shorter than 15 min. The sols were then transferred to a 10 cm diameter borosilicate petri dish, covered with Parafilm® and left for complete gelation and aging at room temperature (RT). The gelation of the sols was determined by visual examination. The complete gelation was taken as the state, at which the gelling product reached a viscosity preserving its shape without any distortion when the petri dish was tilted 45° angle.

After aging at room temperature for 4 days, the *gels* turned into white precipitates that were dried in an oven at 100 °C for a day to obtain xero-gels. Finally, the xero-gels were calcined at 600/800 °C for 1-3 h. The heating and cooling rates were 5 °C/min. The initial precursor compositions and the synthesis conditions of the sol-gel derived PT nanostructures are given in Table 3.1. Note that Ti/K molar ratio was varied by keeping PM amount constant and changing the TEOT amount.

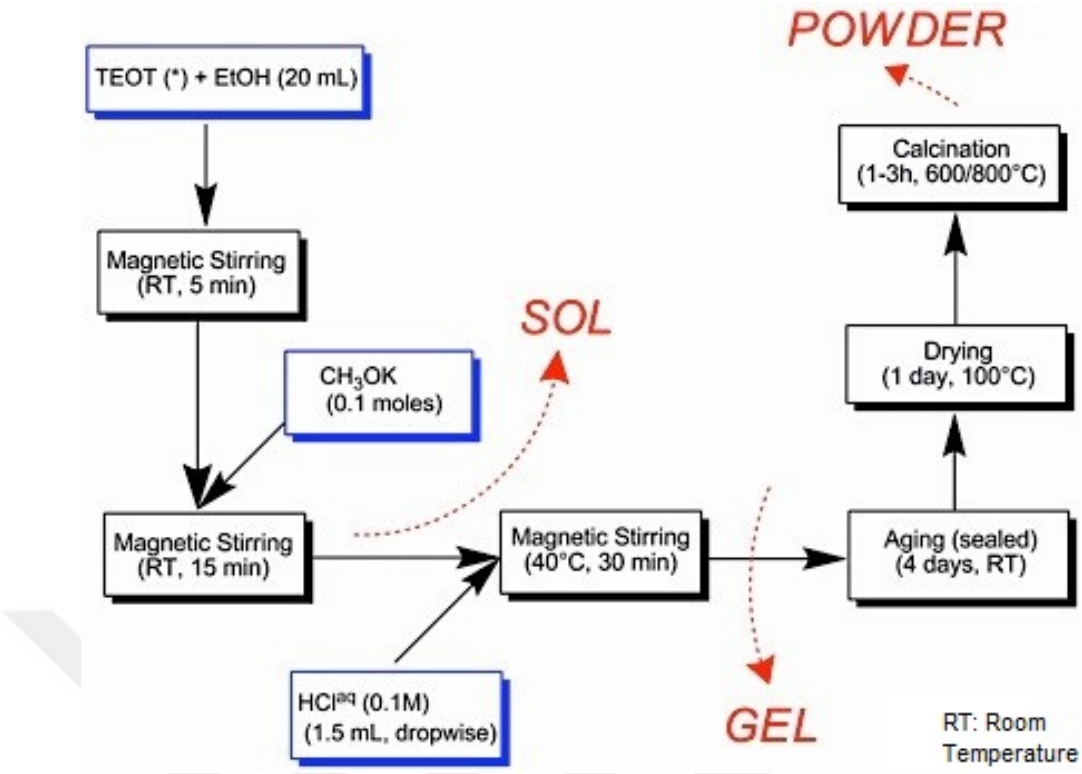


Figure 3. 1 Route followed for the synthesis of PT nanostructures by the sol-gel method.

Table 3. 1 Precursor composition and synthesis conditions of sol-gel derived nanostructures.

Ti/K (molar)	**TEOT (mole)**	**PM (mole)**	**Calcination Temperature (°C)**	**Calcination Time (h)**
1	0.03	0.1	600, 800	1-2-3
1.5	0.045			
2.5	0.09			
3.5	0.105			

3. 2. Synthesis of PTs by hydrothermal treatment

3.2. 1. Materials

Titanium dioxide powder ((TiO_2, P25 Degussa®) and potassium hydroxide (KOH, Merck 105033) were used for the sources of T and potassium, respectively. Aqueous solutions at certain molarity (5-20 M) of KOH were prepared by dissolving KOH pellets in distilled water.

3.2. 2. Procedure

Synthesis of hydrothermally derived PT nanostructures was accomplished by following the work done by Wang et al[29]. All reactions were performed in a high-pressure reactor (ITO Instruments®, max. 120 bar and 250 ºC). First, 0.6 g of commercially available TiO_2 powder (P25) was dissolved in 60 mL of aqueous KOH solution. Then, the P25 powder containing $KOH^{aq.}$ solution was homogenized by sonication followed by stirring on a magnetic stirrer at RT. After that, the solution was transferred to the reactor, sealed and the reaction was performed at temperatures of 120, 150, and 180 °C for 3 to 48 h at a constant stirring rate of 250 rpm. The total volume of the reactor vessel was 300 mL and 30% of it was filled for each experiment.

After the treatment was complete, the condensed liquid containing the precipitates were washed and vacuum-filtered with DI water. The filtered powders were further dried at 100 ºC for overnight. The hydrothermal synthesis route is shown schematically in Figure 3.2. The initial precursor compositions and the treatment conditions of the prepared samples are given in Table 3.2. Note that Ti/K molar ratio was varied by changing $KOH^{aq.}$ molarity and keeping P25 powder weight constant.

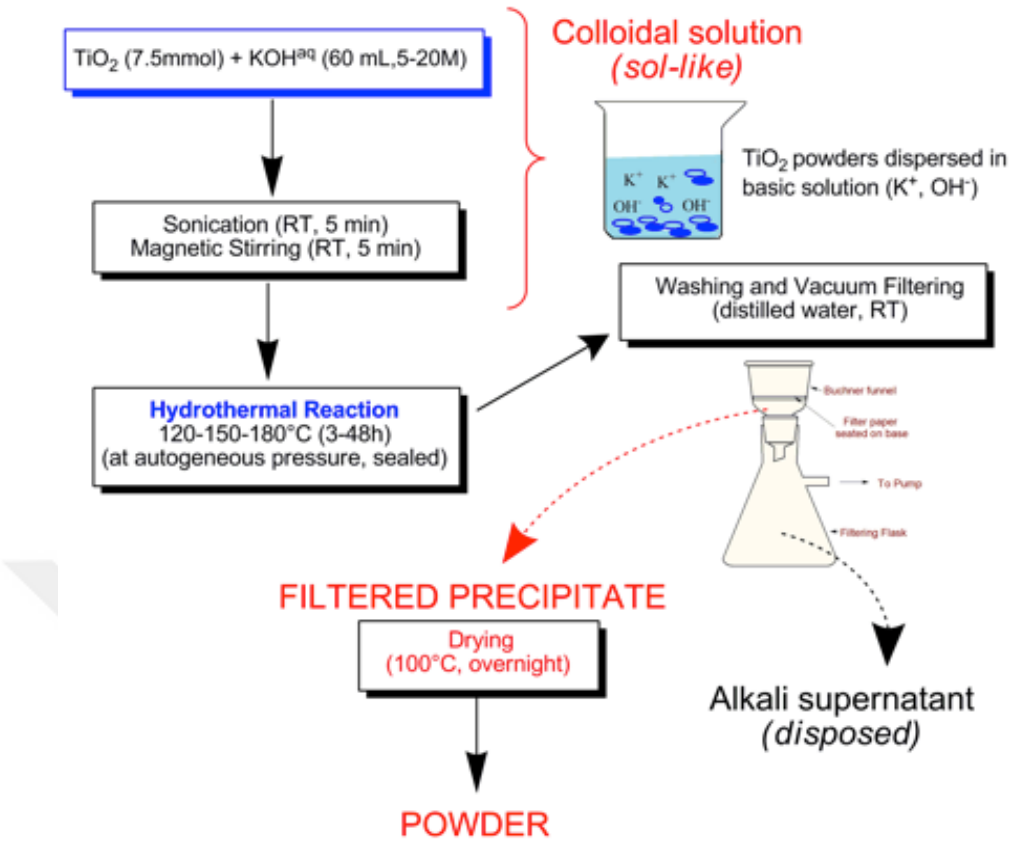


Figure 3.2 Route followed for the synthesis of PT nanostructures by the hydrothermal treatment.

Table 3.2 Precursor composition and synthesis conditions of sol-gel derived nanostructures.

TiO_2 (P25) (mole)	**KOH^{aq} (M) (50 mL)**	**Hydrothermal Temperature (°C)**	**Reaction Time (h)**
$2*10^{-5}$	5	180	3, 12, 24, 48
	10		
	15		
	20		
	20	120, 150	3

3.3 Dispersion of agglomerates by sonication

The preliminary results, which will be presented, in the following sections showed that the particles synthesized cause inhomogeneity in the final composite. Since these particles are relatively heavy, they settle down in the monomer mixture upon curing. Either they create air bubbles upon curing or they settle down and cause big voids during polishing of the bottom surface of the final composite. In addition to that, the agglomeration of nano-sized particles is a serious problem due to the same reasons. The agglomeration also inhibits mechanical interlocking at the resin-particle interfaces. In order to overcome abovementioned inhomogeneity problems, powders were dispersed in ethanol and sonicated for 20 min. It has been recognized that the big agglomerates and the heavy impurity particles settle down in ethanol after 15 min of sonication. The floating whiskers were separated and ethanol was evaporated. The same procedure was repeated with DI water. Water is a polar solvent and effective on separation purposes, but unfortunately, KOH was soluble in water. Hence, it was not possible to separate unreacted KOH by using water. The photographs of the PTs after sonication in water and ethanol are shown in Figure 3.3.

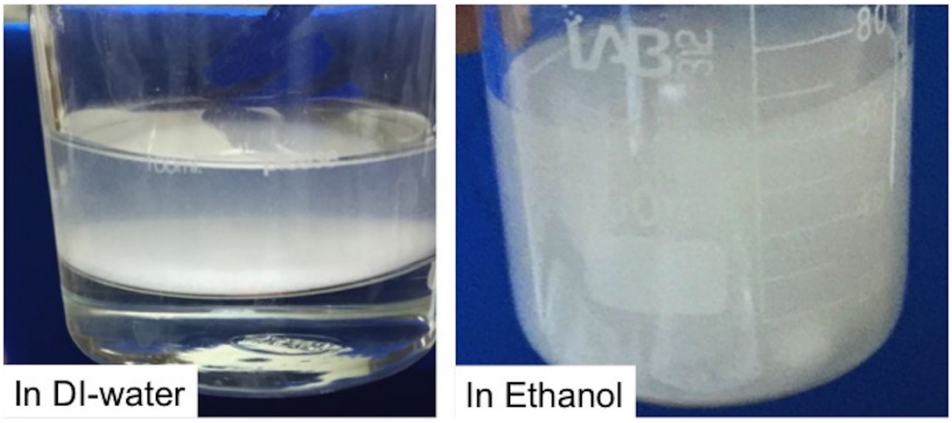


Figure 3. 3 Appearance of PTs after sonication in DI-water and ethanol.

Ethanol sonication was performed before hydrothermally synthesized PT embedment into UT for the preparation of composites. Before sonication, the powders were yellowish in color but the sonicated powders were porcelain white and easily flowable. The sediments after sonication were still yellowish.

3.4 Production of dental resins and composites

3.4. 1. Materials

Diurethane dimethacrylate ($C_{23}H_{38}N_2O_8$- UDMA, 436909, Aldrich) and triethylene glycol dimethacrylate ($C_{14}H_{22}O_6$- TEGDMA, 261548, Aldrich) monomers were used as the base and the co-monomer, respectively for the production of PT nanostructure embedded resin composites. Camphorquinone ($C_{10}H_{14}O_2$,-CQ, 276286, Aldrich) and 2-dimethylamino ethyl methacrylate ($C_8H_{15}NO_2$- DMAEMA, 234907, Aldrich) were used as the visible light activator and the co-initiator, respectively. The molecular structures of these polymeric constituents are shown in Figure 2.5. For silanization of embedded PT powders, cyclohexane (C_6H_{12}, Sigma Aldrich 15329), propyl amine (C_3H_9N, Alfa Aesar 036635) silica (SiO_2, Aldrich 718483) and δ-MPTMS (3-methacryloyloxy) propyl trimethoxy silane, $C_{10}H_{20}O_5Si$, Alfa Aesar A17714) were used.

Both sol-gel derived and hydrothermally derived PTs were used to reinforce UDMA/TEGDMA (UT) resins. The analyses revealed that PTs derived by the sol-gel process were bigger in size and aspect ratio than that by hydrothermal treatment. Thus, the effect of PT nanostructure size on final properties of the composites produced could be anticipated by comparing the sol-gel derived and hydrothermally derived PT embedded UT composites containing identical amount of embedment.

3.4.2 Procedure

3.4.2. 1. Silanization

For mechanical interlocking and chemical bonding between the resin matrix and PT nanostructures, silica powders were mixed with PT whiskers in 2:1 weight ratio. Then, this mixture was dispersed in 50 mL ethanol, continuously stirred on a magnetic stirrer for an hour. After that, the ethanol was evaporated at 100 °C.

In order to interact silica particles with PTs, powder mixture was heated to and kept at 500 °C for 30 min. After furnace cooling, the mixture was added into 200 mL cyclohexane. A 75 mg propyl amine and 200 mg δ-MPTMS were added and stirred vigorously at 70 °C at 800 rpm for 1 h. Finally, the cyclohexane and the by-products were eliminated by drying the mixture at 110 °C followed by washing with methanol and drying again at 110 °C.

3.4.2. 2. Polymerization (Curing)

The molds that were used for casting neat (without PT addition) and PT embedded UT resins are shown along with specimens of the bulk composites in Figure 3.4. The circular mold (mold 1) was made of stainless steel at 20 mm diameter. The thickness of the cast was controlled manually at approximately 4 mm. The diameter of the cured specimens varied at 19±2 mm. The specimens obtained from mold 1 were used for hardness, nano-indentation, wear, and MB degradation tests. The second mold (mold 2) was designed to get dog-bone shaped tensile test specimens and was made from silicone rubber. The nominal dimensions of the cured specimens are illustrated in Figure 3.4. The length and width were 58±1 mm and 10±1 mm, respectively. The final thickness was as low as 2 mm not to cause any problem on polymerization in terms of depth of cure. Blue light (5 Watt, LED, blue lighting diode 450-490 nm) was used for the curing. The monomer, co-initiator and the activator mixtures were exposed to blue light for 200 s with 1 on - 1 off pulses in casting molds.

Three different monomer formulations namely UT-1, UT-2 and UT-3 were chosen for the production of neat and PT embedded resins. The compositions of UT monomer mixtures are given in Table 3.3. Each formulation was prepared using these monomer ratios. Neat resins were taken as the control samples. Note that comparison between neat resin formulations are based on molar ratio between UDMA and TEGDMA.

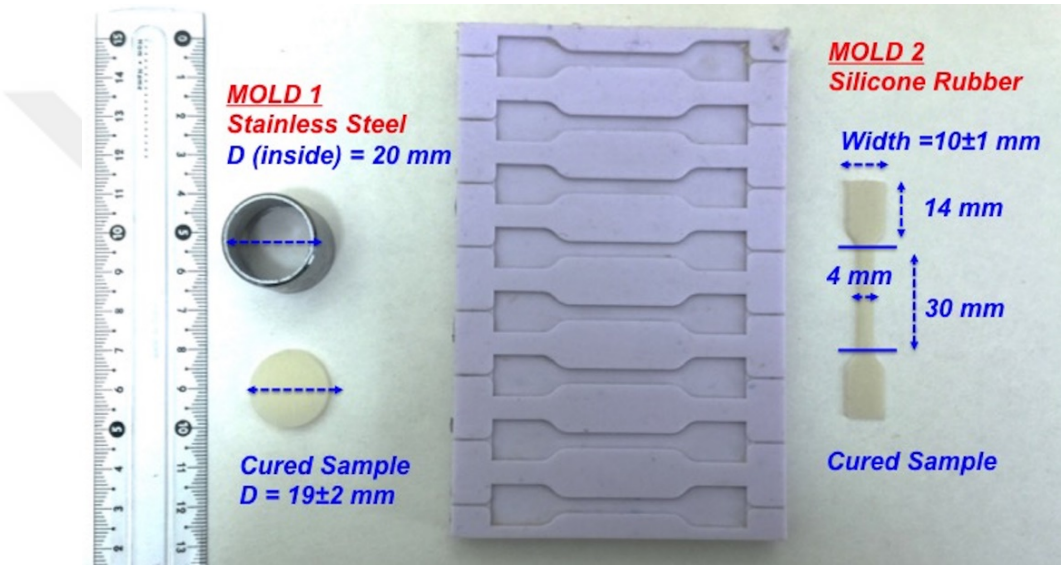


Figure 3. 4 Photographs of the molds and samples produced showing the size and shape of the final composite products.

As mentioned previously, UDMA monomer has the biggest viscosity hence it is harder to mix. Thus, in a typical composite preparation, PT whiskers were mixed first with UDMA under continuous mixing. After 5 min, TEGDMA was added and the diluted mixture was stirred for 10 min. The beaker was covered with aluminum foil to avoid any light interaction. Then, 0.5 wt% (0.038 g) of CQ and DMAEMA were added into the monomer mixture and stirred for 10 min. Finally, the mixtures were cast into the mold and cured.

It is important to note that embedded PTs were produced at Ti/K=2.5 and by calcination at 800°C for 1h. As measured in SEM images, the diameters of PTs were smaller than 100 nm and length were between 400-900 nm. The calculated average aspect ratio (length/diameter) of PTs were varying from 4 to 38.

Table 3. 3 Composition of neat resin mixtures.

Resin Mixture	**UDMA (g)**	**TEGDMA (g)**	**CQ (g)**	**DMAEMA (g)**	**U/T (mol %)**	**U/T (wt. %)**
UT-1	4.70	2.86	0.038		50/50	62/38
UT-2	5.99	1.55			70/30	79/21
UT-3	3.12	4.43			30/70	41/59

The compositions of the composites prepared by adding sol-gel derived PTs can be summarized as shown in Table 3.4. As it is indicated, 5 wt % of PT were embedded in UT-1/3 resins without sonication and/or silanization treatment. These were the preliminary experiments to investigate surface properties of PT embedded UT composites with respect to that of neat UT resins. It is important to note that embedded PTs were produced at Ti/K of 2.5 and by calcination at 800 °C for 1 h. As measured in SEM images, the diameters of PTs were smaller than 100 nm and length were between 400-900 nm. The calculated average aspect ratio (length/diameter) of PTs varied from 4 to 38.

Table 3. 4 Composition of sol-gel derived PT embedded UT resin composites.

Composite	**TEGDMA mol %**	**PT wt %**	**Aspect Ratio of PT**
UT-1-SG-5	50	5	4 to 38
UT-2-SG-5	30		
UT-3-SG-5	70		

As it is clearly reported in the following findings, embedding sol-gel derived PT powder products directly into the UT resins caused inhomogeneous dispersion throughout the resin matrix, due to the presence of sphere-like whisker agglomerates with KCl and TiO_2 by-products.

PTs produced by hydrothermal treatment at 180 °C for 24 h were also used for embedment into UT resins at varying ratios. The average sizes of hydrothermally produced PTs obtained from SEM image measurements were 39 ± 14 nm in diameter, 1.14 ± 0.4 μm in length. The length and aspect ratio of hydrothermally synthesized PT nanostructures were bigger than that of sol-gel. The aspect ratio of the nanostructures varied between 14 and 60. In Table 3.5, the compositions of the hydrothermally synthesized PT embedded composites are shown. In these composites, PT powders were embedded into UT monomer mixtures without sonication and/or silanization treatment. The embedment was 10 to 50-wt %. Composites were not obtained using UT-3 mixture because identical light source and mold were not sufficient for curing. Since the UDMA content was not sufficient for complete polymerization, cured specimens could not preserve their shape and rigidity when taken out from the molds.

Table 3. 5 Composition of hydrothermally synthesized PT embedded UT resin composites.

Composite	TEGDMA mol %	PT wt %	Aspect Ratio of PT
UT-1-HD-10	50	10	14 to 60
UT-1-HD-30		30	
UT-1-HD-50		50	
UT-2-HD-10	30	10	
UT-2-HD-30		30	
UT-2-HD-50		50	

As a second set for hydrothermally synthesized PT embedment, 5 wt % of sonicated and both sonicated and silanized PTs were embedded into UT resins. In Table 3.6, the compositions of these composites are given. The whisker to silica particle weight ratio was 2 to 1 so that 0.6 g of silanized mixture composed of 0.4 g PT was embedded into an identical mixture of UT resin. Hence, the wt % of PT embedment did not change significantly.

Table 3. 6 Composition of 5-wt % hydrothermally synthesized PT embedded UT resin composites.

Composite	TEGDMA mol %	PT wt %	Sonication/ silanization	Aspect Ratio of PT
UT-1-HDS*-5	50	5	Sonicated	14-60
UT-2-HDS-5	30			
UT-3-HDS-5	70			
UT-1-HDSS**-5	50		Sonicated/ Silanized	
UT-2-HDSS-5	30			
UT-3-HDSS-5	70			

* HDS: hydrothermally synthesized PT embedded after sonication
**HDSS: hydrothermally synthesized PT embedded after sonication and silanization

3. 5. Characterization and testing

3.5. 1. X-Ray diffraction (XRD) analysis

XRD analysis was performed both on sol-gel and hydrothermally derived PTs as well as on the resin composites produced in order to investigate the phase variety, composite structure, and reaction products on the composite surfaces. An XRD diffractometer (Rigaku DMAK/B) was employed for all XRD analyses. In all cases, powder/bulk samples were scanned between two theta of 5-70° at a scan rate of 2°/min. Data were analyzed using the Rigaku Qualitative Analysis software.

3.5. 2. Electron Microscopy analyses

Scanning electron microscopy (SEM) was used to analyze the morphology of PT nanostructures and as well as to investigate the structure of PT-resin interfaces. PT nanostructures were dispersed on a carbon band. Each sample was coated with 10 nm of platinum before analysis. JEOL Nova Nano SEM 430 was used for all SEM analyses.

Pristine PT nanostructures were also analyzed by using transmission electron microscopy (TEM) to understand the growth behavior. Samples were first dispersed in ethanol and sonicated for 20 min. After waiting 5 min for the settlement of the big ones, a single drop of the suspension was deposited onto a holey carbon grid and analyzed after completely dried. JEOL JEM-2100F UHR/HRP was operated at 200 kV.

In order to get solid evidence for the splitting of hydrothermally derived PTs, nanostructures were dispersed in ethanol and sonicated for 20 min. Then, the solution was kept still for 10 min and 0.5 mL of ethanol was dropped on holey carbon grid. This method made possible to monitor single nanowires, whiskers, non-split layers or the aggregates.

Fast Fourier Transforms (FFT) of the TEM images taken from the powders was used for calculations. The images were analyzed using Digital Microscopy® and Carine Crystallography® Softwares. Typically, the FFT of the image was taken by Digital Microscopy®. After brightness and contrast settings were adjusted for clear examination, the spots were marked using numbers. The distance of the spots from the center spot (O) were measured and shown inside vertical lines (e.g. |O1|, |O2|, etc.). The angles between two spots passing through the center of the transform were measured using the Image J® software and shown between angle brackets (e.g. ‹1O2›, ‹2O4›, etc.). The units of the calculated distance and angles are angstrom (Å) and degree (º), respectively. Additionally, it must be noted that the distances (e.g. |O1|) are converted to their reciprocals (e.g.1/O1) since the spots in FFT are indicated at reciprocal space. Afterwards, considering the interplanar spacing and the normalized intensities given in the ICDD cards of the expected phases, the similarities between the spot distance and these interplanar spacing values were researched. Taking two closest distances present in the FFT and in the card (as interplanar spacing of a certain (hkl) into consideration, the angle between these two reflections gives the clue for the right zone axis on which these two planes can be seen simultaneously. By using the Carine Crystallography®- Zone Axis determination function, zone axis was determined and the reciprocal lattice with all possible reflections was obtained. Then, not only the remaining (hkl) reflections, but also the crystallographic directions could be referenced to the center spot. The inverse FFTs (iFFTs) were derived using the FFTs taken, in order to compare with real images and support the accuracy of the FFT measurements and provide a closer look on the atomic structure.

It is important to mention that this method is not the only way to analyze the TEM images and their reflections in reciprocal space for the determination of growth mechanism. The Kikuchi maps of the expected phases could also be used. However, for complex crystals like monoclinic, it is more practical to use Fourier transforms.

3.5.3 Differential thermal analysis

Thermal behavior of the xero-gels synthesized by sol-gel was determined by TG-DTA technique. The powders were examined by differential thermal analysis (DTA) and thermogravimetric analysis (TGA) using a thermal analyzer (EXSTAR TG/DTA 7300). The experiments were performed up to 900 °C at a heating rate of 5 °C/min under nitrogen (N_2) atmosphere.

3.5.4 Gas (N_2) adsorption (BET) analysis

The surface properties such as specific surface area and pore morphology of the sol-gel and hydrothermally derived PTs were tested by N_2 gas adsorption test. Quantachrome AU9 Autosorb-1-C/Ms Analyzer was used as the testing equipment. Samples were degassed at 150 °C for 1 h before measurement. Adsorption tests were performed at -196 °C. The adsorption-desorption isotherms over 0.01 to 0.95 relative pressure (P/P_0) range and the level of porosity was calculated based on the desorption curve of the isotherm by Barrett-Joyner-Halenda (BJH) method. Multipoint surface areas were also determined.

According to International Union of Pure and Applied Chemistry (IUPAC), the physisorption (adsorption) isotherms can be classified in six types[121] as shown in Figure 3.5 (a). Micro-porous solids with small external surfaces show Type 1 isotherms (e.g. activated carbons). Type 2 is specific to the non-porous or macro-porous adsorbents. Type 3 isotherms are not common; best example is the water vapor adsorption on non-porous carbons. Type 4 and 5 isotherms are unique since they form hysteresis loops that are associated with the capillary condensation taking place in the mesopores. Type 5 is an uncommon type related to Type 3 in which adsorbent – adsorbate interaction is weak. Type 6 is specific to the multilayer adsorption on a uniform nonporous surface.

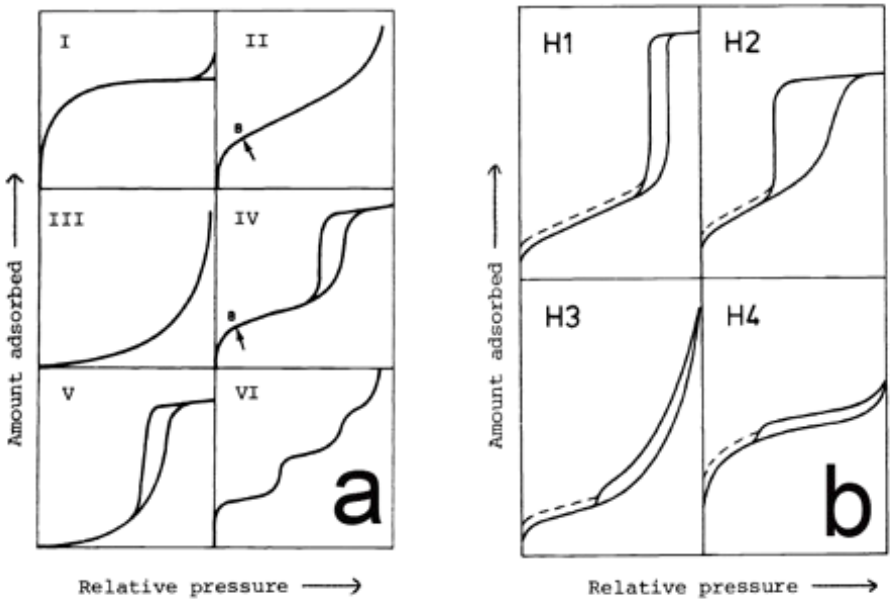


Figure 3. 5 a) BET isotherm types and b) Hysteresis loops according to IUPAC classification.

According to IUPAC, the shape of the hysteresis loops is a sign of multilayer adsorption and provides information on the pore morphology and their connection throughout the surface. Two extreme loop shapes that are related to Type 4 isotherm are H1 and H4 loops as shown in Figure 3.5 (b). H3 and H4 types are intermediates. Type H1 indicates the presence of agglomerates/compacts of uniform spherical structures with narrow size distribution. Type H2 indicates corpuscular systems but pore shapes are not well defined. Pores with narrow neck and wide body are difficult to interpret. Type H3 represents small differences in adsorption-desorption paths and indicates the presence of non-rigid aggregates of plate-particles with slit shaped pores.

3.5. 5. UV-Vis spectroscopy measurements

All of the UV absorbance/reflectance measurements were performed using a DRS equipped UV-Vis spectrophotometer (Scinco S-3100, Seul, Korea).

3.5.5.1 Energy band gap measurement by diffuse reflectance

Energy band gaps of all powders and bulk polymers/composites were recorded by performing diffuse reflectance (DR) measurement using the integrating sphere equipment. Kubelka-Munk (K-M or F(R)) is a common method for the determination of direct or indirect E_g. In K-M method, UV-Vis/DRS spectrum is recorded in reflectance or absorbance mode and transformed to F(R) and plotted versus hυ. F(R) is simply based on the formula shown in Eq. 3.1 where R corresponds to reflection percentage collected by the spectrophotometer.

$$F(R) = (1-R)^2 / 2R \qquad \text{Eq. (3.1)}$$

The type of band-to-band transitions hence the graphical calculation method determines the E_g calculated. For this method, α is assumed to be equal to F(R). The general formula for a modified K-M method according to the type of transition is shown in Eq. 3.2.

$$A(h\upsilon) \approx B*(h\upsilon - E_g)^n \qquad \text{Eq. (3.2)}$$

where; E_g is the band gap energy (eV), B refers to the absorption constant, h is the Planck's constant, (J*s) υ is the light frequency (s^{-1}), and *n* is equal to 2, 3, 1/2 and 3/2 for indirect allowed, indirect forbidden, direct allowed, and direct forbidden transitions, respectively. The extrapolation of the linear portion of $(\alpha h\upsilon)^{1/n}$ versus hυ line would give the intersection, that is E_g[49]. This method is commonly known as Tauc Plot. Direct and indirect transitions can occur simultaneously. However, the latter cannot be detected from the absorbance spectrum due to their high energy and low probability.[49]

The major transition conducts the behavior of the semiconductor but, it is very difficult to differentiate them experimentally. In this dissertation, powder samples were scanned between 200-800 nm in reflectance mode and both direct and indirect band gaps were calculated by using K-M approach.

3.5.5.2 Methylene blue degradation test

Methylene Blue (MB, $C_{16}H_{20}ClN_3OS$, Fluka 66720) degradation test was applied both to PT nanostructures and the resin composites in order to investigate photocatalytic degradation capability of the PTs and the PT embedded resin composites. Typically, MB concentration was kept at 0.01 mg/L DI-water. For all tests, 0.2 g of powder sample was added to 200 mL of MB solution. The samples were kept in aqueous MB solution first at dark for 30 min and then under UV light irradiation until complete degradation of MB in water. The testing conditions are schematically shown in Figure 3.6. The distance from solution surface to UV light source "h" was kept identical for each test. The system was continuously cooled by water flow in order to prevent any heating effect. A 100 Watt (UVP Co, Upland, Canada) UV lamp was used as the light source. Each test was performed in a wooden closed box to avoid daylight interaction.

At first, the UV-Vis absorbance of the aqueous MB solution was measured as the control sample. Then the sample was dispersed in this MB solution and kept at dark for 30 min in order to provide adsorption-desorption equilibrium of MB on particle/composite surfaces. After that, UV-Vis absorption behavior of the samples was measured at 30 min intervals. Before each measurement, 3 mL of sample solution was taken and separated from powders by using syringe filter (Millipore, Millex® Syringe driven filter unit, 22 μm).

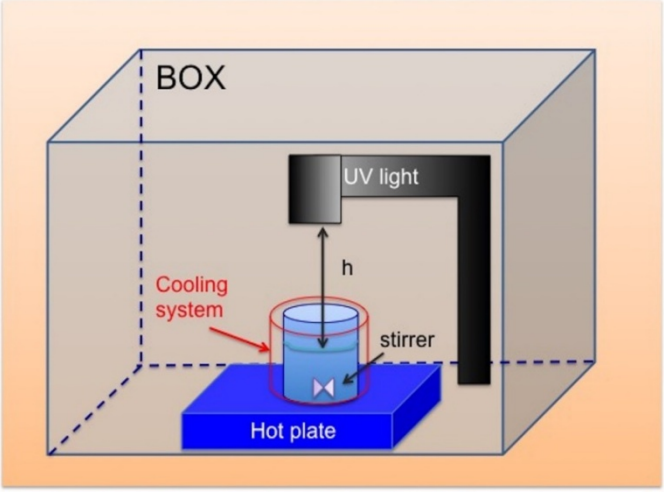


Figure 3. 6 Schematic illustration of the MB degradation testing.

As the concentration of MB in the solution decreases, the UV absorbance at specific wavelength depending on the size of the chromophore molecule decreases. MB molecule is a cationic dye, which can be adsorbed onto negatively charged, anionic surfaces by electrostatic interactions. The aromatic constituent of MB, which contains N and S atoms, is planar with dimethyl amino groups attached as shown in Figure 3.7. The length, width and thickness of MB molecule have been reported as 1.69, 0.74 and 0.38 nm, respectively.[92] It has its chromophore at 664 nm. The change in MB concentration by time was calculated by the change of UV-Vis absorption of supernatant solution at 664 nm, with respect to pure MB solution.

In order to calculate the degradation rate constant (apparent rate, k, min^{-1}) Langmuir–Hinshelwood (L-H) model based on first order kinetics of reactions has been followed. The concentration at time zero, t=0 (C_0) can be expressed by the UV-Vis absorbance of aqueous MB solution before addition of the sample at 664 nm. (A_{664} of pure MB^{aq}).

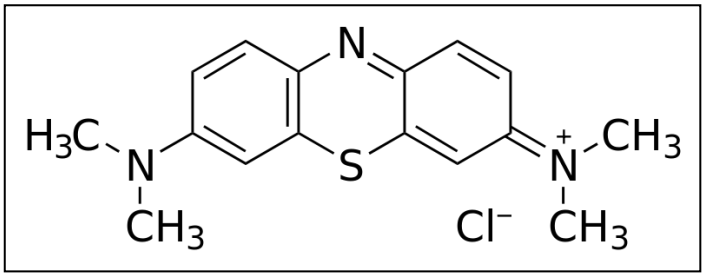


Figure 3. 7 Molecular structure of MB dye.

Likewise, the concentration at any time, t (C_t) can be expressed by the A_{664} at t. The concentration difference at a given t interval can be calculated by using the change in A_{664} by time, taking C_0 as the initial concentration. According to L-H model, if the kinetics of the reaction follows a linear path, it follows the first order kinetics and the apparent degradation rate can be expressed as the slope of -ln C_t/C_0 versus t according to Eq. 3.3. The apparent rate of degradation is expressed by the slope, k (min^{-1}).

$$-\ln (C_t/C_0) = k^* t \qquad \text{Eq. (3.3)}$$

3.5. 6. Wear test

Tribological behavior of neat resin mixtures and the composites was determined by wear tests using a pin-on-disk tribometer (CSM Instruments). Surface roughness and wear volume of the samples were measured using a surface profilometer (Taylor Hobson, Surtronic 3+). Each sample was tested under identical test conditions. The applied load was 10 N. The total distance travelled by the counter material (zirconia ball) was 200 m. Zirconia ball was chosen as the antagonist due its wide use as core and fixed partial dentures. The tests were performed at a speed of 2.5 cm/s. The acquisition rate was 1 Hz. Zirconia ball was renewed after each test to avoid misleading effect of its worn surface.

Wear rate (WR) is expressed mainly by the worn surface volume. It is noteworthy to mention that a reliable method for indication of WR is the Archard model that is used throughout this study. It provides the advantage of taking analysis conditions into account for the determination of rate, rather than showing only the volume of the worn surface. In Archard model, WR is expressed as worn volume (mm^3) per unit sliding distance (L, m) per unit normal load (F_n, N). Thereby the unit of WR is $mm^3/N*m$ and calculated by the Tribox 2.0 software as the worn surface area is introduced into the software manually. This model assumes that worn volume is proportionally related to F_n*L and the slope gives WR according to Eq. 3.4.[93]

One representative surface profile is shown in Figure 3.8 along with the inset photo of the specimen tested. The x-axis of the profile shows the distance travelled by the antagonist in horizontal direction (mm) and y in depth (µm). The worn surface track becomes clearer by naked eye as the track depth is increased.

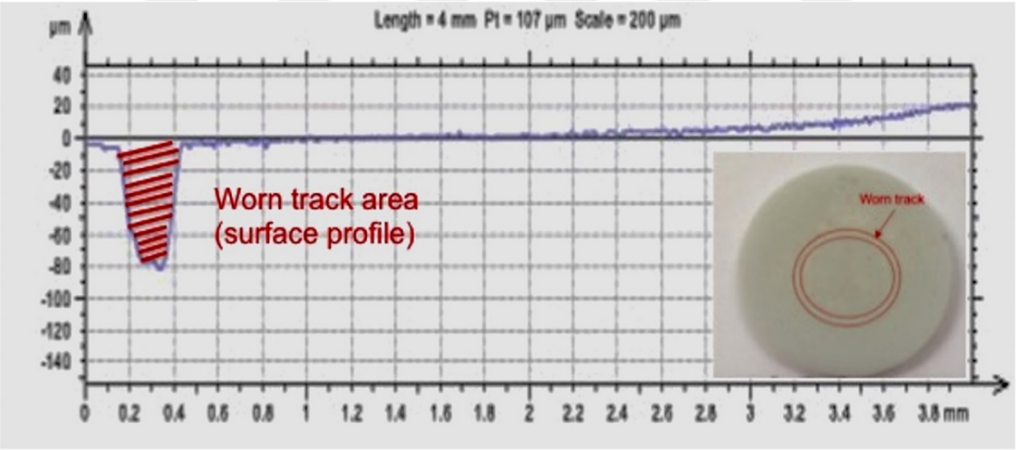


Figure 3. 8 Representative surface profile of the resin specimen tested for wear. The inset is the photo of the specimen with worn surface track.

Worn Volume (Q)= F_n*L*WR Eq. (3.4)

3.5.7 Hardness test

Hardness of the neat resin mixtures and the composites produced by embedding PT whiskers into the resins was measured by two different techniques: i) Nano-indentation (NI) and ii) Vickers Microhardness (HV). Either for NI or HV measurements, bottom and top surfaces of the specimens to be tested were polished gently using 600-grid abrasive paper until a smooth surface finish was obtained. Before testing, the surfaces of the specimens were smooth, pore and dirt free. The parallelism of both sites was preserved upon polishing.

One sample for NI, three samples for HV measurements were tested for each composite. For both NI and HV methods, ten indentations were taken to get a reliable data. It is needed to mention that severe abrasion on surface upon polish creates additional voids due whisker pullout; therefore moderate duration of manual polishing was applied to prevent further deformation on the specimen surface.

NI hardness tests were performed using Berkovich type nano-indenter (CSM Instruments, diamond indenter, 0.1-400 mN, max. depth 100 μm). A 5 mN of maximum load was applied for 15 s on surfaces with a 10-mN/min constant strain rate. In a typical NI test, force and displacement are recorded as the indenter is pressed with a prescribed loading and unloading profile. As the load is applied, the penetration depth into sample surface is measured. The area of contact at the load maxima is determined by the depth and the radius of the Berkovich indenter. Hardness is calculated by dividing the load by the indenter contact area. The elastic modulus is determined by the shape of the unloading curve. A typical load (P) – displacement (h) curve is shown in Figure 3.9.

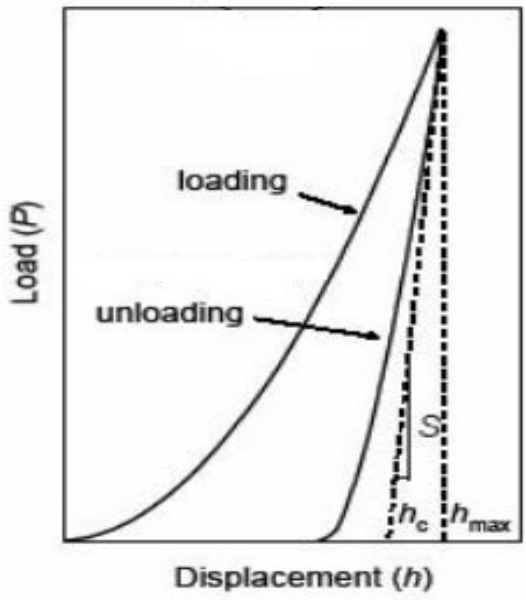


Figure 3. 9 Typical load-displacement curve obtained via NI testing.

The general formula for hardness (H) and elastic modulus (E) by NI measurement are given in Eqs. 3.5 and 3.6[94]. The geometry correction factor (β) is 1.034 for Berkovich indenter.

$$H=P/(24.5*h^2) \quad \text{Eq. (3.5)}$$

$$E= (dP/dh)*(1/2h)*(1/\beta)*(\sqrt{\pi}/24.5) \quad \text{Eq. (3.6)}$$

Vickers micro-indentation (HV0.3) was used for determination of the hardness values. A 2.94 N force was applied on the specimen for 10 s. The Vickers Diamond indenter and a typical indent shape is schematically shown in Figure 3.10. The Vickers hardness (kg/mm^2) is calculated by the formula shown in Eq.3.7[95]. The Vickers hardness can be converted to MPa by multiplying the value by 9.807.

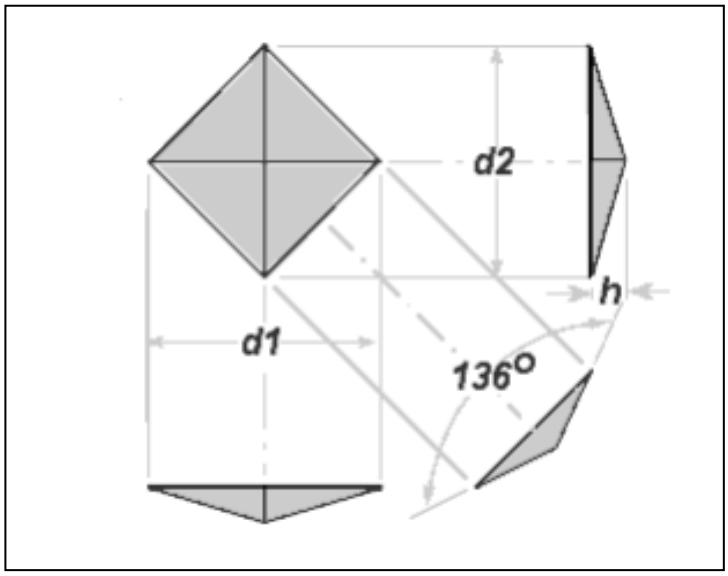


Figure 3. 10 Vickers diamond indenter shape and a typical indent trace on sample surface.

$$HV=(2F*\sin(136°/2)/d^2) =18.54*(F/d^2) \quad \text{Eq. (3.7)}$$

3.5.8 Tensile test

In order to investigate the strength and elastic modulus of the resin mixtures and the composites produced, tensile tests were applied on the dog-bone shaped samples shown in Figure 3.4. The thickness, gauge length and width of the dog-bone samples were measured with a micrometer. Instron 5565, Universal Testing Machine was used with a strain rate of 0.5 mm/min. The average gauge length, thickness and width of the tested samples were 23±0.94 mm, 1.56 ± 0.11 mm and 3.66±0.07 mm, respectively. Three samples were tested for each formulation. By using the Stress (σ) – Strain (ε) curves, the ultimate tensile strength (σ_{UTS}) and elastic modulus (E) and fracture stress were determined. σ_{UTS} is taken as the maximum stress that the sample can withstand.

E is calculated as the slope of the linear portion of the curve, using the formula given in Eq. 3.8. The average of data and deviation from average were calculated statistically.

$$E\ (GPa) = \sigma\ (MPa)/\ \varepsilon \qquad \text{Eq. (3.8)}$$

Where σ is the tensile strength calculated from Eq.3.9 as load (F) divided by initial cross sectional area (A_0)

$$\sigma\ (MPa) = F\ (N)/\ A_0\ (mm^2) \qquad \text{Eq. (3.9)}$$

3.5.9 Water absorption and solubility test

In order to determine the water absorption and solubility behavior of the resins and the composites, samples in 9.91±0.06 mm width, 15.3±1.1 mm length and 1.5±0.15 mm thickness were cut from the dog-bone shaped samples from their wider parts. Three pieces for each composite formulation were tested. The procedure followed was based on recent publication.[96] Polished samples were first dried until constant weight was obtained (W_d). Then they were immersed in distilled water at 37 °C.

After certain time intervals, they were removed and blotted dry and weighed. This weight was referred to as the immersed weight (W_i). The procedure was repeated until no weight change was obtained. At last, the samples were oven-dried in air until no changes in weight occurs (W_f). The water sorption (WS) and solubility (SL) were calculated according to the formula given in Eqs. 3.10 and 3.11. In addition, the exact values of WS and SL in μg/mm^3 were calculated using W_i-W_f and W_d-W_f divided by volume, respectively.

$$WS\ \% = (W_i\text{-}W_f/W_f)*100 \qquad \text{Eq. (3.10)}$$

$$SL\ \% = (W_d\text{-}W_f/W_d)*100 \qquad \text{Eq. (3.11)}$$

3.5.10 Bioactivity test

Bioactivity of the UT polymers and resin composites were investigated using 10 x Kukubo solutions (SBF-simulated body fluid) at pH 7.25. Bulk specimens with similar surface area were exposed to Kukubo solution for 10 days at 37 °C in an oven. Then, the samples were washed gently with distilled water without disturbing their surfaces. Sample surfaces were examined by SEM and XRD techniques in order to determine whether hydroxyapatite (HAp) phase was formed on the surface of the sample at the predetermined durations where the sample was immersed in SBF. The chemicals and their concentrations used are listed in Table 3.7. The HCl (1M) and THMAM were used to stabilize pH at 7 to 7.5. The final solution was transparent.

Table 3. 7 Chemicals used and composition of 10 x SBF solution prepared.

Chemical	**Company (Product number)**	**Weight (g) (per 1L DI-water)**
NaCl	Merck (106400)	15.992
$NaHCO_3$	Merck (106329)	0.70
KCl	Merck (104935)	0.440
$K_2HPO_4.3H_2O$	Merck (105099)	0.456
$MgCl_2.6H_2O$	Merck (105833)	1.302
$CaCl_2.2H_2O$	Merck (102382)	0.736
Na_2SO_4	Horasan Kimya	0.142
THMAM	Merck (108382)	12.114
HCl (1M)	Merck (100317)	90 mL

CHAPTER 4

RESULTS AND DISCUSSION: POTASSIUM TITANATE NANOSTRUCTURES SYNTHESIZED BY SOL-GEL AND HYDROTHERMAL METHODS

4. 1 Sol-Gel synthesis of PT nanostructures

4.1.1 Phase analysis by XRD

4.1.1.1 Powders obtained after calcination at 600 ºC

The XRD patterns of sol-gel derived xero-gels synthesized at different Ti/K ratios are shown in Figure 4.1. The products after drying (xero-gels) were in the form of soft powder chunks that were easily dispersed by using a mortar with pestle. The intensity of the peaks in the patterns is represented in log scale in order to blow up relatively small peaks. The presence of sharp, remarkably intense peaks in each pattern indicates that the xero-gels possessed crystalline phase(s). Each peak could be indexed to potassium chloride- Sylvite (KCl, ICDD: 41-1476). No XRD peaks related to the formation of any type of Ti-O containing phases were detected. Nevertheless, the noisy background and the hump between 20-40º in the patterns suggest the presence of amorphous phase(s). Most probably, there is a portion of Ti-O containing phase. That is why; the Ti/K ratio did not affect the crystalline phase composition of xero-gels. But, more detailed analyses of xero-gels are necessary to get the assurance of this envision.

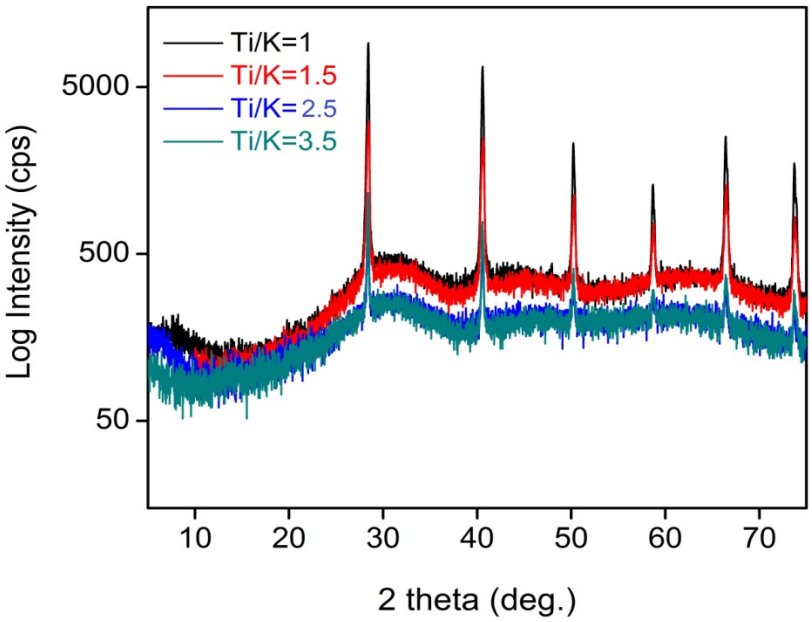


Figure 4. 1 XRD patterns of the xero-gels synthesized at Ti/K ratio of 1, 1.5, 2.5 and 3.5.

The XRD patterns of the sol-gel derived PT powders are presented in Figure 4.2. The patterns were detected after calcination of the powders at 600 ºC for 1, 2, and 3 h. The analysis of the XRD patterns suggests that each product composed of KCl, PHT ($K_2Ti_6O_{13}$, ICDD: 74-0275, Jeppeite), potassium hollandite (PH, KTi_8O_{16}, ICDD: 41-1097), and anatase (TiO_2, ICDD: 21-1272). Although the phases present remained the same, their proportions varied with respect to the Ti/K ratio and calcination time. Between PHT and PTT, it is anticipated that PHT was the first phase forming in the sol-gel derived network by calcination of KCl containing xero-gels at 600 ºC. After PHT, PTT phase formed in the powders by a mechanism to be described later in Section 4.1.4.

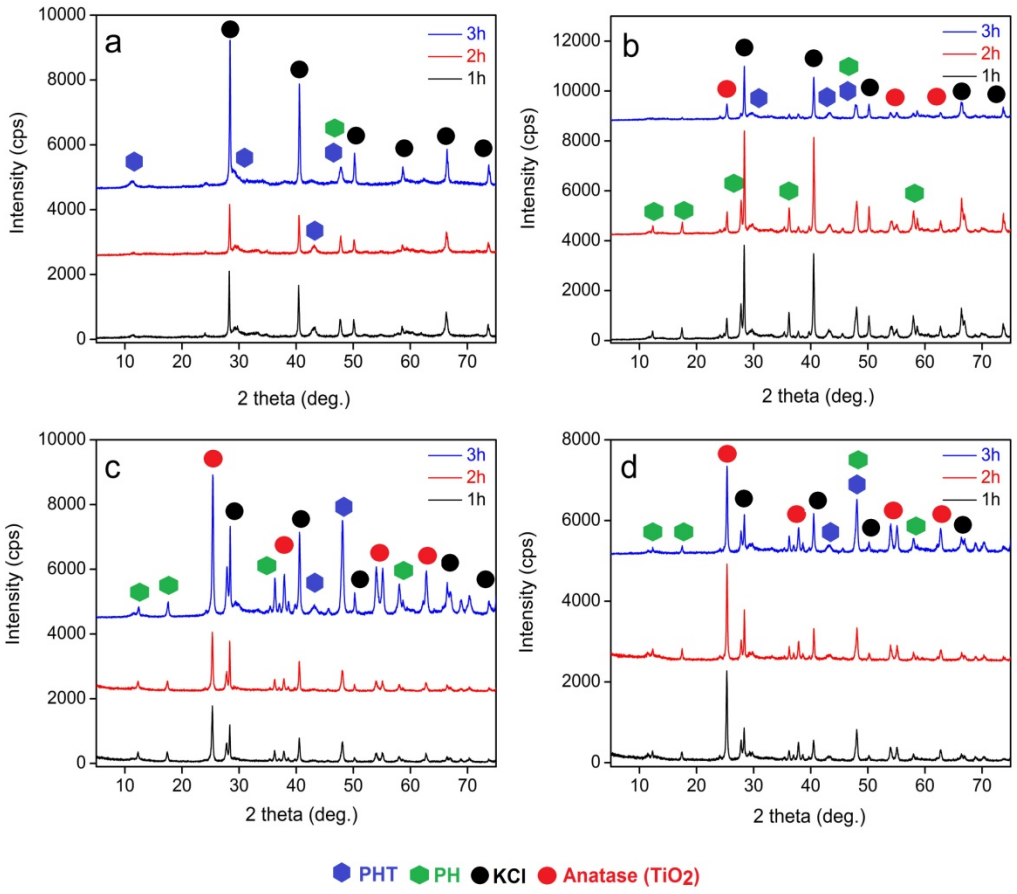


Figure 4. 2 XRD patterns of the powders obtained after calcination for 1-3 h at 600 ºC for Ti/K ratio of a) 1, b) 1.5, c) 2.5, and d) 3.5 (PH: potassium hollandite, PHT: potassium hexa-titanate)

Kang et al.[20] reported that it is the pre-crystallized α-K_2O phase that formed from the xero-gel network and initiated the growth of PT nanostructures by filling the spaces between them and covering the surfaces. They indexed two peaks around 28 and 40º and stated the formation of α-K_2O rather than KCl before calcination in their XRD analysis. Similar peaks were detected in the XRD patterns of the calcined products. In Table 4.1, the original peak positions of the KCl and α-K_2O phases according to their ICDD cards were given together with the peak positions in the XRD patterns of xero-gels presented in Figure 4.1.

Table 4. 1 Comparison of peak positions and intensities in the patterns of xero-gels with ICDD cards of KCl and α-K_2O.

Xero-gels			KCl (ICDD: 41-1476)			α-K_2O (ICDD: 26-1327)		
2-theta (deg.)	**N. I* (%)**	**(d, Å)**	**2-theta (deg.)**	**N. I* (%)**	**(d, Å)**	**2-theta (deg.)**	**N. I* (%)**	**(d, Å)**
28.40	100	3.140	28.34	100	3.146	12.52	40	7.060
40.56	75.3	2.222	40.50	37	2.225	19.80	20	4.480
50.20	25.7	1.815	50.16	10	1.817	22.31	20	3.980
58.67	13.1	1.572	58.63	5	1.573	23.51	20	3.780
66.40	29.9	1.406	66.37	9	1.407	25.17	20	3.535
73.70	21	1.284	73.73	5	1.284	27.07	10	3.290
						28.86	100	3.090
						29.52	10	3.023
						30.21	10	2.955
						31.13	80	2.870
						31.70	60	2.820
						32.53	20	2.750
						34.32	20	2.610
						36.72	40	2.445
						38.01	40	2.365
						38.86	40	2.315
						40.60	20	2.220
						42.71	40	2.115
						43.69	40	2.070
						45.06	20	2.010
						48.73	10	1.867
						57.95	20	1.590
						62.48	10	1.485

N.I (%): normalized intensity to 100%

The data presented in Table 4.1 are the evidence that KCl is pre-crystallizing phase in the amorphous network by using the K^+ originating from PM precursor and Cl^- originating from the Cl^- rich acidic catalyst ($HCl^{aq.}$ concentrated, 6 M). One explanation for the conflict between the results of this study and the results reported by Kang et al.[20] may because they used HCl at lower molarity and the thermodynamics of the system promoted K_2O formation rather than KCl. But, it is for sure that concentrated HCl promoted KCl crystallization in the xero-gels in this study.

Crystallization of PHT and PTT nanostructures from an amorphous network by calcination has been reported earlier by several other researchers. [20,97,98] Jung et al.[97] managed to form PHT after calcination at 700 ºC with a more or less similar approach. Recently, Liu et al.[99] reported concurrent formation of PH and PHT with no titanium left in the final product by heating of potassium borate-titanium mixture at 700 ºC in 3 h. But, when the mixture was heated for 5 h, PH diminished. They have concluded that PH is the meta-stable intermediate phase upon formation of PHT by extracting K_2O from the borate matrix.

In the light of foregoing information, the formation of anatase with some unreacted KCl may imply that less than the desired stoichiometric ratio of KCl was present to react for crystallization of PTs so that the remaining Ti-O crystallized into TiO_2 (anatase). These results imply that Ti/K ratio has a profound effect on the phase variety formed during calcination since the system necessitates a stoichiometric balance for the formation of a specific PT phase.

Conclusively, PM and PHT phases formed together with anatase and unreacted KCl after calcination at 600 °C in all cases, therefore the stoichiometric balance was not provided at any Ti/K ratio at all calcination times. The amount of unreacted KCl and anatase decreased as the time of calcination and the Ti/K ratio increased. Further investigations and comments on this issue will be given later in the following sections.

4.1.1.2 Powders obtained after calcination at 800 ºC

The XRD patterns of the powders obtained after calcination at 800 ºC are shown in Figure 4.3. XRD analysis revealed that the products calcined at 800 ºC were composed of PHT and PTT rather than PH and PHT in contrast to the results obtained for the powders obtained after calcination at 600 ºC.

The decrease in the intensity of the KCl peaks with increasing Ti/K ratio at 600 ºC was likewise observed in the powders obtained after calcination at 800 ºC, but in this case KCl consumption was more evident. The disappearance of KCl peaks implies that the efficiency of PT formation increased by increasing the calcination temperature.

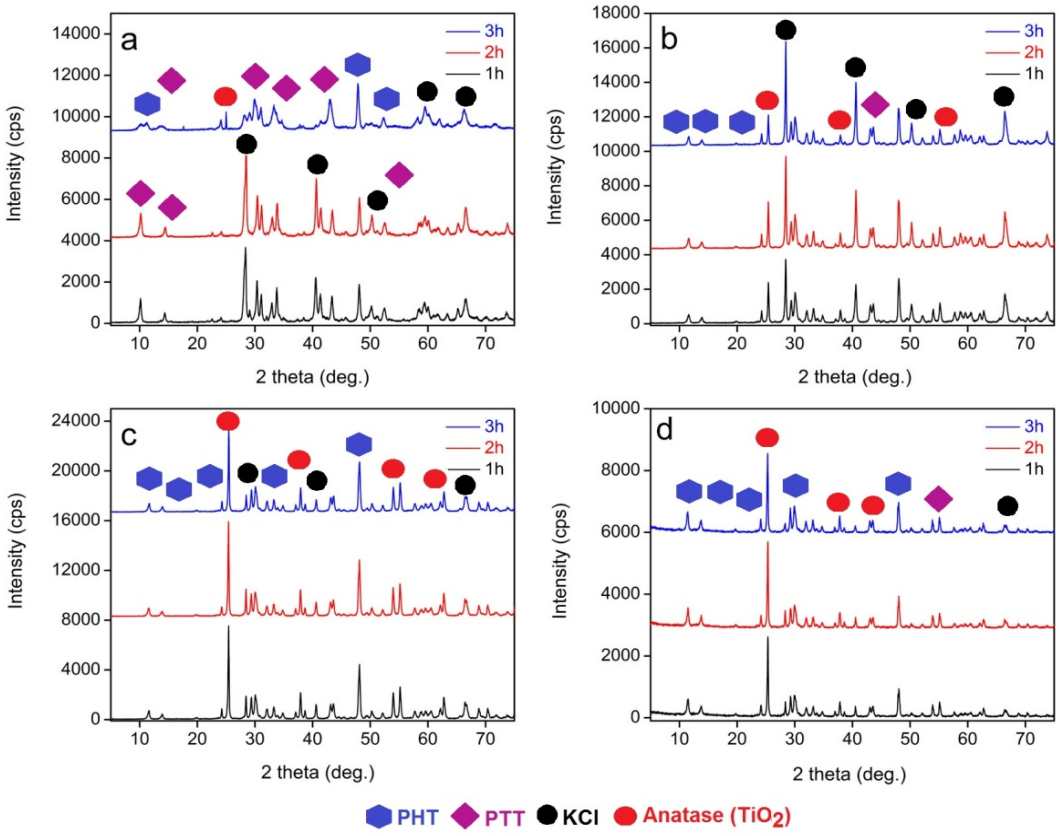


Figure 4. 3 XRD patterns of the powders obtained after calcination for 1-3 h at 800 ºC with Ti/K ratio of a) 1, b) 1.5, c) 2.5, and d) 3.5.

In other words, amorphous network and/or KCl crystals were more reactive at 800 ºC than at 600 ºC. The calcination at 800 ºC caused the formation of PTT rather than PH, even at the lowest Ti/K ratio and at the shortest calcination time. On the contrary, the intensity of the anatase peaks did not change much as the calcination temperature is increased. This finding assures that the formation reactions of PHT and PTT depend mainly on the Ti/K ratio, and the formation of PH is intermediate. However the kinetics of growth depends mainly on the calcination time and it cannot be clarified whether PHT transformed into PTT or not, only by XRD and/or SEM analysis.

4.1.2 SEM analysis

4.1.2.1 Powders obtained after calcination at 600 ºC

The representative images showing the microstructures of sol-gel derived powders obtained after calcination at 600 ºC are shown in Figure 4.4. Regardless of the calcination time or Ti/K ratio, the images indicate high level of agglomeration of nanostructures into spherical particles or irregular shaped chunks. It was not possible to make a precise size measurement on the SEM images due to severe agglomeration of the nanostructures caused by calcination at 600 ºC. But, it is clear that the size and the aspect ratio of the nanostructures increased and the whisker morphology became more evident with increasing calcination time at 600 ºC. Nanosize PHT phase that dominates over PH at Ti/K ratio of 1, see Figure 4.2, has more tendency for agglomeration into irregular chunks as approved by the corresponding SEM images in Figure 4.4. This is an expected result since PHT was reported[19] previously as a highly agglomerated phase, especially when formed by solid-state methods at high calcination temperatures. The SEM analysis reveals that preferential growth and the resultant surface stresses along one dimension cannot dominate the weak chemical interactions taking place on the surfaces and cause severe agglomeration at this temperature.

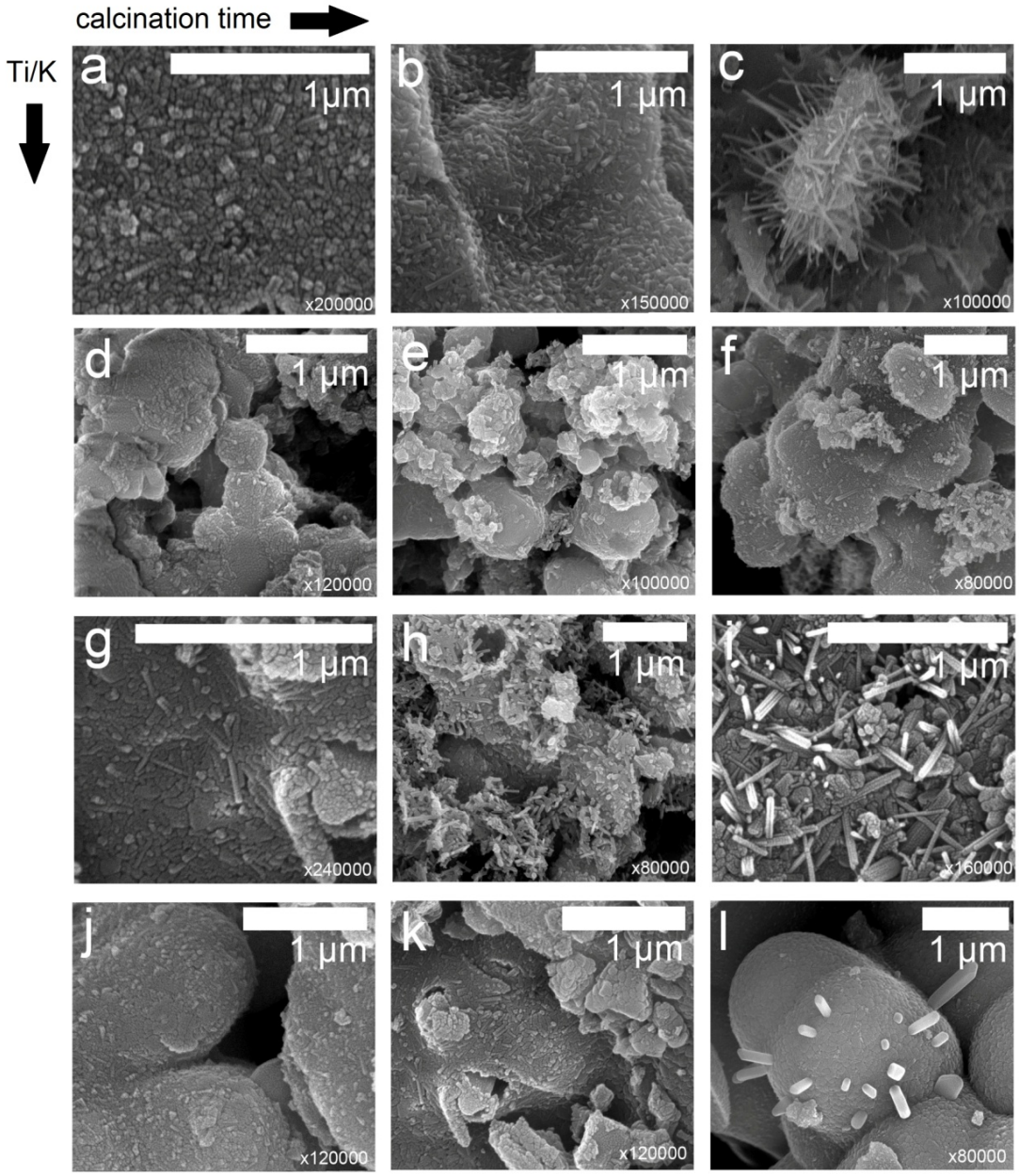


Figure 4. 4 SEM images of the sol-gel derived whiskers obtained after calcination at 600 °C with increasing Ti/K ratio of 1, 1.5, 2.5 and 3.5 (top to bottom), at calcination times of 1, 2 and 3 h (left to right).

4.1.2.2 Powders obtained after calcination at 800 ºC

The representative images showing the microstructures of sol-gel derived powders obtained after calcination at 800 ºC are shown in Figure 4.5. The whisker morphology was evident and the sizes of the nanostructures were measurable in the powders obtained at all calcination times. The measured sizes of the whiskers are shown with respect to the calcination time and temperature in Table 4.2. Twenty measurements were made on the samples prepared for the determination of the nominal dimensions of the whiskers. The agglomeration tendency was relatively lower in PT whiskers obtained after calcination at 800 ºC than those obtained after calcination at 600 ºC.

The calculated sizes of the PTs were quite similar to the findings reported by Kang et al.[20] who stated that the diameter of PHTs is roughly smaller than 60 nm and the PTT phase has relatively higher diameter and length. This finding could be an explanation to why there is no direct relationship between size and the calcination time. The change in size is then related to the phase composition, which is mainly determined by the Ti/K ratio. At Ti/K of 1 for all calcination times, PTT formation was dominant so that the diameter of the whiskers was much higher at this ratio than other ratios. The size decreased with increasing Ti/K ratio because of PHT formation and growth. At Ti/K of 3.5, PHT was still the major phase, but some fraction of PTT was also present and grown in diameter by prolonged time of calcination. i.e. 3 h.

It was not possible to determine the accurate phase composition by all means. Even though Rietveld analysis (GSAS) of these whiskers was computed, data gathered was not manageable due to their photocatalytic properties. Detailed Rietveld analysis is needed for exact phase composition calculation.

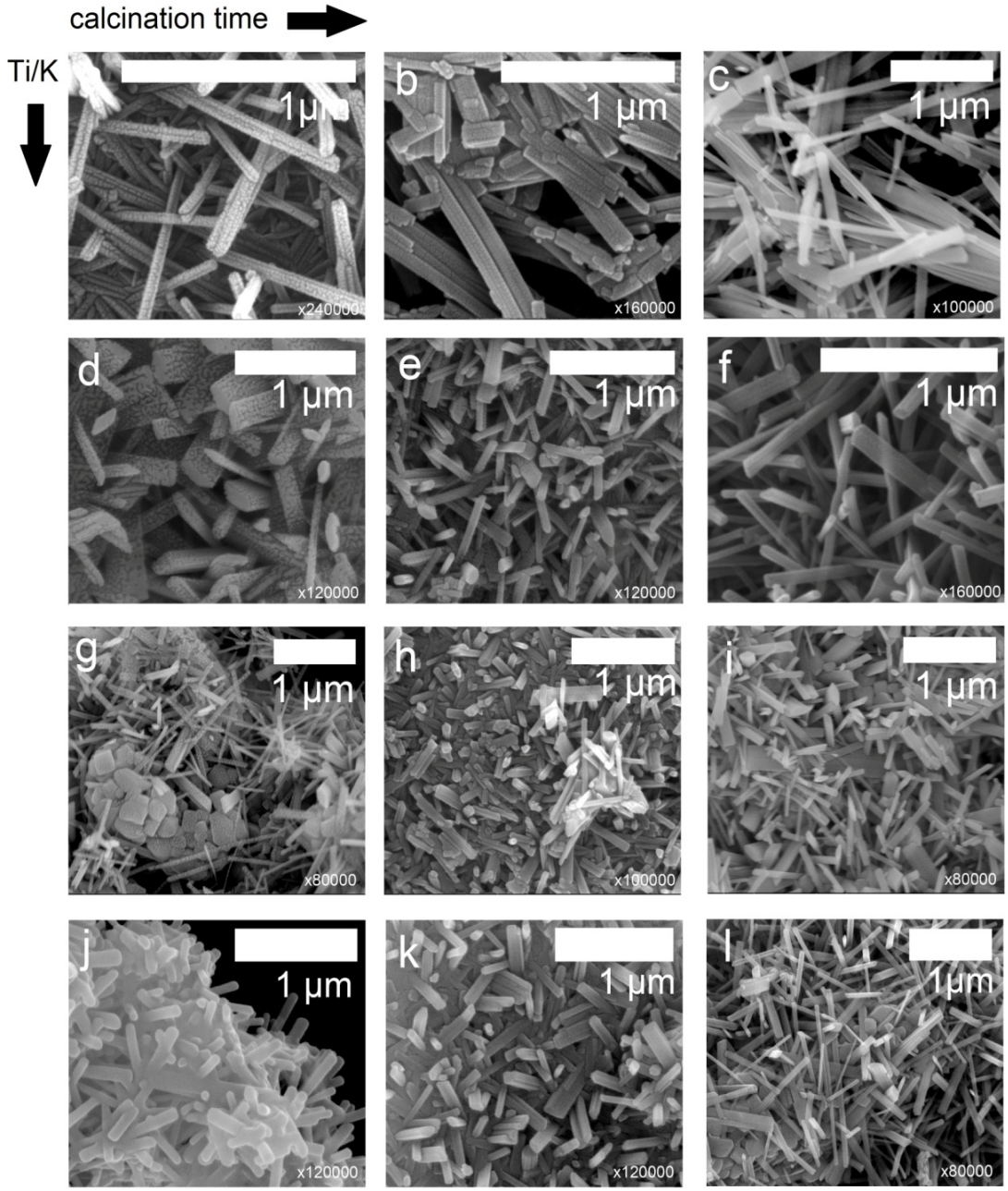


Figure 4. 5 SEM images of the sol-gel derived whiskers obtained after calcination at 800 °C with increasing Ti/K ratio of 1, 1.5, 2.5 and 3.5 (top to bottom), at calcination times of 1, 2 and 3 h (left to right).

Table 4. 2 Diameter and length of PT whiskers obtained after calcination at 800 °C.

Calcination Time (h)	Ti/K ratio	Diameter (nm)	Length (nm)
1	1	214 ± 113	4900 ± 2573
	1.5	50 ± 22	420 ± 154
	2.5	67 ± 32	744 ± 385
	3.5	105 ± 28	Not measurable
2	1	213 ± 122	5378 ± 2997
	1.5	60 ± 25	617 ± 277
	2.5	62 ± 21	594 ± 367
	3.5	85 ± 31	Not measurable
3	1	156 ± 74	4984 ± 2516
	1.5	74 ± 30	700 ± 359
	2.5	87 ± 45	793 ± 347
	3.5	136 ± 60	Not measurable

4.1.3 Surface area (BET) analysis

In order to determine the surface structure of the whiskers, BET analysis has been performed on the powders obtained after calcination at 800 ºC for 3 h at which temperature one-dimensional (1D) morphology was more pronounced. The surface area, pore morphology and average meso-pore size have been determined according to BJH (Barrett–Joyner–Halenda) technique. The BET hysteresis isotherms and the pore size with respect to the pore diameter are shown in Figure 4.6. As mentioned in Section 3.5.4, the increase in pore volume with increasing relative pressure (P/P_0) in the range of 0.3-0.6, causes the formation of hysteresis loops; the form of the loop provides information on pore morphology. The hysteresis loops of the PTs shown in Figure 4.6a fits well to H3 type.

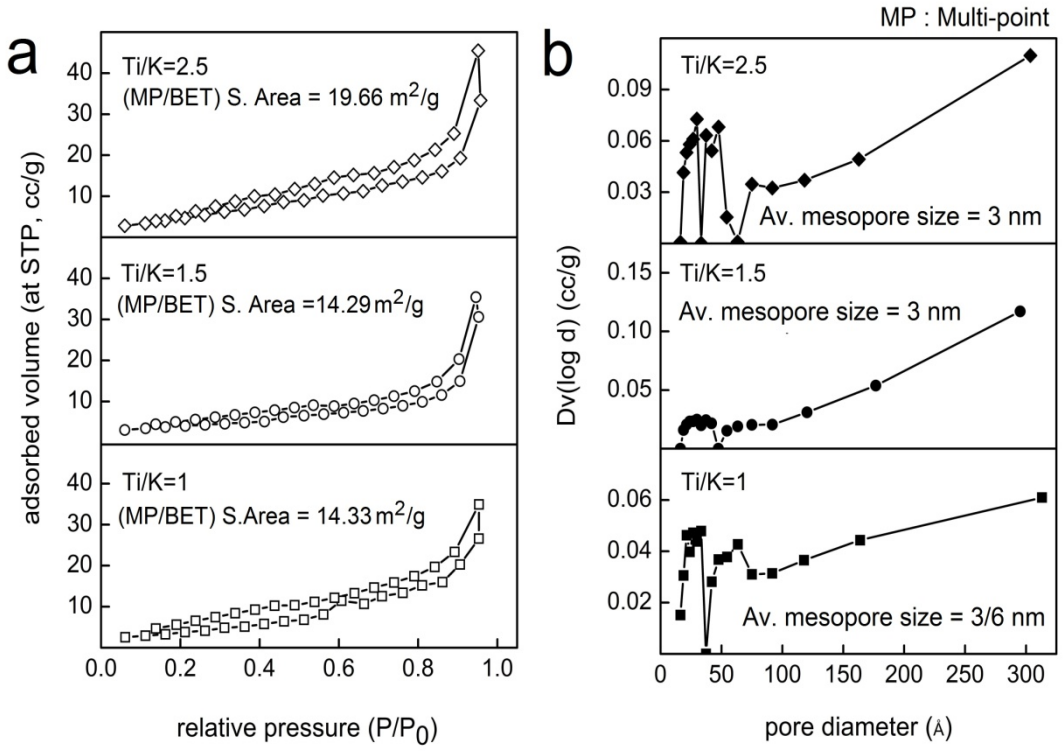


Figure 4. 6 a) BET isotherms and b) BJH mesopores size distribution (Pore diameter versus volume) of sol-gel derived PTs obtained by calcination at 800 °C for 3 h.

The Type 4 isotherm with H3 hysteresis indicates mesoporous PT surfaces with slit-like pore morphology. At all Ti/K, H3 type was evident, meaning that the significant amount of phases analyzed were PTs rather than KCl and/or anatase, which were in irregular and sphere-like morphologies. The surface areas calculated by BET-BJH method were 14.33, 14.29 and 19.66 m^2/g for Ti/K of 1, 1.5 and 2.5, respectively. These values were too low especially when compared to commercial TiO_2 (P25 powder, 57 m^2/g[4]) in spite of their high aspect ratio at diameters in nanoscale. In Figure 4.6b, the pore volumes were so low; this low meso-pore volume evokes the presence of micro-pores that necessitates further surface analysis using other methods (i.e. SF (Saito Foley) -BET) are needed to further clarify the pore structure. Nevertheless, the lower surface area of PTs might be correlated with severe agglomeration[97] and the increase of surface area at Ti/K of 2.5 with the decrease of entanglement due to decreased length.

4.1.4 Growth mechanism of PT whiskers by sol-gel process

Generally, PTs are synthesized at about 800-1000 °C by using solid-state methods such as calcination or molten salt synthesis.[98,100,101] Low surface area (not larger than 10 m^2/g) of PTs due to rapid densification of particles upon crystallization at high temperatures was underlined.[97] The sol-gel method followed by calcination at the lowest possible temperature for crystallization has been reported as an effective method since it provides better surface area as compared to other methods.[98] Basically, sol-gel reactions of materials derived from Ti-alkoxides start with hydrolysis of the alkoxide and proceeds with gelation into Ti-O-Ti network through reactions shown in Eqs. 4.1-4.3[45,102] The hydrolysis of Ti- alkoxide (Eq.4.1) forms Ti-hydroxide (Ti-$(OH)_4$) and alcohol (C_2H_5OH) by the aid of water in HCl (37%). The Ti-hydroxides may combine with the remaining Ti-alkoxides (Eq.4.2) or within themselves (Eq.4.3) to condense into Ti-O-Ti network. The final properties of the products such as morphology, particle size and most importantly the chemistry are determined by the kinetics of hydrolysis and condensation reactions.[102]

$$Ti\text{-}(OC_2H_5)_4 + 4\,H_2O = Ti\text{-}(OH)_4 + 4\,C_2H_5OH \quad \text{Eq. (4.1)}$$

$$Ti\text{-}(OH)_4 + (OC_2H_5OH)_4 - Ti = Ti\text{-}O\text{-}Ti + 4\,C_2H_5OH \quad \text{Eq. (4.2)}$$

$$Ti\text{-}(OH)_4 + (OH)_4 - Ti = Ti\text{-}O\text{-}Ti + 4\,H_2O \quad \text{Eq. (4.3)}$$

In the case of PTs, the sol-gel reaction proceeds likewise except for the presence of K^+ ions dispersed inside the initial sol. In conjunction with previously reported statements[98] and characterization results, the proposed reactions are given in Eqs 4.4-4.9 and reactions during sol-gel transformation of powders are schematically summarized in Figure 4.7.

Upon hydrolysis (sol formation)

$$Ti\text{-}(OC_2H_5)_4 + 4\,H_2O = Ti\text{-}(OH)_4 + 4\,C_2H_5OH \quad \text{Eq. (4.4)}$$

$$CH_3OK = CH_3O^- + K^+_{free} \quad \text{Eq. (4.5)}$$

$$HCl = H^+ + Cl^-_{free} \quad \text{Eq. (4.6)}$$

Upon gelation,

$Ti\text{-}(OH)_4 + (OC_2H_5OH)_4 - Ti = [Ti\text{-}O\text{-}Ti]_x + [Ti\text{-}O\text{-}K_{(surface)}]_{1-x} + 4\ C_2H_5OH$ Eq. (4.7)

$Ti\text{-}(OH)_4 + (OH)_4 - Ti = [Ti\text{-}O\text{-}Ti]_x + [Ti\text{-}O\text{-}K_{(surface)}]_{1-x} + 4\ H_2O$ Eq. (4.8)

$CH_3O^- + H^+ = CH_3OH$ Eq. (4.9)

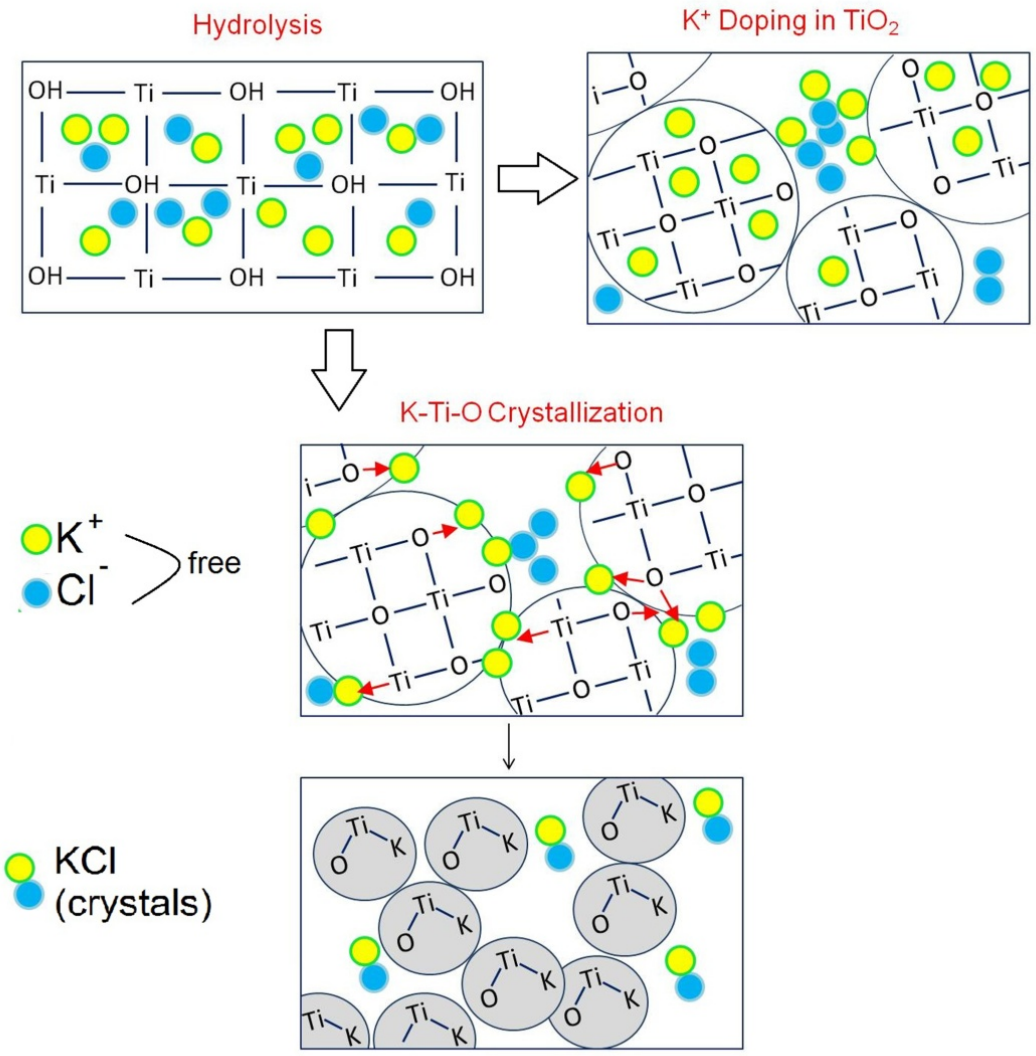


Figure 4. 7 Schematic illustration of the growth stages of sol-gel derived powders.

A limited amount of research on K^+ ion interaction within a sol-gel derived TiO_2 network is available. For the current system, at the initial stages of sol-gel reaction, K^+ and Cl^- ions move freely in the ethanol/water mixture (Eqs 4.5 and 4.6) Upon gelation, these ions were trapped in the amorphous Ti-O network forming solid gel clusters as shown in Figure 4.7. In addition to that, it is reasonable for high number of K^+ ions to proceed to the cluster surfaces due to the strain induced in the network. Bessekhouad et. al.[103] stated that the surface of TiO_2 is more acidic as alkali content is low (1 atomic percentage) and vice versa. Partlow and Yoldas[104] suggested that K^+ ions dispersed in TiO_2 sol should act as a base catalyst in the extent of hydrolysis and condensation reactions in order to form colloids rather than polymeric species reported for acid catalysis. Therefore, at this stage, K^+ ions were expected to take place on the surfaces of the amorphous Ti-O clusters owing to charge attraction and/or strain.

In TiO_2 synthesis by sol-gel process at identical conditions, HCl catalyzes the hydrolysis reaction, and usually an amorphous Ti-O-Ti network is formed. By the aid of calcination, amorphous network transforms first to anatase then rutile crystals. But if there are alkali ions present and they migrate to the solution – which is expected for high alkali content- basicity of surface sites increase. In this case, precipitation – a very fast condensation- is likely to occur in the system. This statement is applicable to the current experiments because it was observed that the sols precipitated into a wet white paste in the average of 10 minutes after all additions were complete under continuous stirring at 40 °C. As shown in Figure 4.7, K^+ ions presented on the surfaces of amorphous Ti-O clusters as –Ti-O-K^+ (Eqs 4.7-4.8).[103] Therefore, at high number of K^+ ions moving freely in solution and/or as attached on the surface of clusters, Cl^- ions also move freely in the system. There are two possible routes that the system thereafter could follow. For the low alkali (K^+) content, the K^+ ions on the surfaces of amorphous Ti-O network become trapped inside as shown in Figure 4.7. Upon calcination, the amorphous network orders itself to anatase crystals, whereas the K^+ ions become trapped still expanding the TiO_2 lattice.

In the current system- where the K^+ content exceeds the doping level – first the KCl crystals are formed by the migration of ions to solution from Ti-O surfaces. Therefore, KCl crystals are formed during gelation/aging of the network. Later on by calcination, K-Ti-O bonds are formed rather than KCl, as shown in Figure 4.7. In addition to the XRD patterns and the proposed sol-gel mechanism, TG-DTA analysis proved crystallization of KCl particles in the amorphous network. XRD patterns of xero-gels revealed clearly that the crystalline phase is the KCl not K_2O. In Figure 4.8, the TG-DTA thermograms of xero-gels with respect to their Ti/K ratio are shown. The thermal analysis of xero-gels is such a faster simulation of calcination of xero-gels. The DTA thermograms show that there is an endothermic peak around 770 °C. The melting temperatures of K_2O and KCl are 740 and 770 °C[105], respectively. Conclusively, it is proved not only by XRD, but also by DTA that the precrystallized phase is KCl rather than K_2O.

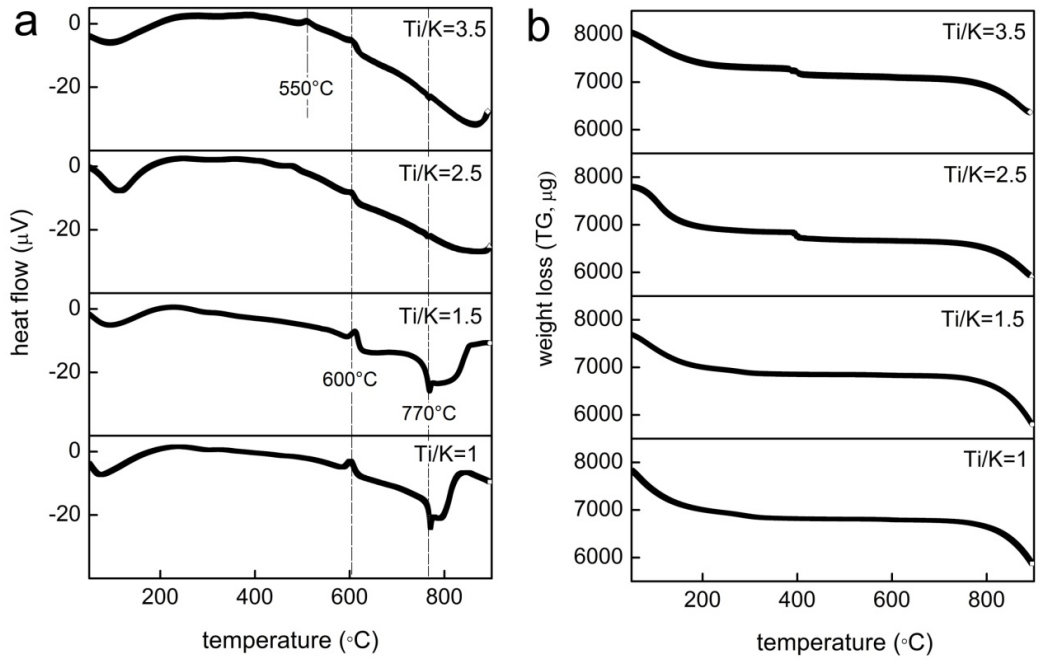


Figure 4. 8 TG-DTA analysis thermograms of xero-gels a) DTA b) TGA

There are two exothermic peaks at 510 and 600 °C. Simonsen and Sagaard[102] stated that the exothermic peaks between 400-550 °C are generally assigned to the crystallization of amorphous TiO_2. In addition, they mentioned that the temperature at which the anatase forms is strongly related to the morphology of the particles. Jung and Shul[98] reported PHT crystallization peak on DTA analysis of sol-gel derived powder at 630 °C without weight loss on TG curve. It may be applicable also for the present system.

The endothermic peak at 770 °C became smaller and invisible but no shift in the peak maxima temperature was noted as the Ti/K ratio increased. The data supports the XRD results in which the KCl peaks decreased in intensity as the Ti/K ratio increased to 2.5/3.5. TG analysis curves indicate gradual decrease in weight starting from 600 °C to 800°C. The weight loss is due to evaporation of Cl_2 gas caused by decomposition of KCl, into K^+ and Cl_2, while K^+ reacts with Ti-O to form PTs. Since, calcination process is prolonged from 1 to 3 h; reactions predicted by heating through DTA analysis are delayed.

Initial Ti/K ratios in the solutions show that the atomic percentage of K^+ is too much for doping. As mentioned earlier, K^+ ions act as base catalysts for the amorphous network to condensate/precipitate. XRD analysis revealed that even after 3 h of calcination at 600 °C at any Ti/K ratio, both PHT and anatase formation was limited compared to PH. Since both PTs – PH and PHT - are tunneled, once K^+ ions are captured, they cannot escape from the tunnels.[100] A detailed analysis of the xero-gel network is needed to ensure whether the crystallized phase at 600 °C is a PT or not.

Chen et. al.[106] stated growth of $K_{4-4x}Ti_xO_2$ at concentrations higher than 4.6 mole % K after calcination at 550 °C. They claimed formation of lamellar K_4TiO_4 and PTT at high alkali contents up to 14.6 %. Similarly, results revealed that the PH is the intermediate phase upon formation of PHT after calcination at 600 °C. Further increase in calcination temperature from 600 to 800 °C caused PH to disappear and form PHT and PTT phases.

Hollandite structures have a general formula; $A_x(B_yTi_{8-y})O_{16}$ in which A is K, Cs, and Ba and B is either a divalent or trivalent ion such as Mg^{2+}, Mn^{2+}, Al^{3+} or Ti^{3+}.[107] The PH structure could be formed basically by the rutile structure rotated alternately clockwise and anticlockwise by 45° of the linear strings of the corner sharing octahedra in case of PH. Further linking of octahedra together would lead to formation of a framework made up of parallel tunnels along c-axis. The comparison of PH and PHT structures and the placement of K^+ in the tunnels are shown in Figure 4.9. The crystals are formed using Carine Crystallography® software. Crystal information, such as the position or the occupancy of the ions were obtained from literature[107] and inserted manually into the software.

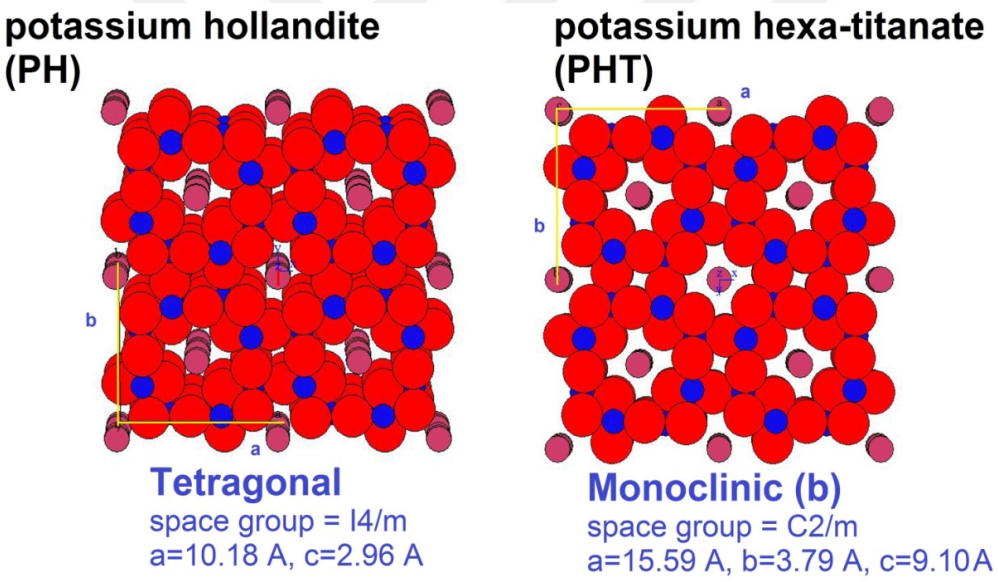


Figure 4. 9 Crystal structures of PH and PHT along [001] projection.

As shown in Figure 4.9, the crystal structures of PH and PHT are alike. Both are formed into tunneled structures in which K^+ ions are enclosed. It was realized from the XRD study that KCl became relatively less with increasing Ti/K ratio that promoted more anatase and PH formation.

How the transformation of PH into PHT occurs in terms of crystal symmetries is another topic, which requires further analysis. However, it is interesting to note that titanium present in 3+ valence in PH and PH has a net negative charge.[107] In order to investigate if any significant splitting occurs during the formation of PTs, TEM analysis was performed on the powders. The TEM images of the sol-gel derived PTs calcined at 800 °C from general to zoomed are shown in Figure 4.10 with respect to increasing Ti/K ratio along with their FFT analyses. Calculations on FFTs revealed that all the nanostructures in the images belong to PHT. At this temperature of calcination, PHT and PTT formation was remarkable. Unfortunately, PH nanostructures were not available for detection in the sample calcined at 600 °C. Moreover, generally it is not possible to monitor PH structures by TEM in any case because of the attack of high TEM voltage on PH resulting in the transformation of PH to rutile. Similar reasoning was reported earlier by Vogth et. al.[107]

The morphology of the PTs was similar after calcination at 600 and 800 °C. The representative TEM images of the nanostructures (Figure 4. 9.a1, b1, c1) show that an increase in Ti/K ratio did not cause any change in the nanostructure morphology but size and aspect ratio changed. The increase in size of the PTs was previously revealed by SEM examinations. The TEM images further reveal that the PT whiskers synthesized by sol-gel process were in rigid structures in rounded rectangular cross-section with small amorphous phase in the periphery. (See Figure 4.10a2). FFT analysis on Figure 4.10.a2-c2 revealed that the PT whiskers were composed of PHT (Figure 4.9.a2) and PTT (Figure 4.10.b2, c2) phases.

In conclusion, it can be said that PH and PHT or PHT and PTT phases form by sol-gel followed by calcination at 600 °C and 800 °C, respectively. The resultant structures reveal that PTs are in whisker morphology in an agglomerated form with KCl and anatase impurities. The reason behind the KCl formation was the basicity in sol-gel reaction due to high K^+ content combined with the concentrated HCl use providing Cl^- to move freely in the sol. Studies suggest that PH is an intermediate phase upon formation of PHT and PTT, however further analysis is needed to ensure PHT transforms to PTT or vice versa.

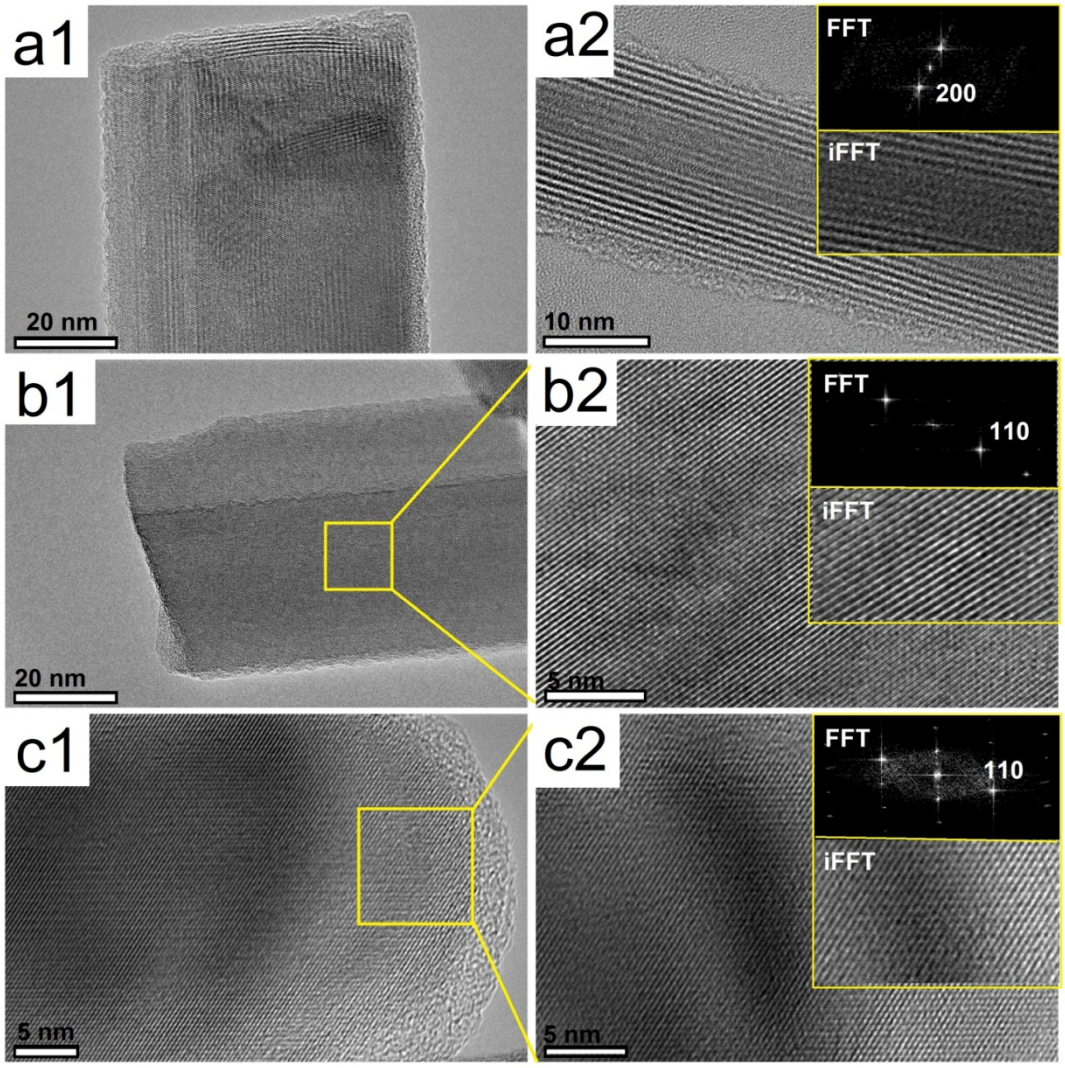


Figure 4. 10 TEM images of the sol-gel derived PTs obtained after calcination at 800 °C for 3 h for Ti/K of a) 1, b) 1.5, and c) 2.5.

4.1.5 Determination of band gap energy of PTs synthesized by sol-gel process

The energy versus R%, F(R), $(F(R)*E)^{1/2}$ and $(F(R)*E)^2$ graphs (Tauc Plots) of the xero-gels are shown in Figure 4.11. The variation in energy with the same parameters for P25 powder is also indicated in the same figures. The energy versus R% curve (Figure 4.11a) was drawn according to the data obtained by UV-Vis/DR spectrophotometer, whereas the other curves were drawn according to the data developed by using Eqs. 3.1 and 3.2, where F(R) was assumed to be ≈ α. In the inset in Figure 4.11b, the extrapolation to the energy axis for E_g determination is represented. The same method was used for each calculation.

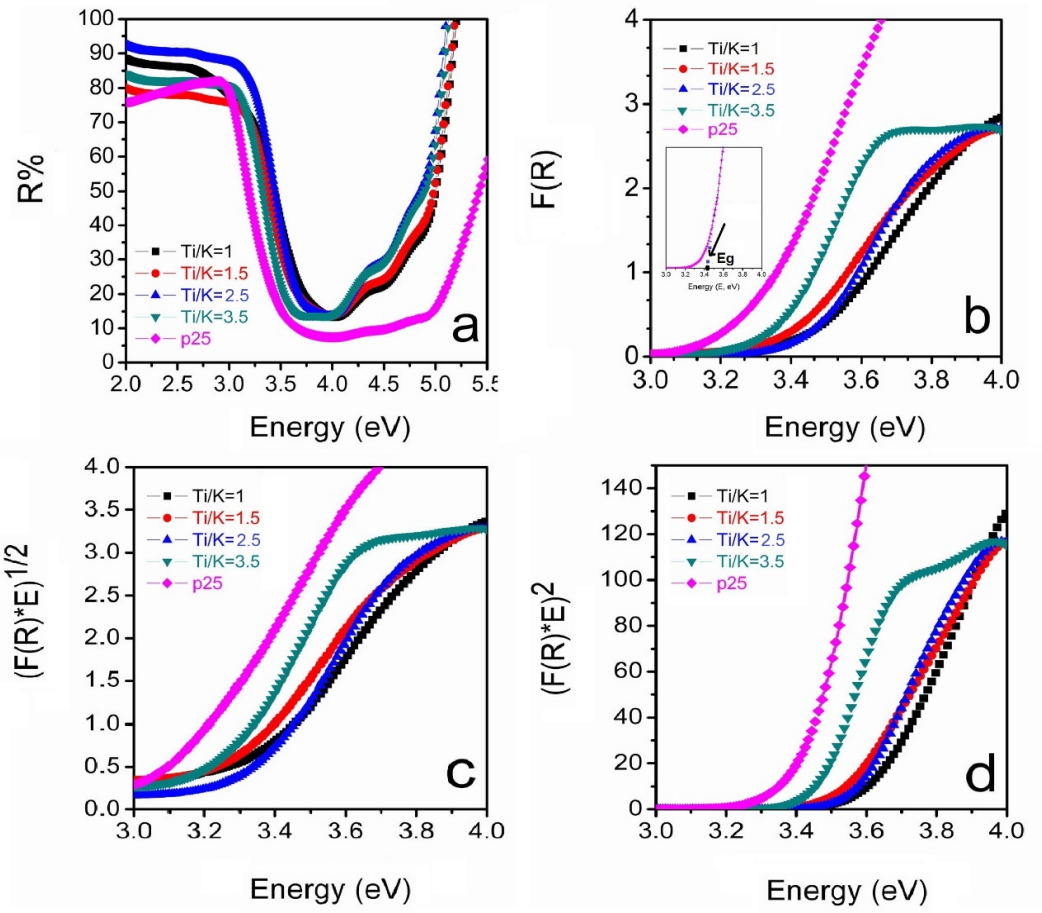


Figure 4. 11 a) R% versus energy b) K-M transform (F(R) and Tauc plots c) indirect and d) direct transitions of the xero-gels.

As mentioned previously, three types of line extrapolation methods were used for calculation of E_g, in order to make a precise comparison between multi-phase sol-gel derived powders (anatase, KCl and PTs) that are composed of phases with both direct and indirect E_g. By extrapolating the lines obtained from each technique, the graph shown in Figure 4.12 was obtained. The graph represents the variation of E_g with respect to change in Ti/K ratio of xero-gels for each extrapolation method, in other words, for both direct and indirect E_g and from F(R) line as an intermediate.

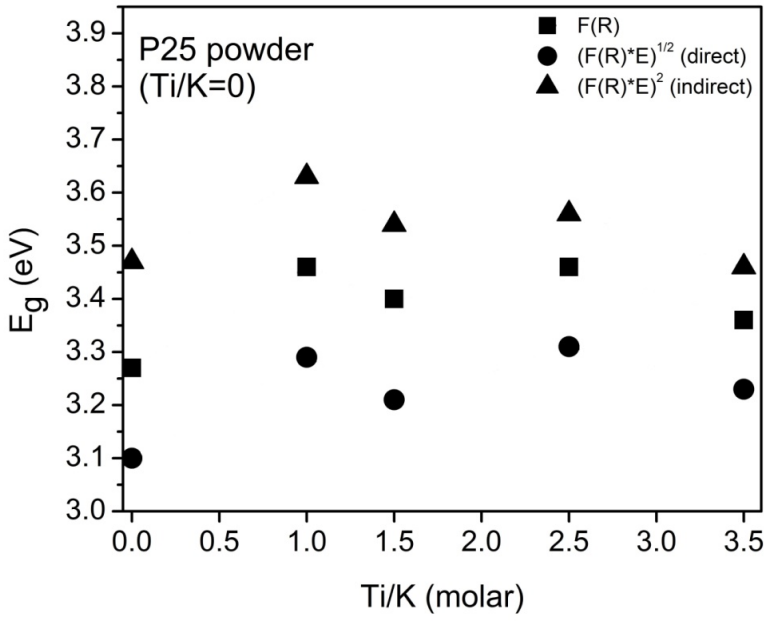


Figure 4. 12 The variation in E_g of sol-gel derived powders before calcination with respect to their Ti/K ratio. Note that the data points for E_g of P25 powder are shown at Ti/K=0.

The calculated E_g of P25 powder is 3.05-3.10 eV (from $(F(R)*E)^{1/2}$ curve) and is 3.20 eV (from F(R) curve where $F(R) \approx \alpha$). Since the xero-gels are composed of KCl crystals within an amorphous Ti-O network, the overall E_g is both linked to KCl and amorphous phase.

KCl is an ionic alkali halide crystal in which the electronic bands are very narrow, usually between 7-14 eV. E_g is reported to be around 9 eV for KCl.[108] IVB oxides such as TiO_2 are reported to form ionic amorphous oxides with band gap energy of 3-4 eV, which is consistent with the current results. Valencia et. al.[45] reported E_g of amorphous TiO_2 above 3.5 eV. They also stated that E_g of a material is like a fingerprint to clarify whether it is crystalline or amorphous since all E_g values of amorphous samples were above 3.4 eV. Therefore, the E_g given in Figure 4.12 for xero-gels designate the E_g of the major amorphous phase.

In Figure 4.13, the values for E_g of powders obtained before and after calcination at 600 and 800 °C for 1-3 h are compared within themselves and P25 powder. Identical calculation methods and representation format with Figure 4.12 are used. The E_g of the powders –especially indirect E_g- decreased after calcination due to formation of crystalline phase(s). Disorder in amorphous structures causes electron states to localize due to the presence of dangling bonds, which require a range of energy to be promoted to the CB. In other words, the mobility edges move further into the bands and localize the whole band.[109] Multiple trapping conduction occurs in amorphous materials when the electrons repeatedly become trapped in these localized states. They continuously absorb energy to become free, and the ones at the deeper traps need more and more energy. Then, the mobility of the carriers' decrease and these lower states act as recombination centers near midgap. The holes reach these midgap states, collide with the electrons and recombine.[110] Therefore, the reason behind higher E_g of amorphous samples is most probably because the crystal defects acted as recombination centers for e^-/h^+ pairs.[111]

A comparison of the E_g data needs further attention in terms of referring E_g to direct or indirect transitions. In addition to that, E_g obtained by using the F(R) curve should be considered. There is a conflict in direct or indirect transitions. Considering the data given in Figure 4.11, it is reasonable to say that both the direct and indirect transitions occur in the sol-gel derived PT powders, before and after calcination since both curves have linear portions.

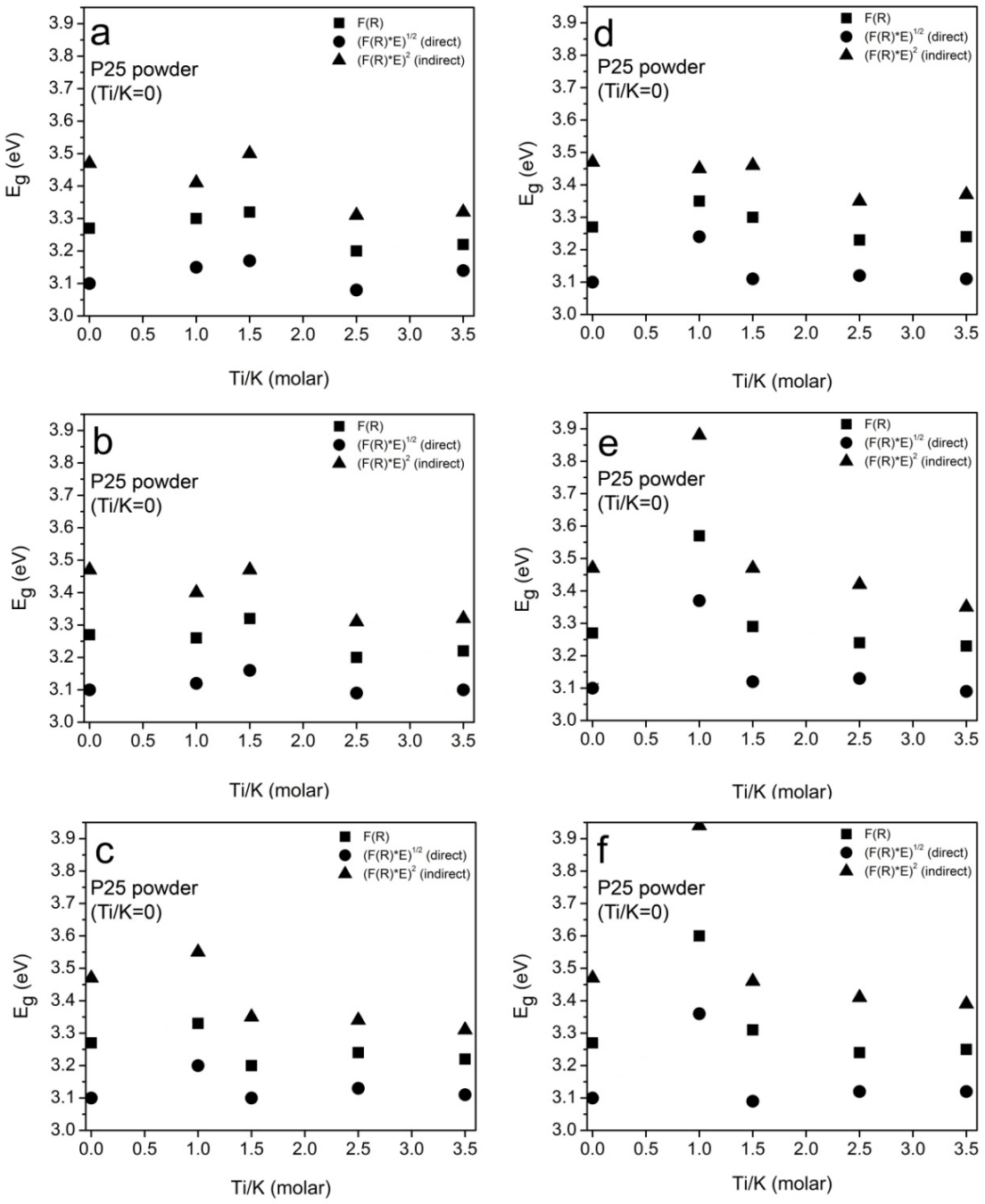


Figure 4. 13 The variation in E_g of sol-gel derived powders obtained after calcination at 600 °C (a, b, c) for 1-3 h and 800 °C (d, e, f) for 1-3 h, respectively. Note that the data points for E_g of P25 powder are shown at Ti/K=0.

The data also suggest that using F(R) line extrapolation and/or $(F(R)*E)^{1/2}$ for E_g calculation give the best comparable results either with P25 powder or with the data reported by Lopez et. al.[49] This means that major portion of the powders make indirect transition that needs the aid from a phonon. F(R) values calculated just by using the reflectance equation involve both transitions. Here, it is proposed that F(R) line extrapolation shows an overall E_g including both direct and indirect transitions and it usually lies between them. The indirect and direct E_g of P25 is 3.10 eV and 3.47 eV, respectively. P25 powder is composed of a mixture of anatase and rutile powders in which the anatase is dominant. Anatase has only an indirect transition around 3.23 eV whereas rutile has both indirect and direct transition at 3.10 eV and 3.06 eV, respectively.[45] F(R) line suggests an intermediate E_g of 3.27 eV where indirect transition of anatase dominates to rutile. The sol-gel derived powders contained KCl, anatase, PH and PHT phases after calcination at 600 °C. Unfortunately, there is no information in literature regarding the E_g of PH whiskers. But, the E_g of PHT nanowires was calculated as 3.40/3.47 eV by using absorbance and K-M approach ($(F(R)*E)^2$).[29,112] Du et. al.[33] calculated E_g as 3.45 eV by using the K-M approach ($(F(R)*E)^{1/2}$). As the samples contained multiphase with different E_g values, it is more accurate to compare the E_g values obtained by using the F(R) lines.

Both the Ti/K ratio and the calcination time were effective on lowering the E_g of powders calcined at 600 °C. After all calcination durations, E_g decreased with increasing Ti/K ratio. Moreover, samples with Ti/K ratio of 2.5 and 3.5 had lower E_g than P25 powder has. E_g of the samples did not change significantly by increasing the calcination time. There was only a minor difference among the E_g of these samples because of increasing crystallite size by the calcination time and Ti/K ratio. It is related to the increase in the crystallinity that decreases the possibility of crystal defects causing charge carrier recombination. By calcination at 800 ºC, PTT formation was evident instead of PH and the sizes measured on SEM images were relatively bigger. The relation between Ti/K ratio and the E_g of the powders calcined at 800 ºC was similar to that calcined at 600 ºC.

But, the increase in E_g was much more noticeable at Ti/K ratio of 1 when the calcination temperature increased, especially after 2 h, see Figure 4.13e. The E_g of the PTT phase was reported by Cui et al.[113] as 3.54 eV as direct transition. XRD results suggested that significant amount of PTT phase was present in these samples, thus an increase in E_g up to 3.60 eV verifies remarkable PTT formation.

4.1.6 Photocatalytic degradation performance of sol-gel derived PTs

The variation of MB degradation rate (k, min^{-1}) of sol-gel derived powders obtained by calcination at 600 and 800 ºC according to the first order kinetics (LH Model) were calculated from the slope of the linear fit lines according to the formula given in Eq. (3.3) and are given in Figure 4.14 in comparison to that of P25 powder tested under identical conditions. One sample for each powder was tested. The UV-Vis absorption lines of MB solutions of each sample with respect to time of test are given in Appendix along with the linear fit graphs including equations of k and goodness-of-fit (R^2) values. The red lines on the scatter points on the graphs shown in Figure 4.14 designate the standard deviation upon formation of linear fit equation.

The data showed that most of the powders indicated a linear degradation path by time following a LH model except for powders obtained after calcination at 800 ºC at Ti/K of 1 and 3.5 for 2 and 3 h, respectively. The data points for these samples are missing in Figure 4.14, since the degradation behaviors of them do not fit to first order kinetics equation (Eq. (3.3)). The MB degradation rate of P25 powder was calculated as (0.046 ± 0.007) min^{-1}. Several researchers have reported the photocatalytic degradation capability of PHT previously.[114,115] But it is not accurate to compare the degradation rates of PTs produced or tested by using different procedures since multiple factors including the particle size, presence of different ionic forces, level of agglomeration or crystallinity affect the total behavior.

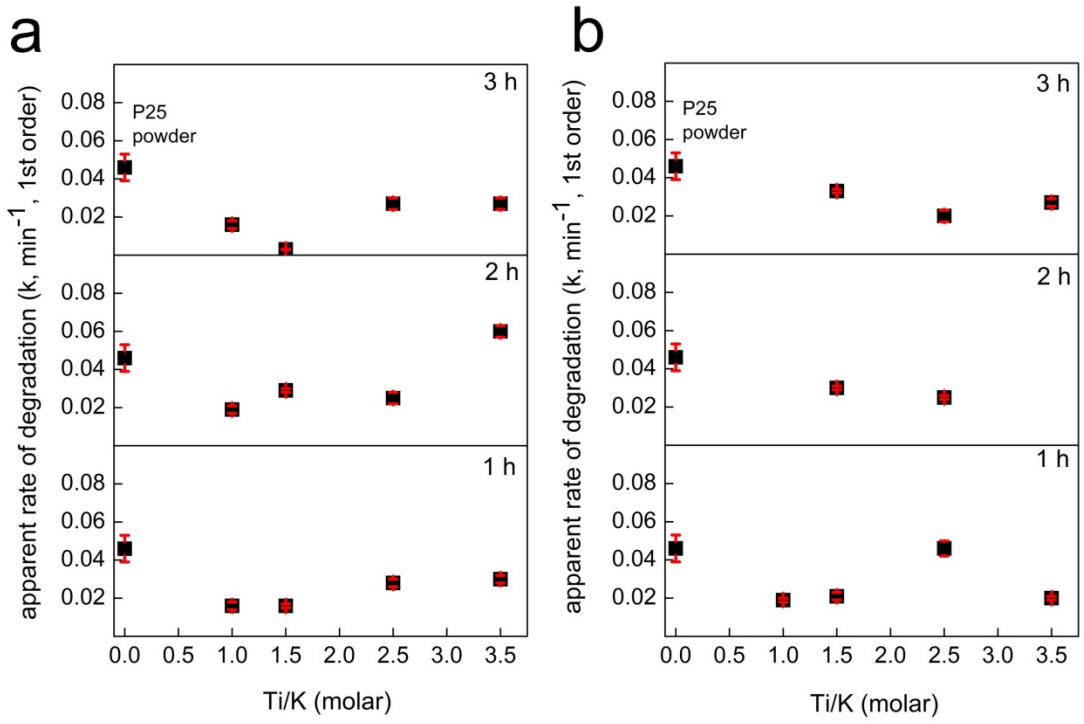


Figure 4. 14 MB degradation rates of sol-gel derived powders obtained after calcination at a) 600 ºC and b) 800 ºC for 1-3 h. Note that the data points shown at Ti/K=0 of each graph represent the MB degradation rate of P25 powders tested under identical conditions.

Figure 4.14a indicates for the powders obtained after calcination at 600 ºC showed the highest rate of degradation by using Ti/K of 3.5 for 2 h of calcination (0.060 ± 0.003 min^{-1}), which is also considerably faster than the degradation rate of P25 powder (0.046 ± 0.007 min^{-1}). XRD results revealed that the powders produced by using Ti/K>1.5 indicated higher number of sharp PHT and PT peaks at higher intensity suggesting growth of PHT and PT phases. The SEM examinations did not confirm a significant increase in the length, thus the size increase was mostly influenced by the diametral growth. It can be proposed that even a slight increase in surface area by the increase in diameter can provide more effective interaction of the MB dye with the surface of PTs. Moreover, the powders contained considerable amount of anatase, which also reacts with MB dye.

The composite structure of photocatalytic phases with increased diameter can enhance photocatalytic activity and reach over the P25 performance. In Figure 4.12b, the degradation rates of sol-gel derived powders obtained by calcination at 800 ºC are shown. Surprisingly, the degradation performance of P25 powders could not be reached at any Ti/K ratio. However it should be noted that the degradation performance of powders calcined at 800 ºC for 2 and 3 h at Ti/K of 1 and 3.5 showed exponential behavior. The rate of MB degradation by these powders was higher than that of P25, but should be calculated using a different model than LH model.

After calcination at 800 ºC, PTT phase formed instead of PH. As mentioned earlier, PTT has a layered structure, which favors the intercalation of planar molecules such as MB chromophore. Also, different from the powders calcined at 600 ºC, a little KCl was present in the structure. The highest rate was achieved by Ti/K of 2.5 as 0.046 ± 0.004 min^{-1} after 1 h calcination. The results bring about the idea that the MB degradation rate is mainly driven by the change in particle size rather than phase fractions of a multi-phase photocatalytic material. As the particle size increases by increasing the calcination temperature, the photocatalytic degradation rates decreases.

It should be noted that these experiments were not repeated for several times and the results are representative to the powder batch chosen from the total batch. Thus, further analysis of degradation should be made to determine direct relations between the PTT amount and the photocatalytic activity. Since the scope of the thesis does not involve these studies, experiments were performed only to have a general idea on photocatalytic activity – Ti/K relation along with the energy band structures.

4.2. Hydrothermal synthesis of PT nanowires

4.2.1 Phase analysis by XRD

PT nanowires having large aspect ratio have been synthesized after hydrothermal treatment at 180 °C by using large submicron titania spheres by Wang et al.[29] They stated that the temperature at which the hydrothermal reaction was performed and the initial KOH concentration had noteworthy effects on the morphology of the final products. In order for a better understanding of the effects of these parameters, hydrothermal treatment was performed at 120, 150, and 180 °C by using KOH aqueous solution at different molarity (5 M-20 M). A well-known nanosize TiO_2 powder (P25) was utilized as TiO_2 precursor. The XRD patterns of the unreacted precursors, which are P25 powder and KOH pellets, are shown in Figure 4.15.

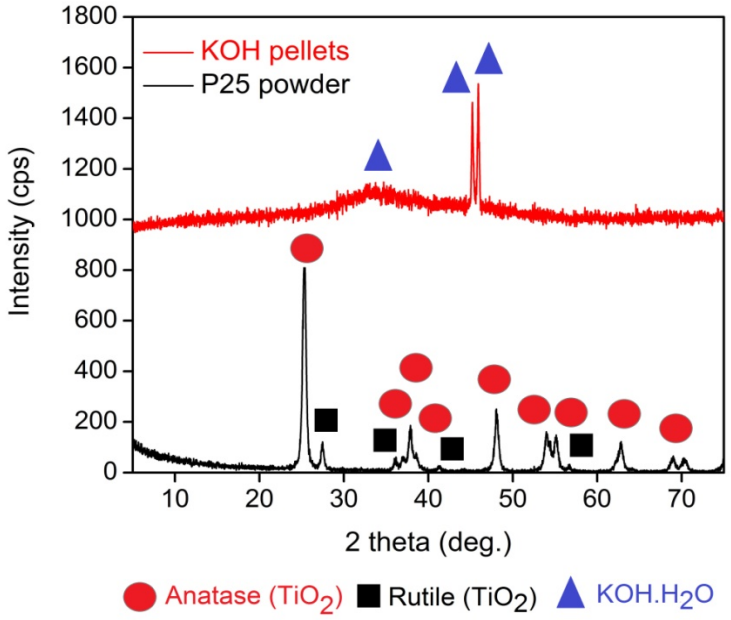


Figure 4. 15 XRD patterns of unreacted P25 powder and KOH pellets.

The XRD peaks of the P25 powder were assigned to the anatase and rutile phases of TiO_2 (Anatase, ICDD: 21-1272/ Rutile, ICDD: 21-1276). The XRD pattern of KOH pellets suggested that the pellets were composed of $KOH.H_2O$ (KH; potassium hydroxide hydrate, ICDD: 36-0791). This was due to intensely hygroscopic nature of KOH that makes it highly reactive to the moisture under ambient conditions. The XRD patterns of the PT powders synthesized by hydrothermal treatment at 180 °C are shown in Figure 4.16. The XRD analysis suggested the presence of four phases; $K_2Ti_6O_{13}$ (PHT, ICDD: 74-0275), $K_2Ti_4O_9$ (PTT, ICDD: 32-0861), Anatase (A), and Rutile (R). The A, R, and KH peaks were distinctly present at short reaction durations (3 h) due to the presence of unreacted P25 and KOH.

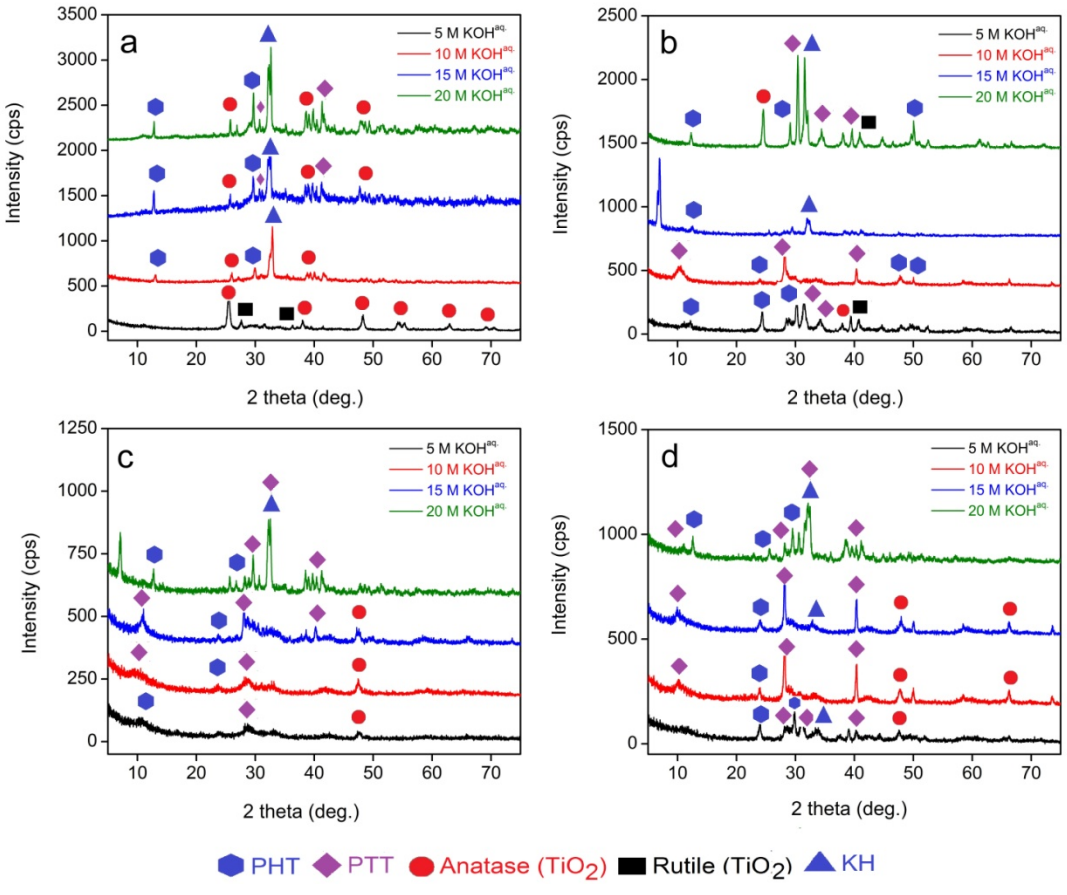


Figure 4. 16 XRD patterns of hydrothermally treated powders using 5-20 M $KOH^{aq.}$ at 180 °C for a)3 h b) 12 h c) 24 h and d) 48 h.

XRD analysis revealed that PTs can be formed by hydrothermal treatment at 180 °C using $KOH^{aq.}$ solution at various molarities. Crystallization of PT using TiO_2 proceeds by rearrangement of TiO_6 octahedra in TiO_2 upon interaction with $KOH^{aq.}$ solution. K^+ ions are placed in between the disturbed TiO_6 octahedra by forming Ti-O-K bonds. Then, some of the long Ti-O bonds are broken, but shorter Ti-O bonds remain intact. This rearrangement makes PHT phases first crystallize and then grow along a specific direction.[42]

At 5 M $KOH^{aq.}$, XRD pattern showed that 3 h of hydrothermal treatment was not sufficient for the formation of PHT at 180 °C. The peaks of P25 powder (anatase and rutile) were dominant. However, the distortion of K^+ ions into the TiO_6 octahedra is evident as lattice expansion after hydrothermal reaction. The initial a lattice parameter (a-LP) of anatase in P25 powder was calculated as 0.378 nm but it was 0.376 nm after 3 h of hydrothermal treatment. The difference was more evident in c-LP that was 0.948 nm before treatment and increased to 0.952 nm after. All peaks of anatase phase were included in calculations. Number of rutile peaks was less in P25 powder thus the data was not sufficient to calculate and compare the lattice change before and after hydrothermal treatment. P25 was almost made of 72 % anatase and the lattice expansion of anatase was very significant in c-direction. This implies that TiO_2 is interacting with K^+ through lattice distortion during hydrothermal treatment.

The Ti/K ratio in sol-gel reactions was previously shown to be effective on the proceeding of the reactions. For hydrothermal reactions, the change in the initial KOH concentration in solution is likewise. In hydrothermal reactions, TiO_2 content was kept constant and KOH amount was varied. That is why the KH peaks become more evident as $KOH^{aq.}$ molarity increases beyond 5 M. XRD patterns indicated that as the initial molarity increased, KOH became excess. In other words dissolution rate was less or treatment time was not sufficient for P25 to react with KOH and possessed an ordered structure at that concentration for short reaction durations (e.g. 3 h). As the treatment time increased, more P25 reacted with more KOH.

The most intense peak of PHT representing the interplanar spacing of (200) plane at 11.51° was more evident as the initial KOH concentration in solution increased from 5 M to higher or after hydrothermal treatment for more than 3 h. It was indicative of relatively higher supersaturation rate of PTs in the presence of more K^+ ions distorting the lattices, which is also directly related to the desired stoichiometric ratio for PHT or PTT formation. By increasing hydrothermal treatment duration from 3 h to 48 h, PHT formation became more favorable with PTT and accordingly P25 and KH contents decreased at all $KOH^{aq.}$ molar concentrations. For better understanding of the kinetics of the reaction, hydrothermal treatment was performed additionally using high $KOH^{aq.}$ molarity (20 M) at 120 and 150 °C for 3 h. The XRD patterns of these products are shown in Figure 4.17.

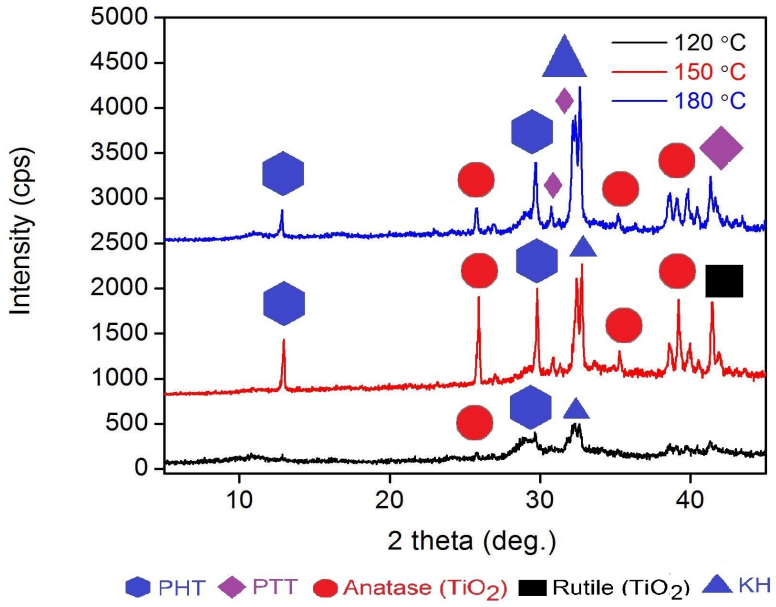


Figure 4. 17 XRD patterns of the powders synthesized by hydrothermal treatment using 20 M $KOH^{aq.}$ at 180 °C for 3 h.

The XRD patterns in Figure 4.17 clarify that hydrothermal temperature and KOH amounts are the main parameters for the determination of the kinetics of treatment. Results show that it is the PHT phase crystallizes in the hydrothermal system and TiO_2 structure is completely destroyed at the initial times of treatment. The (200) peak of PHT - directly resembles the growth direction- at 11.51° was not present after treatment at 120 °C. Moreover, the XRD peaks of the powders obtained at this temperature were relatively much broader implying the size of the crystals in nanoscale.

Chao et al.[32] stated two different mechanisms for the formation of titanate nanostructures by using TiO_2 as the titanium source; exfoliation and dissolution-crystallization model. In the exfoliation model, alkaline solution is considered to disturb the crystal structure and exfoliate 2D sheets from TiO_2 surfaces. For the dissolution-crystallization model, TiO_2 reacts with the strong alkaline solution and form a disordered phase, which then precipitates as layered alkali titanate. In the light of the given details combined with the current results, it is reasonable to say that hydrothermal reaction follows a dissolution-precipitation model rather than exfoliation. Any signs of amorphous intermediate phase formation would support this statement.

4.2.2 SEM analysis

The representative SEM images of the hydrothermally treated powders at different molarities and for different times are shown in Figure 4.18. The images indicate big chunks of agglomerates at low $KOH^{aq.}$ molarity and short reaction durations turning into splitting sheet surfaces with increasing initial $KOH^{aq.}$ molarity after 12 h of reaction. The sheets split further into nanowires by increasing the time of reaction at all $KOH^{aq.}$ concentrations. However, the size of the nanowires increased with increasing $KOH^{aq.}$ molarity at 24 h. After 48 h, the result was the opposite, since the high KOH concentration supported precipitation and agglomeration of newly formed crystals and inhibited growth.

As the K^+ concentration increased more, P25 was consumed by interaction with the dissolved K^+ ions and PHT formation was enhanced. It was an indication of increased supersaturation rate by the increase in molarity at 3 h. Then, it is possible to conclude that, the supersaturation rate increased with increasing molarity at the initial durations of reaction but by further increase in time, growth dominated precipitation. Images show that, splitting is the initial cause of growth dominating precipitation up to 24 h, but still evident even at 48 h at the highest KOH molarity. Then, this also indicates that increasing KOH increased the precipitation rate (Figure 4.18e-p).

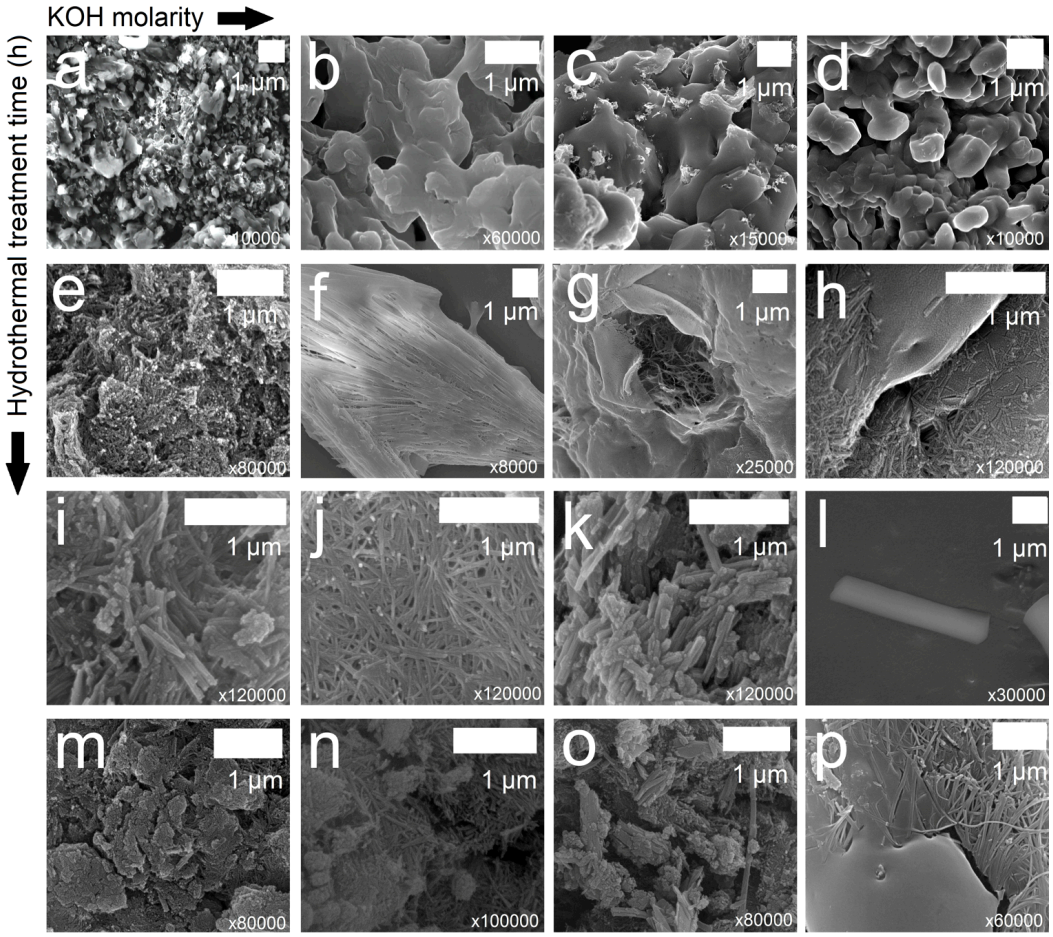


Figure 4. 18 SEM images of PT nanostructures obtained by hydrothermal treatment at 180 °C with increasing hydrothermal treatment time of 3, 12, 24 and 48 h (top to bottom) and $KOH^{aq.}$ molarity of 5, 10, 15 and 20 M (left to right).

In Figure 4.19, SEM images of the powders produced by using 10 M $KOH^{aq.}$ at 120 and 150 °C for 3 h are shown. The XRD of these powders suggested that the reaction proceeded at a slower rate at 120 °C since no PHT peaks were apparent. It was obvious from the microstructure shown in Figure 4.19a that no signs of splitting were present on the surfaces of big chunks after treated at 120 °C. As the temperature increased to 150 °C, short nanowires formed and presented in a highly agglomerated state. Further increase in temperature to 180 °C forced them to combine into thicker irregular shapes due to chemical interactions on their surfaces.

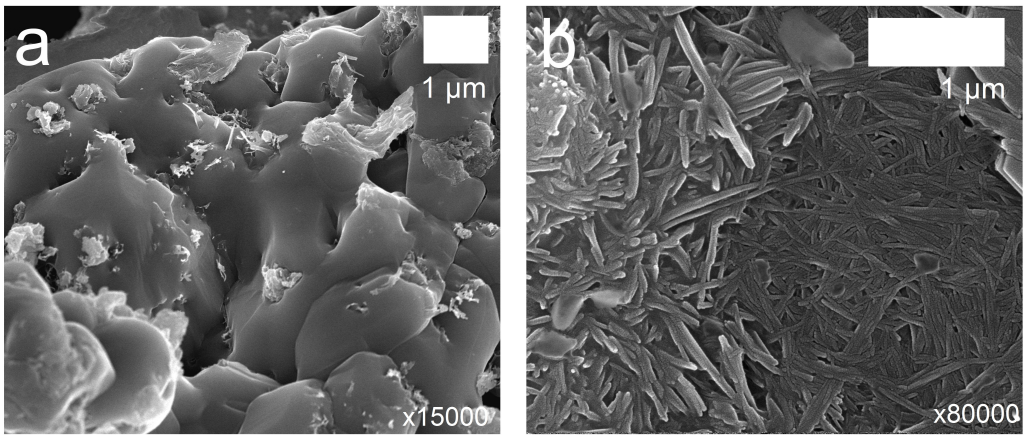


Figure 4. 19 SEM images of PT nanostructures obtained by hydrothermal treatment at a) 120 and b) 150 °C with hydrothermal treatment time of 3 h at 20 M of $KOH^{aq.}$.

4.2.3 Surface area (BET) analysis

The hysteresis loops of hydrothermally synthesized powders shown in Figure 4.20a-b resemble H3 type loops that are indications of slit shaped pores between plate-like particles. Yuan et.al.[116]stated that a hysteresis observed at high relative pressures is an indication of the presence of interparticle space of nanowires. In addition to that, the delayed desorption to very low relative pressures is the fingerprint of slit-like pores[44]. The loops did not show characteristic differences after 3 h of treatment at 5 M $KOH^{aq.}$

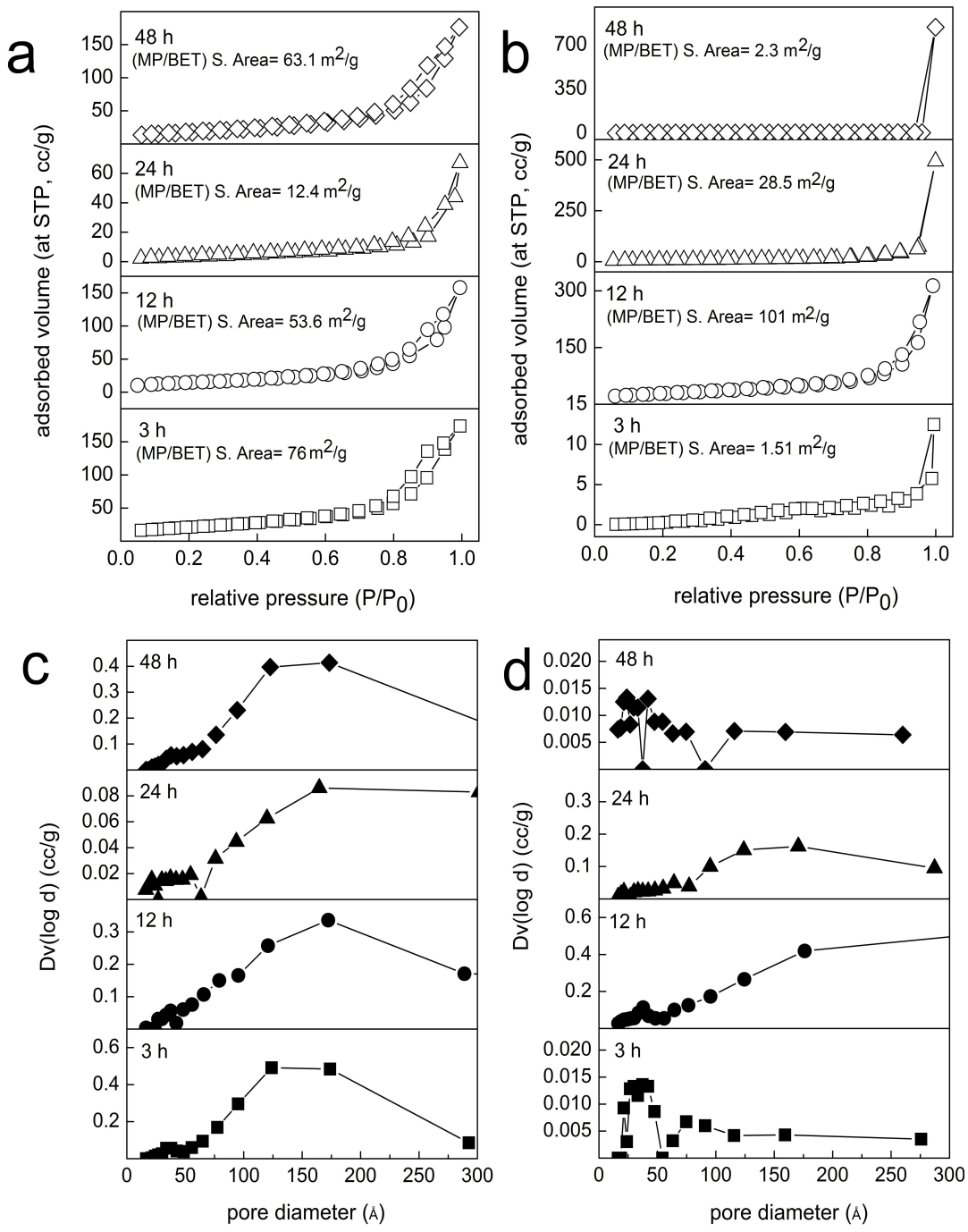


Figure 4. 20 BET isotherms of powders after hydrothermal treatment using a) 5 M b) 10 M $KOH^{aq.}$ and BJH mesopores size distribution (Pore diameter versus adsorbed volume) at c) 5 M and d) 10 M $KOH^{aq.}$ at 180 °C for 3-48 h.

The surface area of powders calculated using multi-point BET method (3 points) are shown on the hysteresis loops in each graph shown in Figure 4.20. By comparing these values, it can be proposed that splitting is the key factor that determines the surface area of the nanostructures. As the splitting is enhanced, surface area is enhanced owing to the split layers of PTs in nano scale. The splitting surfaces were clearly shown in Figure 4.18f-g and BET analysis clarified that these powders had one of the highest surface area (101 m^2/g) where splitting was very significant (12 h of treatment, 10 M).

Generally, decrease in the adsorbed gas volume indicates a decrease in pore size/volume. In order to investigate the change in pore size, BJH pore size analysis - in which the mesopores of powders are considered- has been performed. The results are shown in Figure 4.20c-d. When 5 M of $KOH^{aq.}$ was used, results showed an increasing pore volume in 5-20 nm range. The volume of small pores (<5 nm) was neglectable and the average pore size was in meso-pore range, 16 nm. The average size did not change much, but the pore volume decreased with increasing reaction time to 24 h. Surprisingly, adsorbed volume increased again after 48 h. This might be because splitting was more significant and slower at 5 M $KOH^{aq.}$ condition. The average meso-pore size was around 3.7 nm when 10 M $KOH^{aq.}$ was used, and almost non-porous after 48 h reaction. The decrease in average pore size was most probably due to the increased proportion of splitting of nanowires. The splitting is also anticipated from the broader peaks of PTs in the XRD patterns in Figure 4.16.

Therefore, there is not a direct correlation between the specific surface area and hydrothermal reaction time since splitting dominates over precipitation by increasing reaction time. However, for 12 and 24 h of reaction, surface area is two-fold as the KOH concentration is made two-fold. The specific surface area of P25 powder is 47-57 m^2/g[4,7,46] with an average pore diameter of 8 nm[4]. XRD pattern in Figure 4.15 indicated that the reaction product after 3 h composed mostly of anatase originating from P25 powder precursor. Therefore, 76 m^2/g surface area of 3 h treated powder corresponds mainly to presence of P25 particles and newly formed amorphous-like matrix. At 10 M $KOH^{aq.}$, the reaction proceeded faster and PTs formed.

The sharp decrease in surface area to 1.5 m^2/g by increasing $KOH^{aq.}$ concentration to 10 M is therefore because of the highly disordered matrix composed of freely dispersed K^+ cations promoting the aggregation of primary particles[127]. It has been recognized that the highest specific surface area is achieved after hydrothermal reaction at 180 °C for 12 h, by using 10 M $KOH^{aq.}$ solution in which the splitting of nanowires is the most evident.

4.2.4 Growth of potassium titanate nanowires by hydrothermal treatment

SEM images verified that the origin of nanowire formation by hydrothermal reaction involves splitting of the titanate sheets into smaller pieces. High aspect ratio of these nanowires suggests that the crystal growth is one-dimensional. SEM images of the hydrothermally derived powders indicated splitting branches but the preferential cleavage direction could not be recognized from SEM examinations. TEM analysis may clarify the formation and growth mechanism of PT nanowires synthesized by hydrothermal treatment. In Figure 4.21, a general sequence of nanowire formation is shown through TEM images confirm that the main mechanism behind nanowire formation is splitting as outlined also by SEM examinations. TEM images were taken from a bundle of whiskers. The lamellar structure of the splitting nanowires at different lengths is obvious amongst the bundles. See Figure 4.25c.

The perfect crystal of a PT nanowire with rectangular edges is shown in Figure 4.25d. Similar nanostructures were documented by Du et. al.[33] who used anatase and $KOH^{aq.}$ solution as the precursors. They stated that PHT nanowires had rectangle shaped cross sections with rounded corners rather than perfectly circular.

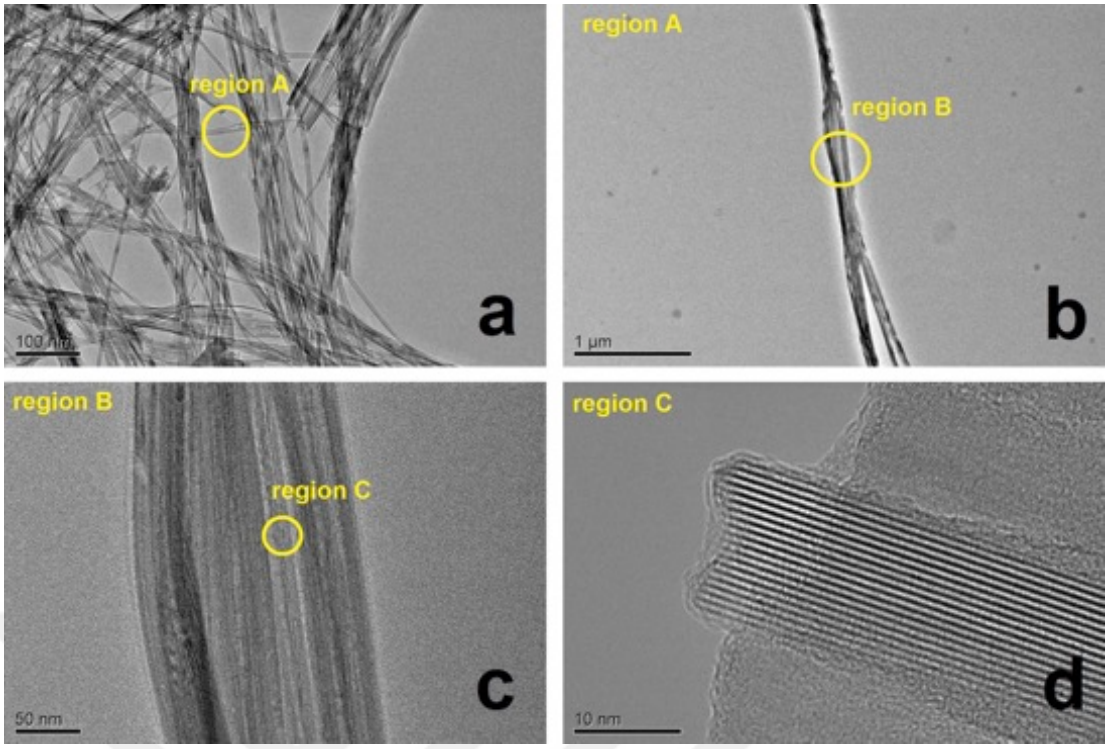


Figure 4. 21 TEM images of PT nanowires a) aggregates, b) whisker, c) splitting nanowires (lamellar), d) single nanowires.

In Figure 4.22, the surface of aggregated, spherical P25powder is shown. The analysis revealed that the zone axis of the image was [001] and the spots were traces of <101> planes. The lattice fringe was measured as 0.35 nm that is consistent with the previously reported values.[117,118]

It is crucial to understand how these nanowires with rectangular edges form by reacting rectangular KOH particles with spherical TiO_2 particles under hydrothermal treatment conditions. A clear cut understanding is necessary to find out whether the crystal structure of TiO_2 during reaction is disrupted completely or not. In other words, it is essential to know if an amorphous K-Ti-O matrix is formed during the early stages of the reaction. The XRD and SEM results underlined that the hydrothermal temperature and $KOH^{aq.}$ concentration have strong effects not only the final phase variety and morphology, but also the kinetics of the reaction.

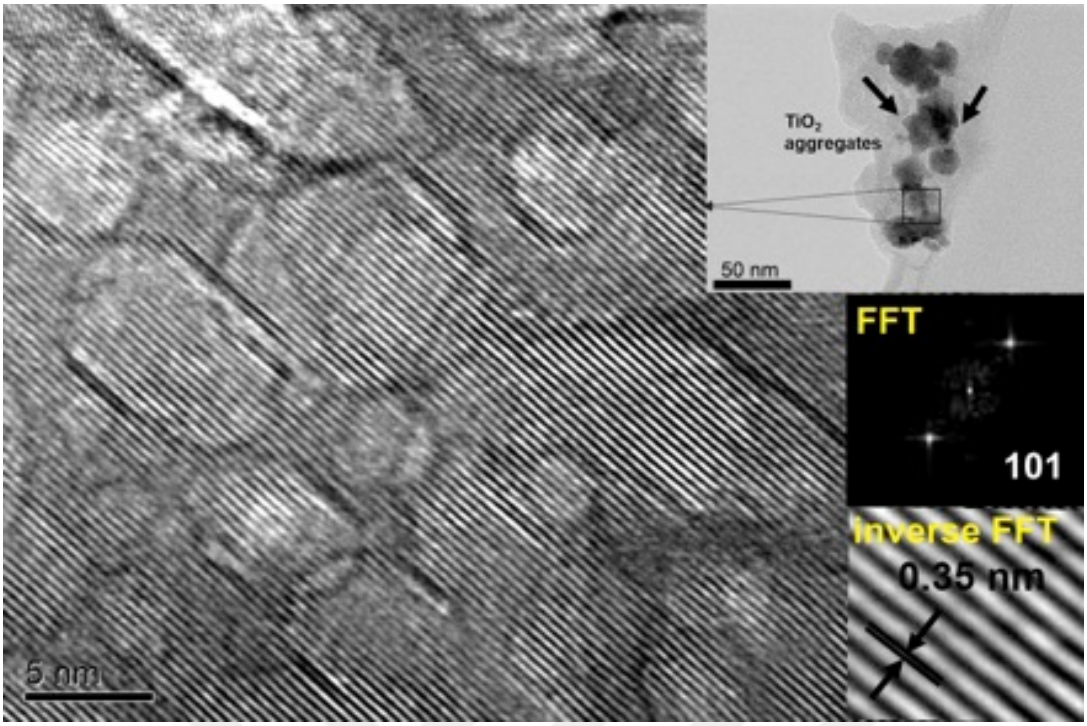


Figure 4. 22 TEM image of P25 powder surface. Insets are P25 aggregates, FFT and iFFT of the P25 surfaces.

In order to understand whether the PT clusters nucleate and grow from a Ti-O-K amorphous/distorted matrix or directly on TiO_2 surfaces by hydrothermal reaction, TEM analysis has to be performed on the nanostructures synthesized at the lowest reaction rate. In order to examine the initial stages of the reaction, lowest $KOH^{aq.}$ molarity (5 M) and reaction time (3 h) were considered. The XRD pattern of the powders synthesized at 5 M $KOH^{aq.}$ after 3 h hydrothermal reaction indicated that the major phase was still crystalline TiO_2 rather than amorphous TiO_2. It was impossible to find and monitor an amorphous part by TEM imaging of very small particles in TEM study. For this reason, the TEM analysis of the surfaces synthesized by using 10 M $KOH^{aq.}$ after 3 h of hydrothermal treatment was performed. TEM images of the powders synthesized are shown in Figure 4.23. The latter study revealed signs of crystal clusters dispersed in an amorphous-like matrix.

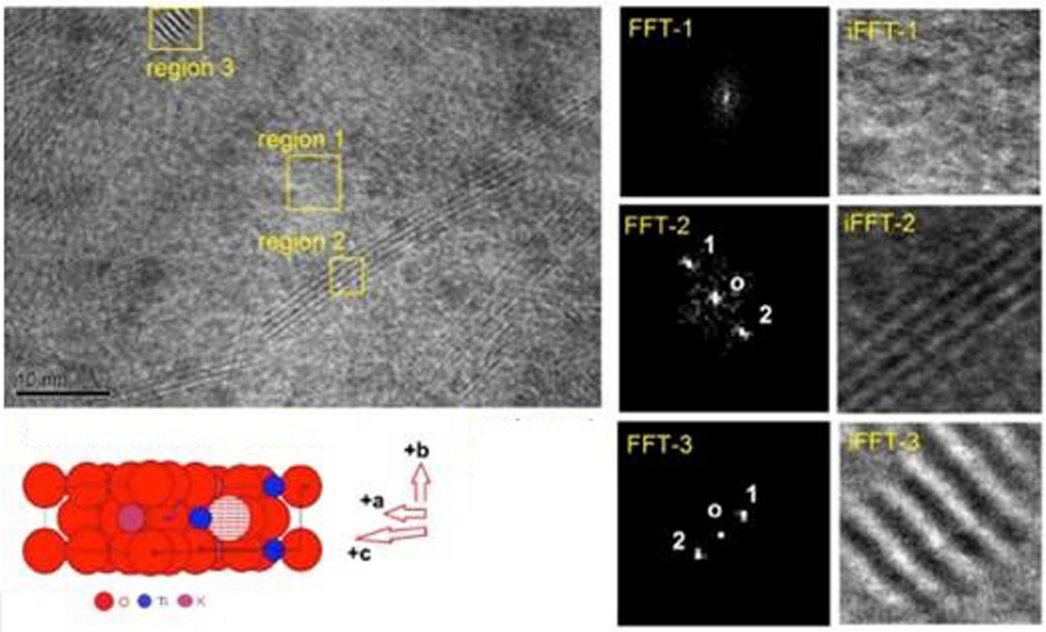


Figure 4. 23 TEM images of the nanostructures hydrothermally synthesized by using 10 M $KOH^{aq.}$ at 180 °C for 3 h, showing the growth of nanowires from an amorphous Ti-O-K network.

Three regions in the TEM image were analyzed. There was no physical order among the atoms in region 1 meaning that region 1 is amorphous. On the other hand, the atoms in region the other two regions (region 2 and region 3) were ordered, i.e. crystalline. The analysis by using the FFTs in Figure 4.23 clarified that an amorphous Ti-O-K region formed first. The TiO_2 structure was disrupted by the autogeneous pressure and heat at the early minutes of hydrothermal treatment in the autoclave. Considering the XRD peaks of anatase in this sample either lessening intensity or disappearing, this is an expected result. The amorphous structure of region 1 was also evident from the corresponding FFT and iFFT, since there was no diffraction spot in the reciprocal space. Conversely, regions 2 and 3, seem as early clusters of an ordered structure that was growing. The analysis of FFTs, indicates that the spots correspond to the reflections of <200> family of PHT phase. It should be noted that the other crystalline regions have identical FFT spots corresponding to the same interplanar spacing. At the present, it is reasonable to declare that the phase growing mainly from the amorphous network is PHT.

In Figure 4.24, another TEM image taken from the nanostructure synthesized at 180 °C for 3 h clearly shows the amorphous periphery around the nanowires. The analysis revealed that it was also a PHT nanowire and the spots correspond to <200> reflections. The other regions on this image showed identical FFT spots. The amorphous periphery may be an indication of growing PHT crystals by consuming the amorphous Ti-O-K network from inside along the growth direction. However, further analysis is needed to support this judgement.

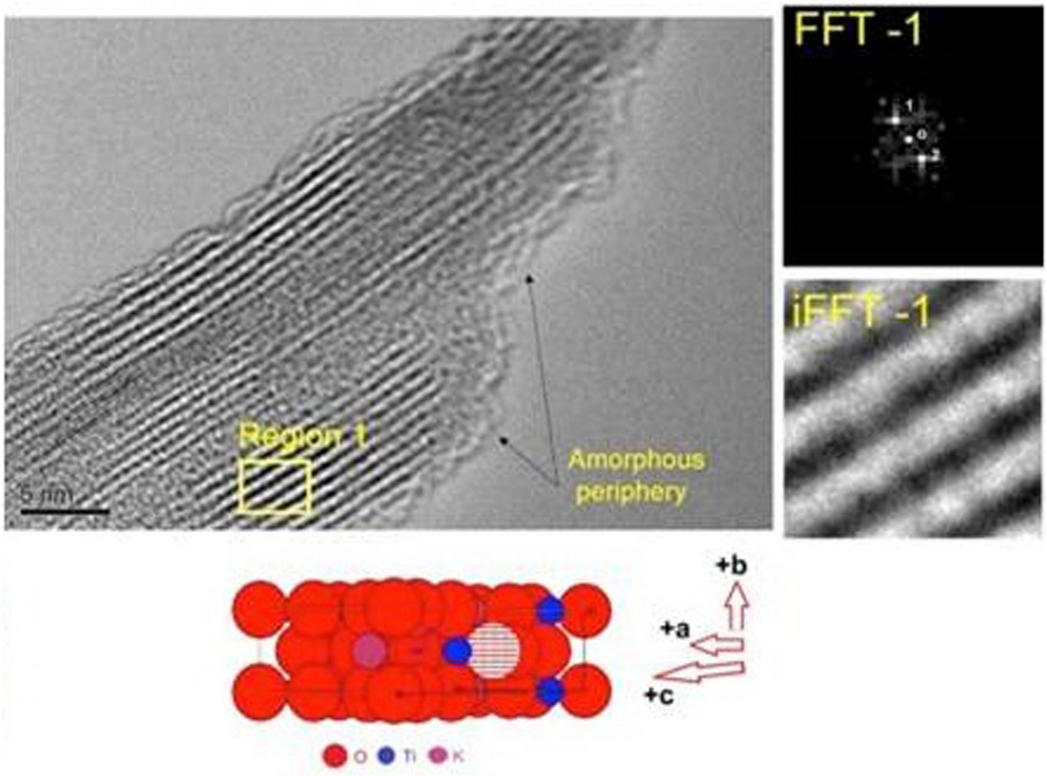


Figure 4. 24 TEM images of the nanostructures hydrothermally synthesized by using 10 M $KOH^{aq.}$ at 180 °C for 3 h.

An identical analysis was performed on another TEM image taken from the same sample showing splitting branch of a nanowire from the sheet surface. The TEM investigations supported the SEM findings of the presence of splitting sheets in microscale. The splitting surface of the PT nanostructures synthesized by hydrothermal reaction at 180 °C for 3 h is shown with the corresponding FFT, iFFT, and the reciprocal lattice and the crystal projection along the calculated zone axis [001] in Figure 4.25.

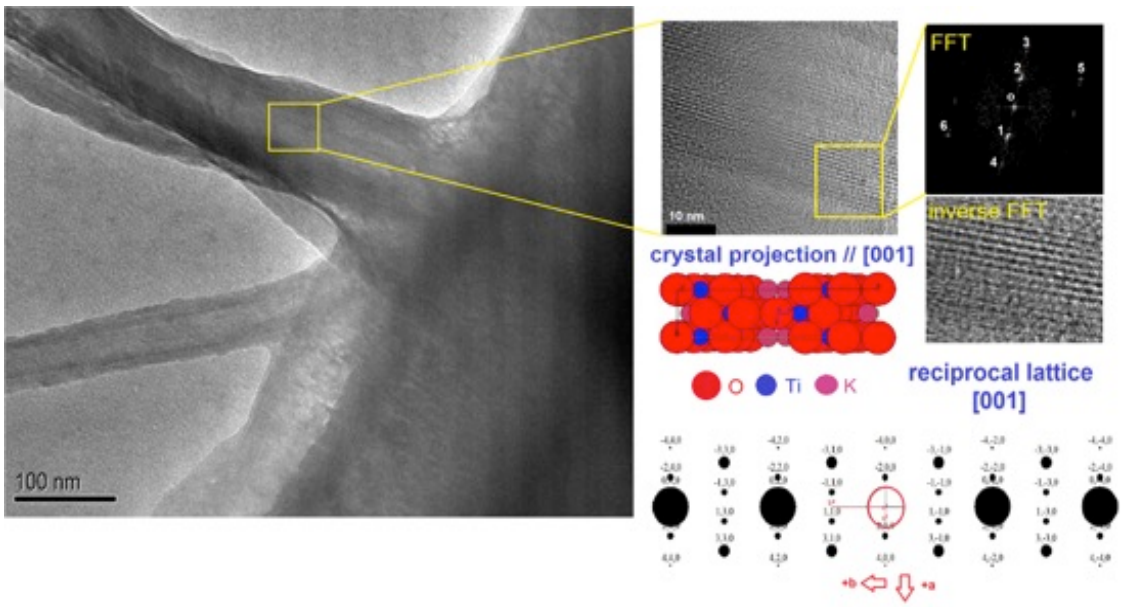


Figure 4. 25 TEM image of splitting surface of the nanostructures hydrothermally synthesized by using 10 M $KOH^{aq.}$ at 180 °C for 3 h.

The key mechanism in the atomic scale is the intercalation of the alkali ions during formation of these layered or tunnel structures. The intercalation forced TiO_2 matrix to expand due to intercalation of K^+ ions which have larger ionic radii then Ti^{4+} ions.[27] FFT analysis showed that the 1D structure that split from the sheet and grew was PHT. The spots in the FFT represent the <200>, <110> and <310> reflections, as shown in the reciprocal lattice. The projection, namely the zone axis, was along [001] and the growth direction of the PHT was [010], in b direction.

The growth direction of PHT nanowires was reported as [010].[29] The lattice fringe spacing is 0.78 nm, which corresponds well to the reported interplanar spacing of (200) plane of PHT. The main mechanism for the nucleation of PT phases by hydrothermal treatment starts with the formation of an amorphous network and splitting from sheets. However, how these nanowires grow and what the driving force for splitting of the flakes is, are still unknown. In order to understand the mechanism behind it, further TEM analysis was performed on the images taken from the nanostructures hydrothermally synthesized for 24 h since sufficient amount of PTT formation was detected in the XRD patterns of these samples. The splitting of nanowires is clearly seen in the image in Figure 4.26 that also shows strain produced during splitting. The nanowire on which the regions 1-3 are marked is PTT. The other one on which the regions 4-6 are marked is PHT. There is a small portion of amorphous network in between PTT and PHT.

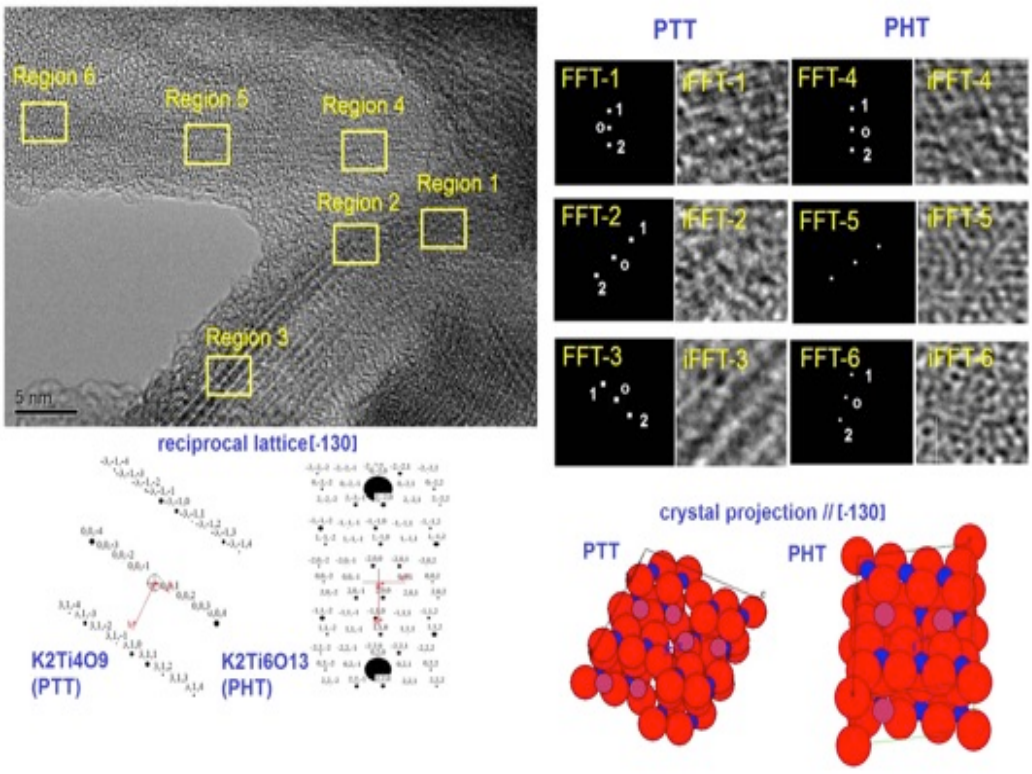


Figure 4. 26 TEM image of splitting surface of the nanostructures hydrothermally synthesized by using 10 M $KOH^{aq.}$ at 180 °C for 24 h.

Figure 4.26 proves that PTT and PHT split from each other. FFT analyses revealed that there was a strong/cohesive strain on the PTT nanowire, which may in turn cause splitting. The interplanar spacing of (201) plane in regions 1 and 3 are different, and in region 2 it is broken. By using the formula given in (f.1) below, the amount of strain on the PTT nanowire that split is estimated as 15%.

$$\text{Strain (\%)} = [(d_1-d_2)/d_1]*100 \quad \text{.....(f.1)}$$

The analysis results presented till now only verify PTT and PHT split. But, evidences on the origination of PTT from the amorphous matrix or transformation of PHT to PTT has not been gotten yet. In order to clarify these issues, thermodynamic approach could be used. A thermodynamic study on the formation of PTT and PHT by hydrothermal treatment was performed based on the reaction given below.

$$K_2Ti_6O_{13} + 2KOH = K_2Ti_4O_9 + H_2O \qquad \text{Eq. (4.1)}$$

The Gibbs Free Energy change ($\Delta G_{r,453K}$) of the PHT and PTT phases at 180 ºC was calculated by using the standard data reported by Zhou et. al.[119] The results are tabulated in Table 4.4. The effect of pressure change was overlooked in the calculations since the variation of autogeneous pressure was low in the autoclave. Conclusively, since $\Delta G_{r,453K}$ is bigger than zero, the formation of PTT from PHT is not thermodynamically feasible under these hydrothermal conditions.

Table 4. 3 Thermodynamic data for the formation of PT. [119] Note that the data given for $KOH^{aq.}$ is given for 10 M.

Material	**$\Delta G°_{f,298}$ (kj/mol)**	**$\Delta H°_{f,298}$ (kj/mol)**	**Cp (j/mol.K)**	**$\Delta G°_{R,453}$ (kj/mol)**
KOH^{aq*}	-378.86	-424.73	$2918.87-3.96*T+0.0085*T^2$	155.33
$K_2Ti_6O_{13}$	-5849.53	-6553.32	$80.90+44.91*10^{-3}*T-21*10^5*T^2$	
$K_2Ti_4O_9$	-4054.24	-4479.98	$80.47+21.60*10^{-3}*T-15*10^5*T^2$	

Neither the thermodynamic data nor the crystal structure supports the occurrence of the chemical reaction given in Eq. (4.1). Xie et. al.[120] stated that the whisker must split due to the strain in the cohesive sections when the tunnel structure was converted into layered structure. PHT splitting needs more energy than formation. Transformation from a tunnel structure into a layered structure causes entropy loss. However, the energy barrier for transformation of $(Ti_3O_7)^{2-}$ in PHT to $(Ti_4O_9)^{2-}$ layers in PTT is so high that an additional energy is needed. Since the autogeneous pressure does not change significantly and the temperature is constant, no additional energy is provided for this transformation during the hydrothermal treatment.

The TEM analysis results combined with XRD and SEM analyses results validate the formation and growth of PHT selectively on b axis [010] extending their <200> planes. The formation of a PT with relatively lower K^+ content (PHT) in an amorphous Ti-O-K network is expected under autogeneous pressure at short reaction durations. The sharing of three TiO_6 octahedra enclosing 2 K^+ ions per tunnel is easier to arrange within an amorphous structure under pressure. By considering the amorphous network as a highly distorted and expanded TiO_2 network, the tunnel formation can be understood more clearly. In terms of crystalline structure, it is well known that nature prefers the lowest energy possible and forms the simplest lattice from an amorphous-like structure. For this reason, the formation of PHT at low KOH concentrations and shorter hydrothermal treatment times is favored. This explanation is in concomitant with the thermodynamic data and TEM analysis results.

The formation of potassium n-titanates with an increase in KOH concentration after 24 h of hydrothermal treatment is then explained by the stoichiometric balance of Ti-K in the network and the effect of pressure linking the ribbons on their corners. For PT nanostructures formation, stoichiometric amount of cationic K^+ and anionic Ti_xO_y ribbons, and a basic (pH 8) solution are required. In the present study, the basicity was regulated by the autoclave filling level, wherein OH^- was increased by increasing the volume of the solution and the K^+ content. Consequently, the increase in K^+ content promoted the formation of layered and high-K containing PTT.

As a result, titanate nanowires in the present condition can be formed by the so-called dissolution-precipitation mechanism, in which the starting TiO_2 was dissolved into the $KOH^{aq.}$ and the dissolved Ti species were precipitated in the form of PT. Thus, both diameter and length of titanate nanowires increase as the dissolution rate for TiO_2 decreases and as the number of nuclei of titanate in the $KOH^{aq.}$ solution decreases. [40]

An atomic-scale analysis using HRTEM indicated the formation of KT nanowires via a combined mechanism of oriented attachment and strain-induced splitting mechanisms. The splitting of PTT from PHT was evidenced by HRTEM examination for the first time in the open literature. The formation reaction depends on the distribution and amount of K^+ ions in the amorphous-like matrix. The strain associated with the variety of K^+ ions determines the final crystal structure. Similar to the mechanism of the PTs synthesized by sol-gel followed by calcination, tunneled structures are more likely to form from amorphous-like matrices under autogeneous pressure. Solute (KOH) lowers the vapor pressure of $KOH^{aq.}$ solution.

At last, why the sheets form and do not roll during splitting could be explained with the kinetics of treatment. It was reported that the increase of the local concentration of Ti^{4+} results in a faster rate of nanosheet growth hindering the scrolling of the sheets. If the crystallization is fast enough, the thickness of the growing sheets exceeds a certain value where they become too rigid to bend. The rigidity favor the formation of nanowires rather nanotubes. Thermodynamically, nanowires/fibers are more stable than nanotubes owing to their increased surface area.

4.2.5 Determination of E_g of hydrothermally synthesized PT by UV-Vis/DRS

4.2.5.1 Effect of reaction time on energy band structure

The energy versus R%, F(R), $(F(R)*E)^{1/2}$ and $(F(R)*E)^2$ graphs (Tauc Plots) of the hydrothermally synthesized powders using 5 M an 10 M $KOH^{aq.}$ at 180 ºC are shown for various treatment durations in Figures 4.27 and 4.28, respectively. The variations for P25 powder are also included in the figures for comparison purpose.

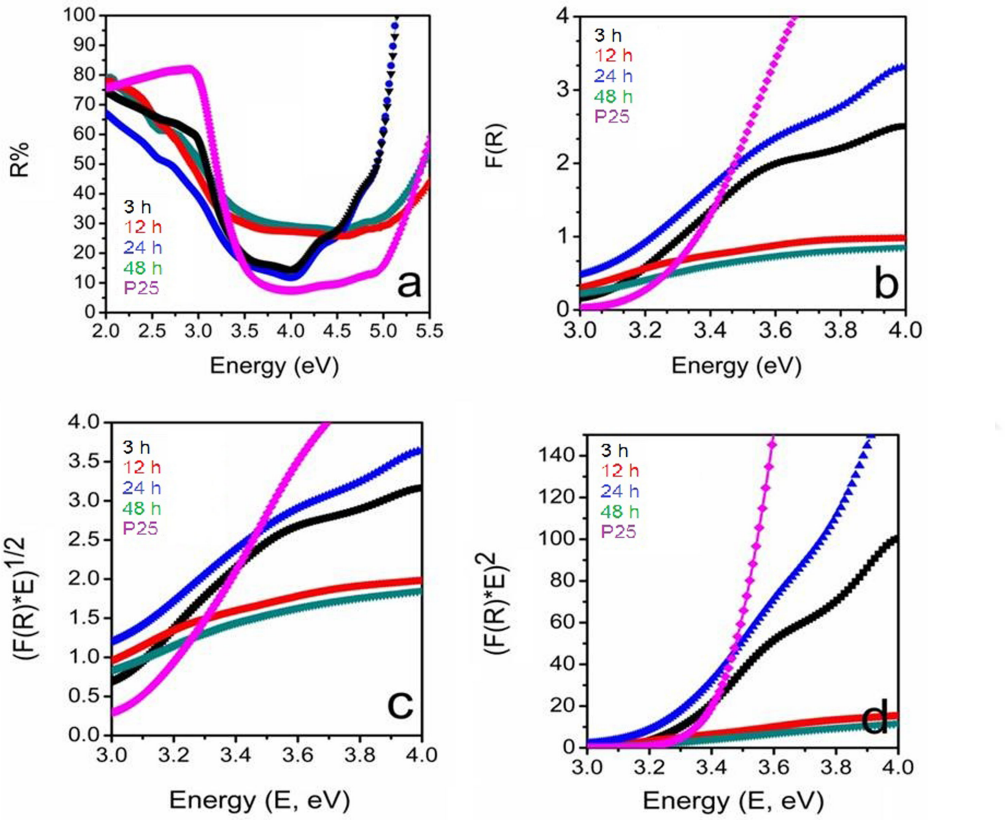


Figure 4. 27 a) R% versus energy b) K-M transform (F(R)) and Tauc plots c) indirect and d) direct band transitions of the nanostructures hydrothermally synthesized at 180 °C using 5 M $KOH^{aq.}$.

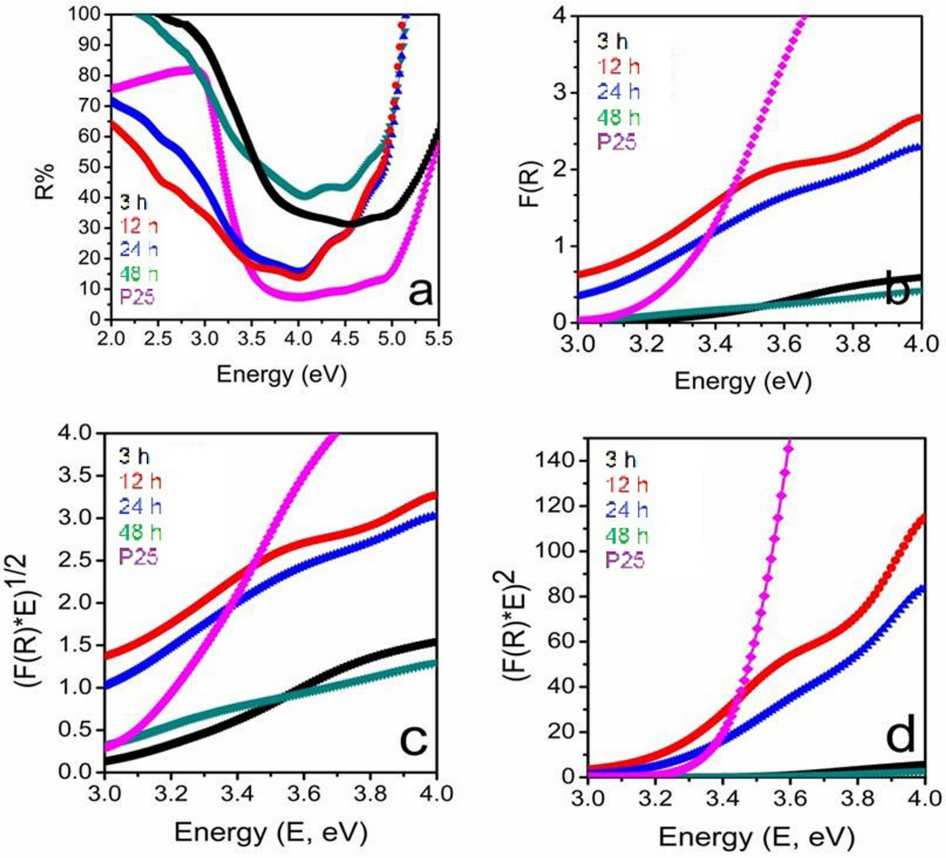


Figure 4. 28 a) R% versus energy b) K-M transform (F(R)) and Tauc plots c) indirect and d) direct band transitions of the nanostructures hydrothermally synthesized at 180 °C using 10 M $KOH^{aq.}$

In Figure 4.29, the values for E_g of hydrothermally treated powders at 180 C for various times and using 5-10 M $KOH^{aq.}$ are compared within themselves and with P25 powder. Identical calculation method and representation format with Figure 4.13 was used. E_g of hydrothermally treated powders are much lower than that of P25 powder using each extrapolation method, except for the powder treated for 3 h at 10 M $KOH^{aq.}$ molarity. In addition to that, the direct E_g of the powders treated for 48 h was also slightly higher than P25 powder.

The calculated E_g values of powders treated for 3h was expected since XRD patterns indicated an incipient transformation to PTs using the TiO_2 crystals. Hence, the E_g was close to that of anatase and affected by the presence of disordered Ti-O-K structure.

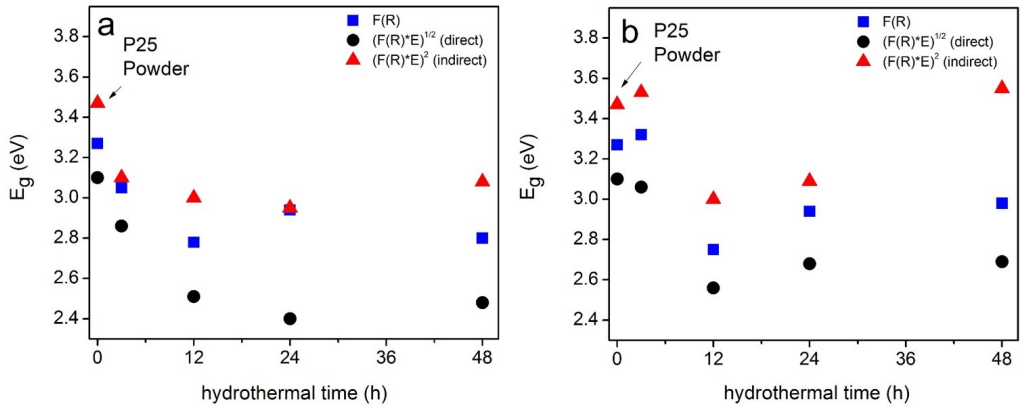


Figure 4. 29 The variation in E_g of hydrothermally treated powders at 180 °C for 3-48 h using a) 5 M b) 10 M $KOH^{aq.}$ Note that the data points for E_g of P25 powder are shown at time=0.

The smallest E_g of 2.75 eV was obtained after hydrothermal treatment at 180 ºC for 12 h using 10 M $KOH^{aq.}$. It corresponds to an absorption edge of 450 nm. This sample was composed of PTT and PHT nanowires and had considerably large surface area (101 m^2/g) with slit-shaped mesopores. Remarkably small E_g of PT nanostructures is due to their increased surface area and effectively inhibited carrier recombination. Wang et.al.[29], by using a similar procedure, reported the direct E_g of PHT nanowires produced at 180 ºC for 72 h, as 3.40 eV. Li et.al.[112] also reported it as 3.47 eV after calcination at 700 ºC. The decrease in E_g is mainly because of the reduced (nanosize) of PT. In Figure 4.30, energy versus R%, F(R), and Tauc Plots of the nanostructure hydrothermally treated using 20 M $KOH^{aq.}$ at 120 ºC for 3 h are shown.

The calculated E_g from F(R) line extrapolation is 3.25 eV, whereas indirect and direct transitions are 3.06 eV and 3.43 eV, respectively. These values are close to those obtained for P25 powder but higher than those for the nanostructures hydrothermally synthesized using 10 M $KOH^{aq.}$ solution. The XRD patterns revealed that the powders synthesized by hydrothermal treatment at 20 M $KOH^{aq.}$ condition for 3 h were composed of a mixture of PHT, PTT and unreacted TiO_2. Therefore it is obvious why E_g of the powders are close to that of unreacted P25 powder. E_g decreases with increase in surface area and PHT concentration.

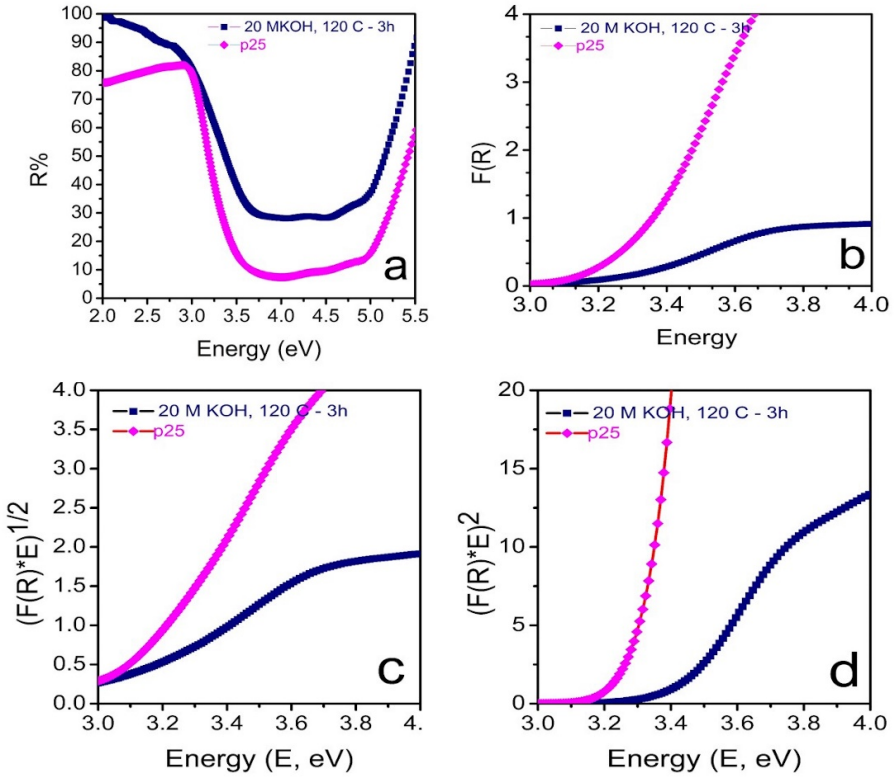


Figure 4. 30 a) R% versus energy b) K-M transform (F(R)) and Tauc plots c) indirect and d) direct band transitions of the nanostructure hydrothermally synthesized at 180 °C using 20 M $KOH^{aq.}$ for 3 h.

4.2.5.2 Effect of potassium concentration ($KOH^{aq.}$) on energy band structure

In Figure 4.31, the energy versus R%, F(R), and Tauc Plots of the nanostructures hydrothermally synthesized at 180 ºC for 24 h using 5-20 M are shown. In Figure 4.32 E_g values are compared with those of P25 powder.

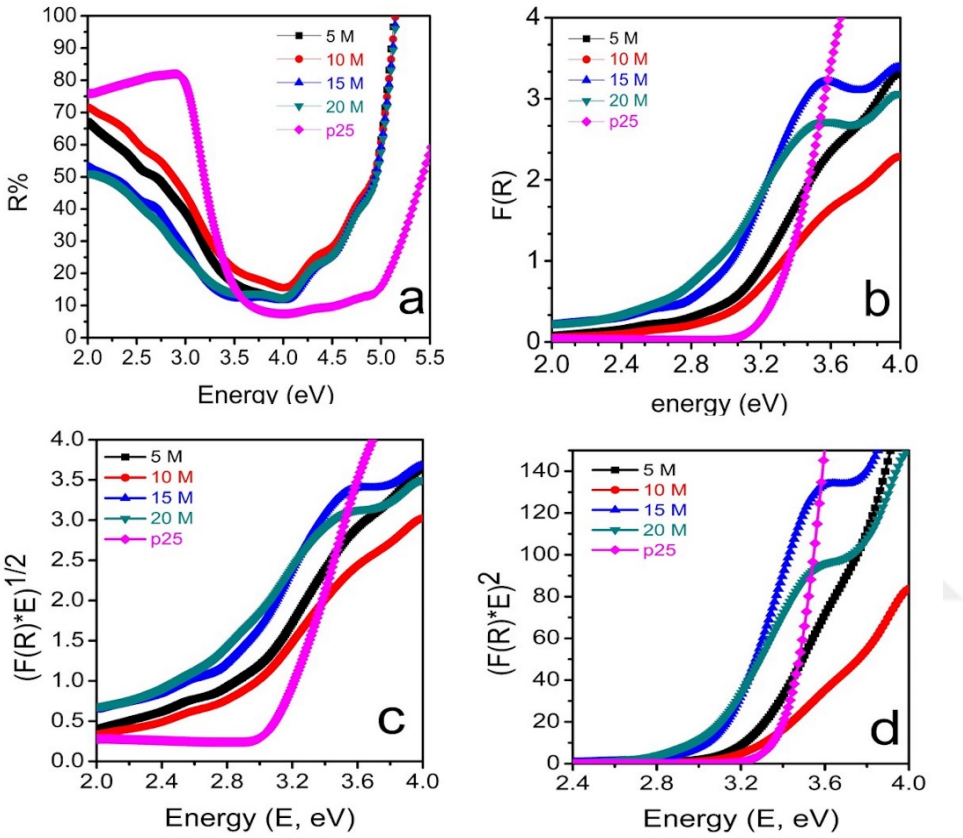


Figure 4. 31 a) R% versus energy b) K-M transform (F(R)) and Tauc plots c) indirect and d) direct band transitions of the nanostructures hydrothermally synthesized at 180 °C for 24 h using 5-20 M KOH^{aq}.

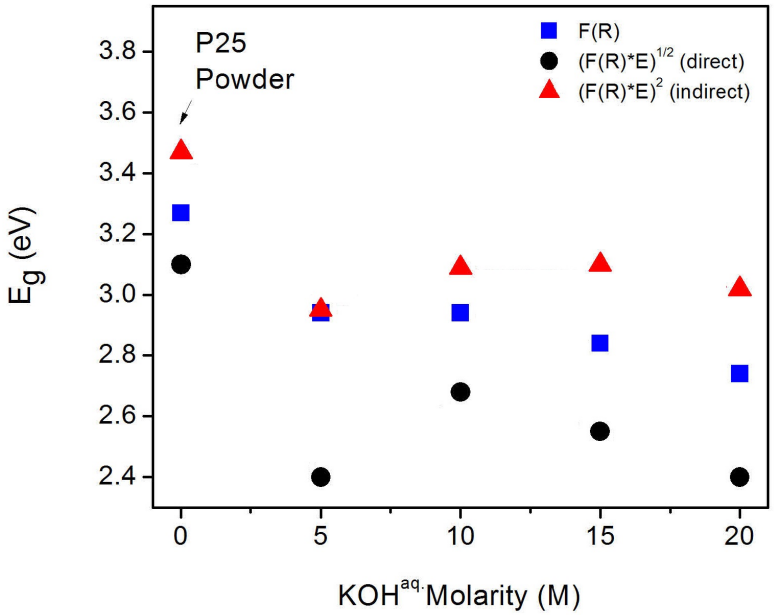


Figure 4. 32 The variation in E_g of hydrothermally treated powders at 180 °C for 24 h using a) 5 - 20 M $KOH^{aq.}$ Note that the data points for E_g of P25 powder are shown at $KOH^{aq.}$ molarity=0.

Figure 4.32 reveals that the E_g calculated by each method has a decreasing trend line with the increase in the molarity of the $KOH^{aq.}$ solution. The values were smaller than 3.0 eV indicating that these materials might be photoactivated by solar light. Nevertheless, before getting to a solid conclusion, the analyses and the experimental conditions should be repeated and revised. The reason behind the decrease in E_g may be due some leaching from inside surfaces of the autoclave chamber. But in any case, E_g decreased and this is related to the decrease in size of nanowires by splitting.

4.2.6 Photocatalytic degradation performance of hydrothermally synthesized PTs

The MB degradation performance of hydrothermally synthesized powders are shown in Figure 4.33 and compared to that of P25 powder (at $KOH^{aq.}$=0). The MB absorption The UV-Vis absorption lines of MB solutions of each sample with respect to time of test are given in Appendix along with the linear fit graphs including equations of k and goodness-of-fit (R^2) values. The data in Figure 4.33 show that the degradation rate increased with increasing $KOH^{aq.}$ from 5 to 10 M, as expected. XRD and SEM analyses showed that the powders were composed of PHT and PTT nanowires with a relatively small amount of unreacted anatase and KH.

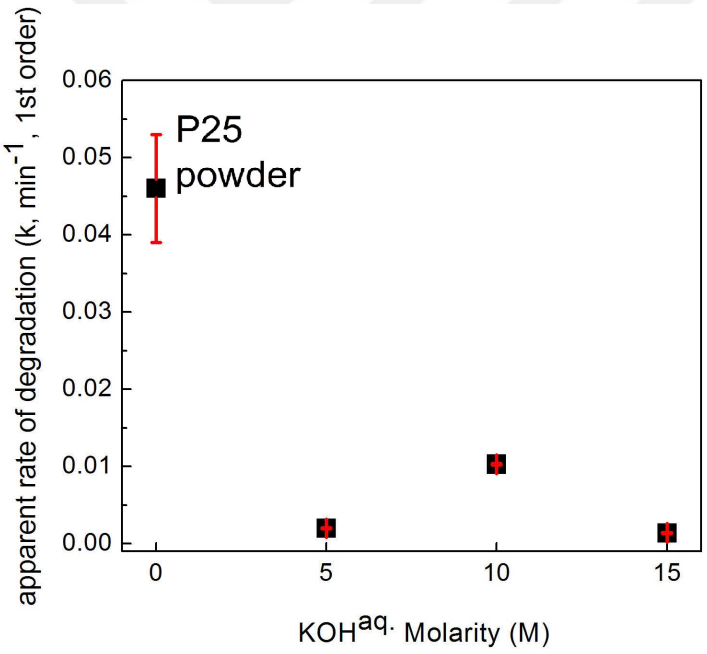


Figure 4. 33 The variation in E_g of hydrothermally synthesized powders at 180 °C for 24 h, with respect to variation of $KOH^{aq.}$ molarity. Note that the data points for E_g of P25 powder are shown at $KOH^{aq.}$ molarity=0.

KH was not responsible for the degradation reaction, however, these particles may account for the increased adsorption of MB species onto nanowire surfaces due their hydroxylated structure. The degradation rates were much smaller than that for P25, almost one-forth. For the highest $KOH^{aq.}$ molarity in which the unreacted KH was relevant, the degradation followed a nonlinear path, which is neither exponential nor constant.

CHAPTER 5

RESULTS AND DISCUSSION: POTASSIUM TITANATE NANOSTRUCTURE EMBEDDED UDMA-TEGDMA RESIN COMPOSITES

In this chapter, characterization and testing results of neat UDMA-TEGDMA (UT) resin mixtures and PT nanostructure embedded UT resin composites are presented and discussed. Both sol-gel derived and hydrothermally synthesized PTs have been embedded in three types of resin mixtures. As preliminary experiments, the results of 5-wt % of sol-gel derived PT embedment without any further post-treatment processes were discussed. Secondly, embedment of hydrothermally synthesized PTs with and without sonication and silanization treatments was discussed. The length and aspect ratio of the PTs synthesized by hydrothermal treatment were larger than that of sol-gel.

Structural characteristics were determined using XRD and SEM characterization techniques. Nano-indentation (NI) hardness, tensile strength, wear resistance, MB degradation, water sorption, and bioactivity testing results were evaluated in order to investigate whether PT embedment in UT composites is promising to be utilized in biomedical applications, primarily as restorative material in dental applications.

5.1 Neat UT resin mixtures

As shown in Table 3.3, three different monomer formulations were prepared. The CQ and DMAEMA amounts were kept constant and the UDMA-to-TEGDMA molar ratio was varied. Identical formulations were used for the preparation of PT embedded UT resin composites.

5.1.1 Wear analysis

Mair et. al.[121] emphasized two main mechanisms of wear of dental composites; abrasion and attrition. Attrition is caused by the direct contact of opposing teeth (two-body wear) whereas abrasion occurs during the sliding action of two teeth with a third body (layer of food) between them (three-body wear). In vitro wear tests such as the two-body wear testing by pin-on-disk apparatus cannot fully simulate the in vivo conditions.[122] However, the findings are useful and could give an indication of the performance of the materials in vivo conditions. Wear resistance (WR) of samples could be compared using the opposite relation with specific wear rate, see Eq. 3.9. In addition to WR, friction coefficient (μ, dimensionless) has crucial importance to prevent failure of composite surfaces. The stress transmitted to matrix-filler interface could be minimized by reducing friction coefficient.[123]

In this manner, the WR and friction coefficient of neat UT resins are compared and the effect of TEGDMA content was investigated along with the variation in surface roughness (R_a). In Table 5.1, WR, friction coefficient and the initial surface roughness of neat UT resin mixtures are listed. Three samples were used for testing. The numbers next to the data points are the ± standard deviation of the determination values.

Table 5. 1 Specific wear rate (WR), average friction coefficient (μ), and surface roughness of neat UT resin mixtures.

Resin Mixture	**WR*10^{-4} (mm^3/Nm)**	**μ**	**R_a (μm)**
UT-1	2.61 ± 0.01	0.12 ± 0.003	2.1 ± 0.04
UT-2	1.57 ± 0.27	0.13 ± 0.002	2.2 ± 0.10
UT-3	2.60 ± 0.66	0.12 ± 0.004	2.2 ± 0.11

The valid wear mechanism for WR above 10^{-6} mm^3/Nm is considered as delamination-type model and it is common for ceramics. The model assumes surface wear is governed by brittle fracture in which tensile stresses is induced on the surface microcracks due to mechanical contact and/or thermal strain.[124] In this mechanism, sample surfaces are generally rough (R_a = 1-3 μm) compared to the smooth surfaces (R_a = 0.1-0.4 μm) with 10^{-9} - 10^{-7} mm^3/N m WRs. WR and R_a values presented in Table 5.1 suggest that the acceptable mechanism in neat UT resin mixtures is delamination type wear. The lowest WR - highest wear resistance - was achieved by decreasing TEGDMA content from 50-mole % (UT-1) to 30-mole % (UT-2). Further increasing TEGDMA content up to 70-mole % did not change the average WR though the deviation from average was more significant (UT-3).

Both UDMA and TEGDMA monomers have good potential to make hydrogen bonds to produce free radicals for polymerization through crosslinking. UDMA has this ability due its flexible aliphatic core and two urethane linkages, but it is rigid and less mobile in nature.[125,126] TEGDMA monomer does not possess such groups. It is much smaller and mobile thus able to make the tightest network due its high crosslinking ability. Unfortunately, the decreased chain mobility in UT resins avoids complete polymerization and causes heterogeneities in the micro-gel network.[125] Therefore, crosslinking efficiency is mainly controlled by limitations on diffusion that causes heterogeneity between micro-gel clusters rather than the amount of unreacted monomers in the whole polymerizing network.[68]

Fracture on a material surface propagates through the defect points. Delamination type wear is empowered by the presence of these weakness regions. Therefore, the highest wear resistance of UT-2 composition is governed by the structural homogeneity that is offered by UDMA rather than the mobile TEGDMA monomers offering higher double bond conversion. The remarkable deviation of wear rate between UT-2 and UT-3, are the proof of the heterogeneity in the polymerized network.

5.1.2 Hardness test

Elastic modulus (E) and hardness (H) of a material play important role especially on the performance of dental restoratives express the resistance of occlusal surfaces against penetration.[127]The hardness testing of neat UT resins revealed the effects of PT embedment on hardness. Measured nano-indentation (NI) and Vickers micro-hardness (HV0.3 - 300 g, 20 s) of UT resin mixtures are given in Table 5.2.

Table 5. 2 Hardness (HV 0.3, NI) and NI-E of neat UT resin mixtures.

Sample	**HV 0.3**	**NI-H (MPa)**	**NI-E (GPa)**
UT-1	28 ± 2	1621 ± 522	51 ± 32
UT-2	20 ± 2	1322 ± 702	42 ± 18
UT-3	17 ± 4	1715 ± 713	123 ± 66

Data presented in Table 5.2 indicate that the hardness increases as the proportion of UDMA in the UT resin mixtures increases. The rigidity of UDMA arises from the strong urethane linkages in its microstructure and its moderate viscosity between TEGDMA and BisGMA is a simple indication of this rigidity.

NI hardness decreased from 1715 ± 713 to 1621 ± 522 MPa when U and T were at equivalent molar amount. The lowest hardness of 1322 ± 702 MPa was achieved when UDMA exceeded TEGDMA. This was due the effects of heterogeneity of micro-gel clusters as similarly mentioned for the change in wear resistance. Wear rate and hardness results of UT neat resin mixtures showed similar decreasing tendency as the UDMA amount is increased. It was an expected relation since wear and hardness both resemble the resistance of composite surfaces against mechanical forces.[128]

Vickers hardness showed a similar behavior, but the deviation from average was smaller. This was most probably because the Vickers indenter size is much bigger than the nano-indenter. Hence it deforms a bigger area of resin. For composites, it is better to use Vickers micro-indentation. El-Safty et al.[127] reported that nano-indentation techniques are useful for characterization of homogeneous surfaces but inappropriate for biphasic materials such as dental composites. E showed an identical behavior since it is directly related to the total deformation when external forces are applied on the polymer specimen.

Especially for the posterior dental fillings where high masticatory forces are applied, the elastic modulus must strictly be adequate.[129] The elastic modulus of natural tooth enamel was reported as 70-100 GPa, therefore UT-1 and UT-2 resin mixtures offer good potential to be applicable as filling materials when reinforced by stiff PT nanowires/whiskers. UT-3 on the other hand, has already closer stiffness to enamel, PT reinforcement at high levels would most probably increase the viscosity and decrease polymerization efficiency due insufficient UDMA molecules to reach and react through cross-linking.

5.1.3 Tensile test

The typical stress-strain curves of neat UT resins (one for each) are shown in Figure 5.1. Three samples were tested for each resin mixture. The calculated yield stress (σ_y, MPa), ultimate tensile strength (σ_{UTS}, MPa) and E (GPa) are presented in Table 5.3. It is important to mention that the yield stress is calculated by using the 0.2 % offset method and E is calculated by taking the slope of the linear region between 0.05 % and 2.5 % strain using the Origin Pro8 software.

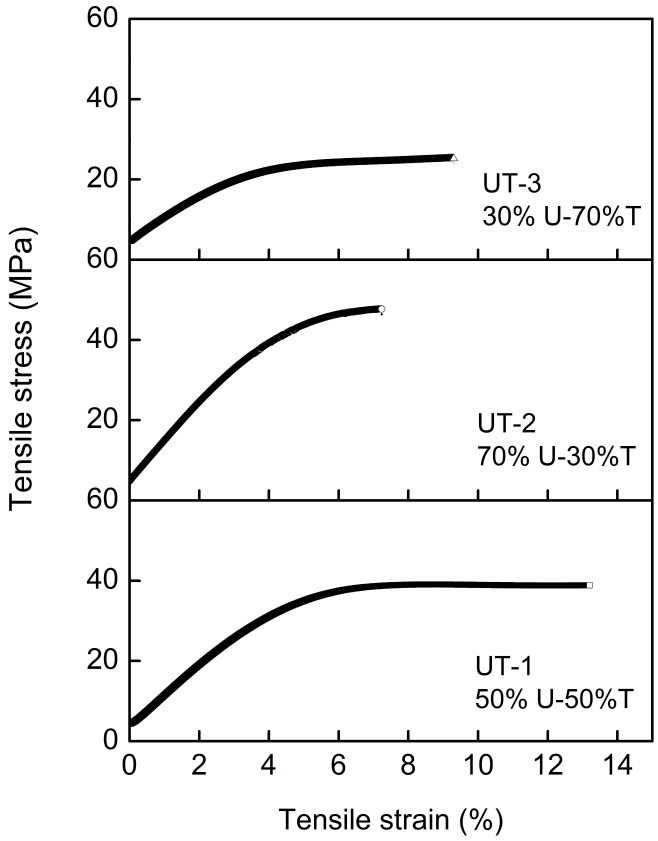


Figure 5. 1 Typical stress-strain curves of neat UT resin mixtures.

Table 5. 3 Ultimate tensile stress (σ_{UTS}), elastic modulus (E) and yield stress (σ_y) of UT neat resin mixtures.

Resin Mixture	**σ_{UTS} (MPa)**	**E (GPa)**	**σ_y (MPa) (0.2 % Offset)**
UT-1	40.42 ± 1.74	0.72 ± 0.04	32.85 ± 0.66
UT-2	43.88 ± 3.88	0.84 ± 0.08	35.58 ± 2.01
UT-3	36.00 ± 6.00	0.64 ± 0.16	27.01 ± 6.20

Data presented in Table 5.3 indicate that the neat resins fail in a brittle manner. They show conchoidal (catastrophic) fracture behavior. After yield point, they slightly deform plastically and mostly fail at σ_{UTS}. The fracture surfaces were smooth and rectangular indicating a brittle failure. The highest σ_y and σ_{UTS}, and E were obtained by UT-2 resin, in which the strength is directly related to its relatively high UDMA content corresponding to a rigid molecular structure.

An optimized value of E in a composite microstructure is an important factor to prevent filling dislodgement due to microleakage. Dental fillings with low modulus deform more and fail catastrophically in a brittle manner.[130] The most appropriate E could be comparable to that of dentin.[131] According to the composition triangle developed by Emami and Söderholm[132], E of UT resin mixtures is expected to be between 2.4 and 3.1 GPa. However, the modulus values given in Table 5.3 are lower. The lower E than expected can be attributed to the effects of testing conditions and/or sample size differences. But it is for sure that as the UDMA is increased, E is increased in neat UT resin mixtures. The increasing effect of UDMA on E is attributed to its molecular structure; see Figure 2.5, to the urethane linkages providing rigidity on polymerized network. On the contrary, TEGDMA, as the diluent monomer with lower viscosity is a small molecule that provides flexibility upon cross-linking. Thus, TEGDMA increase in composition has an opposite effect on E due to formation of heterogeneities by trapping unreacted monomers inside clusters.

5.1.4 Water sorption and solubility

Water sorption and solubility of neat UT resin mixtures are shown as percentage and as weight/volume ($\mu g/mm^3$) in Table 5.4. According to ISO 4049-2009 standard for dental restoratives, water sorption of a dental resin must be lower than 40 $\mu g/mm^3$ and solubility lower than 7.5 $\mu g/mm^3$ after soaking in water for 7 days.[133,134]

Table 5. 4 Water sorption and solubility of UT resin mixtures.

Resin Mixture	**Water Sorption %**	**Water Sorption (μg/mm^3)**	**Solubility %**	**Solubility (μg/mm^3)**
UT-1	1.92 ± 0.65	20.4 ± 6.8	0.71 ± 0.30	4.13 ± 1.80
UT-2	1.07 ± 0.10	11.4 ± 1.6	0.07 ± 0.05	0.78 ± 0.55
UT-3	1.58 ± 0.24	18.2 ± 2.8	1.30 ± 0.88	9.20 ± 5.00

For neat UT resin mixtures, water sorption and solubility values given in Table 5.4 are acceptable except for the solubility of UT-3 mixture that exceeds the limits designated by ISO. TEGDMA has been reported as an hydrophilic monomer due to the presence of hydrophilic ether linkages.[135] Sideridou et. al.[125] stated water sorption of TEGDMA and UDMA as 69.21 ± 0.32 and 29.46 ± 0.16 μg/mm^3, respectively. Their study revealed that UDMA has a significantly lower water sorption than TEGDMA. Additionally, Venz and Dickens[136] have shown that the hydrophilicity of monomers to be in the following order: TEGDMA>BisGMA>UDMA. Regarding the current UT resin mixtures in which the TEGDMA content follows the order as UT-3>UT-1>UT-2, the findings are in accordance with the expected results.

TEGDMA has been reported as the smallest hence the fastest molecule that can be eluted from dental resins. The results are consistent to the nature of TEGDMA structure regarding its molecular size. However, the solubility of UDMA monomer was much higher than TEGDMA. Sideridou et. al.[125] stated solubility of TEGDMA and UDMA as 2.41 ± 0.14 and 6.62 ± 0.12 μg/mm^3, respectively. UT-2 mixture had the smallest water solubility despite its highest UDMA content. The findings reveal that the structural homogeneity rather than the molecular constituents of the monomers majorly pronounces the solubility of a resin formulation.

5.2 Sol-gel derived PT embedded UT resin composites

Sol-gel derived PTs embedded UT resin composites were prepared following the procedure described in Chapter 3.4. The compositions of the composites are given in in Table 3.4.

5.2.1 XRD analysis

It is noteworthy to mention that XRD analysis performed on bulk composites must be further investigated in detail to get a reliable conclusion. The following results are the preliminary results obtained to determine the orientation of PTs in a polymer matrix. Figure 5.2 shows the XRD patterns of 5-wt % of sol-gel derived PT embedded UT composites.

Almost all composite samples produced by using sol-gel derived PTs resulted in similar XRD patterns. Some peaks belonging to PTs were detected in the composites either because of the orientation difference of the PTs on the surface or their deformation upon embedment. The wide hump in the two-theta (2θ) range of 15-25° is for the amorphous resin structure in all cases. Patterns indicated anatase, KCl and PT phases in the embedded powders. The blue arrows on the patterns were to emphasize small peaks around 10° which indicate the (200) plane of PTs on their growth direction (11.56° for PHT, 10.08° for PTT). It is obvious that the (200) peak of PTs were slightly present in UT-1 and UT-2 composites but completely vanished in UT-3 composite. As mentioned above, the orientation difference is the main factor and further analysis is needed to make a conclusion. However, the disappearance of most peaks in the XRD pattern of UT-3-SG-5 designates the effect of orientation difference of PTs on the bulk surface. Most probably, the heavier particles settled on the bottom of the mold as the viscosity of UT-3 was low during mixing of UDMA monomer with relatively higher amount of TEGDMA. Hence, the peaks of embedded particles are vanished in the XRD pattern.

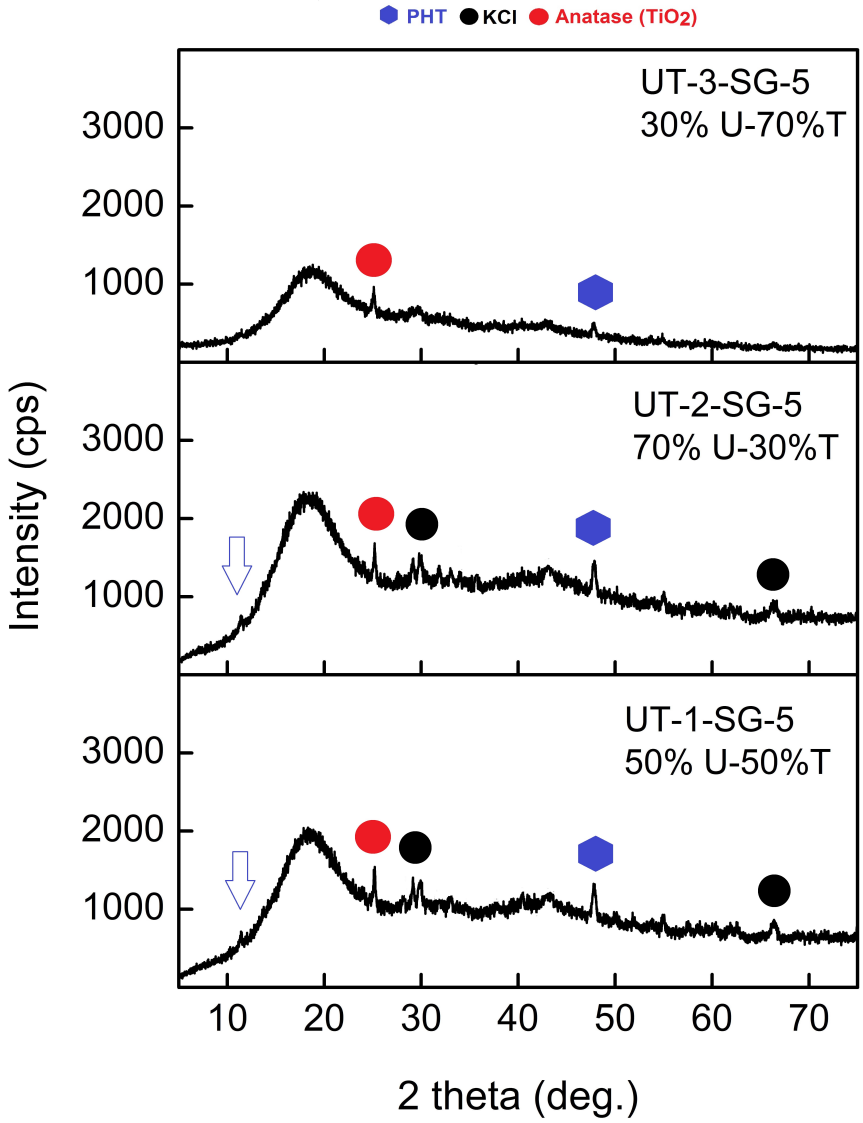


Figure 5. 2 XRD patterns of the 5-wt % of sol-gel derived PT embedded UT resin mixtures.

5.2.2 Wear analysis

In Figure 5.3, WR, μ and R_a of sol-gel derived PT embedded UT resin composites are compared to those of neat UT resin mixtures. Figure 5.3a-b shows that composites had significantly lower WR but higher μ than UT resin mixtures. The most remarkable decrease in WR was provided by the UT-1 composition. The deviation and increase in μ compared to neat resins is a direct indication of stress that is transmitted to matrix-filler interface. R_a, on the other hand, increased with larger deviation from average. The increase in R_a can be attributed to the presence of long and rigid sol-gel derived PTs acting as continuous fibers or fiber agglomerates inside the matrix.

Results indicate that even 5-wt% of PT reinforcement can enhance wear resistance of UT dental resins. In addition to that, for long, high aspect ratio whiskers embedment, the wear mechanism is still ceramic-like delamination type wear since the values are in 10^{-4}-10^{-3} mm^3/Nm ranges. The better performance of UT-1 composition in which UDMA and TEGDMA molar fractions are equivalent, can be attributed to the optimized viscosity when PTs were introduced to the system. However, for further reinforcement levels, the mobility of TEGDMA monomers at this fraction may not be enough to prevent structural heterogeneity formed due to incomplete interaction between UDMA and TEGDMA monomers.

5.2.3 Hardness

In Figure 5.4, the NI-H and E of 5-wt % sol-gel derived PT embedded UT composites are shown. Results indicate that E increased with the addition of PTs into the UT resins, except for UT-3 composition. The decrease in E of UT-3 with PT addition is strongly related to the dispersion of PTs in the matrix where the formation of structural heterogeneity during cross-linking is promoted.

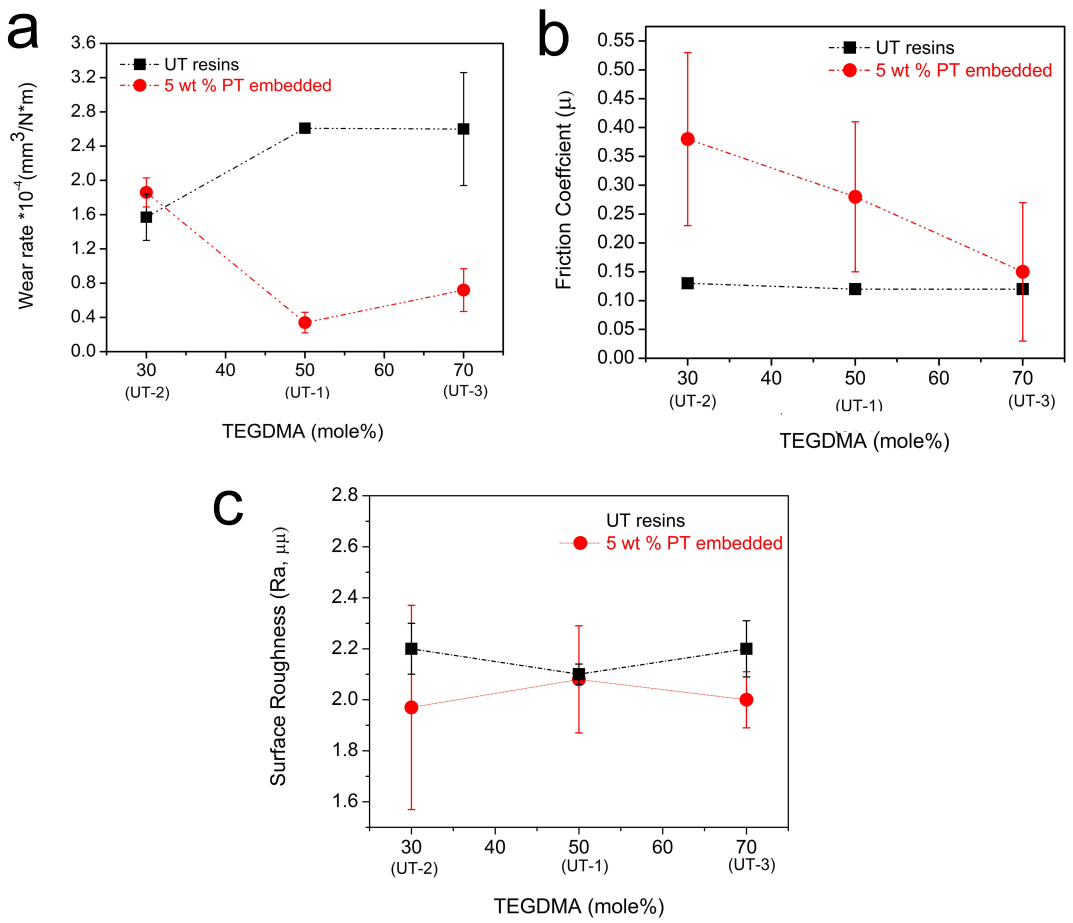


Figure 5. 3 a) WR, b) friction coefficient (μ) and c) surface roughness (R_a) of 5-wt% sol-gel derived PT embedded UT composites compared to neat UT resin mixtures. (UT- (1-3)-SG-5)

When PTs were introduced, TEGDMA could not wet that small amount of UDMA efficiently. The increase in E was most evident for UT-2 composition where higher content of UDMA in UT-2 provided a more rigid structure than UT-1. As the hardness is resistance to surface indentation, it is expected to decrease by the presence of weakness points and/or heterogeneity on the surface microstructure. Opposite to E, H decreased when PTs were added into UT-1 and UT-2. The results may be conflicting due inconsistency of the measurement method.

The standard deviations from average would also reflect this inconsistency mentioned also for neat resins in Section 5.1.2. For, this reason, further hardness measurements were made using Vickers micro-hardness technique.

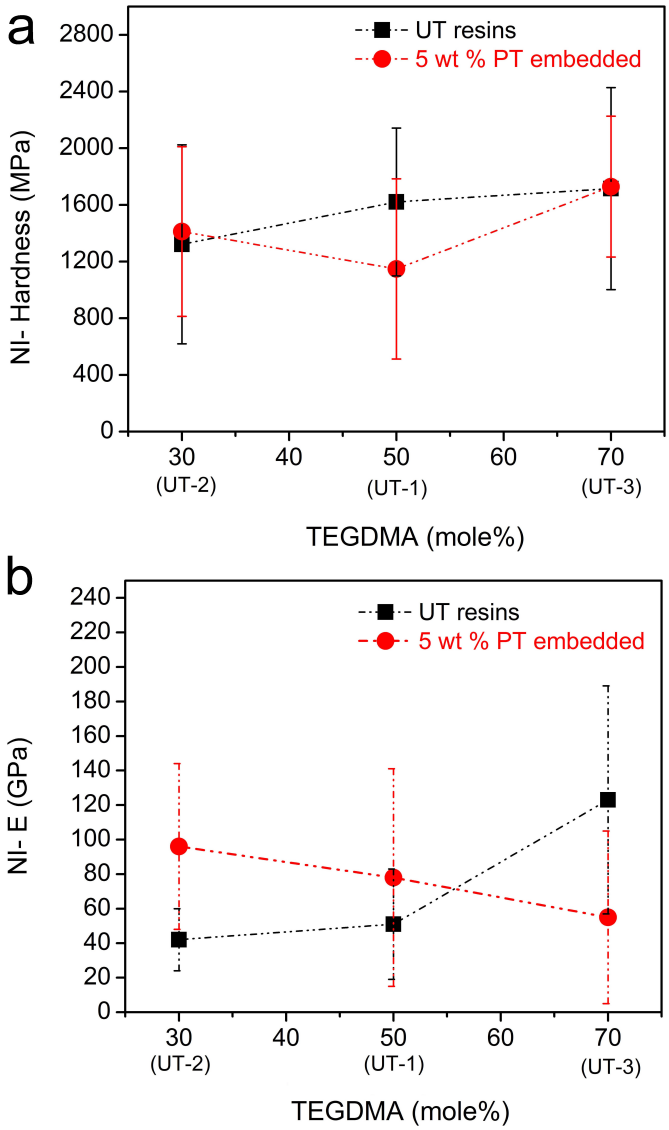


Figure 5. 4 a) Nano-indentation (NI) hardness (H) and b) elastic modulus (E) of 5-wt % sol-gel derived PT embedded UT resins.

5.2.4 Conclusive remarks of preliminary experiments on sol-gel derived PT embedded UT resin composites

Wear resistance, E and H increased when 5 wt% sol-gel derived PT was embedded into UT resins. Since NI technique could not reveal a direct and consistent relationship between H/E and WR, it is not possible to make a safe conclusion on wear-hardness relation. Friedich[137] described a inverse relationship between mechanical properties and wear resistance. Similarly, Nagarajan[138] and Tamura et. al.[128] reported that harder composites suffer higher wear than softer composites. But Ramalho and Antunes[139] suggested the H as a function of wear resistance. Faria et al [140] stated that material wear decreases as H increases. Results showed that E and wear resistance of UT-1 increased, whereas H decreased by PT addition. For UT-2 composition, E increased but wear resistance decreased where H remained unchanged. For UT-3, H unchanged but E decreased, whereas wear resistance increased.

Due to the above-mentioned reasons, Vickers micro-indentation technique was employed for measuring the hardness of hydrothermally synthesized PT embedded UT resin composites. Moreover, it is important to mention that for sol-gel derived PTs; separation of TiO_2 impurities from the nanostructures was not managed. Hence, the spherical TiO_2 particles most probably in agglomerated state acted as weakness points at the matrix-filler interface for all composites. It was more evident in UT-3 resin mixture where complete polymerization was inhibited.

5.3 Hydrothermally synthesized PT embedded UT resin composites

It has been recognized that identical dispersion problems with using sol-gel derived PTs due to the phase impurities (TiO_2 and KOH) were present in the composites prepared by using hydrothermally synthesized PTs. Sol-gel experiments also showed that embedment of PTs at higher than 5-wt % might be possible without disturbing polymerization (crosslinking) reactions. This section reveals the characterization results of i) highly loaded >5-50 wt% UT resin mixtures with as-prepared PT powders and ii) 5 wt% loaded UT resin mixtures with PTs after sonication and silanization.

5.3.1 XRD analysis

As a typical study, the XRD patterns of 5-wt % PT embedded UT composites are given in Figure 5.5. The effects of sonication and silanization treatments have been investigated. There were three distinct XRD peaks in the patterns of 5-wt% PT embedded UT-1 composite at 2θ of 24.02, 29.05, and 30.01°. The first two were not intense, but each peak could be ascribed to PHT. However, the (200) peak - the most intense peak - was not present in the patterns. It is interesting that silanization of the PTs caused the XRD peaks of PTs to disappear.

Since PTs grow in b-axis by extending (200) planes, the disappearance of the peak may be an indication of cropped whiskers due to shear produced upon mixing in UT monomers. But, the orientation of whiskers/nanowires may be such that the diffraction of planes annihilates each other. Since dispersion in nanosize silica combined with silanization of whisker surfaces showed a similar disappearance effect, it is most probably due to some attraction, taking place at the whisker-resin interface. However, further TEM analysis is needed to support this thought.

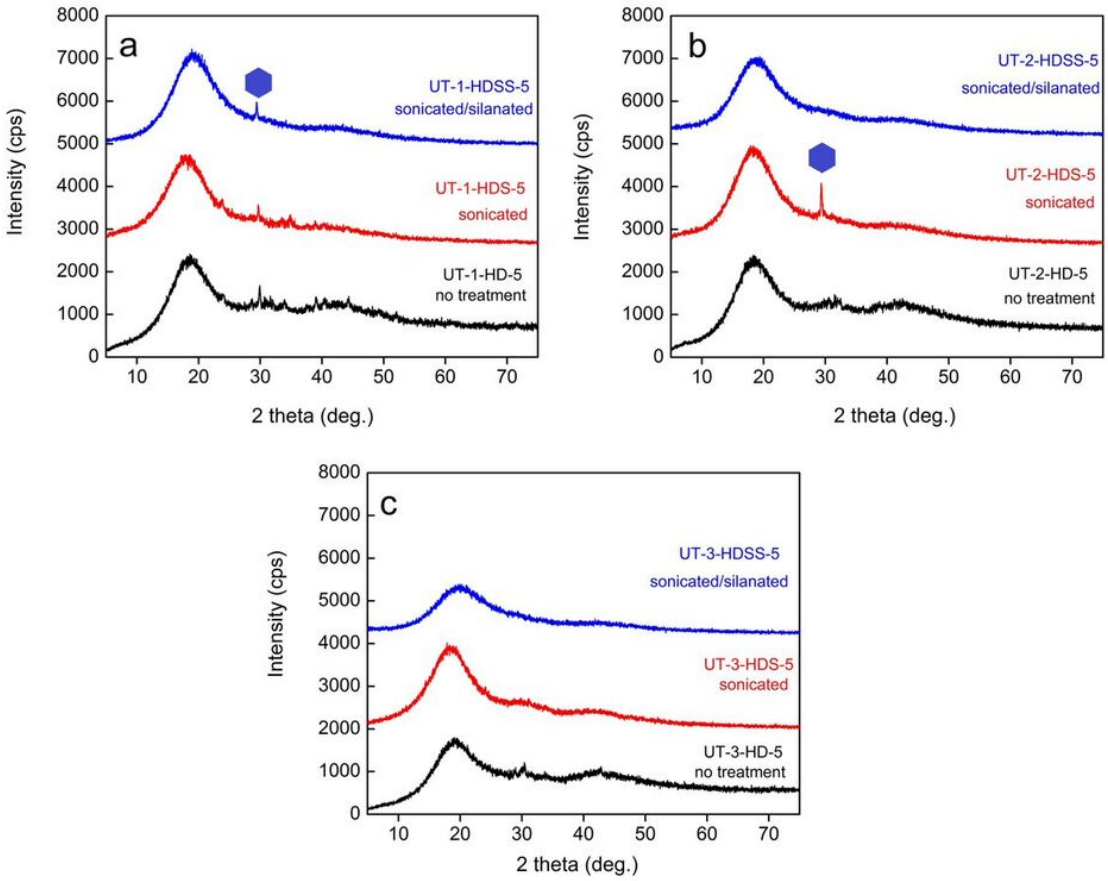


Figure 5. 5 XRD patterns of 5-wt % hydrothermally synthesized PT embedded UT composites before and after sonication and/or silanization.

5.3.2 Wear analysis

5.3.2.1 As- prepared PTs

In Figure 5.6, the wear rate, friction coefficient, and surface roughness of hydrothermally synthesized PT embedded resin composites are shown with respect to amount of PT embedment. Results reveal that wear resistance of hydrothermally synthesized PT embedded resin composites increased when compared with that of the neat UT resin mixtures but not to that of 5 wt% sol-gel derived PT embedded resin composites.

Results indicate that WR was higher compared to 5-wt % embedded composites prepared using sol-gel derived PTs. On the other hand, as the PT % increased, WR increased. This is attributed to two reasons which are i) heterogeneous dispersion of nanosize PTs inside the matrix and their severe agglomeration, and ii) depth of cure problems causing inhomogeneity in the structure during inefficient polymerization. For this reason, sonication treatment was performed to disperse severely agglomerated PTs from each other and separate spherical and relatively heavier TiO_2 impurities. The dispersion inhomogeneity was remarkable when R_a was compared. As the PT embedment increased, the deviation in R_a from average was larger.

5.3.2.2 Post-treated PTs (sonication, silanization)

In Figure 5.7, the WR, μ and R_a of hydrothermally synthesized PT embedded resin composites are shown with respect to the UT content and silanization treatment. Using macro-sized particles to enhance mechanical properties of the dental resins was the initial approach in dental composite research. The release of large fillers during mastication wear was the main problem for posterior restorations. Recent studies revealed the advantageous use of nano-sized particles.[141] It has been shown that superior surface area of nanostructures decreases the interparticle spacing.[142] Decreased particle spacing enhances homogeneity in the composite matrix.

Even natural tooth has shown the same advantageous response against wear. TEM analysis of enamel revealed that HAp crystals dispersed in organic phase of enamel fracture during wear. These fractured parts are pulled out but not easily released to the sliding interface because of the binding ability of the organic phase.[143] Likewise, if reinforcing fillers are not detached from the resin matrix easily they cannot stick to the antagonist and hence promote excess wear. [122] For this reason, the mechanical interlock at the filler-matrix interface is of great importance.

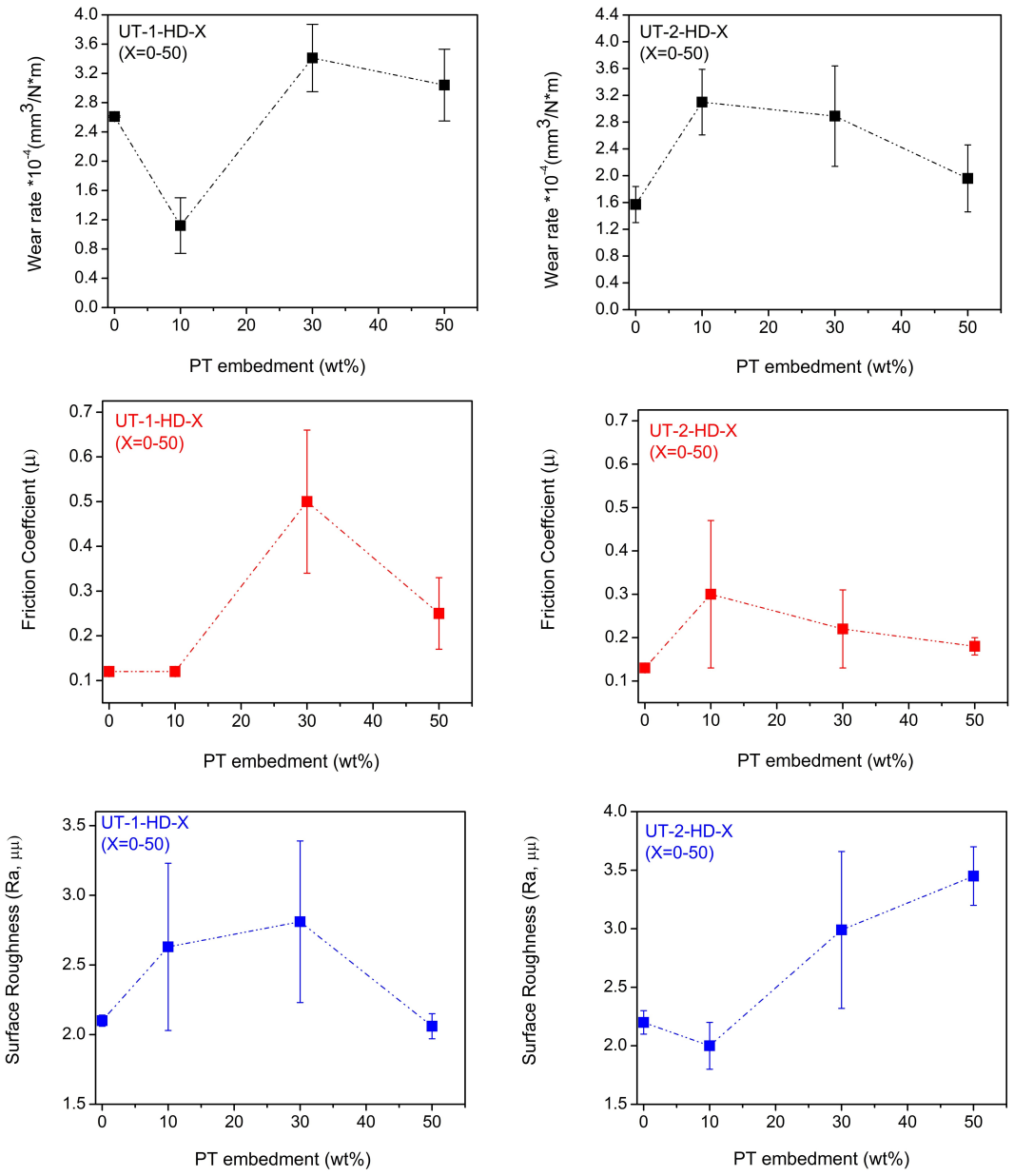


Figure 5. 6 Specific WR, friction coefficient (μ) and surface roughness (R_a) of 10-50-wt% hydrothermally synthesized PT embedded UT composites compared to neat UT resin mixtures. (UT- (1-2)-HD-(10-50))

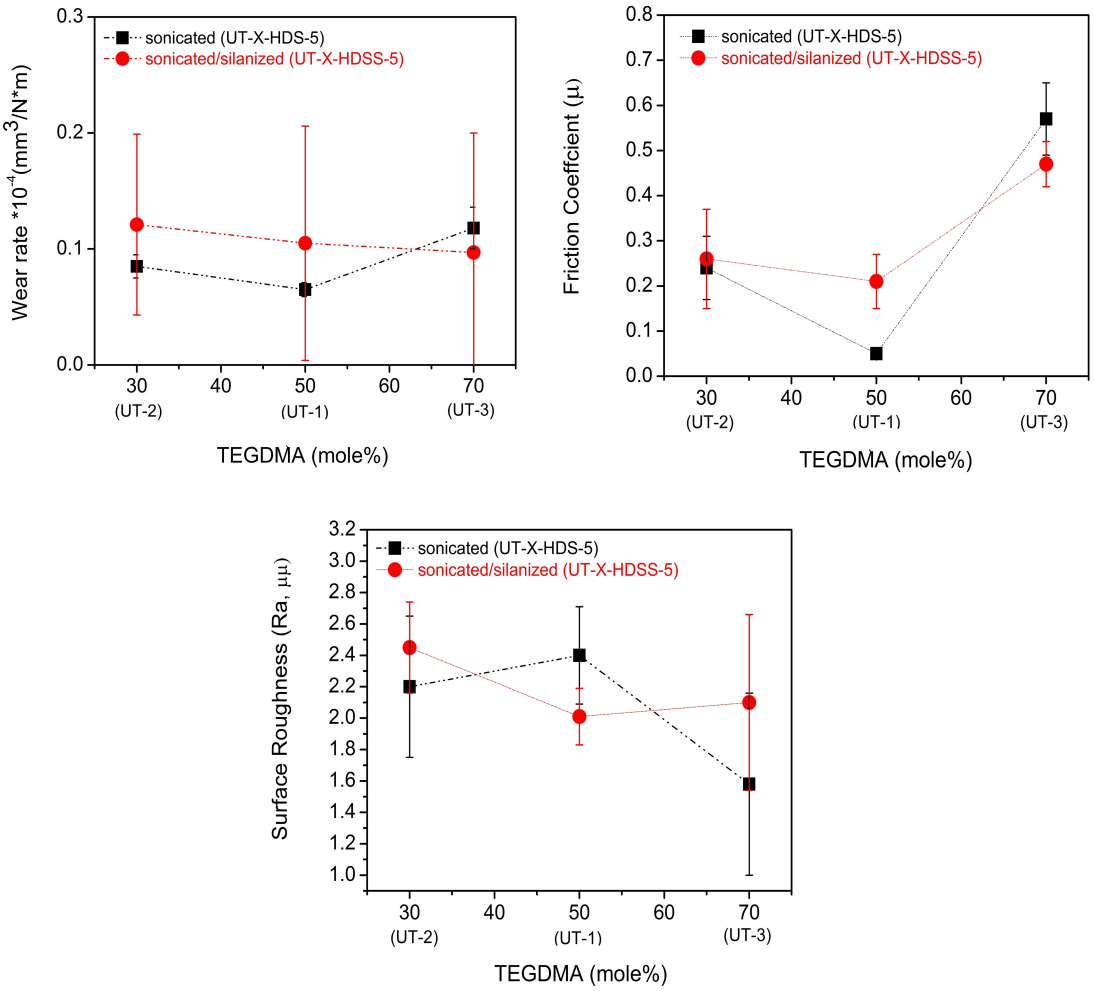


Figure 5. 7 Specific WR, friction coefficient (μ) and surface roughness (R_a) of 5-wt% hydrothermally synthesized PT embedded UT composites after sonication and silanization (UT-(1-3)-HDS/HDSS-5)

Manhart et. al.[144] tested several commercial composites and revealed that resin composites reinforced with large size rod shaped fillers caused filler plucking from surface under occlusal attrition. Though, composites reinforced with porous SiO_2 provided good interlock with the fillers wet by resin with aid of pores in between. They concluded that the amount and the size of the largest size fillers dominate the effect of mean particle size of fillers on wear.[144]

Consequently, the pluck out of large and/or agglomerated fillers during wear is much easier because of their less interaction area with polymer matrix per unit volume. The interface strength is not sufficient to keep the fillers bonded to the matrix as the organic matrix keeping HAp rods inside during wear.[145]

Therefore, the mixing process is critical as well as the chemical and structural properties of the monomer mixture. The mixing was carried on a hot plate at room temperature and the procedure followed was identical for each composite formulation. As mentioned before, high aspect ratio particles provide potential benefits to the resin matrix by bridging matrix micro cracks and prevent crack propagation as well as dislodgement from the matrix during wear process. [146,147]

UT neat resins indicated wear rates above $1.5*10^{-4}$ mm^3/Nm, whereas the wear rate decreased remarkably by addition of 5-wt% as-prepared % PT powders into the resins ($0.065*10^{-4}$ mm^3/Nm). Sonication and silanization treatment enhanced the wear resistance remarkably. It can be foreseen that homogeneously dispersed PT reinforced resins can resemble natural tooth microstructure by mimicking HAp mineral rods in enamel.[147] Enhanced wear resistance is attributed to the porous structure‘s ability to anchor the filler particle in the matrix, resisting the plucking out of particles commonly observed in composite wear.[148] In other words, high WR is related to the larger filler particles in the composite materials.[149]

5.3.3 Hardness test

Hardness of PT reinforced resins is shown in Table 5.5. When compared to that neat resins, results indicate that micro-indentation hardness slightly decreased by the addition of PTs. Increasing PT reinforcement to 30 wt% decreased hardness of UT-1 and UT-2 resins further, however, 50 wt-% reinforcement enhanced hardness of UT-1 remarkably.

Table 5. 5 Vickers hardness (HV 0.3) of 10-50-wt % hydrothermally synthesized PT embedded UT composites.

Composite	**(HV0.3)**
UT-1-HD-10	23 ± 4
UT-2-HD-10	19 ± 4
UT-1-HD-30	18 ± 4
UT-2-HD-30	26 ± 11
UT-1-HD-50	32 ± 1
UT-2-HD-50	24 ± 4

The enhancement in H can be attributed to the decreased interparticle spacing in the polymeric matrix. But, the in homogeneities in the structure increased. The viscosity upon curing increased and created more strain during polymerization at thickness higher than 3 mm. Therefore, enhancement of mechanical properties can be provided by silanizing 5-wt % reinforced composites first by performing sonication treatment and then silanization. The enhancement was very remarkable in wear resistance. The hardness of the composites prepared by PTs after sonication and silanization treatment are shown in Table 5.6.

Table 5. 6 Vickers hardness of 5-wt % hydrothermally synthesized PT embedded UT composites after sonication and silanization.

Composite	**(HV0.3)**
UT-1-HDS-5	14 ± 1
UT-2-HDS-5	15 ± 1
UT-3-HDS-5	17 ± 10
UT-1-HDSS-5	22 ± 11
UT-2-HDSS-5	17 ± 8
UT-3-HDSS-5	-

Results showed that H was not enhanced by PT treatment. It can be concluded that the homogeneous dispersion of agglomerates – tough they are the weak points – dominate the effect of structural homogeneity in terms of hardness.

5.3.4 Tensile test

The typical stress-strain curves of neat and PT reinforced UT resins are shown in Figure 5.8. Figure 5.8 shows that both σ_{UTS} and E decreased with 5-wt % PT reinforcement. The calculated values of σ_{UTS}, E and σ_y are given in Table 5.7.

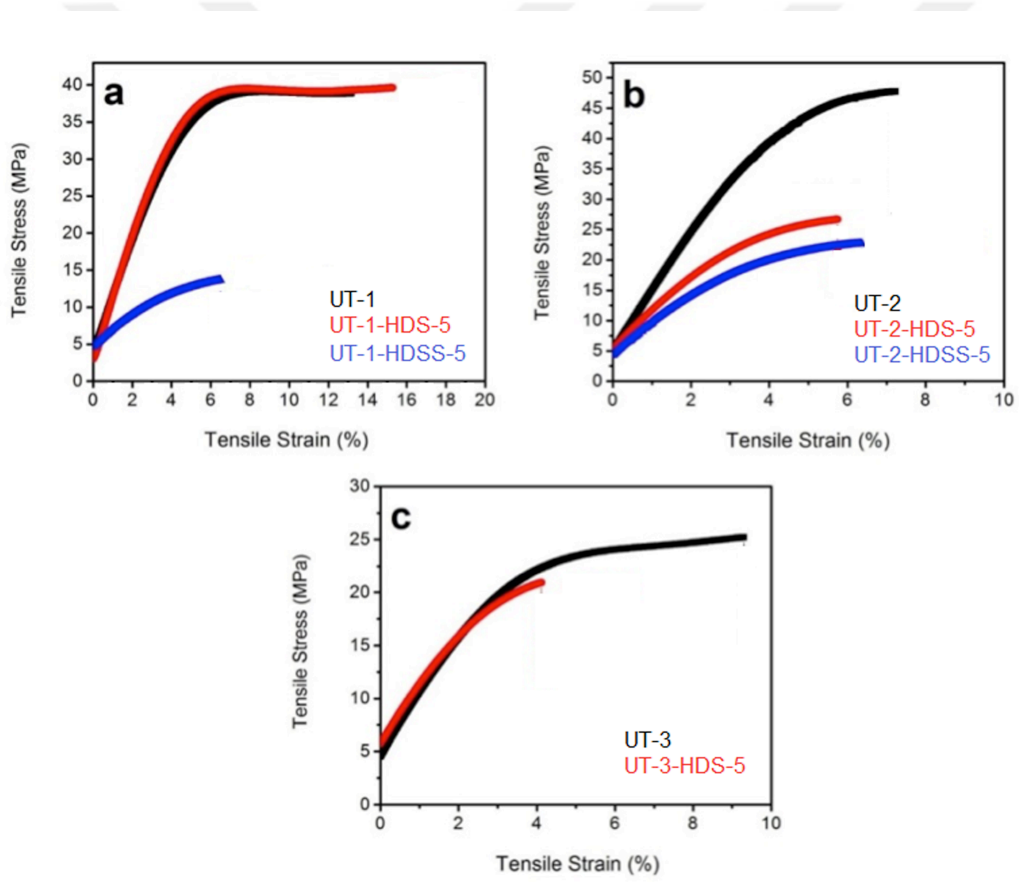


Figure 5. 8 Typical stress-strain curves of neat and 5-wt % hydrothermally synthesized PT embedded UT resin composites: a) UT-1, b) UT-2 and c) UT-3 after sonication and silanization.

It has to be noted that the dog-bone shaped sample of UT-3 embedded by 5-wt % silanized PT (UT-3-HDSS-5) composite was very soft that it could not preserve its shape upon testing. The results show that mechanical performance of the PT embedded composites was lower with/without silanization treatment when tested under tensile forces. Only 5-wt% PT embedded UT-1 composite had slightly higher performance.

Table 5. 7 Tensile test results of 5-wt % hydrothermally synthesized PT embedded UT resin composites after sonication and silanization.

Composite	**σ_{UTS} (MPa)**	**E (GPa)**	**σ_y (MPa) (0.2 % Offset)**
UT-1-HDS-5	42.5 ± 0.3	0.9 ± 0.1	39.7 ± 1.2
UT-2-HDS-5	25.6 ± 1.8	0.6 ± 0.1	23.6 ± 2.1
UT-3-HDS-5	26.4 ± 7.7	0.6 ± 0.2	24.7 ± 7.1
UT-1-HDSS-5	13.0 ± 0.5	0.2 ± 0.8	12.1 ± 0.6
UT-2-HDSS-5	19.9 ± 1.9	0.5 ± 0.2	17.1 ± 1.6

Among UT resin mixtures, UT-2 had better properties due its UDMA content. By the introduction of PTs into the matrix, UT-1 had more advantageous properties including the ease of handling. The results indicate that high viscosity of UDMA monomer prevented efficient mechanical interlocking at the monomer-PT interfaces. Moreover, it can be stated that the viscosity increased with the addition of nanosize PTs and this caused a significant level of heterogeneity in the cured microstructure creating potential defect sites under tensile testing. Similar findings were reported by Kardos.[150] They stated that heterogeneity in the resin matrix due agglomeration and/or random alignment of the discontinuous fibers decreased the σ_{UTS} of the composite.

Then the reason behind slightly better performance of UT-1 formulation when PTs embedded is better handling due to relatively lower viscosity offered by TEGDMA. Then, it can be stated that better monomer-PT interaction provided by lower viscosity of the monomer mixture resulted in higher polymerization efficiency and higher E. It is also evident that PT morphology and dispersion is crucial to influence strength and modulus.

5.3.5 SEM analysis of fracture surfaces

After the tensile test was applied, the fracture surfaces of neat polymers and composites were analyzed by SEM in order to obtain information on the cause and mechanism of the tensile failure in detail. One of three representative samples tested was chosen for each composition. In Figure 5.9, the general view of fracture surfaces of neat and composite samples is shown. Crack pinning, deflection or micro-crack formation are reported toughening mechanisms for nanosize particle reinforced composites.[151,152]

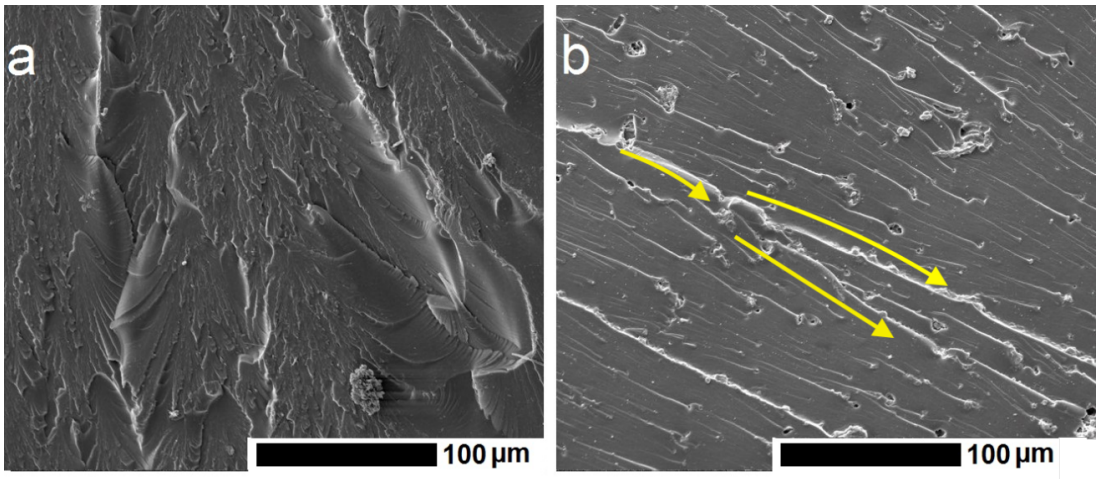


Figure 5. 9 Typical fracture surfaces of a) neat, b) 5-wt % hydrothermally synthesized PT embedded UT resin.

The large smooth fracture areas in Figure 5.9 indicate that either neat or PT embedded UT resins fail in a brittle manner. The morphology of crack surfaces supports the tensile test results. The marked areas in the composite surfaces reveal a possible crack path deflection occurred in composite surfaces while propagating during the tensile test.

The origin of failure in composite resin matrices was shown to originate from agglomeration of particles causing problems upon mixing with viscous monomers or nonuniform distribution of fillers inside the matrix or even particles themselves if larger than 100 μm.[153] These factors mainly related to the strength of mechanical interlock at the filler-matrix interface. Further SEM analysis has been carried out on fracture surfaces of composites as shown in Figure 5.10.

On the contrary to neat resins, the SEM surfaces of 5 wt.% PT embedded (Figure 5.10(b-e-h)) and silanized-PT (Figure 5.10(c-f-i)) reinforced resins revealed rougher surfaces, see Figure 5.7 for initial surface roughness. The micrometer-sized agglomerates were evident on the direction of crack propagation. In addition, the images clarify that PTs were dispersed heterogeneously in the resin matrices with/without silanization treatment. The SEM images shown in Figure 5.11 further clarify the agglomeration in the matrix.

For UT-2 and UT-3 composites, see Figures 5.10(e-h), the agglomeration was more evident causing a more porous surface after failure. In Figure 5.11(a), pullout of a long whisker from the resin matrix is shown. In Figure 5.11(b), rather than a single whisker, a bundle of whisker agglomerates can be seen. These images were taken from PT embedded UT-1 and UT-2 composites, respectively but it should be mentioned that they also reflect the structure of UT-3 composites. In Figure 5.11(c) crack bridging which is normal to the crack propagation direction can be seen. The marked area in the image reveals that crack is bridged by thick bundles of agglomerated PTs. In Figure 5.11(d) is a zoomed version of Figure 5.10(c), inside the pore, that is showing the inhomogeneous dispersion of silanized silica particles and PT whiskers within the porous resin matrix.

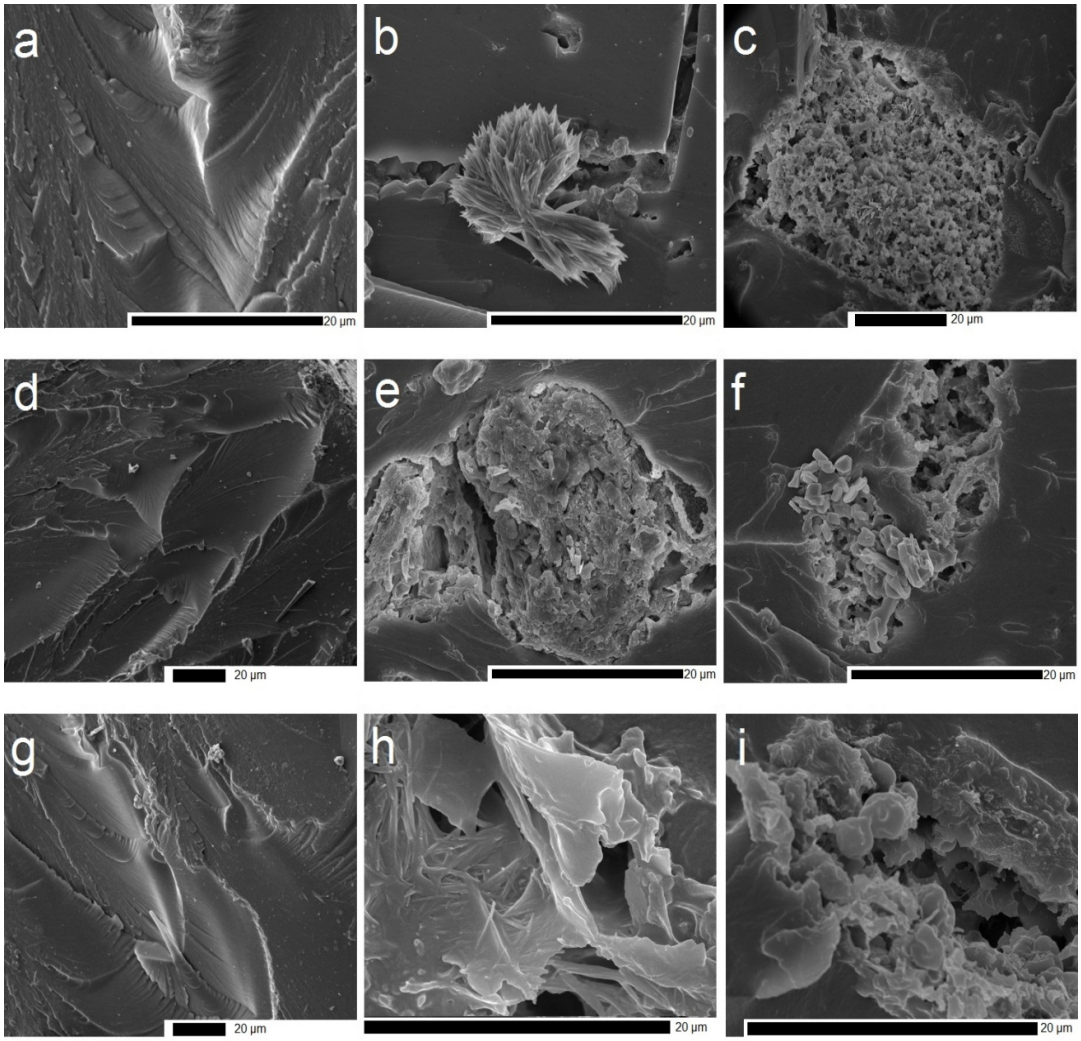


Figure 5. 10 Fracture surfaces of samples failed under tensile test. a) UT-1 b) UT-1-HDS-5 c) UT-1-HDSS-5 d) UT-2 e) UT-2-HDS-5 f) UT-2-HDSS-5 g) UT-3 h) UT-3-HDS-5 and i) UT-3-HDSS-5. Bar is 20 µm.

Embedded PTs or PT agglomerates acted as obstacles during crack propagation to some extent. The images revealed that the cracks were inhibited to some extent either by being deviated through bridging of PT bundles or by transfer of load to the whiskers' (bundles) resulting in pullout from the matrix. These results show that the dispersion inside the resin matrix upon mixing is the major factor that determines the final mechanical performance. But, dispersion is directly related to the initial viscosity of the monomer mixture.

The nanosize of PTs is effective on increasing the mechanical performance as a consequence of reducing the interparticle distance.[154] Results show that the anisotropy of the structure in terms of whisker alignment and dispersion is another key parameter and should be prevented. However, anisotropy because of random alignment of discontinuous short fibers minimize the gaps between filling and the natural teeth tissue by lowering polymerization contraction.[155]

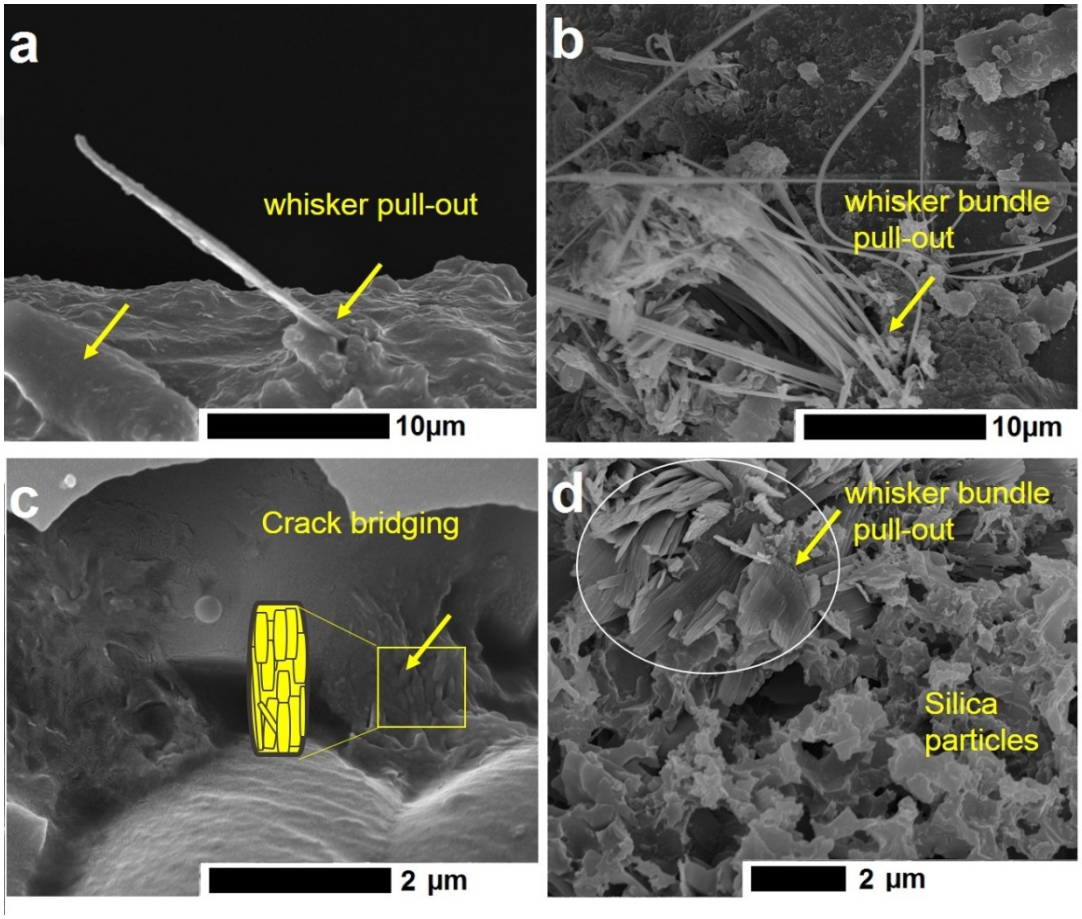


Figure 5. 11 Fracture surfaces of samples failed under tensile testing showing a) whisker pull out b) whisker bundle pull out c) crack bridging normal to crack propagation direction d) heterogeneous dispersion of PT and silica within the resin matrix caused by silanization treatment.

As mentioned for the crack bridging of thick agglomerated PT bundles, the anisotropy can enhance mechanical performance. It can be concluded that the objective should be the uniform dispersion of nanosize PT agglomerates in the polymer matrix rather than their dispersion as single nanowires/whiskers. By this perspective, the irregular shaped agglomerates could be wet by the monomer and provide better mechanical interlock at the interface. It has been reported that fillers are responsible for forming curvature on the periphery of a crack front and inhibit further propagation.[153]

5.3.6 Water sorption and solubility

As mentioned before, the ISO 4049-2009 standard for dental restorative resins claims that the products must have water sorption lower than 40 μg/mm^3 and solubility lower than 7.5 μg/mm^3. For neat UT resin mixtures, both water sorption and solubility values were acceptable to be used as dental restoratives. In Table 5.8, those of 5-wt % hydrothermally synthesized PT embedded UT composites after sonication and silanization are given.

Table 5. 8 Water sorption and solubility of PT reinforced UT resin composites.

Composite	**Water Sorption %**	**Water Sorption (μg/mm^3)**	**Solubility %**	**Solubility (μg/mm^3)**
UT-1-HDS-5	6.3 ± 1.4	71.6 ± 12.6	0	0
UT-2-HDS-5	6.9 ± 1.1	69.9 ± 12.4	0	0
UT-3-HDS-5	2.4 ± 0.2	25.4 ± 2.4	2.3 ± 1.1	25.3 ± 13.6
UT-1-HDSS-5	7.0 ± 0.9	76.6 ± 11.3	3.1 ± 0.9	34.7 ± 10.7
UT-2-HDSS-5	6.8 ± 1.2	70.7 ± 11.7	0	0
UT-3-HDSS-5	16.5 ± 5.7	156.7 ± 49.5	15.6 ± 7.5	179.0 ± 95.8

Results in Table 5.8 indicate that none of the composites were acceptable in terms of water sorption and solubility. The heavy loading of fillers may prevent efficient polymerization of the matrix. The lower degree of polymerization could account for an increase of solubility. Likewise, the presence of pores is another important factor where the polymerization is inhibited at the internal air-void surfaces.[156] In addition, there is a possibility that filler phase may contribute to the water absorption due to its surface coating of silanol (Si-O-H) groups which will absorb water onto its surface.[156]

5.3.7 Methylene blue degradation

In Figure 5.12, the MB degradation of highly embedded (10-50 -wt%) UT-2 composite is shown. It was investigated whether the PTs can preserve their MB degradation capability inside UT resin matrices. Since the samples were bulk, there were more time needed to reach the PTs near to surface. Therefore 24 h performances of bulk samples were recorded. As shown in Figure 5.12, neat UT-2 resin did not show any degradation performance whereas increased PT embedment increased MB degradation in 24 h. This is direct evidence and a novel finding in literature that dental resins that are produced by using PT embedment can react with UV light for degradation of contaminant. As the embedded weight increased, the response would be faster owing to decreased interparticle spacing of PTs between each other and to the surface.

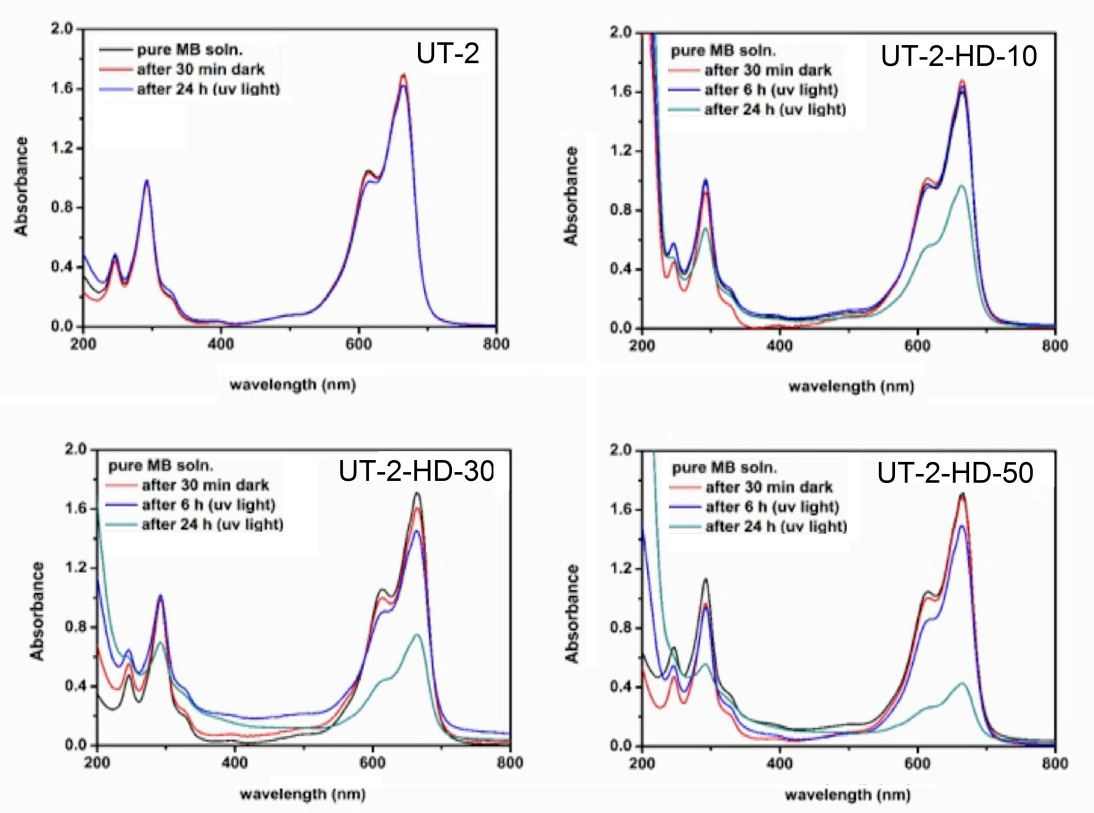


Figure 5. 12 MB degradation performance of UT-2 resin mixture and UT-2-HD composites in which 10-50-wt % hydrothermally synthesized PT embedded without sonication and silanization.

5.3.8 Bioactivity of PT embedded UT resin composites

In order to investigate the bioactivity of composite surfaces, as preliminary studies; bulk composites were immersed in SBF for 10 days. In Figure 5.13, the XRD patterns of the surfaces after immersion are shown. The data clearly shows that each composite was active upon formation of calcium-phosphate compounds in 10 days. The neat resins were also capable, but peak intensities were relatively lower indicating that the presence of PTs in the polymer matrix enhanced the bioactivity. The two phases that could be detected were Brushite (B, $Ca_3(PO_3)OH.2H_2O$, ICDD: 9-00777) and hydroxyapatite (HAp, $Ca_5(PO_4)_3OH$, ICDD: 73-171).

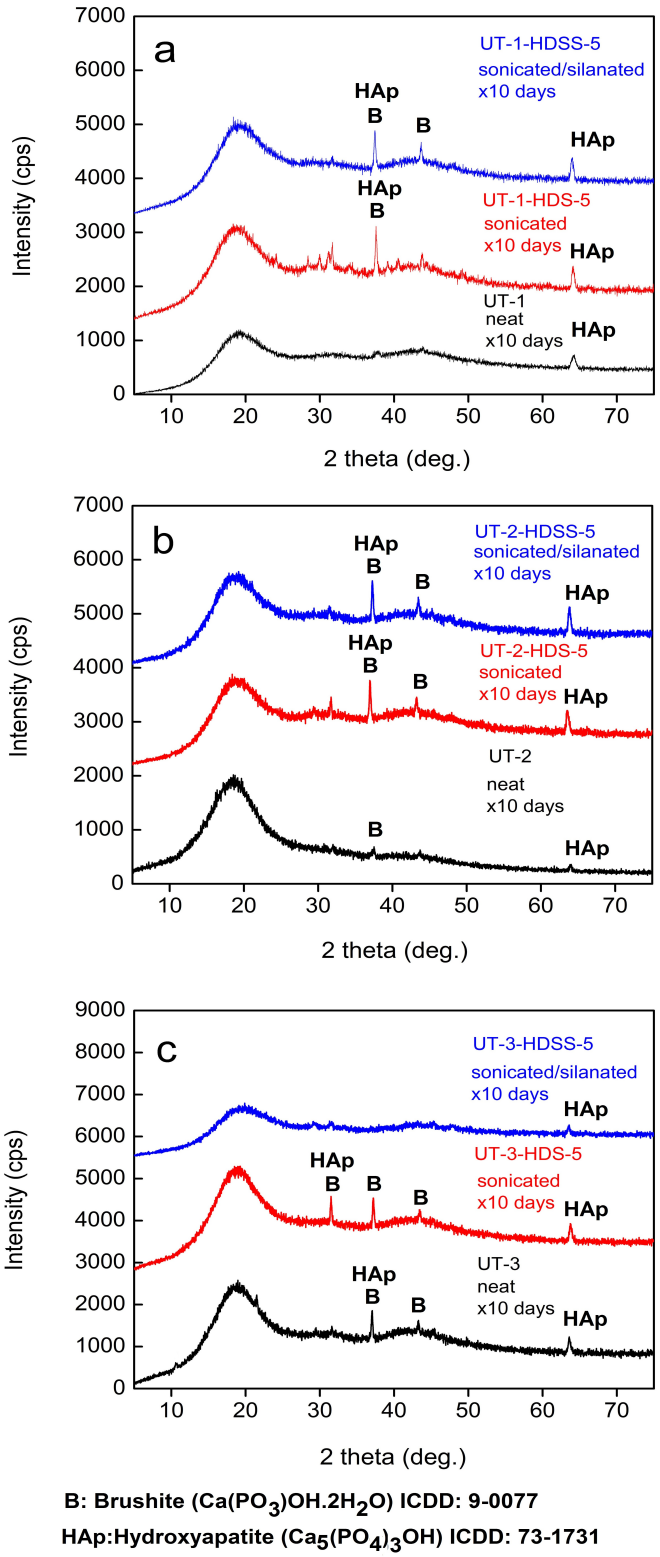


Figure 5. 13 XRD patterns of SBF treated neat and 5-wt % hydrothermally synthesized PT embedded (sonicated and/or silanized) UT resin mixtures for 10 days.

In Figure 5.14, the EDS spectra of the neat resin surfaces are given with insets showing the SEM images of the surfaces tested. Both EDS and SEM supported the XRD results with the detection of Na (sodium), Ca (calcium), and P (phosphorus) in EDS spectra as can also be recognized as a layer formed on the surface in SEM images. Na element was present due chemicals dissolved in SBF, see Table 3.7. P peak remarkably increased with PT embedment compared to neat resins and it was most evident in UT-1. Silanization did not reveal any change in response to SBF. The remarkable Ca and P peaks in EDS spectra are due formation of apatite phases rather than presence of solvated chemicals in SBF solution.

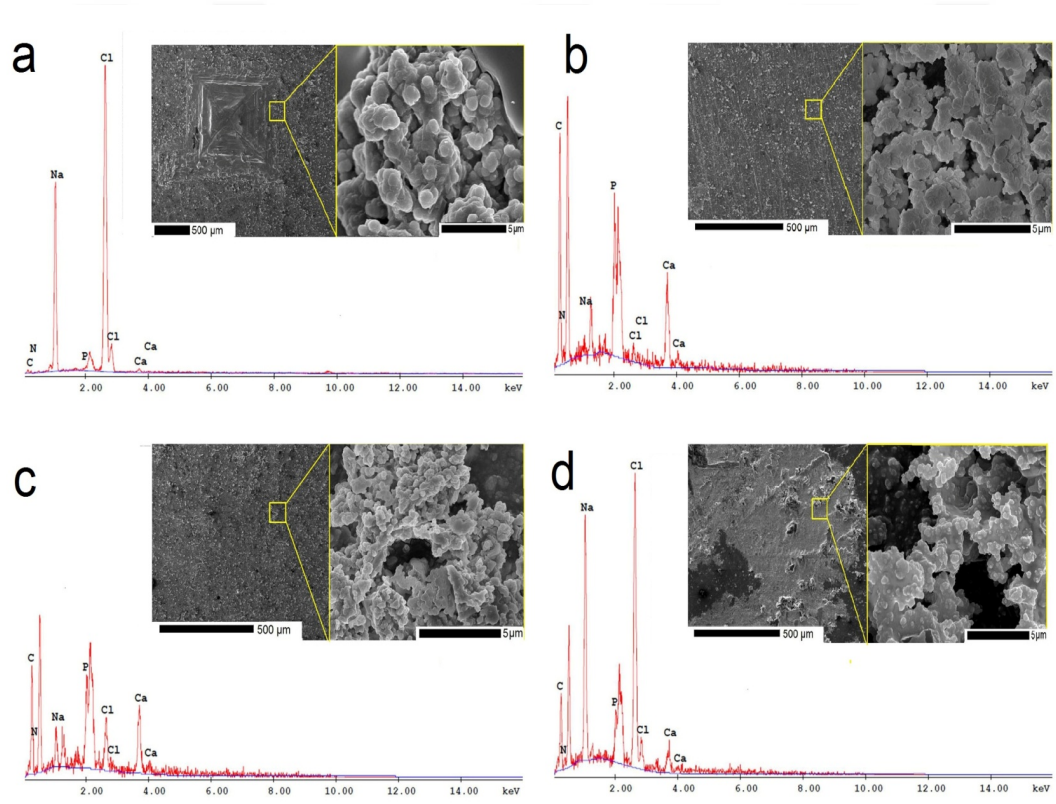


Figure 5. 14 EDS spectra of a) neat UT1 resin and 5-wt % sonicated PT embedded UT composites b) UT-1- HDS-5 c) UT-2-HDS-5 d) UT-3-HDS-5 after 10 days of SBF immersion (Insets: SEM images of SBF treated composite surfaces; left; bars100µm, right: bars 5 µm)

The XRD and SEM analysis showed that PT embedded UT composites are responsive to apatite formation. The neat UT resins, as control samples, did not reveal remarkable HAp formation in 10 days. Previously, J. Park[8] had stated that PTs are effective on formation of HAp on their surfaces. Therefore, HAp formation on dental composites is directly related to the presence and reachability of PTs inside the polymeric matrix that are located close to surface of the bulk composite.

5.4 Evaluation of PT embedded UT composites and comparison to commercial composites

There are a variety of studies reporting the performed analysis on several types of commercial composites, however, it is difficult to make accurate comparison with produced PT embedded UT resins in this dissertation due to differences in experimental/analysis conditions. In addition, there are a variety of commercial composites that can be compared. But since this dissertation is specific to UDMA-TEGDMA resins with nanosize, high aspect ratio fillers, comparison with similar ones should be more pronounced. Nonetheless, it is possible to form a general view of where these composites can be placed among different composites.

Among reported, the specific details on structure and properties of most commercials are not given due copyright reasons. One of the composites available in literature is Filtek Z250. It is a micro-filled composite composed of UDMA/BisGMA/BisEMA monomers filled with 60-vol % of silica/zirconia at 10-3500 nm size. [91] Ding et. al.[96] reported water sorption and solubility of Filtek Z250 as 1.68±0.26 % and 1.32±0.14 % respectively. As shown in Table 5.8, both water sorption and solubility percentages of the produced composites are significantly higher than Z250. This is mainly due to inhomogeneous dispersion of PTs inside the matrix. But also, this high difference can be attributed to relatively lower degree of reinforcement. One other example is Tetric Flow (Ivoclar, Vivident), which is a copolymer made up of UDMA/BisGMA/TEGDMA filled with 40 vol. % of 40-3000 nm fillers.

Janda et. al. [134] reported that it is one of the best in terms of water sorption and solubility resistance. They also stated that it is not possible to make a correlation between filler level and solubility. Especially for Tetric Flow, they confirmed major effect of the resin composition on the water sorption than that of embedment.

On the other hand, Sagsoz et. al[122] measured wear rates of several composites. They reported mean wear rates lower than 10^{-6} mm^3/Nm obtained by a three-body wear test at 10 N load.(in saliva, pH=7) In addition to their results, three different types of commercial composites which were tested in for wear rate and HV 0.3 at identical conditions for comparison are Reflectys (Itena), Supreme XT (3M ESPE) and microhybrid (Mendental). Filtek Supreme is nanofilled composite made up of BisGMA/TEGDMA/UDMA/BisEMA filled with 72.5-wt % silica/zirconia.[122] All three samples prepared at identical conditions showed WR smaller than $2.5*10^{-4}$ mm^3/Nm. In this dissertation, lowest wear rate was obtained by UT-1 composition in which hydrothermally produced PTs were added after sonication treatment (UT-1-HDS-5). Sol-gel derived PTs were promising due their rigidity preventing entanglement, however, elimination of KCl and anatase has not be studied yet.

From these results and comparison, it can be concluded that viscosity plays the key role in terms of the final performance of the composites, which is directly related to the morphology and state of the PTs inside the monomer mixture upon mixing. Conclusively, results indicate that nano size PT whiskers can be used to reinforce dental resins. Their mechanical and physical properties like water sorption/solubility can be enhanced by increasing embedment levels and/or with more effective mixing and curing intensity.

The color of the composites was also evaluated. In Figure 5.15, photographs of produced samples are shown. As evident from the photographs, the color of the composites varies between white to slightly yellowish. The yellow color depends on the initiator amount, CQ. Since it is dark yellow, if it is not dispersed well, it creates yellow dots on the cured samples.

In this dissertation, the whole study was based on using CQ/DMAEMA=1 (0.5-wt % for each) because it was one of the most efficient ratio for complete polymerization given in literature.[157] By decreasing CQ content, the white color can be more pronounced.

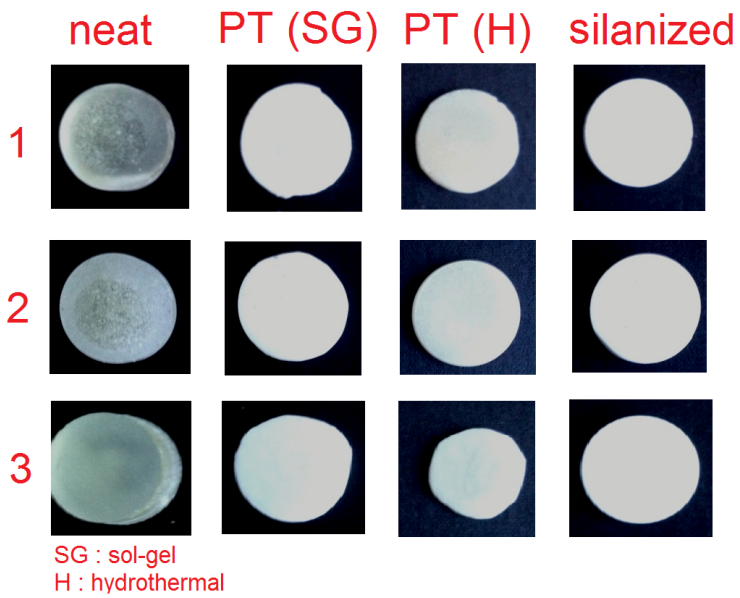


Figure 5. 15 Photographs of produced resin and composites.

CHAPTER 6

CONCLUSIONS

6.1 Sol-gel synthesis of PT nanostructures

Sol-gel derived synthesis of PT nanostructures using Ti/K molar ratio of 1 to 3.5 has led to following conclusions.

- Morphology and size of the PT nanostructures could be controlled but the production of single PHT/PTT phase is a challenging task by this production route.

- XRD analysis revealed that KCl crystallites form inside an amorphous network upon sol-gel reactions. By calcination, the KCl crystallites dispersed amorphous network transforms into PT nanostructures. After calcination at 600 °C, PH forms before PHT and transforms to PHT. This transformation is evident from the disappearance of distinct PH peaks and appearance of PHT peaks as the calcination time is increased. After calcination at 800 °C, no PH formation is observed, instead PTT is formed.

- PTs grow in amorphous Ti-O-(K) network where K^+ ions present on the surfaces of amorphous clusters formed during gelation. By aging of the gels, KCl crystals form on the surfaces then decompose and K^+ ions combine with Ti-O network crystallizing into PTs.

- SEM analysis suggests that PH and PHT nanostructures are in the form of severely agglomerated high aspect ratio whiskers. Size of the PT whiskers increases with increasing calcination time.
- It is not possible to obtain single phase and/or impurity free PT nanostructures due to the low reaction efficiency necessitating calcination durations longer than 3 h.

- BET analysis confirmed the presence of slit-shaped mesopores between high aspect ratio PHT and PTT, but revealed that sol-gel derived PTs have moderately low surface area (14-20 m^2/g).

- Eg of nanostructures synthesized are similar to that of P25 powder at both calcination temperatures.

- MB degradation tests revealed that PTs synthesized have photocatalytic ability with highest MB degradation rate of 0.030 min^{-1} obtained at Ti/K of 3.5 and 1.5 after calcination at 600°C for 1 h and at 800 °C for 3 h, respectively.

6.2 Hydrothermal synthesis of PT nanostructures

Hydrothermal synthesis of PT nanostructures under controlled conditions using various $KOH^{aq.}$ concentrations, reaction durations and temperatures has led to following conclusions.

- The hydrothermal reaction temperature and time, and the type of the initial TiO_2 precursor have a profound effect on the formation and morphology of PT nanostructures. It is possible to obtain PHT nanowires even at 120 °C, but the optimum synthesis temperature of high aspect ratio PTs is 180 °C for 24 h.

- An atomic-scale analysis using HRTEM indicated the formation of PT nanowires via a combined mechanism of oriented attachment and strain-induced splitting mechanisms. The formation reaction depends on the distribution and amount of K^+ ions in the amorphous-like matrix. The strain associated with the variety of K^+ ions determines the final crystal structure.

- Tunneled structures are more likely to form from amorphous-like matrices under autogeneous pressure.

- Splitting was most evident for reaction time of 12 h and the highest surface area of 101 m^2/g was obtained using 10 M KOH^{aq} after 12 h of hydrothermal treatment.

- The E_g of the nanostructures synthesized is significantly lower than that of P25 powder indicating that energy needed to activate the powders for photocatalytic reactions shifted to lower energy levels.

- Hydrothermally synthesized powders showed photocatalytic activity comparable to the photocatalytic activity of P25 powder and the highest MB degradation rate of 0.010 min^{-1} was obtained using 10 M $KOH^{aq.}$ after 24 h of treatment at 180 °C. The degradation rate of the hydrothermal synthesis of PT nanostructures is lower than that of the sol-gel derived powders.

6.3 PT embedded UT composites

Production of PT nanostructure embedded UT resin composites has led to following conclusions.

- The filler size and distribution have significant effects on the final mechanical properties of the composites. As the amount of PT embedment increases, the mechanical performance degrades.

- Sol-gel derived PT embedded UT resin composites provide lower wear resistance and hardness than the hydrothermally synthesized PT embedded UT resin composites at identical PT embedment and as-prepared condition.

- The sonication treatment of PT nanowires was efficient for elimination of water insoluble impurities and for de-agglomeration of big particles. Hence, the wear resistance was greatly enhanced.
- The lowest wear rate of 0.065±0.006 mm^3/Nm was achieved for the composite UT-1-HDS-5 that was prepared by reinforcing 5 wt% of sonicated, hydrothermally synthesized PTs. Similarly, the highest tensile strength and modulus were obtained for the same composite as 42.57 ±0.26 MPa and 0.90 ±0.14 GPa, respectively.

- SEM analysis revealed that both crack bridging and whisker pull out mechanisms are seen at the fracture surfaces of the specimens under tensile loading. Both mechanisms were most common for the composites prepared using UT-1 in which an optimized viscosity was achieved.

- SEM examination has revealed that silanization treatment was not efficient in terms of providing a uniform dispersion of silica and silanized PTs throughout the matrix.

- The measured water sorption and solubility of 5 wt% PT embedded UT resin composites were above the limits provided by ISO. The lowest water sorption was obtained in the UT-3-5 composite with 25.43 ± 2.35 $\mu g/mm^3$, but its solubility was significantly high due inefficient interaction of light causing depth of cure problems. The other composites reinforced by sonication treated PTs had zero solubility with higher water sorption values (~70 $\mu g/mm^3$). Silanization had adverse effects on water sorption and solubility due to inhomogeneous dispersion of PT and silica agglomerates. Moreover, the silica particles were hydrophilic and they increased hydrolytic break down at the filler-matrix interfaces.

- XRD and SEM/EDS analysis of SBF immersed samples indicated that HAp crystals form on composite surfaces.

- MB degradation tests of composites indicated an increasing rate of MB degradation as the PT reinforcement in the composite was increased.

REFERENCES

(1) Zaremba, T.; Witkowska, D. *Materials Science-Poland* **2010**, *28*, 25.

(2) Wang, Q.; Guo, Z.; Chung, J. S. *Materials Research Bulletin* **2009**, *44*, 1973.

(3) Bavykin, D. V.; Walsh, F. C. *The Journal of Physical Chemistry C* **2007**, *111*, 14644.

(4) Shahid, M.; El Saliby, I.; McDonagh, A.; Tijing, L. D.; Kim, J. H.; Shon, H. K. *J Environ Sci (China)* **2014**, *26*, 2348.

(5) Zielińska, B.; Borowiak-Palen, E.; Grzmil, B.; Kalenczuk, R. J. *Journal of Alloys and Compounds* **2011**, *509*, 5414.

(6) Allen, M. R.; Thibert, A.; Sabio, E. M.; Browning, N. D.; Larsen, D. S.; Osterloh, F. E. *Chemistry of Materials* **2010**, *22*, 1220.

(7) Amano, F.; Yasumoto, T.; Shibayama, T.; Uchida, S.; Ohtani, B. *Applied Catalysis B: Environmental* **2009**, *89*, 583.

(8) Park, J. *Journal of Alloys and Compounds* **2010**, *492*, L57.

(9) Teshima, K.; Yubuta, K.; Shimodaira, T.; Suzuki, T.; Endo, M.; Shishido, T.; Oishi, S. *Crystal Growth & Design* **2008**, *8*, 465.

(10) Liu, C.; Yin, H.; Liu, Y.; Ren, M.; Wang, A.; Ge, C.; Yao, H.; Feng, H.; Chen, J.; Jiang, T. *Materials Research Bulletin* **2009**, *44*, 1173.

(11) Yoshida, H.; Takeuchi, M.; Sato, M.; Zhang, L.; Teshima, T.; Chaskar, M. G. *Catalysis Today* **2014**, *232*, 158.

(12) Cheung, K. Y.; Yip, C. T.; Djurišić, A. B.; Leung, Y. H.; Chan, W. K. *Advanced Functional Materials* **2007**, *17*, 555.

(13) Tan, S.; Zhang, Y.; Gong, H. *Journal of Water and Environment Technology* **2007**, *5*, 13.

(14) Wang, B. L.; Chen, Q.; Hu, J.; Li, H.; Hu, Y. F.; Peng, L. M. *Chemical Physics Letters* **2005**, *406*, 95.

(15) Yu, J.; Xiang, Q.; Zhou, M. *Applied Catalysis B: Environmental* **2009**, *90*, 595.
(16) Yun, R.; Filip, P.; Lu, Y. *Tribology International* **2010**, *43*, 2010.

(17) Kim, Y. C.; Cho, M. H.; Kim, S. J.; Jang, H. *Wear* **2008**, *264*, 204.

(18) Melo, M. A. S.; Guedes, S. F. F.; Xu, H. H. K.; Rodrigues, L. K. A. *Trends in Biotechnology* **2013**, *31*, 459.

(19) Siddiqui, M. A.; Chandel, V. S.; Azam, A. *Applied Surface Science* **2012**, *258*, 7354.

(20) Kang, S.-O.; Jang, H.-S.; Kim, Y.-I.; Kim, K.-B.; Jung, M.-J. *Materials Letters* **2007**, *61*, 473.

(21) Janes, R.; Knightley, L. J. *J Mater Sci* **2004**, *39*, 2589.

(22) Wang, Q.; Guo, Q.; Wang, H.; Li, B. *Materials Letters* **2015**, *155*, 38.

(23) Takaya, S.; Lu, Y.; Guan, S.; Miyazawa, K.; Yoshida, H.; Asanuma, H. *Surface and Coatings Technology* **2015**.

(24) Tanaka, S.; Tobimatsu, H.; Maruyama, Y.; Tanaki, T.; Jerkiewicz, G. *ACS Appl Mater Interfaces* **2009**, *1*, 2312.

(25) Sreekantan, S.; Wei, L. C. *Journal of Alloys and Compounds* **2010**, *490*, 436.

(26) Wang, J.; Li, C.; Liang, B.; Wang, X. *Rare Metals* **2009**, *28*, 24.

(27) Sikhwivhilu, L. M.; Sinha Ray, S.; Coville, N. J. *Applied Physics A* **2008**, *94*, 963.

(28) Zhao, Y.; Jin, J.; Yang, X. *Materials Letters* **2007**, *61*, 384.

(29) Wang, B.; Shi, Y.; Xue, D. *Journal of Solid State Chemistry* **2007**, *180*, 1028.

(30) Yury V. Kolen'ko, †,‡ Kirill A. Kovnir,†,§ Anton I. Gavrilov,† Alexei V. Garshev,†; Johannes Frantti, | Oleg I. Lebedev, ⊥,# Bulat R. Churagulov,O Gustaaf Van Tendeloo, ⊥ and Masahiro Yoshimura‡ **2006**.

(31) Rau, H.; Rabenau, A. *Solid State Communications* **1967**, *5*, 331.

(32) Chunying Chao, Z. R., Simin Yin, Gang Xu, Siyu Gong, Xin Yang, Xiang Li, Ge Shen, Gaorong Han **2014**.

(33) Du, G. H.; Chen, Q.; Han, P. D.; Yu, Y.; Peng, L. M. *Physical Review B* **2003**, *67*, 035323.

(34) Ponce-Peña, P.; González-Lozano, M. A.; Escobedo-Bretado, M. A.; de Lira-Gómez, P.; García-Sánchez, E.; Rivera, E.; Alexandrova, L. *Ceramics International* **2015**.

(35) Yokoyama, M.; Ota, T.; Yamai, I. *J Mater Sci* **1989**, *24*, 3787.

(36) Kajiwara, M. *J Mater Sci* **1988**, *23*, 3600.

(37) Kajiwara, M. *J Mater Sci* **1987**, *22*, 1223.

(38) Masaki, N.; Uchida, S.; Yamane, H.; Sato, T. *J Mater Sci* **2000**, *35*, 3307.

(39) Sasani Ghamsari, M.; Rahim, S.; Radiman, S.; Hasani, J. *Materials Letters* **2012**, *85*, 81.

(40) Tsumura, T.; Sogabe, K.; Kiyo, T.; Toyoda, M. *Materials Letters* **2011**, *65*, 2322.

(41) Zhang, J.; Wang, Y.-a.; Yang, J.; Chen, J.; Zhang, Z. *Materials Letters* **2006**, *60*, 3015.

(42) Meng, X.; Wang, D.; Liu, J.; Lin, B.; Fu, Z. *Solid State Communications* **2006**, *137*, 146.

(43) Qian, Q. H.; Zhou, X. F.; Hu, Y. Y.; Liu, C.; Feng, X.; Lu, X. H. *J Mater Sci* **2007**, *42*, 8222.

(44) Seftel, E. M.; Niarchos, M.; Mitropoulos, C.; Mertens, M.; Vansant, E. F.; Cool, P. *Catalysis Today* **2015**, *252*, 120.

(45) Sergio Valencia, J. M. M., Gloria Restrepo *The Open Materials Science Journal* **2010**, *4*, 6.

(46) K. Nagaveni, M. S. H., N. Ravishankar, G.N. Subbanna, Gridhar Madras *Langmuir* **2004**, *20*, 8.

(47) Zhao, J.; Chen, C.; Ma, W. *Topics in Catalysis* **2005**, *35*, 269.

(48) Natarajan, T. S.; Bajaj, H. C.; Tayade, R. J. *Journal of Colloid and Interface Science* **2014**, *433*, 104.

(49) López, R.; Gómez, R. *Journal of Sol-Gel Science and Technology* **2012**, *61*, 1.

(50) Welte, A.; Waldauf, C.; Brabec, C.; Wellmann, P. J. *Thin Solid Films* **2008**, *516*, 7256.

(51) Reddy, K. M.; Manorama, S. V.; Reddy, A. R. *Materials Chemistry and Physics* **2003**, *78*, 239.

(52) Lee, C.-T.; Um, M.-H.; Kumazawa, H. *Journal of the American Ceramic Society* **2000**, *83*, 1098.

(53) Izawa, H.; Kikkawa, S.; Koizumi, M. *The Journal of Physical Chemistry* **1982**, *86*, 5023.

(54) Li, Q.; Kako, T.; Ye, J. *International Journal of Hydrogen Energy* **2011**, *36*, 4716.

(55) Zhou, W.; Liu, X.; Sang, Y.; Zhao, Z.; Zhou, K.; Liu, H.; Chen, S. *ACS Applied Materials & Interfaces* **2014**, *6*, 4578.

(56) Kim, S. J.; Cho, M. H.; Basch, R. H.; Fash, J. W.; Jang, H. *Tribology Letters* **2004**, *17*, 655.

(57) Tjong, S. C.; Meng, Y. Z. *Journal of Applied Polymer Science* **1998**, *70*, 431.

(58) Cai, K.; Lai, M.; Yang, W.; Hu, R.; Xin, R.; Liu, Q.; Sung, K. L. P. *Acta Biomaterialia* **2010**, *6*, 2314.

(59) Yan Bao Li, Q. L., Jun Sheng Chen, Xiang Hui Lan, Chun Hua Lu, Dong Xu Li, Zhong Zi Xu *Advanced Materials Research* **2008**, *47*, 5.

(60) Bektas, O. O.; Eren, D.; Akin, G. G.; Polat, Z. A. *Cumhuriyet Dent J* **2012**, *15*, 327.

(61) Zhang, H.; Darvell, B. W. *Dental Materials* **2012**, *28*, 824.

(62) Xu, H. H. K.; Quinn, J. B.; Smith, D. T.; Giuseppetti, A. A.; Eichmiller, F. C. *Dental Materials* **2003**, *19*, 359.

(63) Bowen, R. L. *Journal of American Dental Association* **1964**, 15.

(64) John F. McCabe, a. A. W. *Applied Dental Materials*; Wiley-Blackwell, 2008.

(65) Lavigueur, C.; Zhu, X. X. *RSC Advances* **2012**, *2*, 59.

(66) Chen, L.; Yu, Q.; Wang, Y.; Li, H. *Dental Materials* **2011**, *27*, 1187.

(67) Floyd, C. J. E.; Dickens, S. H. *Dental Materials* **2006**, *22*, 1143.

(68) Furuse, A. Y.; Mondelli, J.; Watts, D. C. *Dental Materials* **2011**, *27*, 497.

(69) Jakubiak, J.; Wrzyszczyński, A.; Lindén, L.; Rabek, J. *Journal of Macromolecular Science, Part A: Pure and Applied Chemistry* **2007**, *44*, 239.

(70) Anusavice, K. J. *Phillips' Science of Dental Materials*; 11th ed.; Elsevier: China, 2003.

(71) Stansbury, J. W. *Journal of Esthetic and Restorative Dentistry* **2000**, *12*, 300.

(72) Watts, D. C. *Dental Materials* **2005**, *21*, 27.

(73) Turssi, C. P.; de Moraes Purquerio, B.; Serra, M. C. *Journal of Biomedical Materials Research Part B: Applied Biomaterials* **2003**, *65B*, 280.

(74) Labella, R.; Braden, M.; Deb, S. *Biomaterials* **1994**, *15*, 1197.

(75) Xia, Y.; Zhang, F.; Xie, H.; Gu, N. *Journal of Dentistry* **2008**, *36*, 450.

(76) Sun, J.; Forster, A. M.; Johnson, P. M.; Eidelman, N.; Quinn, G.; Schumacher, G.; Zhang, X.; Wu, W.-l. *Dental Materials* **2011**, *27*, 972.

(77) Xu, H. H. K.; Schumacher, G. E.; Eichmiller, F. C.; Peterson, R. C.; Antonucci, J. M.; Mueller, H. J. *Dental Materials* **2003**, *19*, 523.

(78) Guo, G.; Fan, Y.; Zhang, J.-F.; Hagan, J. L.; Xu, X. *Dental Materials* **2012**, *28*, 360.

(79) Liu, F.; Sun, B.; Jiang, X.; Aldeyab, S. S.; Zhang, Q.; Zhu, M. *Dental Materials* **2014**, *30*, 1358.

(80) Tammaro, L.; Vittoria, V.; Calarco, A.; Petillo, O.; Riccitiello, F.; Peluso, G. *Journal of Dentistry* **2014**, *42*, 60.

(81) Nishiyama, N.; Ishizaki, T.; Horie, K.; Tomari, M.; Someya, M. *Journal of biomedical materials research* **1991**, *25*, 213.

(82) Plueddemann, E. P. **1970**.

(83) Brown, S. K. *British Polymer Journal* **1980**, *12*, 24.

(84) Mohsen, N.; Craig, R. *Journal of oral rehabilitation* **1995**, *22*, 183.

(85) Calais, J.; Soderholm, K.-J. *Journal of Dental Research* **1988**, *67*, 836.

(86) Halvorson, R. H.; Erickson, R. L.; Davidson, C. L. *Dental Materials* **2003**, *19*, 327.

(87) Sideridou, I. D.; Karabela, M. M. *Dental Materials* **2009**, *25*, 1315.

(88) Emami, N.; Sjödahl, M.; Söderholm, K.-J. M. *Dental Materials* **2005**, *21*, 721.

(89) Didem, A.; Yalcin, G. *Open Journal of Composite Materials* **2014**, *2014*.

(90) Avery, J. K. *Essentials of Oral Histology and Embryology : A Clinical Approach*, 1992.

(91) Kleverlaan, C. J.; Feilzer, A. J. *Dental Materials* **2005**, *21*, 1150.

(92) Dogan, M.; Abak, H.; Alkan, M. *J Hazard Mater* **2009**, *164*, 172.

(93) Archard, J. F.; Hirst, W. In *Proceedings of the Royal Society of London A: Mathematical, Physical and Engineering Sciences*; The Royal Society: 1956; Vol. 236, p 397.

(94) Oliver, W. C.; Pharr, G. M. *Journal of Materials Research* **2004**, *19*, 3.

(95) Elssner, G.; Hoven, H.; Kiessler, G.; Wellner, P.; Wert, R.; Wert, G. E. H. K. W. In *Ceramics and Ceramic Composites*; Elsevier Science: New York, 1999, p 144.

(96) Ding, Y.; Li, B.; Wang, M.; Liu, F.; He, J. *Advances in Polymer Technology* **2015**, n/a.

(97) Jung, K.; Shul, Y. *Journal of Sol-Gel Science and Technology* **1996**, *6*, 227.

(98) Jung, K.; Shul, Y.; Moon, J.; Oh, W. *Waste treatment and technologies involving inorganic sorbents* **1997**, 163.

(99) Liu, Y.; Tsuru, K.; Hayakawa, S.; Osaka, A. *Journal of the Ceramic Society of Japan* **2004**, *112*, 634.

(100) Zaremba, T. *Materials Science-Poland* **2012**, *30*, 180.

(101) Bao, N.; Feng, X.; Lu, X.; Yang, Z. *J Mater Sci* **2002**, *37*, 3035.

(102) Simonsen, M. E.; Sogaard, E. G. *Journal of Sol-Gel Science and Technology* **2010**, *53*, 485.

(103) Bessekhouad, Y.; Robert, D.; Weber, J. V.; Chaoui, N. *Journal of Photochemistry and Photobiology A: Chemistry* **2004**, *167*, 49.

(104) Partlow, D. P.; Yoldas, B. E. *Journal of Non-Crystalline Solids* **1981**, *46*, 153.

(105) Chou, I.-M. *Geochimica et Cosmochimica Acta* **1987**, *51*, 1965.

(106) Chen, L.-C.; Huang, C.-M.; Tsai, F.-R. *Journal of Molecular Catalysis A: Chemical* **2007**, *265*, 133.

(107) Vogt, T.; Schweda, E.; WÃ¼stefeld, C.; StrÃ¤hle, J.; Cheetham, A. K. *Journal of Solid State Chemistry* **1989**, *83*, 61.
(108) Roessler, D.; Walker, W. *Physical Review* **1968**, *166*, 599.

(109) Robertson, J. *Journal of Non-Crystalline Solids* **2008**, *354*, 2791.

(110) Parker, M. A. *Physics of optoelectronics*; CRC Press, 2005.

(111) Yin, S.; Sato, T. *Industrial & engineering chemistry research* **2000**, *39*, 4526.

(112) Li, J.; Zhang, Y. C.; Zhang, M. *Materials Letters* **2012**, *79*, 136.

(113) Cui, W.; Ma, S.; Liu, L.; Liang, Y. *Chemical Engineering Journal* **2012**, *204-206*, 1.

(114) Xu, J.; Zhang, H.; Zhang, J.; Liu, X.; He, X.; Xu, D.; Qian, J.; Liu, L.; Sun, J. Hydrothermal synthesis of potassium/sodium titanate nanofibres and their ultraviolet properties. *Micro & Nano Letters* [Online Early Access]. Published Online: 2012 http://digitallibrary.theiet.org/content/journals/10.1049/mnl.2012.0116.

(115) Hakuta, Y.; Hayashi, H.; Arai, K. *J Mater Sci*, *39*, 4977.

(116) Yuan, Z. Y.; Zhang, X. B.; Su, B. L. *Applied Physics A* **2004**, *78*, 1063.

(117) Li, X.-L.; Peng, Q.; Yi, J.-X.; Wang, X.; Li, Y. *Chemistry – A European Journal* **2006**, *12*, 2383.

(118) Wu, H. B.; Hng, H. H.; Lou, X. W. D. *Advanced Materials* **2012**, *24*, 2567.

(119) Zhou, Y.; Liu, C.; He, M.; Lu, X.; Feng, X.; Yang, Z. *J Mater Sci* **2008**, *43*, 155.

(120) Xie, J.; Lu, X.; Zhu, Y.; Liu, C.; Bao, N.; Feng, X. *J Mater Sci* **2003**, *38*, 3641.

(121) Mair, L. *Journal of Dentistry* **1992**, *20*, 140.

(122) Sagsoz, O.; Ilday, N. O.; Sagsoz, N. P.; Bayindir, Y. Z.; Alsaran, A. *International Journal of Composite Materials* **2014**, *4*, 179.

(123) Jin, Z.; Stone, M.; Ingham, E.; Fisher, J. *Current Orthopaedics* **2006**, *20*, 32.

(124) Kato, K.; Adachi, K. *Wear* **2002**, *253*, 1097.

(125) Sideridou, I.; Tserki, V.; Papanastasiou, G. *Biomaterials* **2003**, *24*, 655.

(126) Asmussen, E.; Peutzfeldt, A. *Dental Materials* **1998**, *14*, 51.

(127) El-Safty, S.; Akhtar, R.; Silikas, N.; Watts, D. *Dental Materials* **2012**, *28*, 1292.

(128) Tamura, Y.; Kakuta, K.; Ogura, H. *Odontology* **2013**, *101*, 156.

(129) Chung, S. M.; Yap, A. U. J.; Tsai, K. T.; Yap, F. L. *Journal of Biomedical Materials Research Part B: Applied Biomaterials* **2005**, *72B*, 246.

(130) Yap, A. U. J.; Wang, X.; Wu, X.; Chung, S. M. *Biomaterials* **2004**, *25*, 2179.

(131) Nakayama, W. T.; Hall, D. R.; Grenoble, D. E.; Katz, J. L. *Journal of dental research* **1974**, *53*, 1121.

(132) Emami, N.; Söderholm, K. *The open dentistry journal* **2009**, *3*, 202.

(133) Liu, F.; Jiang, X.; Bao, S.; Wang, R.; Sun, B.; Zhu, M. *Materials Science and Engineering: C* **2015**, *53*, 150.

(134) Janda, R.; Roulet, J. F.; Latta, M.; Rüttermann, S. *Journal of Biomedical Materials Research Part B: Applied Biomaterials* **2007**, *82*, 545.

(135) Ferracane, J. L. *Dental Materials* **2006**, *22*, 211.

(136) Venz, S.; Dickens, B. *Journal of biomedical materials research* **1991**, *25*, 1231.

(137) Friedrich, K. *Friction and wear of polymer composites* **1986**, *1*, 233.

(138) Nagarajan, V. S.; Jahanmir, S.; Thompson, V. P. *Dental Materials* **2004**, *20*, 63.

(139) Ramalho, A.; Antunes, P. V. *Wear* **2005**, *259*, 1005.

(140) Faria, A. C. L.; Benassi, U. M.; Rodrigues, R. C. S.; Ribeiro, R. F.; Mattos, M. d. G. C. d. *Brazilian dental journal* **2007**, *18*, 60.

(141) Lavigueur, C.; Zhu, X. *RSC Advances* **2012**, *2*, 59.

(142) Mayworm, C. D.; Camargo, S. S.; Bastian, F. L. *Journal of dentistry* **2008**, *36*, 703.

(143) Arsecularatne, J.; Hoffman, M. *Journal of the mechanical behavior of biomedical materials* **2012**, *8*, 47.

(144) Manhart, J.; Kunzelmann, K.-H.; Chen, H.; Hickel, R. *Dental Materials* **2000**, *16*, 33.

(145) Miyasaka *Dental materials journal* **1996**, *15*, 98.

(146) Xu, H. H.; Ostertag, C. P.; Braun, L. M.; Lloyd, I. K. *Journal of the American Ceramic Society* **1994**, *77*, 1889.

(147) Xu, H.; Smith, D.; Jahanmir, S.; Romberg, E.; Kelly, J.; Thompson, V.; Rekow, E. *Journal of Dental Research* **1998**, *77*, 472.

(148) Ehrnford, L. *Acta Odontologica* **1984**, *42*, 59.

(149) Leinfelder, K. *Dental Clinics of North America* **1993**, *37*, 411.

(150) Kardos, J. *International encyclopedia of composites* **1991**, *5*, 130.

(151) Yap, A.; Chung, S.; Chow, W.; Tsai, K.; Lim, C. *OPERATIVE DENTISTRY-UNIVERSITY OF WASHINGTON-* **2004**, *29*, 29.

(152) Ilie, N.; Hickel, R.; Valceanu, A.; Huth, K. *Clinical Oral Investigations* **2012**, *16*, 489.

(153) Quinn, J. B.; Quinn, G. D. *dental materials* **2010**, *26*, 589.

(154) Wagner, H. D.; Vaia, R. A. *Materials Today* **2004**, *7*, 38.

(155) Vallittu, P. K. *Dental Materials* **2015**, *31*, 1.

(156) Santos, C.; Clarke, R.; Braden, M.; Guitian, F.; Davy, K. *Biomaterials* **2002**, *23*, 1897.

(157) Jan, C. M.; Nomura, Y.; Urabe, H.; Okazaki, M.; Shintani, H. *Journal of biomedical materials research* **2001**, *58*, 42.

APPENDIX A

METHYLENE BLUE DEGRADATION CALCULATIONS

A1. MB degradation of sol-gel derived powders

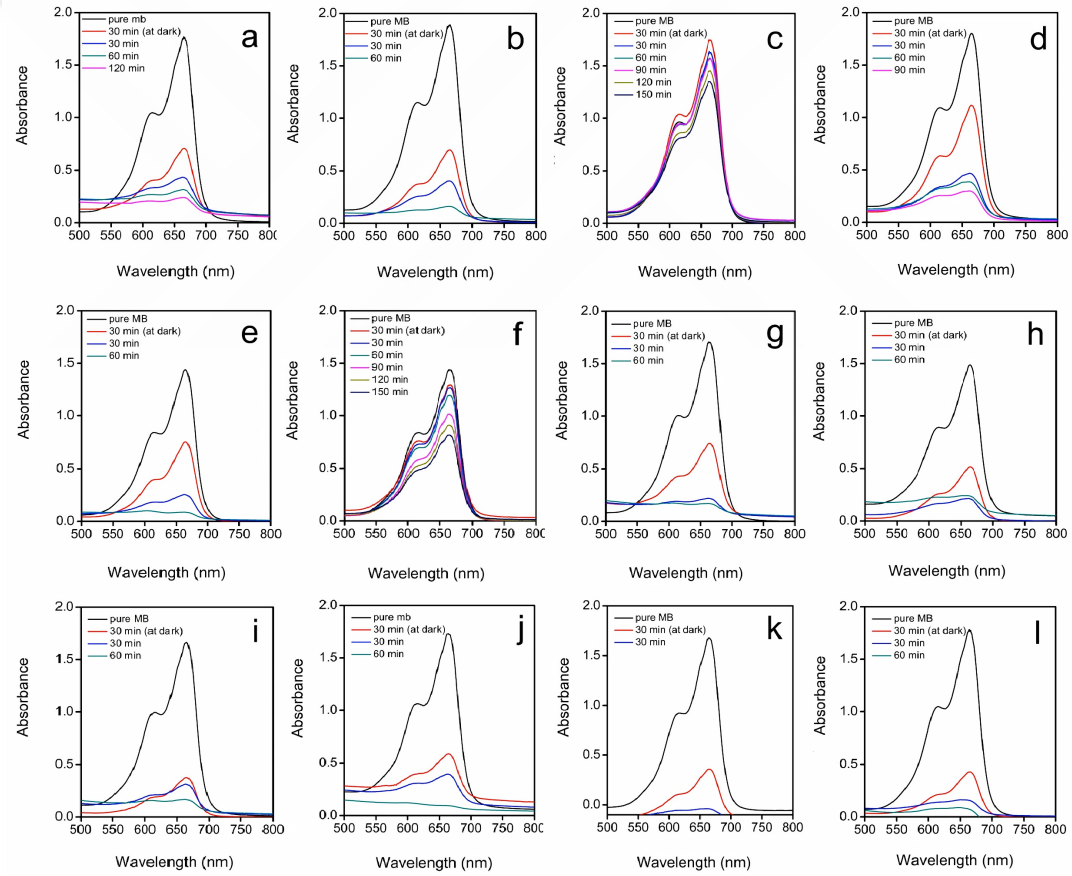


Figure A.1 UV-Vis absorbance curves of MB solutions interacted with sol-gel derived powders calcined at 600 ºC: a) Ti/K=1 b) Ti/K=1.5 c) Ti/K=2.5 d) Ti/K=3.5 for 1 h e) Ti/K=1 f) Ti/K=1.5 g) Ti/K=2.5 h) Ti/K=3.5 for 2 h and i) Ti/K=1 j) Ti/K=1.5 k) Ti/K=2.5 l) Ti/K=3.5 for 3 h.

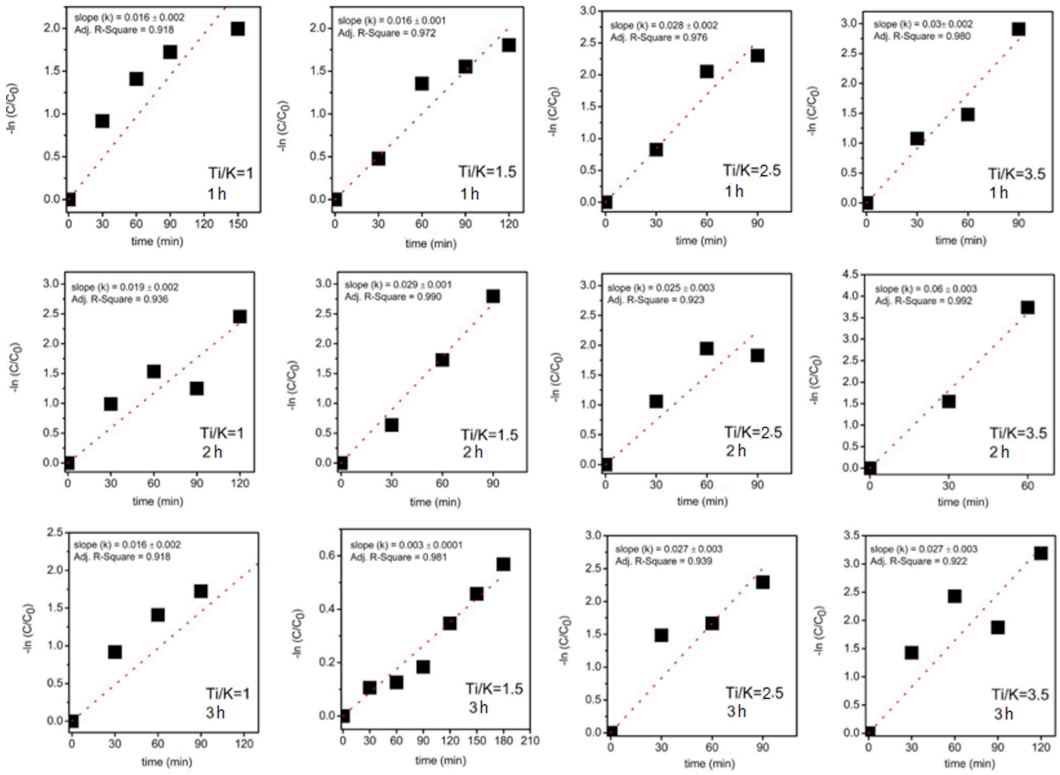


Figure A.2 Linear fit curves of MB degradation of sol-gel derived powders obtained by calcination at 600 °C with respect to time according to 1st order kinetics approach. (ln (C/C_o) versus t).

Table A. 1 Apparent degradation rate (k; min^{-1}) of sol-gel derived powders calcined at 600ºC.

Ti/K	Calcination time (h)	k (min^{-1})	Adj. R^2
1	1	0.016 ± 0.002	0.92
1.5		0.016 ± 0.001	0.97
2.5		0.028 ± 0.002	0.98
3.5		0.030 ± 0.002	0.98
1	2	0.019 ± 0.002	0.94
1.5		0.029 ± 0.001	0.99
2.5		0.025 ± 0.003	0.92
3.5		0.060 ± 0.003	0.99
1	3	0.016 ± 0.002	0.92
1.5		0.003 ± 0.0001	0.98
2.5		0.027 ± 0.003	0.94
3.5		0.027 ± 0.003	0.92

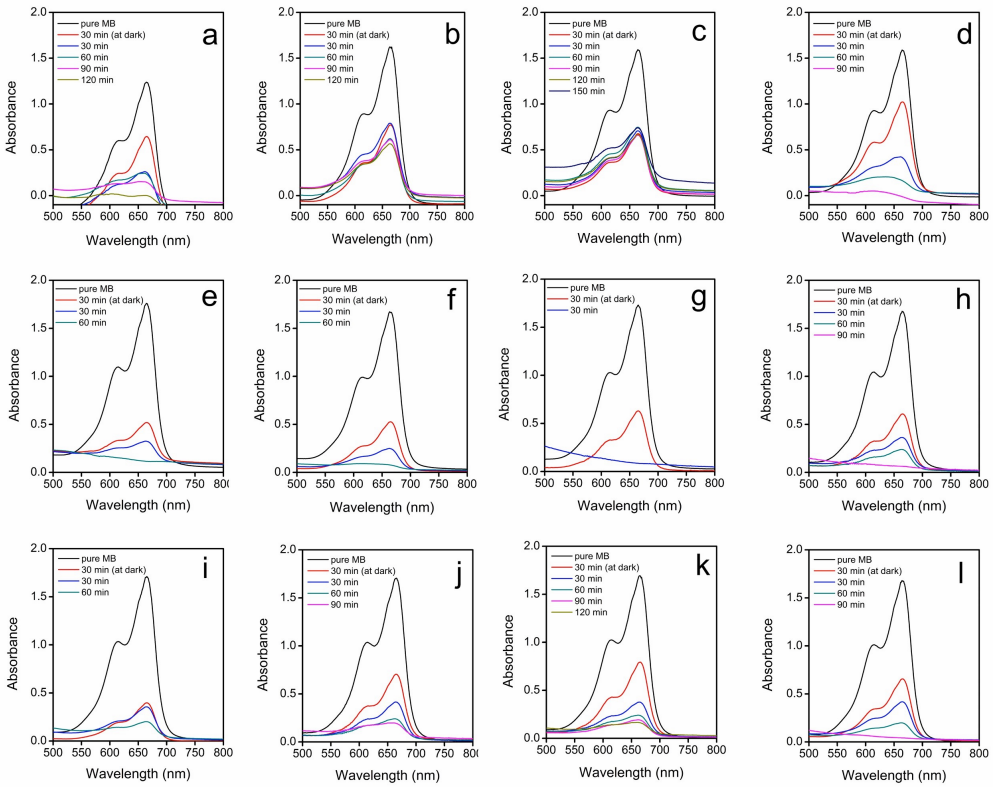


Figure A.3 UV-Vis absorbance curves of MB solutions interacted with sol-gel derived powders calcined at 800 ºC: a) Ti/K=1 b) Ti/K=1.5 c) Ti/K=2.5 d) Ti/K=3.5 for 1 h e) Ti/K=1 f) Ti/K=1.5 g) Ti/K=2.5 h) Ti/K=3.5 for 2 h and i) Ti/K=1 j) Ti/K=1.5 k) Ti/K=2.5 l) Ti/K=3.5 for 3 h.

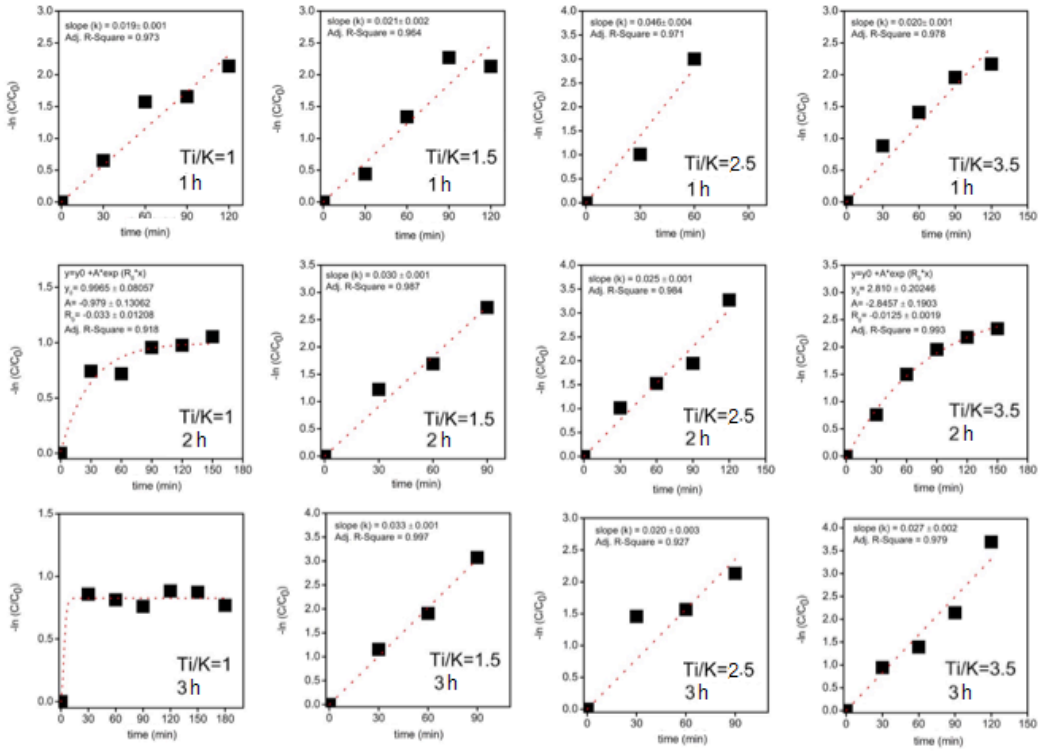


Figure A. 4 Linear fit curves of MB degradation of sol-gel derived powders obtained by calcination at 800 °C with respect to time according to 1st order kinetics approach. (ln (C/C_o) versus t).

Table A.2 Apparent degradation rate (k; min^{-1}) of sol-gel derived powders calcined at 800 ºC.

Ti/K	Calcination time (h)	k (min^{-1})	Adj. R^2
1	1	0.019 ± 0.001	0.97
1.5		0.021 ± 0.002	0.96
3		0.046 ± 0.004	0.97
3.5		0.020 ± 0.001	0.98
1	2	exponential	
1.5		0.030 ± 0.001	0.97
3		0.025 ± 0.001	0.98
3.5		exponential	
1	3	constant degradation	
1.5		0.033 ± 0.001	0.99
3		0.020 ± 0.003	0.93
3.5		0.027 ± 0.002	0.98

A2. MB degradation of hydrothermally synthesized powders

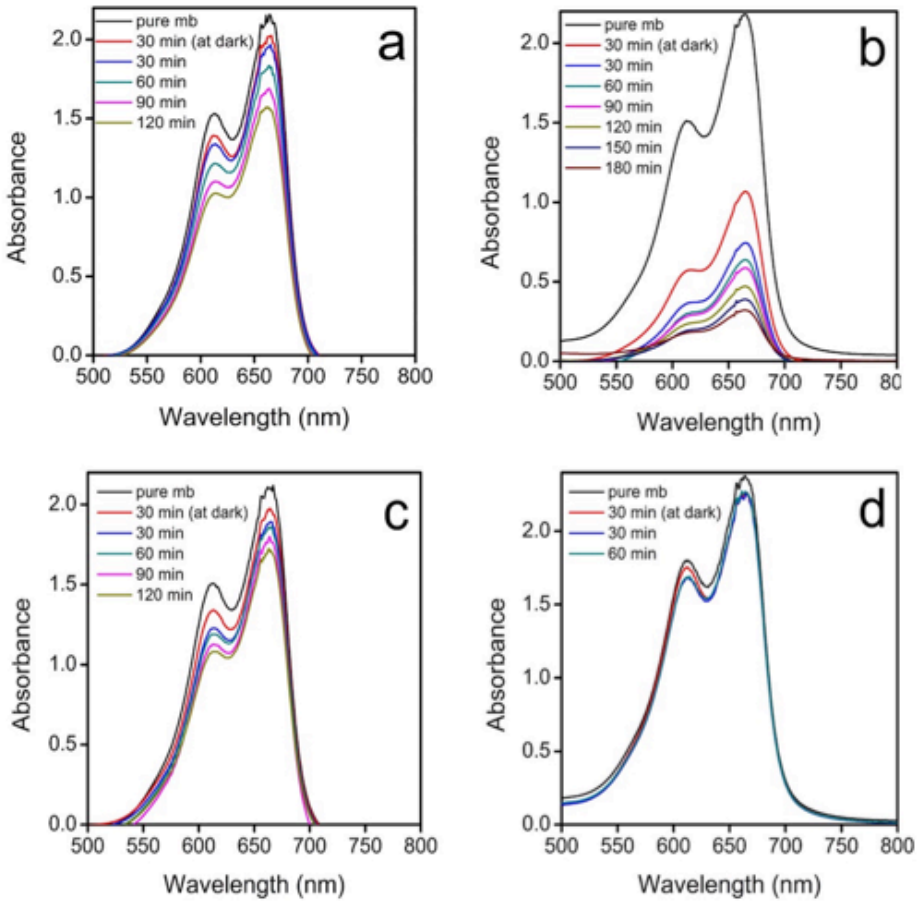


Figure A.5 UV-Vis absorbance curves of MB solutions interacted with hydrothermally synthesized powders at 180 ºC for 24 h at a) 5 M b) 10 M c) 15 M d) 20 M $KOH^{aq.}$

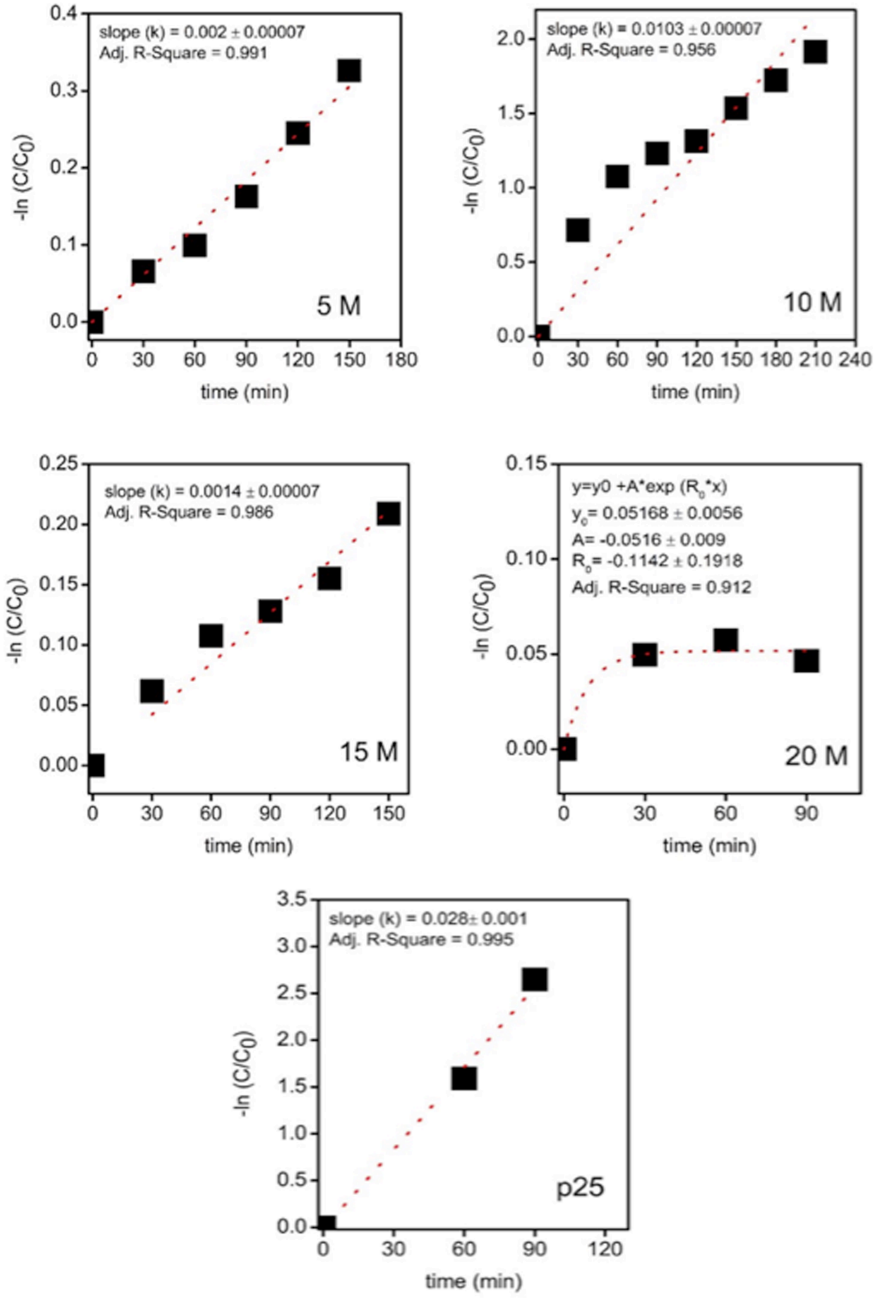


Figure A.6 Linear fit curves of MB degradation of hydrothermally synthesized powders at 180 °C for 24 h at 5-20 M $KOH^{aq.}$ with respect to time, according to 1st order kinetics approach. (ln (C/C_o) versus t).

Table A.3 Apparent degradation rate (k; min^{-1}) of hydrothermally synthesized powders at 180 ºC for 24 h at 5-20 M $KOH^{aq.}$

KOH molarity	Reaction time (H)	k (min^{-1})	Adj. R^2
5	24	0.002 ± 0.00007	0.99
10		0.0103 ± 0.00007	0.98
15		0.0014 ± 0.00007	0.99
20		Non-linear	

CIRRICULUM VITAE

DERYA KAPUSUZ

RESEARCH EXPERIENCE

Visiting Researcher (TUBITAK 2214 Scholar)
MAX/MXene Research Group
Department of Materials Science and Engineering, Drexel University, PA, USA (2014-2015)
Projects: Worked as a researcher to develop MXene (two-dimensional titanium carbide) nanostructures and MXene reinforced polymers. Moreover, drug release capability of MXenes has been explored.

Research /Teaching Assistant
METU-Scientific Human Resources Development Program (OYP)
Department of Metallurgical and Materials Engineering,
Middle East Technical University
Ankara, TR (2007-2016)

EDUCATION

Doctor of Philosophy in Metallurgical and Materials Engineering
(2009- Feb. 2016)
Middle East Technical University, Ankara, TR
Dissertation: "Production of potassium titanate whisker reinforced polymer composites for dental applications"
Advisor: Prof. Dr. Abdullah Ozturk, Department of Metallurgical and Materials Engineering,
Middle East Technical University, Ankara, TR

Master of Science in Metallurgical and Materials Engineering
(2007-2009)
Middle East Technical University, Ankara, TR
Thesis: "Sol-gel synthesis of DNA encapsulated silica"
Advisor: Prof. Dr. Caner Durucan, Department of Metallurgical and Materials Engineering,
Middle East Technical University, Ankara, TR

Bachelor of Science in Materials Science and Engineering
(2002-2006)
Anadolu University, Eskisehir, TR
Graduation Project: "Effects of processing parameters to the physical properties of B_4C-Al armor composites"
Advisor: Assoc. Prof. Dr. Gursoy Arslan, Department of Materials Science and Engineering,
Anadolu University, Eskisehir, TR

PUBLICATIONS

Peer-Reviewed Journal Publications

Journals in Science Citation Index

1. D. Kapusuz, J. Halim, C. Cunningham, R. Habas, M. Barsoum and C.L. Schauer, "Two-dimensional titanium carbide (MXene) for controlled drug release", *Journal of American Ceramic Society* (submitted)
2. D. Kapusuz, Y.E. Kalay, J. Park and A. Ozturk, "Synthesis and characterization of hydrothermally grown potassium titanate nanowires", Journal of Ceramic Processing Research, 16(3), 291-297, (2015).
3. L. Agartan, D. Kapusuz, J. Park and A. Ozturk, "Effect of initial water content and calcination temperature on photocatalytic properties of TiO_2 nanopowders synthesized by the sol-gel process", *Ceramics International*, 41(10), 12788-12797, (2015).
4. D. Kapusuz, J. Park and A. Ozturk, "Sol-gel synthesis and photocatalytic activity of B and Zr co-doped TiO_2", *Journal of Physics and Chemistry of Solids*, 74(7), 1026-1031, (2013).
5. D. Kapusuz and C. Durucan, "Synthesis of DNA-encapsulated silica elaborated by sol-gel routes", Journal of Materials Research, 28(2), 175-184, (2013).

Other Journals

1. L. Agartan, D. Kapusuz, J. Park and A. Ozturk, "Effect of H_2O/TEOT ratio on photocatalytic activity of sol-gel derived TiO_2", *Nanomaterials and Energy*, 2(6), 280-287, (2013).

Proceeding Book Chapters

1. D. Kapusuz, J. Park and A. Ozturk, " Production of potassium titanate whisker reinforced dental composites" in Advances in Bioceramics and Porous Ceramics VI, Eds. R. Narayan, P. Colombo, S. Kirihara and S. Widjaja, *John Wiley&Sons Inc*., 35-43, (2013).
2. D. Kapusuz, J. Park and A. Ozturk, " Influence of boron and/or zirconium doping on morphology and optical properties of titania", 3rd International Conference on NANOCON, *Tanger Ltd.*, 81-87, (2011).

CONFERENCES

Oral Presentations

1. L. Agartan*, D. Kapusuz, J. Park and A. Ozturk, "Effect of water/tetraethyl orthotitanate ratio on the morphology of sol-gel derived TiO2 powder and its photocatalytic activity", presented at *TMS Annual Meeting&Exhibition*, San Diego, CA, USA, (2014).
2. D. Kapusuz*, J. Park and A. Ozturk, "Production of potassium titanate whisker reinforced dental composites", presented at *37th International Conference on Advanced Ceramics and Composites*, Daytona Beach, FL, USA, (2013).

3. D. Kapusuz*, J. Park and A. Ozturk, "Influence of boron and/or zirconium doping on morphology and Optical Properties of Titania", presented at *3rd International Conference NANOCON 2011*, Brno, Czech Republic, (2011).
4. D. Kapusuz*, J. Park and A. Ozturk, "Sol-gel synthesis of B and Zr codoped titania photocatalysts" presented at *17th International Symposium on Boron, Borides and Related Materials*, Istanbul, TR, (2011).
5. D. Kapusuz* and C. Durucan, ""Encapsulation of DNA in sol-gel derived nanoporous silica" presented at *5th International Nanoscience and Nanotechnology Conference (NANOTR5*), Eskisehir, TR, (2009).

Poster Presentations

1. L. Agartan, D. Kapusuz, J. Park and A. Ozturk*, " Photocatalytic properties of TiO_2 powders synthesized by sol-gel process using different water/Ti-precursor ratio", presented at *17th International Metallurgy & Materials Congress*, TUYAP, Istanbul, TR, (2014).
2. D. Kapusuz, J. Park and A. Ozturk*, "Photocatalytic properties of potassium titanate whiskers synthesized by sol-gel process", presented at *17th International Metallurgy & Materials Congress*, TUYAP, Istanbul, TR, (2014).
3. D. Kapusuz and C. Durucan*, " Synthesis of sol-gel derived DNA encapsulating silica matrices", presented at Materials Research Society Fall Meeting, Boston, MA, USA, (2012).
4. D. Kapusuz* and C. Durucan, " Sol-gel derived nanoporous silica for DNA encapsulation", presented at *1st International Ceramic, Glass, Porcelain, Enamel, Glaze and Pigment Congress (SERES*), Eskisehir, TR, (2009).
5. D. Kapusuz* and C. Durucan, "Encapsulation of biomolecules in nanoporous silica" presented at *32nd International Conference on Advanced Ceramics and Composites*, Daytona Beach, FL, USA, (2008).
6. D. Kapusuz* and C. Durucan, "Biomolecule entrapment in/on sol-gel derived silica matrices" presented at *Workshop on Nanobiotechnology and Genome Technologies*, Antalya, TR, (2008).
7. D. Kapusuz* and C. Durucan, "Encapsulation of DNA Molecules in Sol- Gel Derived Matrices" presented at *Somer Symposium Series-1*, METU, Ankara, TR, (2007).

* *Presented by*

PEER-REVIEWER FOR JOURNALS

- Journal of Materials Science (2015-2016)
- Applied Surface Science (2015)

AWARDS

- TUBITAK 2214-A Scholarship (2013-2)
- TUBITAK 2224-A Scholarship (2012)
- Honor Award due to academic excellence (Undergraduate, 2005-2006)

GRANT APPLICATIONS

2013 -2014	METU- BAP (Researcher) No: BAP-03-08-2013-001. Coordinator: Prof. Dr. Abdullah Ozturk Synthesis of boron and/or zirconium doped TiO_2 nanoparticles by using sol-gel and solvothermal techniques.
	METU- BAP (Researcher) No: BAP-03-08-2013-004. Coordinator: Prof. Dr. Abdullah Ozturk Production and characterization of potassium titanate whisker reinforced polymer composites.
2010--2012	TUBITAK (Researcher) No: 110M206 Coordinator: Assoc. Prof. Dr. Jongee Park Production of photocatalytic and discontinuous whisker reinforced dental composites.
2010--2011	BOREN (Researcher) No: 2010.Ç0275 Coordinator: Assoc. Prof. Dr. Jongee Park Synthesis of visible-light responsive boron and zirconium doped TiO_2.
2013 -2014	METU- BAP (Researcher) No: BAP-2007-03-08-05 Coordinator: Prof. Dr. Caner Durucan Production of biomolecule encapsulation platforms to be used in biosensing.

TEACHING EXPERIENCE

- Teaching Assistant for *Basic Concepts in Materials Science* Class (MET E 227)
  METU, Fall 2015,
  Instructor: Asst. Prof. Dr. Batur Ercan
- Teaching Assistant for *Glass Science and Technology* Class (METE 421)
  METU, Fall 2009-2013, 2015
  Instructor: Prof. Dr. Abdullah Ozturk
- Teaching Assistant for *Ceramic Materials* Class (METE 451)
  METU, Fall 2009-2013, 2015
  Instructors: Prof. Dr. Abdullah Ozturk, Prof. Dr. Caner Durucan
- Teaching Assistant for *Phase Equilibria* Class (METE 301)
  METU, Fall 2009-2013
  Instructors: Prof. Dr. Abdullah Ozturk, Prof. Dr. Caner Durucan
- Teaching Assistant for *Properties of Metals and Alloys* Class (METE 222/230)
  METU, Spring 2012-2013
  Instructor: Prof. Dr. Rıza Gurbuz

- Teaching Assistant for *Structural Ceramics and Ceramic Composites* Class (METE 422)
  METU, Spring 2009-2013
  Instructor: Prof. Dr. Abdullah Ozturk
- Teaching Assistant for *Properties of Glasses* Class (METE 544)
  METU, Spring 2009-2013
  Instructor: Prof. Dr. Abdullah Ozturk
- Teaching Assistant for *Principles of Ceramic Processing* Class (METE 434)
  METU, Spring 2009-2013
  Instructor: Prof. Dr. Abdullah Ozturk
- Teaching and Laboratory Assistant for *Materials Characterization* Class (METE 310)
  METU, Fall 2008-2011
  Instructors: Prof. Dr. Caner Durucan, Prof. Dr. Tayfur Ozturk

MENTORSHIP EXPERIENCE STUDENTS

Lütfi Ağartan, METU, undergraduate/graduate studies (2011-2014). "Synthesis of B and Zr co-doped titania nanopowders by sol-gel Technique "
Currently: PhD student at Drexel University.

RELEVANT SKILLS

Language Skills (reading, writing and speaking)

- Turkish (Native)
- English (Fluent)
- German (Beginner)

Computer/Software

- Windows 7-10, OS X El Capitan
- Microsoft Office (Word, Excel, PowerPoint)
- Origin Pro8
- SigmaPlot
- Digital Microscopy (TEM Analysis)
- Carine Crystallography
- MDI Jade and Rigaku Qualitative Analysis (XRD analysis)
- GSAS, Maud, Beartex (Rietveld Analysis)
- Minitab Pro 16.0

Laboratory Skills

- Scanning Electron Microscopy (FEI Nova NanoSEM 430, Zeiss Supra 50 VP)
- Transmission Electron Microscopy (Data analysis only)
- X-Ray Diffraction (Rigaku Smart Lab)
- UV-Vis Spectroscopy (Scinco 3100, Varian Cary 200, Ocean Optics USB 2000)

- Instron 5560 Universal Analysis
- Tribometry equipped with surface profilometer (CSM Instruments/Taylor Hobson)
- High Pressure Synthesis Reactor (UTO Instruments)
- Microhardness Tester (Shimadzu)

WORKSHOPS

- 2015, Mettler Toledo, Advanced Thermal Analysis Techniques Seminar, Ankara, TR.
- 2009, School and Workshop on the Electron Microscopy of Ceramic Materials, Eskisehir, TR.
- 2009, Rietveld Analysis by Rudy Wenk, METU, Ankara, TR.

MEMBERSHIPS

Young Professionals Network, American Ceramic Society

REFERENCES

(1) Prof. Dr. Abdullah Ozturk
Address: Department of Metallurgical and Materials Engineering, E-220
Middle East Technical University, ANKARA, TR.
E-mail: abdullah@metu.edu.tr
Phone: (312) 210 5932

(2) Prof. Dr. Caner Durucan
Address: Department of Metallurgical and Materials Engineering, D-306
Middle East Technical University, ANKARA, TR.
E-mail: cdurucan@metu.edu.tr
Phone: (312) 210 5840

(3) Prof. Dr. Michel Barsoum
Address: Department of Materials Science and Engineering, Lebow 445
Drexel University, Philadelphia, PA, USA.
E-mail: barsoumw@drexel.edu
Phone: (215) 895 2338